Title

Probing Active Sites of Heterogeneous Catalysts by X-Ray Absorption Spectroscopy

Author

Li, Li

Publication Date

2021

UNIVERSITY OF CALIFORNIA

Santa Barbara

Probing Active Sites of Heterogeneous Catalysts by X-Ray Absorption Spectroscopy

A dissertation submitted in partial satisfaction of the
requirements for the degree Doctor of Philosophy
in Chemistry

by

Li Li

Committee in charge:
Professor Susannah L. Scott, Chair
Professor Mahdi Abu-Omar
Professor Phillip Christopher
Professor Gabriel Ménard

September 2021

The dissertation of Li Li is approved.

Prof. Mahdi Abu-Omar

Prof. Phillip Christopher

Prof. Gabriel Ménard

Prof. Susannah L. Scott, Committee Chair

September 2021

Probing Active Sites of Heterogeneous Catalysts by X-Ray Absorption Spectroscopy

by

Li Li

ACKNOWLEDGEMENTS

I would like to thank my graduate advisor, Professor Susannah L. Scott, for the guidance over the past five years. She has been passionate about science, inspiring me to work on challenging projects. I appreciate her logical thinking and communicative skills, which are beneficial to me inside and outside academia. I am grateful for her flexibility and support in various projects, which allows me to thrive. I would like to thank my committee members, Dr. Mahdi Abu-Omar, Dr. Phillip Christopher, and Dr. Gabriel Ménard, for their guidance.

Stanford Synchrotron Radiation Lightsource (SSRL) is my second research home, where world-class science is happening. I want to thank Dr. Simon Bare, Dr. Adam S. Hoffmen, Dr. Alexey Boubnov, and Dr. Jiyun Hong at Co-ACCESS. They have consistently been professional and supportive at the beamline, where I learned diverse and fruitful knowledge. It is my privilege to collaborate with Co-ACCESS. I am grateful to the SSRL beamline scientists, Dr. Ryan Davis, Dr. Matthew Lattimer, and Dr. Erik Nelson, for all the help and guidance in many XAS trips. Everyone at SSRL is devoted to helping me succeed in learning science. The experience at SSRL is unique to me. Because of SSRL, I met dozens of collaborators. I thank them for offering me opportunities to work on so many different projects.

It is not easy to start a graduate school journey, but thankfully I had great lab colleagues. Prof. Fan Zhang has helped me initial my research and consistently provided suggestions to my research projects. I want to thank Dr. Abigail Serrando, Dr. Jing Wu, and Tarnuma Tabassum as both colleagues and friends. I also want to thank many colleagues who came to SSRL with me because XAS trips are so tough. Besides labmates, I want to thank the UCSB staff in the glass shop, CNSI, and MRL. They are knowledgeable and always willing to help me out of trouble.

Such an adventure must have friends. I would like to thank a group of friends at UC Santa Barbara: Yuanxin Li, Zhikai Zeng, and 410 Ellwood squad (Jiren Zeng, Beihang Yu, Yuning Shen, Ganghua Mei, and Nan Wu). It is terrific to share both enjoyment and stress with them along my PhD journey. I also want to thank Shipeng Chen, my childhood friend and a UCSB Gaucho. He made sure that my life at UCSB started without any worry and showed me how wonderful California could be outside of academic life. I am grateful to have bunches of college and childhood friends that I can count on over these years. Finally, I leave a friend`s name in this thesis, Chuanchuan Zhang, just in case we forget him at some point.

My best luck is my supportive family members. Thank my mother, Ruxian Zhong, for everything, in particular the nature of resilience and optimism. She is the best, no doubt. I am fortunate enough to inherit curiosity and courage from my father, Jie Li. I appreciate their confidence in me, encouraging me to be ambitious. I want to thank my partner, Qichang Li. He has been my reliable mood stabilizer and cheerleader over the past seven years, no matter how far the physical distance between us is. I cannot say enough appreciation to express my gratitude.

Last but not least, I would like to acknowledge funding sources in my PhD research because the experiments are really expensive: Financial support of the U.S. Department of Energy, Office of Science, Division of Basic Energy Sciences, under the Catalysis Science Initiative (DE-FG-02-03ER15467) is gratefully acknowledged. Use of the Stanford Synchrotron Radiation Lightsource, SLAC National Accelerator Laboratory, is supported by the U.S. Department of Energy, Office of Science, Office of Basic Energy Sciences, under Contract DE-AC02-76SF00515. Co-ACCESS, is supported by the U.S. Department of Energy, Office of Basic Energy Sciences, Chemical Sciences, Geosciences and Biosciences Division. The use of the research facilities within the California NanoSystems Institute, supported by the University of California, Santa Barbara and the University of California, Office of the President. The MRL Shared Experimental Facilities are supported by the MRSEC Program of the NSF under Award No. DMR 1720256; a member of the NSF-funded Materials Research Facilities Network. Thank UC Santa Barbara's Mellichamp Academic Initiative in Sustainability for summer fellowship support.

VITA OF LI LI

September 2021

EDUCATION

Doctor of Philosophy in Chemistry, University of California, Santa Barbara, 2021

Bachelor of Science in Chemistry, Nanjing University, China, 2016

PROFESSIONAL EMPLOYMENT

2016-2018: Teaching Assistant, Department of Chemistry, University of California, Santa Barbara

PUBLICATIONS

1. Jain, S. K.; Tabassum, T.; Li, L.; Ren, L.; Fan, W.; Tsapatsis, M.; Caratzoulas, S.; Han, S.; Scott, S. L. P-Site Structural Diversity and Evolution in a Zeosil Catalyst. *J. Am. Chem. Soc.* **2021,** *143*, 1968-1983.
2. Li, L.; Scott, S. L. X-ray Absorption Spectroscopy Investigation into the Origins of Heterogeneity in Silica-supported Dioxomonomolybdates. *J. Phys. Chem. C* In revision.
3. Groden, K.; Vila, F. D.; Li, L; Bare, S. R.; Scott, S. L.; McEwen, J.-S. First Principles Approach to Extracting Chemical Information from X-Ray Absorption Near-Edge Spectra of Ga-Containing Materials. Submitted.
4. Li, L; Nakad, J. A.; Vila, F.D.; Hoffman, A. S.; Boubnov, A.; Bare, S. R.; Taoufik, M.; Scott, S. L. Investigation of $Ga^{i}Bu_3/Al_2O_3$ structural evolution for propane dehydrogenation by *operando* X-ray absorption spectroscopy. In preparation.
5. Li, L; Vila, F.D.; Hoffman, A. S.; Slattery J.; Bare, S. R.; Scott, S. L. X-ray absorption signatures of Ga(I) in molecular complexes and heterogeneous catalysts. In preparation.
6. Luo, Z.; Li, L.; Nguyen, V. T.; Nie, R.; Kanbur, U.; Biswas, A.; Sadow, A.; Wang, B.; Scott, S. L.; Huang, W.; Qi, L. Non-Innocent Carbon Support Enables a Redox-active Atomically-Dispersed Iron Catalyst for C–O Hydrogenolysis. In preparation.

PRESENTATIONS

Li Li, Susannah L. Scott. Synthesis and activation of a well-defined dioxomolybdenum(VI) site in a MoO_3/SiO_2 olefin metathesis catalyst, Oral presentation at ACS National Fall Meeting, Aug 25th, 2019, San Diego, CA

AWARDS

Mellichamp Academic Initiative in Sustainability Fellowship (2017-2018)

ACS Travel Grant (2018)

Young scientist award (2020)

FIELDS OF STUDY

Heterogeneous catalysis, X-ray absorption spectroscopy, *operando* techniques

ABSTRACT

Probing Active Sites of Heterogeneous Catalysts by X-Ray Absorption Spectroscopy

by

Li Li

In order to design more effective catalysts, we deployed X-ray absorption spectroscopy (XAS) to develop structure-activity relationships for supported heterogeneous catalysts. Starting from carefully-designed synthesis, the metal ions are uniformly dispersed on the support. The pre-treatment and other synthetic modifications are strategically chosen to alter the structure and reactivity of the metal sites. Specially, we explored catalytic systems in which the active sites are mononuclear metal complexes grafted on the oxide supports. XAS is essential for probing the local structures of the metal centers, such as electronic properties and coordination geometry. The applications of the catalysts include olefin metathesis, propane dehydrogenation and C-O hydrogenolysis.

Monomolybdate sites with relatively uniform first coordination spheres were synthesized by a direct solid-solid reaction between MoO_2Cl_2 and silica. The resulting $Mo(=O)_2(OSi)_2$ sites were characterized and compared to the spectra of several well-defined model molybdate compounds. In extended X-ray absorption fine structure (EXAFS) analysis, the attenuation of the long-range EXAFS features at ca. 3 Å in $Mo(=O)_2(OSi)_2$ sites suggests the attachment to the silica surface as molybdasiloxane rings of variable ring size. The partially well-defined $Mo(=O)_2(OSi)_2$ sites were treated with a few common activation methods, but failed to

catalyze propylene metathesis. Only exposure to olefins at high temperatures (>500 °C) leads to promoting propylene metathesis at 23 °C and resulting in an active site fraction as high as 36%. However, the co-existence of multiple types of metal sites makes it difficult to identify the active sites.

$Ga^{i}Bu_3/\gamma$-Al_2O_3 catalyst promotes propane dehydrogenation at 550 °C, and the Ga species present under reaction conditions were unknown. We used *operando* XAS to monitor the evolution of Ga K-edge from as-prepared to catalytic conditions. The X-ray absorption near edge structure (XANES) reveals that isobutyl ligands are replaced by oxygen-donor ligands derived from the alumina surface in a single, gradual process, leading to a 3-coordinate mononuclear Ga site at 550 °C. Additional, minor Ga(I) species may form simultaneously. DFT-based simulations elucidate the ligand influence on the Ga K-edge XANES features, such as the white line intensity and edge position. This structural insight sheds light on the correlation between the mononuclear Ga site and the subsequent catalytic activity.

The direct synthesis of single-atom Fe catalysts supported on nitrogen-doped carbon gives five-coordinate Fe(III), with four in-plane pyridinic nitrogen donors and one axial hydroxyl ligand. These Fe catalysts exhibit high selectivity, activity, and reusability for C–O bond hydrogenolysis using H_2 at temperatures as low as 170 °C. The characterization of the catalyst shows the reduction of Fe(III) to Fe(II) sites with loss of the hydroxyl ligand under reaction conditions. The four-coordinate Fe(II) sites are the active sites for H_2-splitting. The interaction between metal sites and the support is critical to promote activity.

Table of Contents Page

LIST OF FIGURES

LIST OF TABLES

Chapter 1. Introduction

1.1 X-ray absorption spectroscopy in heterogenous catalysis

X-ray absorption spectroscopy (XAS) probes atomic structures directly.[29] The XAS data reflect the nature of the neighboring environment. The catalysts are scanned by tunable synchrotron X-rays near the binding energy (-200 – 1000 eV) of core electrons. Once the incident X-ray energy surpasses the binding energy, the atom will strongly absorb X-rays and show a sharp increase in the X-ray absorption coefficient, μ(E). This sharp increase is described as an “edge jump.” As the energy increases, μ(E) consists of oscillations that gradually fade near the end of the scan. Due to different electronic transition mechanisms, XAS data are divided into two regions, and analyzed by different approaches: X-ray absorption near-edge spectroscopy (XANES) and extended X-ray absorption fine structure (EXAFS).

XAS has several advantages in heterogeneous catalysis research. Firstly, the measurement selectively targets the element of interest without interference from other elements. The test capability is independent of crystallinity, isotope labeling, etc.[48] More importantly, the low concentration limit (as low as 50 ppm) is suitable for dilute supported catalysts under a flexible range of testing conditions, from -269 – 1200 °C, from vacuum to high pressure.[49] These advantages make XAS a unique technique for understanding supported metal sites. However, it also comes with limitations. As a bulk characterization technique, the XAS spectrum represents average structural information; namely, the minor species in the sample cannot be identified. In particular, if the active site fraction in metal-supported catalysts is unknown or small, the conclusion deduced from XAS may be misleading. Moreover, XAS data analysis relies on model input; thus, preliminary characterization of the sample should be conducted before XAS characterization.

1.1.1 X-ray Absorption Near-Edge Spectroscopy (XANES)

The XANES region (-50 – 150 eV from the absorption edge) is associated with the electronic transition from the inner shell to the valence orbitals (i.e., 1*s* electron excitation at the K-edge), following the dipole selection rule ($\Delta l = \pm 1$).[50] As a result, the XANES features can be used as a fingerprint to quickly access structural information, such as oxidation states and geometry. The higher oxidation states require higher incident energies to excite core electrons. As a result, the rising edges of higher oxidation state materials are expected to be at higher energy positions. For example, the edges from Mo foil, MoO_2, and MoO_3 shift to progressively higher energy positions, Figure 1.1. However, the oxidation state is not the only factor to determine the edge locations. Spin states, ligands, and coordination numbers affect the edge position simultaneously, complicating the correlation between oxidation state and edge energy.[51-52] Therefore, the determination of oxidation state should not only reply on the edge position.

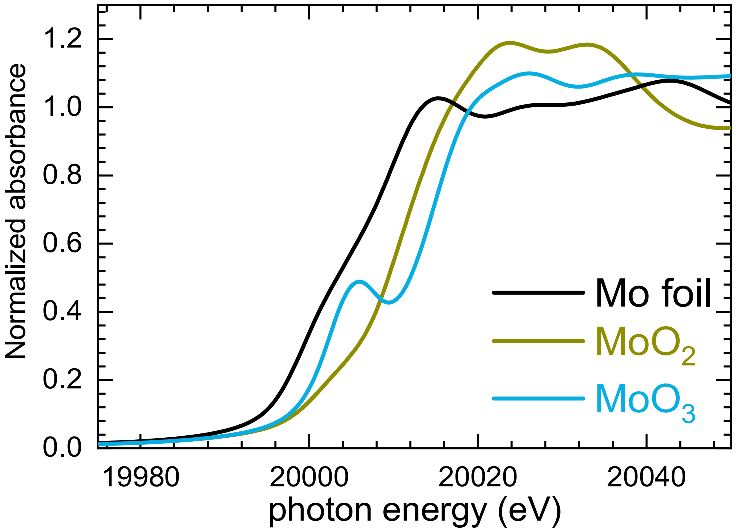

Figure 1.1 The Mo K-edge XANES comparison for Mo foil, MoO_2, and MoO_3.

In addition to the main edge, pre-edge features appear in the rising edge region. They arise from transitions to valence orbitals or quadrupolar transitions ($\Delta l = \pm 2$); thus, the pre-edge intensity is weaker than the main edge (dipole transition).[53] In the Mo K-edge XANES, the pre-edge intensity is primarily affected by the Mo geometry. Non-centrosymmetric structures have strong pre-edge features due to the *p-d* mixing, whereas non-centrosymmetric structures show little pre-edge intensity. For instance, MoO_2 contains octahedral MoO_6 and does not show any pre-edge feature, Figure 1.2. Na_2MoO_4 has tetrahedral MoO_4 and shows a strong pre-edge. If the octahedral geometry is distorted, a pre-edge feature can still be observed, but the intensity is lower than in tetrahedral geometry.[54] In addition to these qualitative interpretations, principal component analysis (PCA),[55] linear combination fitting (LCF),[56] and XANES deconvolution[57] are often used to assess changes in concentrations of species over time, providing kinetic information about reactions.

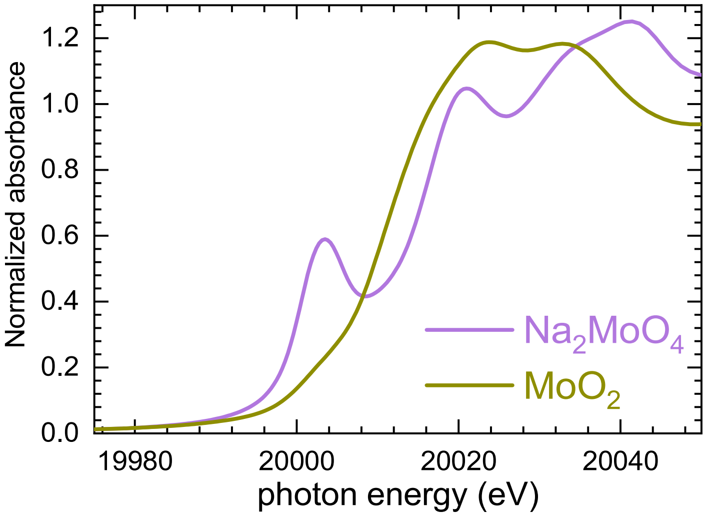

Figure 1.2 The Mo K-edge XANES comparison for Na_2MoO_4 and MoO_2.

Although the XANES interpretation can be as easy as described above, a deeper understanding of the electronic transition benefits from theoretical approaches. The various simulation methods are widely used to decipher the experimental XANES data, including FEFF,[12] StoBe,[13] ORCA,[14] etc. [15] Recently, the advanced algorithm such as neutral network and machine learning was introduced to investigate nanoparticles in catalytic reactions.[16-18] These simulation approaches become more critical when oxidation states or geometry cannot easily explain unusual features.

1.1.2 Extended X-ray Absorption Fine Structure (EXAFS)

EXAFS is collected after the XANES region, at ca. 150 – 1000 eV after the edge energy. EXAFS can offer the average atomic neighboring information, such as atomic species and distances. Unlike XANES, the EXAFS data analysis requires several steps: normalization, background subtraction, conversion to *k*-space (wavenumber of photo-electron), visualization by Fourier transform (R-space), and quantitative curvefittings. The local information is acquired by simulating the back-scattering paths with the EXAFS equation in eq. 1.[19]

$$\chi(k) = \sum_i \frac{(N_i S_0^2) F_i(k)}{k R_i^2} \sin\left[2kR_i + \delta_i(k)\right] e^{-2\sigma_i^2 k^2} e^{-\frac{2R_i}{\lambda(k)}} \tag{1}$$

The amplitude factors include reduction term S_0^2, degeneracy N, Debye-Waller factor σ^2, and amplitude term $F_i(k)$. Except for $F_i(k)$, the rest parameters are refined, constrained, or fixed in the fitting process. $F_i(k)$ is directly stimulated and given in the data process software because it primarily depends on the atomic weight, Z. Thus, the EXAFS is unable to differentiate the atoms with similar weights ($\Delta Z < 5$) at the same distances, like oxygen and carbon atoms at ca. 2.0 Å. The weight-dependent $F_i(k)$ term also means the hydrogen atom is too light to be detected in the EXAFS. $\delta_i(k)$ and distance R are the phase shift terms.

1.1.3 Quick-EXAFS

The typical EXAFS setup in the beamline hutch consists of a monochromator, ion chambers, sample stations, and fluorescence detectors (if needed).[66] The incident beam from the synchrotron ring is tuned by a monochromator (a set of two parallel Si-made crystals), following Bragg`s law, $n\lambda = 2d\ sin\theta$. As a result, the change of incident energy is achieved by moving the monochromator vertically. Then, the beam passes the first ion chamber (I_0), sample, second ion chamber (I_1), reference foil, and third ion chamber (I_2) in order. Inert gases filling in ion chambers are ionized upon X-ray passes through. The applied electric field on the ion chamber panels drives charged ions to the opposite sides, which generates a small current (proportional to X-ray intensity). This small current is amplified and converted to I_0, I_1, and I_2 readings during the experiments. The XAS measurement generally takes 15 – 40 min per scan to record the EXAFS region up to k = 16 Å^{-1}. The number of XAS scans is usually 4 – 6, depending on the data quality. Such an acquisition time is sufficient for *ex-situ* experiments but too slow to capture the evolution of catalysts under reaction conditions, which can happen within minutes.

The demand for *in-situ/operando* XAS experiments in catalysis kinetic research led to the development of quick scanning EXAFS.[67-68] To speed up XAS scanning, the monochromator and ion chambers are redesigned. The monochromator for quick-EXAFS is operated with a camshaft or a direct-drive motor, reducing the mechanical complexity of crystal movement.[69] Thus, the data acquirement no longer needs deadtime between every data point. The monochromator rotation is driven by a high-torque alternative-current motor, allowing for scanning one EXAFS spectrum as fast as 10 ms.[70] The standard ion chambers suffer from slow response time if the acquisition rate is within seconds per scan. The response time is primarily compromised by the slow velocity of positively charged ions; thus, a grid electrode is inserted into the ion chamber to take up these positive ions.[71] By doing so, the remodeled ion chamber will only count electrons for measuring X-ray intensity to meet the quick-EXAFS speed.

1.2 Mo-based Olefin Metathesis Catalysts

In an olefin metathesis reaction, the C=C bonds of two identical or different olefins exchange substituents to form a pair of new olefins. The participation of a catalyst is essential. Generally, olefin metathesis catalysts can be classified as homogeneous or heterogeneous. The molecular catalysts developed by Schrock[26] and Grubbs[27] are the most representative homogeneous metathesis catalysts and have been widely used in organic synthesis (for which the inventors were awarded the Nobel Prize). For large-scale industrial processes, heterogeneous catalysts are preferred for ease of use in continuous (flow) reactors and because they are readily regenerated. Starting in the 1960s, these types of olefin metathesis catalysts have been used in a limited number of petrochemical processes (e.g., the Phillips Triolefin Process, the Shell Higher Olefins Process (SHOP) and the production of neohexene).[28] Their synthesis and activation are simple: typically, Mo or W oxides are dispersed on a porous support such as silica or alumina and calcined. Recent improvements have led to higher catalytic activities, longer catalyst lifetimes, better tolerance of polar groups and solvents, and varying E/Z selectivity. However, the activation mechanisms are often poorly understood, limited to empirical parameter optimization without molecular-level information.

The synthesis of a conventional, heterogeneous olefin metathesis catalyst usually involves impregnating a support with an aqueous solution containing a soluble metal precursor, evaporating the excess solvent, then activating the solid.[29] In addition to activation by high-temperature calcination[30], researchers have investigated treatment with various reducing agents[31], or alkylating co-catalysts.[32-33] Although these methods can improve activity, a major obstacle in mechanistic studies remains the low fraction of active sites, typically ca. 1% according to active site counting[34] and poisoning experiments.[35] There are always multiple types of sites, and it is difficult to correlate them directly with the active sites in a heterogeneous catalyst prepared by a conventional synthesis route. Furthermore, the heterogeneity of the support complicates the identification of active sites.[12]

Spectroscopic characterization can provide helpful evidence for active site structures and activation mechanisms. IR[36], Raman[37], UV-vis[38], XAS[39], and isotopic exchange[40] have been widely applied to heterogeneous metal oxide catalysts. However, most spectroscopic studies describe the majority inactive sites rather than the minority active sites.[36] *In-situ* or *operando* techniques may help identify changes that occur upon activation, but they have limitations. First, sensitivity is an issue because of the low fraction of active sites. Second, peak assignments are based on models whose validity is still debated. Finally, some techniques like X-ray absorption spectroscopy give average structural information about mixtures. Thus, all spectroscopic information should be analyzed cautiously and not over-interpreted.

One strategy to minimize the number of variables involves dispersing a well-defined metal complex precursor uniformly on a simple support to create a material with a single type (or small number) of sites. Such materials can explain the relationships between particular structures and their catalytic activity in olefin metathesis. Re_2O_7/Al_2O_3 is the most active metathesis catalyst at room temperature; however, Re is one of the rarest metals on Earth.[41] WO_3/SiO_2 catalysts are cheaper but less active and can only promote metathesis reactions at 250 °C or higher.[42] In our study, we focus on molybdenum oxide supported on silica (MoO_3/SiO_2). MoO_3/SiO_2 system uses cheaper and abundant metal, which is active at temperatures from 25 to 200 °C, depending on the activation method.

The pseudo-tetrahedral dioxomolybdenum(VI) structure, $Mo(=O)_2(OSi)_2$ has been discussed most frequently in activation mechanisms; many researchers regard this structure to be the immediate precursor to the active sites, by analogy to the well-known molecular Schrock catalysts.[43] The presence of $Mo(=O)_2(OSi)_2$ structures is based on the assignment of the Raman spectrum,[38] however, this does not prove that they are present or that they are the precursors of the active sites. Unfortunately, little previous work has intentionally ruled out other possibilities.

Investigating activation mechanisms for well-defined catalyst structures can provide fundamental information about how active sites form and more efficient promotion. The first stage is the synthesis and characterization of a well-defined, dioxomonomolybdenum structure supported on silica via grafting of a molecular precursor under mild conditions. To ensure four-coordiante geometry at molybdenum, the requirements for an effective molecular precursor are (1) pre-existing di-oxomolybdenum structure; (2) good leaving groups such as halide or alkyl ligands; (3) enough stability to maintain the same molybdenum geometry after grafting. The second stage is to observe the reactivity of the grafted di-oxomolybdenum sites towards olefins. Several possible activation mechanisms are shown in Scheme 1.1.[36] We will investigate whether any of them occur when the well-defined dioxomolybdenum sites react with olefins. One approach is to analyze the organic products of these reactions. Two main challenges are: (1) ensuring the fraction of active sites is large enough to detect the organic products; (2) maintaining the uniformity of the molybdenum sites during the grafting process and subsequent reactions.

Scheme 1.1 Proposed mechanisms for initial carbene formation upon contact of the catalyst with olefins.

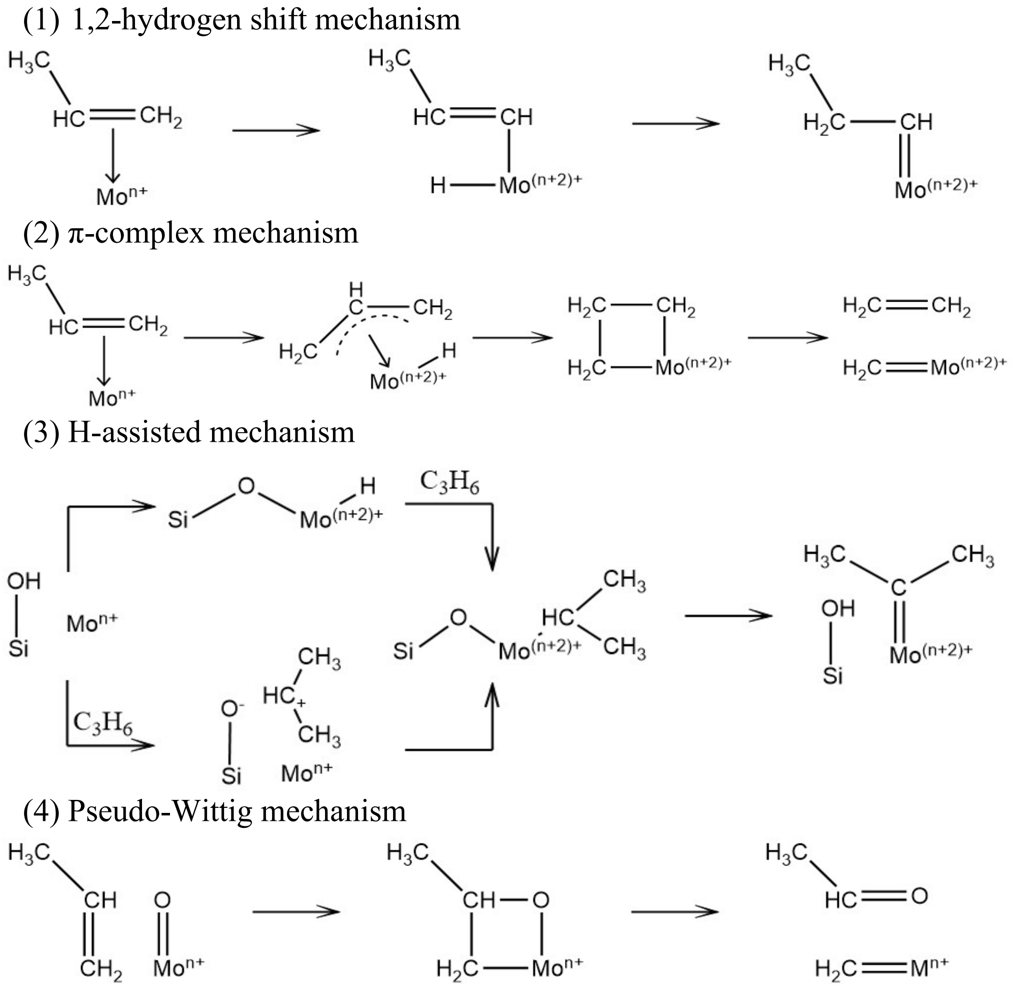

(1) 1,2-hydrogen shift mechanism

(2) π-complex mechanism

(3) H-assisted mechanism

(4) Pseudo-Wittig mechanism

1.3 Ga-based Propane Dehydrogenation Catalysts

Propane dehydrogenation benefits from providing propylene directly with high selectivity, along with H_2 as a valuable co-product. The propane feedstock can be obtained from natural gas liquids, often at a cost advantage over propylene from naphtha cracking.[44] Two commercial on-purpose propylene processes, Catofin and Oleflex, are based on CrO_x/Al_2O_3 and Pt-Sn/Al_2O_3 catalysts, respectively.[45-47] The environmental hazards of Cr and the high cost of Pt, together with their complex modes of catalyst regeneration, motivate the search for alternative catalysts. One active area of research focuses on Ga dispersed on oxides. These catalysts are likely related in their function to Ga-modified zeolite catalysts used in alkane dehydroaromatization (including the Cyclar process which converts propane and butanes to BTX aromatics),[48] in which ion-exchanged Ga catalyzes alkane dehydrogenation, then Brønsted acid sites catalyze subsequent olefin oligomerization and cyclization.[49]

The synthesis of Ga-based oxide catalysts for propane dehydrogenation is typically achieved by impregnating a high surface area support with an aqueous solution of Ga(III) ions, which are then activated by calcination.[45] These materials can also be made by anhydrous deposition of an organogallium(III) complex onto the dry support, without calcination.[50-53] Since propane dehydrogenation is highly endothermic; the reaction is typically conducted at 500 – 800 °C. Under these conditions, the desired reaction is often accompanied by undesired cracking and coking. The experimental availability of information regarding the active sites is limited by the severe conditions, resulting in an on-going controversy about the catalytic mechanism.

High temperature reduction in H_2 (> 500 °C) is reported to improve dehydrogenation activity in Ga-based catalysts,[1] suggesting a role for lower Ga oxidation states. The redox mechanism invokes a Ga(I) site, which reacts with propane by C-H oxidative addition.[1] Ensuing β-H elimination from a propylGa(III) hydride intermediate is proposed to be followed by reductive elimination of H_2 from a Ga(III) dihydride, regenerating Ga(I). Alternatively, oxidation of Ga(I) was proposed to occur by proton transfer from a nearby Brønsted acid site, resulting in a hydridoGa(III) site that activates propane.[54] Heterolytic cleavage of the C-H bond in propane by Ga(III) has also been proposed, generating a propylGa(III) site and a proton associated with support oxygen.[54-58] Alternatively, the reaction has been suggested to generate a hydridoGa(III) site and a propylcarbenium ion associated with the support.[59-60] In both heterolytic cleavage mechanisms, propylene and H_2 are formed in subsequent steps, which may or may not be concerted.[61] Yet another mechanistic suggestion involves the synergistic action of neighboring Al(III) and Ga(III) sites.[62] Computational discrimination of these mechanisms is hampered by a lack of direct evidence for the active sites.[56] Therefore, identifying the spectroscopic signatures of various Ga sites that may be present in supported Ga catalysts will be critical for guiding future simulations.

As a prelude to attempting to describe the active sites, it is necessary to understand the types of dispersed Ga sites created during catalyst synthesis. The proposed sites present in Ga/oxide materials have been variously described as mononuclear $[Ga]^+$, $[GaO]^+$, $[GaH(OH)]^+$, $[Ga(OH)_2]^+$, $[GaH]^{2+}$, and $[GaH_2]^+$,[1, 57, 63-64] as well as dinuclear $[Ga_2O_2]^{2+}$ and $[Ga_2O_2H_2]^{2+}$.[65-66] All are formally Ga(III), except for $[Ga]^+$. The range of ligands includes hydrido, terminal oxo, hydroxo, bridging oxo (GaOGa), and support oxygens. Stoichiometric uptake of H_2 and formation of H_2O at 600 °C were also interpreted as support for $[Ga]^+$.[54] Similarly, titration of the proposed $[Ga]^+$ sites with N_2O was presented as evidence for their existence and quantitative conversion to $[GaO]^+$.[50] IR peaks in the range 1980 - 2059 cm^{-1} that appear after exposure to H_2 at 500 – 800 °C were assigned to a variety of Ga(III) hydrides.[64, 67-68]

After calcination, coordination numbers for Ga/silica and Ga/zeolite catalysts are close to 4, with Ga-O distances from 1.73 to 1.93 Å.[63-64, 69] The shorter distances are associated with anionic ligands (1.73 – 1.80 Å), while the longer distances are typical of neutral oxygen donors (1.90 – 1.93 Å). Upon flowing H_2 at 650 °C, the intensity of the first major peak in the non-phase-corrected FT-EXAFS at ca. 1.5 Å decreases, consistent with a reduction in average coordination number and/or replacement of one or more oxygen-donor ligands by hydrogen.[63,

[69] Since Ga scattering is distinctly different, Ga nuclearity can also be established by XAS analysis of these longer-distance peaks in the Fourier transform (FT).[53, 63] However, their intensities are often weak in catalytic materials due to static disorder, and the thermal disorder in high-temperature *in-situ* experiments makes their interpretation even more challenging.

Subtle changes in the XANES are often more sensitive than EXAFS, especially when a distribution of sites is present, although rigorous XANES assignments can be more difficult. The energies and intensities of the $1s \rightarrow 4p$ transitions at the Ga K-edge reflect both oxidation state and local bonding geometry (e.g., tetrahedral vs. octahedral). After calcination, supported Ga catalysts show broad white lines at 10,375 – 10,380 eV, in the range of peak positions for inorganic Ga(III) standards such as Ga_2O_3 and $Ga(acac)_3$.[69-70] In a study of β-Ga_2O_3 and Ga/silica materials, deconvolution of the overlapping peaks at 10,375 and 10,379 eV (assigned empirically to tetrahedral and octahedral Ga(III), respectively) was used to estimate the fraction of 4- vs. 6- coordinate Ga.[71]

The Ga K-edge XAS is crucial for identifying the active sites in supported Ga dehydrogenation catalysts and proposing reaction mechanisms. However, the systematic interpretation of Ga XANES is not well established. For example, the peak at 10,368 – 10,373 eV can arise from Ga(I) or 3-coordinate Ga(III).[70] Such an ambiguous assignment does not help pinpoint any active sites. Moreover, Ga(III)-hydride species are proposed as the active sites, primarily based on IR and stoichiometry experiements.[55-56, 72] Although Hydrogen is too light to contribute EXAFS signal, the XANES of Ga-hydride may have some characteristics. Investigating and simulating the XAS spectra of $[Ga]^+$, Ga(III)-hydride, and 3-coordinate Ga(III) give more confidently assign the spectra of the heterogeneous catalysts.

1.4 Objectives

Our goal is to use XAS to investigate well-defined catalysts in various reactions. We aim to graft uniform metal sites onto the surfaces, and characterize them by XAS and other techniques. Then, the structural information is correlated with catalytic activity to identify the active sites and propose activation mechanisms.

In Chapter 2, we describe the synthesis of partially uniform dioxomolybdate sites on fumed silica, $Mo(=O)_2(OSi)_2$. XAS characterization provides details of the structural evolution during the grafting process. Although the first coordination sphere is well-defined, the long-range paths are challenging to observe. We show how single- and multiple-scattering paths interfere, reducing the EXAFS amplitude at ca. 3 Å. The impact of the intrinsic heterogeneity of the attachments to the support on reactivity should be considered.

In Chapter 3, we examine the activation of $Mo(=O)_2(OSi)_2$ for olefin metathesis, compared with conventionally made MoO_3/SiO_2 catalysts. The comparison of catalytic performances explains why $Mo(=O)_2(OSi)_2$ site is not likely to represent an active site on MoO_3/SiO_2 catalysts. The high-temperature olefin treatment is only effective for some supported Mo catalysts, which may undergo the pseudo-Wittig mechanism to activate $Mo(=O)_2(OSi)_2$.

In Chapter 4, we used *operando* XAS to monitor the evolution of as-prepared Ga^iBu_3/Al_2O_3 during activation and reaction. *Ex-situ* characterization of Ga^iBu_3/Al_2O_3 shows a 3-coordinate mononuclear Ga site $(AlO)Ga^iBu_2$, with a long, non-bonded Ga-O path. We observe how the di-isobutylgallium(III) ion is transformed into a 3-coordinate Ga oxide on the support. The C/O ligand exchange at similar distances is not obvious in EXAFS, whereas Ga K-edge XANES shows clear changes in energy positions and white line intensities.

In Chapter 5, we investigate single-atom Fe catalysts on the nitrogen-doped carbon support. These Fe catalysts catalyze C–O bond hydrogenolysis with H_2 at temperatures as low as 170 °C, and their activities are affected by carbonization temperatures at the catalyst synthesis step. The EXAFS curvefitting analysis provides the metal-support interaction information, including the average coordination number of Fe and ligand distances from Fe.

Chapter 2. X-ray Absorption Spectroscopy Investigation into the Origins of Heterogeneity in Silica-supported Dioxomonomolybdates

2.1 Introduction

Mo oxides have long been known as components of catalysts in diverse reactions such as alkane dehydrogenation,[45, 72-73] selective oxygenation of hydrocarbons and oxidation of oxygenates,[74-79] ammoxidation of alkenes,[80-81] as well as in olefin epoxidation and metathesis.[82-83] Many of these catalysts have simple compositions, consisting of an active Mo oxide phase dispersed on a relatively inert support such as silica or alumina. A typical synthesis involves impregnation of the support with an aqueous solution of a Mo precursor (typically, ammonium paramolybdate), followed by evaporation of the water and calcination at high temperature.[30] In these conventionally-made Mo-based catalysts, several molybdate structures with different coordination numbers and nuclearities are proposed to co-exist, Scheme 2.1a-d.[84-85]

Scheme 2.1 Comparison of proposed structures for supported molybdate sites: (a) 4-coordinate supported dioxomolybdate; (b) 5-coordinate supported mono-oxomolybdate; (c) a supported dimolybdate; (d) a supported polymolybdate, as well as (e) structures of two molecular molybdenum oxoalkoxides,[86-88] (f) active site structures of two molybdate-containing enzymes: sulfite oxidase and DMSO reductase,[89] (g) dimethoxyethane adduct of MoO_2Cl_2,[90] and (h) the extended solid structure of MoO_2Br_2.[91]

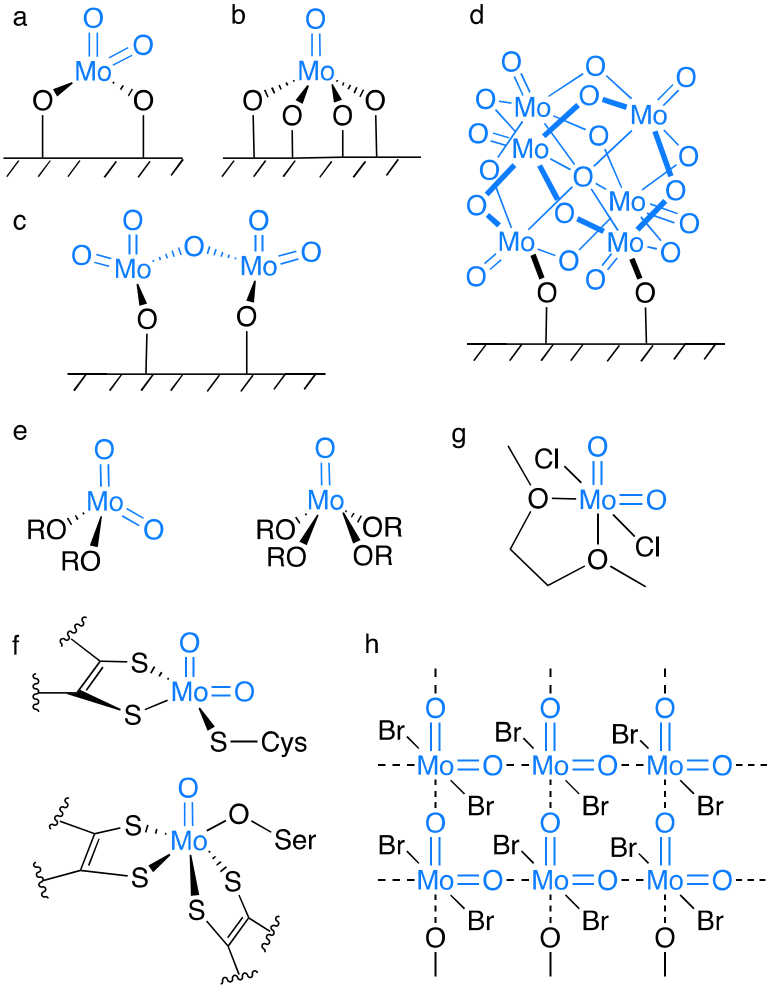

At lower Mo loadings, four-coordinate monomeric $Mo(=O)_2(OSi)_2$ sites (Scheme 2.1a) are proposed to dominate the site distribution,[92-93] and are inferred to be the immediate precursors of the active sites. They often serve as a starting point for computational modeling of supported Mo catalysts.[94-95] An alternate monomeric structure, the 5-coordinate $Mo(=O)(OSi)_4$ site in Scheme 2.1b, was also proposed in silica-supported catalysts on the basis of Raman and UV-vis spectroscopic assignments.[96-97] Both monomeric structures have analogs in well-characterized molecular molybdenum oxoalkoxides (Scheme 2.1e). However, a computational study suggested that formation of supported $Mo(=O)(OSi)_4$ on partially dehydroxylated silica is unlikely, since the initial density of hydroxyl groups is rarely high enough to generate four closely co-located Mo-O-Si linkages.[98] The $Mo(=O)_2(OSi)_2$ structure resembles that of Schrock-type olefin metathesis catalysts, with two multiply-bonded ligands and two bulky alkoxide ligands.[43] For the silica-supported analog, there is as yet little direct evidence for its spontaneous activation (oxo→alkylidene transformation).[36, 99] In addition, the low coordination number (4) contrasts with the strong preference for higher coordination numbers in molybdate-containing enzymes (Scheme 2.1f), *cis*-dioxoMo(VI) complexes that lack bulky anionic ligands, such as $MoO_2Cl_2L_2$ (where L may be an ether, amine, or phosphine, Scheme 2.1g),[100-102] and solid MoO_2Br_2 (Scheme 2.1h).[91]

Oligomeric Mo sites that co-exist with monomeric molybdates in supported catalysts may include dimolybdates and sites with even higher Mo nuclearities (Scheme 2.1c,d).[103] These oligomers are generally considered to be less catalytically active than monomeric sites (particularly in olefin metathesis).[30, 104] The presence of multiple types of Mo sites, combined with the heterogeneity of the amorphous support,[105] continue to thwart efforts to definitively correlate molybdate structures with their activity. Furthermore, given the low active site fractions in conventional catalysts, features belonging to the active sites may have intensities below the detection limits of many techniques such as Raman, UV-vis, NMR and XAS spectroscopies. Lacking molecular-level information, much catalyst development therefore relies on empirical parameter optimization. Access to uniform silica-supported molybdates would facilitate investigations of the relationships between the structure of an active site and its immediate precursor, leading to insight about activation mechanisms.

A powerful approach for obtaining uniform dispersed molybdenum sites involves grafting molecular complexes onto a support under mild conditions. Several reported attempts have resulted in at least partial success. $MoO_2Cl_2(DME)$ grafted onto carbon was characterized as a dispersed, 4-coordinate dioxomolybdate, although the precise nature of the anchoring to the carbon surface was not specified.[106] An attempt to graft $MoO_2Cl_2(THF)_2$ onto MCM-41 silica led to 6-coordinate $Mo(=O)_2(OSi)_2(THF)_2$.[8] The molecular complexes $Mo(=O)_2[OSi(O^tBu)_3]_2$ and $Mo(=O)(O^tBu)_4$ were deposited onto silica with the goal of creating well-dispersed $Mo(=O)_2(OSi)_2$ sites via a two-step reaction sequence.[107-108] While both experiments were deemed successful, their reported Mo K-edge EXAFS data differ markedly, suggesting variability (of unknown origin) in the resulting structures.

In this work, we report a new, direct route to well-defined monomeric dioxomolybdate sites via the solid-solid reaction of SiO_2 with MoO_2Cl_2. Although it has an extended, 6-coordinate structure in the solid state, MoO_2Cl_2 generates isolated, 4-coordinate molybdates anchored at surface hydroxyl sites. Structural insight about molybdate-silica interactions provided by X-ray absorption spectroscopy, with careful comparison to molecular analogs, lays a foundation to relate the structures of grafted molybdates to their activation and subsequent catalytic performance.

2.2 Experimental Methods

Materials. MoO_2Cl_2 and several Mo-containing standards (MoO_3, MoO_2, and Na_2MoO_4) were purchased from Sigma-Aldrich and used as-received. Since MoO_2Cl_2 is easily hydrolyzed, it was stored and used inside a N_2-filled glovebox. Ag_2MoO_4 (99%, Alfa Aesar), Ph_3SiCl (96%, Sigma-Aldrich), 1,2-dichloroethane (anhydrous, 99.8%, Sigma-Aldrich) and acetonitrile (anhydrous, 99.8%, Sigma-Aldrich) were used as-received. $MoO_2(OSiPh_3)_2$ was synthesized from Ag_2MoO_4 and Ph_3SiCl, according to a published method.[88] Fumed SiO_2 (Aerosil 380, B.E.T. surface area 383 m^2/g) was obtained from Evonik Degussa. BN (99.5%, Alfa Aesar) was used as-received, except for when it served as a solid diluent for air-sensitive materials. Then it was dried under dynamic vacuum (0.1 mTorr) at 500 °C for at least 12 h. Anhydrous dichloromethane, toluene, and pentane (UHP grade, Glass Contours) were passed through a distillation-free solvent purification system (JC Meyer) and stored over 4 Å molecular sieves (Sigma-Aldrich) inside a N_2-filled glovebox. O_2 (UHP grade, Airgas) was transferred into a storage bulb containing 3 Å molecular sieves (Sigma-Aldrich) prior to use.

Synthesis of supported molybdate. SiO_2 was heated under dynamic vacuum (0.1 mTorr) at 200 °C for at least 12 h before use, and stored in a N_2-filled glovebox. MoO_2Cl_2 (pale yellow flakes) was ground using a mortar and pestle into a fine powder. The pretreated SiO_2 (500 mg) was combined under N_2 with the MoO_2Cl_2 powder (30 mg, 0.15 mmol) in a 120 mL Schlenk flask. The amount of MoO_2Cl_2 was chosen to achieve a Mo loading suitable for transmission XAS measurements (ca. 3 wt%). The solid mixture was agitated using a magnetic stirring bar at room temperature under dynamic vacuum (0.1 mTorr) for 3 h. It was washed with anhydrous dichloromethane (20 mL, chosen for MoO_2Cl_2 solubility) and filtered. Because of the low volatility of dichloromethane, the solid was also washed sequentially with toluene and *n*-

pentane (20 mL each) and filtered following a previously described procedure.[109] The resulting solid was dried under vacuum (0.1 mTorr) at room temperature overnight.

To remove residual chlorine, the solid was loaded into a quartz flask and heated in 100 Torr O_2 at 10 °C/min to 600 °C and held at that temperature for 1 h. The reactor was evacuated for 10 min, then cooled to room temperature while evacuating. Grafted Mo was extracted by stirring the solid (ca. 20 mg) in 0.1 M HNO_3 at 70 °C for 1 h and filtering. The Mo content was determined by ICP-AES (Thermo iCAP 6300). Cl analysis was performed on a 400 mg sample by ALS Environmental Laboratory (Tucson, AZ). The reported detection limit is 0.0025 wt% Cl.

Spectroscopy. IR spectra were acquired using self-supporting pellets (ca. 20 mg, 5 mm diameter), made with a quick press (International Crystal Laboratories) inside an Ar-filled glovebox. Spectra were recorded in transmission mode over the range 4000–400 cm^{-1} using a Bruker Alpha FTIR spectrometer, accumulating 32 scans at a resolution of 2 cm^{-1}. The absorbance was normalized by the peak intensity of the silica overtone at 1856 cm^{-1}.

XAS spectra were recorded at the Mo K-edge (20,000 eV) on beamline 4-1 at the Stanford Synchrotron Radiation Lightsource, which operates at 3.0 GeV with a current of 500 mA. Data were acquired in transmission mode, using N_2-filled ionization chambers as detectors. Spectra were acquired under a protective atmosphere of He in a cryostat at 10 K. Mo standards were diluted to ca. 3 wt% Mo with BN. For energy calibration, a Mo foil was placed after the second ionization chamber, following the incident beam direction. The energy of the first maximum in the first derivative of its XANES was defined to be 20,000 eV.[110]

XAS data were processed and analyzed using the Demeter software package.[111] A linear function was subtracted from the pre-edge region, then the edge jump was normalized using

Athena software. The $\chi(k)$ data were isolated by subtracting a smooth, third-order polynomial approximating the absorption background of an isolated atom. The cut-off value for R_{bkg} was set to 1.0 to ensure removal of the artificial peak that can appear below 1.0 Å. The k^3-weighted $\chi(k)$ data were Fourier-transformed after applying a Hanning window function. The amplitude reduction factor (S_0^2), coordination numbers (N_i), distances to the scattering atoms (R_i), and mean-squared displacements (σ_i^2) were obtained by nonlinear fitting, with least-squares refinement, of the EXAFS equation to the Fourier-transformed data in R-space, using Artemis software. EXAFS spectra of individual paths were simulated using FEFF6,[111] using imported crystallographic information files of model compounds.

2.3 Results and Discussion

Grafting MoO_2Cl_2 onto silica. Molecular oxometal halide complexes (M = Cr, Mo, W) are known to react with partially dehydroxylated silica surfaces via M-X bond protonolysis to give high-valent oxometal sites. Depending on the reaction stoichiometry, the outcome may be a single type of grafted site (with or without residual halide ligands), or a mixture (Scheme 2.2). For example, CrO_2Cl_2 vapor reacts with silica at room temperature to give exclusively monopodal $\equiv SiOCrO_2Cl$ sites.[112] MoO_2Cl_2 is not readily grafted from the vapor phase, due to its low volatility. In solution, it forms monomeric $MoO_2Cl_2L_2$ complexes, with coordinated solvent (L).[113] Attempts at its solution-phase grafting onto silica were reported to give materials with low Mo loadings (ca. 1 wt%), suggesting that protonolysis is reversible.[8, 114] Our attempts to graft MoO_2Cl_2 onto silica (pretreated at 200 °C) from a THF solution at room temperature led to $Mo(=O)_2(OSi)_2(THF)_x$ sites which, according to IR spectroscopy, retain

THF ligands. The solvent was not removed even after heating at 300 °C under dynamic evacuation overnight. Consequently, we sought a solvent-free route to prepare $Mo(=O)_2(OSi)_2$.

Scheme 2.2 Examples of silica grafting reactions reported for oxometal(VI) chloride complexes[8, 109, 115]

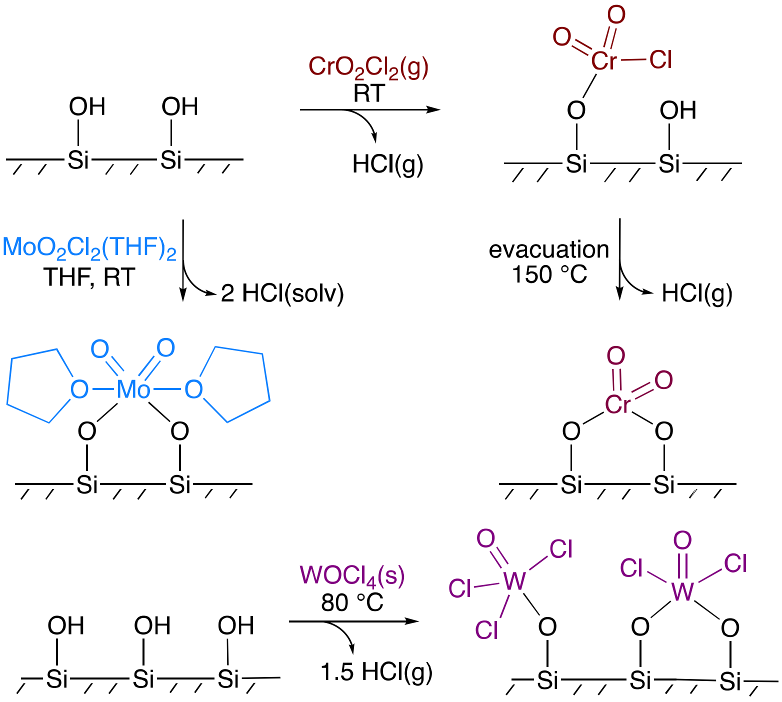

In a previous report, the solid-solid reaction of $WOCl_4$ with SiO_2 (partially dehydroxylated at 200 °C) was achieved at 80 °C.[109] The compound has a polymeric structure[116] and a low vapor pressure (ca. 3.5 Torr at 120 °C).[117] The outcome of the grafting reaction was a mixture of monopodal and bipodal W sites (Scheme 2.2). Expecting analogous reactivity for solid MoO_2Cl_2, the yellow powder was combined with dry, partially dehydroxylated SiO_2 in a mixture containing 2.7 wt% Mo. The initial density of accessible silanols on the silica (partially dehydroxylated at 200 °C) was ca. 1.9 OH/nm^2 (1.2 mmol OH/g),[118] such that the Mo/SiOH ratio was 1:4, i.e., silanols were present in excess. The mixture was allowed to react under dynamic vacuum (0.1 mTorr) for 3 h at room temperature, during which time it changed color from yellow to white. The solid was thoroughly washed with various organic solvents (see Methods) to ensure complete removal of unreacted MoO_2Cl_2 and residual solvent.

The IR spectra in Figure 2.1 show that grafting causes a decrease in the intensity of the SiO-H stretching modes. The change is consistent with protonolysis of MoO_2Cl_2 by surface silanols. Based on the difference spectrum (Figure S2.1), the reactive silanols include non-H-bonded hydroxyls that give rise to the sharp peak at 3747 cm^{-1},[119-120] as well as internal hydroxyls in H-bonded silanol chains that give rise to the band at 3524 cm^{-1}.[119] Internal (i.e., inaccessible) silanols, responsible for the band at 3620 cm^{-1},[121] appear to be unreactive.

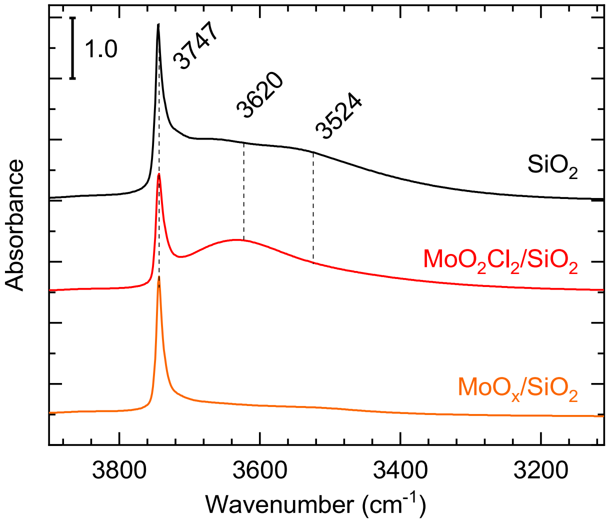

Figure 2.1 IR spectra of silica (Aerosil A380, pretreated overnight at 200 °C under dynamic vacuum), before (black) and after (red) grafting MoO_2Cl_2 in a solid-solid reaction at room temperature, and after calcination at 600 °C (orange). All spectra were baseline-corrected, then normalized to the absorbance of the silica overtone at 1865 cm^{-1}. Spectra are offset vertically for clarity.

According to elemental analysis, the resulting solid contains 2.6 wt% Mo, confirming that most of the MoO_2Cl_2 reacted with the silica. The solid also contains 2.7 wt% Cl, corresponding to an atomic ratio Cl:Mo = 0.28. Thus, MoO_2Cl_2 grafting appears to lead to a mixture of monopodal and bipodal molybdate sites (Scheme 2.3), in a 1:2.6 ratio.

Scheme 2.3 Grafting of MoO_2Cl_2 onto partially dehydroxylated silica, via a solid-solid reaction.

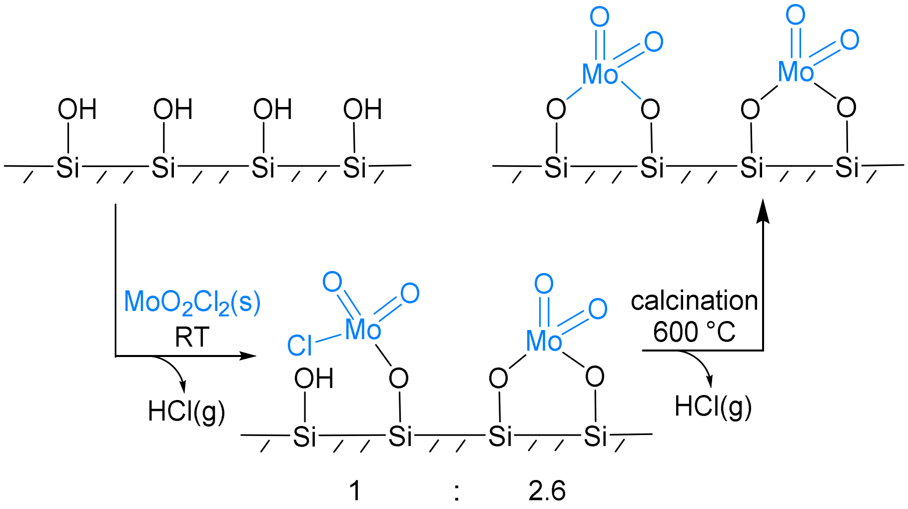

XANES investigation of local molybdate symmetry. To assess the local structure of the grafted molybdate sites, we first explored the Mo K-edge XANES of four well-defined Mo compounds: Na_2MoO_4, $MoO_2(SiPh_3)_2$, MoO_2, and MoO_3. Their spectra are shown in Figure 2.2. The Mo K-edge position is assigned operationally as the first maximum after the pre-edge peak in the first derivative. As expected, the edge energy is lower for MoO_2 (20,011.0 eV) than for any of the Mo(VI) standards (20,011.6 – 20,016.7 eV), Table S2.1.

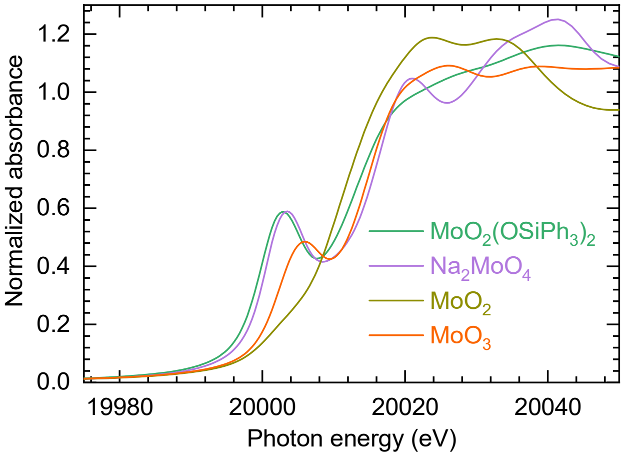

Figure 2.2 Comparison of Mo K-edge XANES for four model compounds: $MoO_2(OSiPh_3)_2$ (green), Na_2MoO_4 (purple), MoO_3 (orange), and MoO_2 (olive).

The 1*s*→4*d* quadrupole transition appears in the XANES as a pre-edge peak. Since this transition is only allowed in non-centrosymmetric systems, its intensity reflects the local Mo symmetry. As expected, the spectra of both four-coordinate compounds, Na_2MoO_4 (T_d) and $MoO_2(OSiPh_3)_2$ (C_{2v}), show strong, well-resolved pre-edge features, at 20,003.4 and 20,003.2 eV, respectively (Figure 2.2). In distorted six-coordinate MoO_3 (C_{3v}), the pre-edge feature is slightly less intense and appears at a higher energy (20,006.4 eV). Octahedral MoO_2 has a very weak shoulder in the pre-edge region (seen more clearly in the first derivative of its XANES, Figure S2.2).

The Mo K-edge XANES of MoO_2Cl_2 is shown in Figure 2.3a (and is also directly compared to those of the molybdate model compounds in Figure S2.2**)**. The edge is located at 20,011.6 eV. This position is considerably lower than for MoO_3 (20,015.0 eV), and more closely resembles the edge energy for MoO_2 (20,011.0 eV). However, the presence of other peaks in the edge region complicates precise identification of the edge position.[15] In particular, the 1*s*→4*p* shakedown transition associated with Cl-to-Mo charge transfer appears superposed on the edge, lowering the apparent edge position.[122-123]

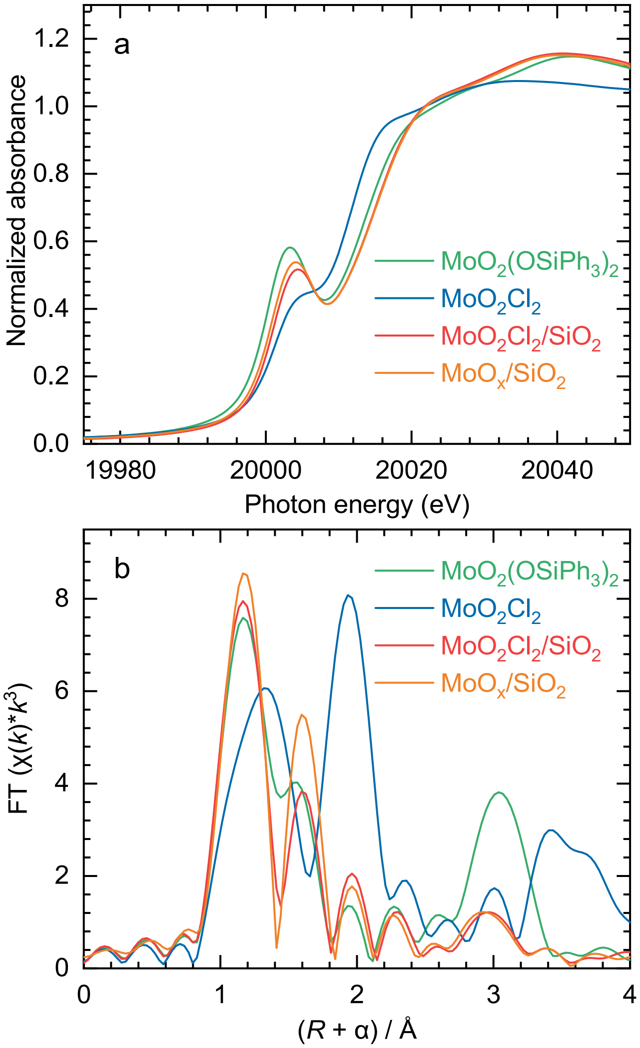

Figure 2.3 Comparison of Mo K-edge XAS: (a) XANES, and (b) FT-EXAFS magnitude, for $MoO_2(OSiPh_3)_2$ (green), MoO_2Cl_2 (blue), MoO_2Cl_2/SiO_2 (red) and MoO_x/SiO_2 (orange).

Although the crystal structure of MoO_2Cl_2 has not been reported, one study[124] suggested that it likely has an extended, layered structure similar to those of MoO_2Br_2 (Scheme 2.1h) and

WO_2Cl_2. In both compounds, the metal atoms are 6-coordinate, with 4 bridging oxygen atoms and 2 terminal halide atoms.[91, 125] In position and intensity, the incompletely resolved pre-edge peak in the XANES of MoO_2Cl_2 resembles that of MoO_3, consistent with a distorted octahedral geometry for MoO_2Cl_2. A similar weak pre-edge feature was observed in the XANES of 6-coordinate $MoO_2Cl_2(THF)_2$.[8]

Grafting onto silica causes the pre-edge peak of MoO_2Cl_2 to become more intense and better resolved, Figure 2.3. In both its shape and position (20,004.3 eV), it now resembles closely the spectrum of 4-coordinate $MoO_2(OSiPh_3)_2$ (C_{2v}). These changes are consistent with a decrease in Mo coordination number upon grafting, from 6 to 4. In addition, the apparent Mo K-edge energy increases, from 20,011.6 to 20,015.2 eV. This value lies between the edge positions for $MoO_2(OSiPh_3)_2$ and Na_2MoO_4, Figure S2.3 and Table S2.1. Since an increase in Mo formal oxidation state is obviously not possible for MoO_2Cl_2, the apparent edge shift upon grafting instead reflects the loss of chloride ligands, and the resulting lower intensity of the peak associated with the shakedown transition.

EXAFS investigation of molybdate structure. The FT-EXAFS of MoO_2Cl_2 is shown in Figure 2.3b. Two major peaks at 1.3 and 1.9 Å in the FT magnitude (not phase-corrected) arise due to Mo-O and Mo-Cl single-scattering, respectively. The peak at 1.9 Å likely also includes contributions from the expected longer Mo-O path, by analogy to the structure of MoO_2Br_2 (Scheme 2.1h). The broad intensity in the region 3 – 4 Å in the FT-EXAFS of MoO_2Cl_2 is consistent with Mo-Mo single-scattering in the extended solid-state structure.

Grafting MoO_2Cl_2 onto silica causes the broad peak at ca. 1.4 Å to resolve into two peaks, located at 1.1 and 1.6 Å (Figure 2.3b). The intensities in the FT magnitude at ca. 1.9 and 3.5 Å decrease strongly relative to the spectrum of MoO_2Cl_2, Figure 2.3b. Suppression of the peak at ca. 1.9 Å suggests replacement of most chloride ligands by less strongly-scattering oxygen-donor ligands, while the loss of the peak at 3.5 Å is consistent with disruption of the extended structure (and therefore disappearance of the Mo-Mo path). Below 2 Å in *R*-space, the appearance of grafted MoO_2Cl_2 closely resembles the EXAFS of $MoO_2(OSiPh_3)_2$.

In the FT-EXAFS of MoO_2Cl_2/SiO_2, a weak feature at ca. 2.9 Å (more visible in the imaginary component of the FT, see below) represents a scattering interaction involving atoms of the silica support. The spectrum of $MoO_2(OSiPh_3)_2$ has a surprisingly intense peak at about the same distance. It represents contributions principally from three paths: Mo-Si single-scattering at 3.45 Å, and two multiple-scattering paths: Mo-O-Si at 3.47 Å, and Mo-O-Si-O at 3.48 Å (Scheme 2.4). FEFF6 simulation predicts the highest intensity for the Mo-O-Si double-scattering path due to its higher degeneracy, Figure 2.4a. Other multiple-scattering paths involving the $Mo(=O)_2$ moiety, such as Mo-O-O-Mo double- or rattle-scattering, are predicted to have much smaller intensities and are not considered further here.

Scheme 2.4 Paths predicted by FEFF to contribute to the FT-EXAFS magnitude at ca. 3 Å in the non-phase-corrected spectrum of $MoO_2(OSiPh_3)_2$: (a) Mo-Si single-scattering path ($N = 2$, light blue); (b) Mo-O-Si-O triple-scattering path ($N = 2$, dark blue); (c) Mo-O-Si double-scattering path ($N = 4$, pink).

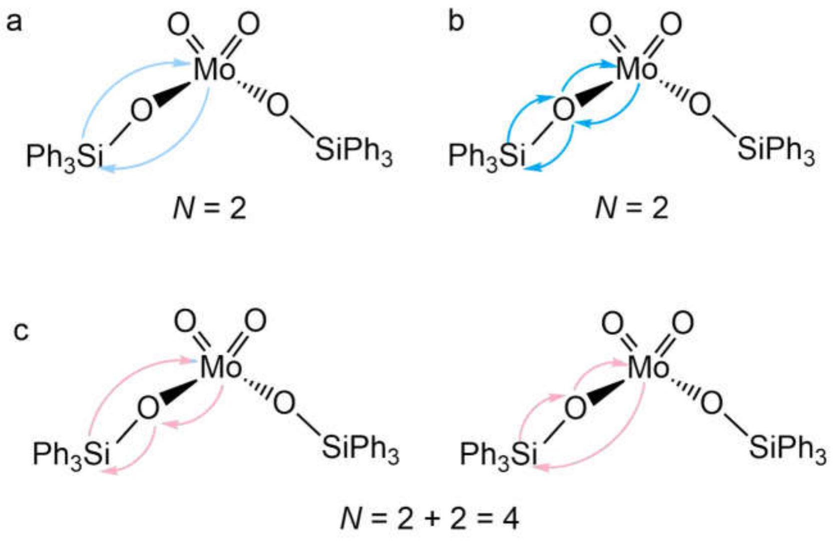

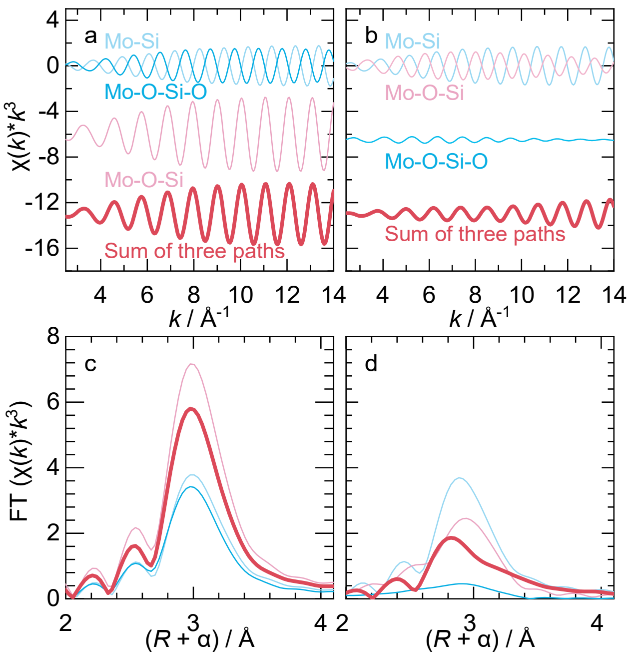

Figure 2.4 FEFF-predicted long-range paths in the Mo K-edge EXAFS of (a,c) $MoO_2(OSiPh_3)_2$, with a MoOSi angle of 164 °, and (b,d) $MoO_2(OSiPh_3)_2(PPh_3)$, with MoOSi angles of 139 and 144 °: (a,b) k^3-weighted $\chi(k)$ functions, and (c,d) k^3-weighed EXAFS, for Mo-Si (light blue, $N = 2$), Mo-O-Si (pink, $N = 4$), Mo-O-Si-O (blue, $N = 2$) paths, and their

sum (heavy red line). The following parameters were fixed in the FEFF6 simulation: $S_0^2 = 1$, $\Delta E_0 = 0$ eV, $\sigma^2 = 0$ Å^2.

The FT-EXAFS magnitude of $MoO_2(OSiPh_3)_2$ at ca. 3 Å reflects the contributions of three Si-containing paths. For the Mo-Si single-scattering path, the $\chi(k)$ contribution is similar in amplitude but out-of-phase with that for the Mo-O-Si-O triple-scattering path. Thus, the major contributor to the long-range path in the FT-EXAFS magnitude is the Mo-O-Si double-scattering path, Figure 2.4c. However, the EXAFS intensity of a multiple-scattering (MS) path depends strongly on its bond angle. In particular, MS intensities are significant for larger angles (in the range 150 – 180 °), due to the focusing effect.[126-127] According to the crystal structure of $MoO_2(OSiPh_3)_2$, ∠Mo-O-Si is 163.6 °.[88] Coordination of PPh_3 results in smaller ∠Mo-O-Si values for $MoO_2(OSiPh_3)_2(PPh_3)$, 138.7 and 143.9 °. Although FEFF predicts little change in the intensity of the Mo-Si single-scattering path as a result of PPh_3 coordination, the intensities of the multiple-scattering paths (especially that of the Mo-O-Si-O path) are much weaker (Figure 2.4b). Since the simulated $\chi(k)$ functions for the Mo-Si and Mo-O-Si paths are out-of-phase, the overall result is a much lower total intensity in k-space (Figure 2.4d). Therefore, a decrease in ∠Mo-O-Si is manifested in strong suppression of the corresponding feature in the FT-EXAFS spectrum. A similar phenomenon is also observed in the spectrum of grafted MoO_2Cl_2, consistent with a smaller average ∠Mo-O-Si values for linkages between the molybdate and the silica surface.

The structure of the grafted sites was investigated further by curvefitting. In order to reduce the number of adjustable parameters in the fit, the Cl:Mo molar ratio of 0.3 measured by elemental analysis was used to fix the Mo-Cl and long Mo-O coordination numbers to 0.3

and 1.7, respectively, consistent with a four-coordinate dioxomolybdate structure. The fits are shown in Figure 2.5 and Figure S2.4, with curvefit parameters summarized in Table 2.1 Curvefit parameters [a] for the analysis of the Mo K-edge EXAFS of MoO2Cl2/SiO2, before and after calcination The short Mo=O distance is (1.69 ± 0.01) Å, consistent with the value reported for $MoO_2(OSiPh_3)_2$ (1.690 Å).[88] The Mo-OSi path at (1.87 ± 0.01 Å) is significantly longer than the corresponding bond distance in $MoO_2(OSiPh_3)_2$ (1.815 Å), presumably due to electronic differences between the silica "ligand" and the triphenylsilanolate ligand. However, the EXAFS result is consistent with DFT simulations of silica-supported molybdates, which report distances of 1.892 and 1.895 Å for these long Mo-O paths.[98] At 2.30 Å, the Mo-Cl distance resembles the corresponding bond distance in $MoO_2Cl_2(H_2O)_2$ (2.346 Å).[128] Overall, the EXAFS is consistent with MoO_2Cl_2/SiO_2 being a mixture of ca. 70% $Mo(=O)_2(OSi)_2$, and ca. 30% $Mo(=O)_2(OSi)Cl$, as shown in Scheme 2.3.

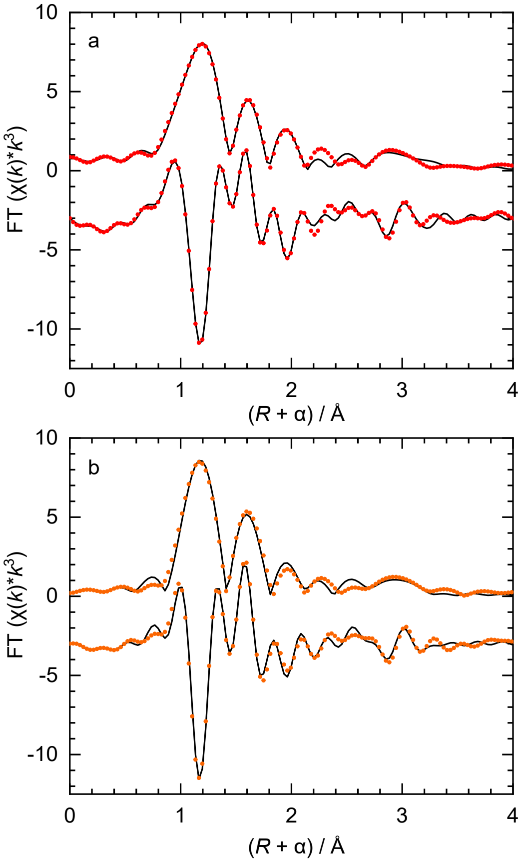

Figure 2.5 Curvefits of the Mo K-edge EXAFS for MoO_2Cl_2/SiO_2, (a) before, and (b) after calcination, showing the fit (black lines) superposed on the FT magnitude and its imaginary component (points). Fits in *k*-space are shown in Figure S2.4.

Table 2.1 Curvefit parameters [a] for the analysis of the Mo K-edge EXAFS of MoO_2Cl_2/SiO_2, before and after calcination

Material	Path	d / Å [b]	N	R / Å	$10^{-3}\ \sigma^2/\text{Å}^2$
	Mo=O	1.690	2 [d]	1.69(1)	1.5(5)

MoO_2Cl_2/SiO_2 [c]	Mo-O	1.816	1.7 [e]	1.87(1)	2(1) [f]
	Mo-Cl	2.346	0.3 [e]	2.30(2)	2(1) [f]
	Mo-Si	3.448	1.7 [e]	3.47(2)	5(1)
	Mo-O-Si	3.466	3.4 [e]	3.52(3)	7(3)
MoO_x/SiO_2 [g]	Mo=O	1.690	2 [d]	1.68(1)	2(1)
	Mo-O	1.816	2 [h]	1.88(2)	3(1)
	Mo-Si	3.448	2 [h]	3.48(4)	7(3)
	Mo-O-Si	3.466	4 [h]	3.53(3)	9(4)

[a] S_0^2 was fixed at the value refined for Na_2MoO_4, 0.98. Data ranges: $2.4 \leq k \leq 14.0$ Å^{-1}, $1.0 \leq R \leq 4.0$ Å. The total number of independent data points is 22.1. [b] Reference distances for Mo=O, Mo-O and Mo-Si paths are from the crystal structure of $MoO_2(OSiPh_3)_2$.[88] The reference distance for the Mo-Cl path is from the crystal structure of $MoO_2Cl_2(H_2O)_2$.[128] [c] ΔE_0 = 1(2) eV was refined as a global fit parameter. The total number of variable parameters in the fit is 10, with an R-factor of 0.011. [d] This coordination number was fixed at $N = 2$. [e] To limit the number of variables in the fit, these coordination numbers were fixed based on elemental analysis (Cl/Mo = 0.3), i.e., N(Mo-O) + N(Mo-Cl) = 2.0 and 2N(Mo-O) = 2N(Mo-Si) = N(Mo-O-Si). Since N is correlated with σ^2, and since the contributions of these paths vary with ∠Mo-O-Si, fixing N in this way will cause the corresponding σ^2 values to increase. [f] These disorder terms were constrained to the same value to limit the number of variable parameters in the fit. [g] ΔE_0 = 3(1) eV was refined as a global fit parameter. The total number of variable parameters in the fit is 9, with an R-factor of 0.013. [h] To limit the number of variables in the fit, these

coordination numbers were constrained such that *N*(Mo-O) = *N*(Mo-Si) = 2 and *N*(Mo-O-Si) = 4. Since *N* is correlated with σ^2, and since the contributions of these paths vary with ∠Mo-O-Si, fixing *N* in this way will cause the corresponding σ^2 values to increase.

Although the FT magnitude for MoO_2Cl_2/SiO_2 has no prominent long-range peaks, a small feature is clearly visible at 2.9 Å in the imaginary component of the FT, Figure 2.5b. In studies of MoO_3/SiO_2 made by conventional routes,[97, 129-131] similar features have been assigned to Mo-Mo paths because their Raman spectra also contain bands at ca. 994 and 818 cm^{-1} that resemble the Mo-O-Mo stretching modes of MoO_3. However, assignment to a Mo-Mo path is unlikely for grafted MoO_2Cl_2. Furthermore, modeling this EXAFS feature with such a path was unsuccessful. Weak features in this region are typical of the EXAFS of dispersed metal complexes supported on oxides, where they are often attributed to scattering paths involving atoms in the support. The curvefit in Figure 2.5b and Table 2.1 reproduces this feature with a combination of a Mo-Si single-scattering path at 3.47 Å and a Mo-O-Si double-scattering path at 3.52 Å. (The Mo-O-Si-O path was omitted from the curvefit, because according to FEFF, it is expected to have the lowest intensity.) Using the curvefit values for the Mo-O and Mo-Si distances and the reported Si-O bond length in $MoO_2(OSiPh_3)_2$ (1.669 Å), we estimate ∠Mo-O-Si ≈157 °. We note that computational studies of silica-supported oxomethylideneMo(VI) sites anchored to silica via two Mo-O-Si linkages report *d*(Mo-Si) values from 3.4 to 3.6 Å, as well as ∠Mo-O-Si values from 121 to 175 °.[95, 132] The double-scattering Mo-O-Si path is moderately intense, but since it is out-of-phase with the single-scattering Mo-Si path, the resulting peak intensity in the FT magnitude is not intense (Figure S2.5).

Although the small peak at 2.9 Å may reflect the interaction of the molybdate with the silica support, its very low intensity is surprising, considering how strong the feature is in the spectrum of $MoO_2(OSiPh_3)_2$, and the similarity between the ∠Mo-O-Si value for the grafted molybdate (157 °) and the molecular complex (164 °). It is possible that the very low intensity arises due to heterogeneity in the Mo-O-Si distances for the grafted sites. However, the σ^2 values for the Mo-Si and Mo-O-Si paths, (0.005 ± 0.001) $Å^2$ and (0.007 ± 0.003) $Å^2$, respectively, are not unreasonable for such long paths. Consequently, we suggest that the small peak at 2.9 Å arises from a subset of grafted molybdates with relatively large ∠Mo-O-Si values, while sites with smaller ∠Mo-O-Si values contribute little due to the much lower intensity of the double-scattering path and its destructive interference with the single-scattering path.

The value of ∠Mo-O-Si is a strong function of the molybdasiloxane ring size. DFT simulations show that grafted molybdates have smaller Mo-O-Si angles (< 138 °) when the Mo atom is part of a 6-membered ($MoSi_2O_3$) ring.[93, 95] The high fraction of vicinal silanols present on partially dehydroxylated amorphous silicas could result in a large fraction of these smaller molybdasiloxane rings, which contribute little to the peak intensity at 2.9 Å.[120, 133]

Elimination of residual chloride ligands. The remaining chloride in MoO_2Cl_2/SiO_2 (0.3 Cl/Mo) was removed by calcining in O_2 at 600 °C for 1 h, resulting in the material denoted MoO_x/SiO_2. While the Mo content of the solid was unchanged (2.6 wt% Mo), the Cl content decreased to 0.025 wt%. In the IR spectrum (Figure 2.1), the broad peak for H-bonded silanols disappears as some react with $Mo(=O)_2(OSi)Cl$ sites to form $Mo(=O)_2(OSi)_2$ sites and HCl (Scheme 2.3), while others condense to give water.

The XANES of MoO_x/SiO_2 shows little change relative to MoO_2Cl_2/SiO_2 (Figure 2.3a). The edge position does not move, although the pre-edge intensity increases slightly and shifts to lower energy (resembling the spectrum of $MoO_2(OSiPh_3)_2$ even more closely). Therefore the XANES is also consistent with conversion of the minority $Mo(=O)_2(OSi)Cl$ sites to $Mo(=O)_2(OSi)_2$. The Mo K-edge EXAFS also changes slightly, the most significant difference being a small increase in the peak amplitude at ca. 1.6 Å in the FT magnitude (attributed to the higher average coordination number for the longer Mo-O path), Figure 2.3b and Table 2.1. Notably, the intensity of the weak feature at 2.9 Å in *R*-space does not change, suggesting that new molybdate sites formed upon high temperature calcination likely contain small molybdasiloxane rings, which generate little new intensity in this region. In the EXAFS curvefit, the Mo=O, Mo-O, Mo-Si and Mo-O-Si distances are almost unchanged after the calcination. Possible structures for the grafted monomolybdate sites are represented in Scheme 2.5.

Scheme 2.5 Structures of grafted molybdate sites obtained by calcination of MoO_2Cl_2/SiO_2, illustrating uniformity in the first coordination sphere and variability in ∠Mo-O-Si: (a,b) between molybdate sites, and (c) within a single molybdate site.

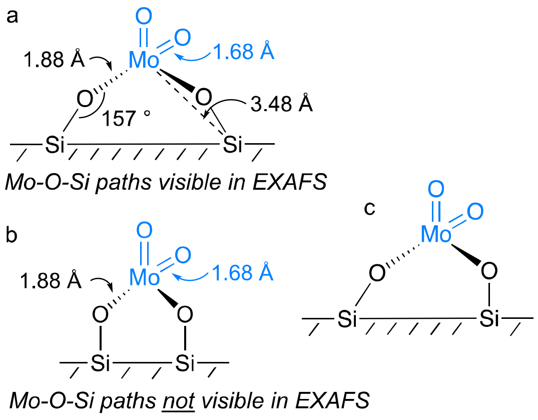

Structural comparison to other grafted molybdates. In previous reports, the molecular complexes $Mo(=O)(O^tBu)_4$ and $Mo(=O)_2[OSi(O^tBu)_3]_2$ were grafted onto partially dehydroxylated silicas, then subjected to thermal treatment to generate supported molybdates in a 2-step process. The proposed reaction of $Mo(=O)(O^tBu)_4$ with a silica pretreated at 200 °C is shown in Scheme 2.6a.[32] Initially formed $Mo(=O)(O^tBu)_2(OSi)_2$ was suggested to convert under dynamic vacuum at 250 °C to $Mo(=O)_2(OSi)_2$, accompanied by elimination of ^tBuOH and isobutene. The proposed reaction of $Mo(=O)_2[OSi(O^tBu)_3]_2$ with a silica partially dehydroxylated at 700 °C is shown in Scheme 2.6b.[33] Initially formed $Mo(=O)_2[OSi(O^tBu)_3](OSi)$ was suggested to convert to $Mo(=O)_2(OSi)_2$ upon thermal treatment at 200 – 400 °C. However, the mechanism for forming the second Mo-O-Si linkage was not described.

Scheme 2.6 Grafting and subsequent reactions of Mo(VI) oxoalkoxides reported to give $Mo(=O)_2(OSi)_2$ sites[107-108]

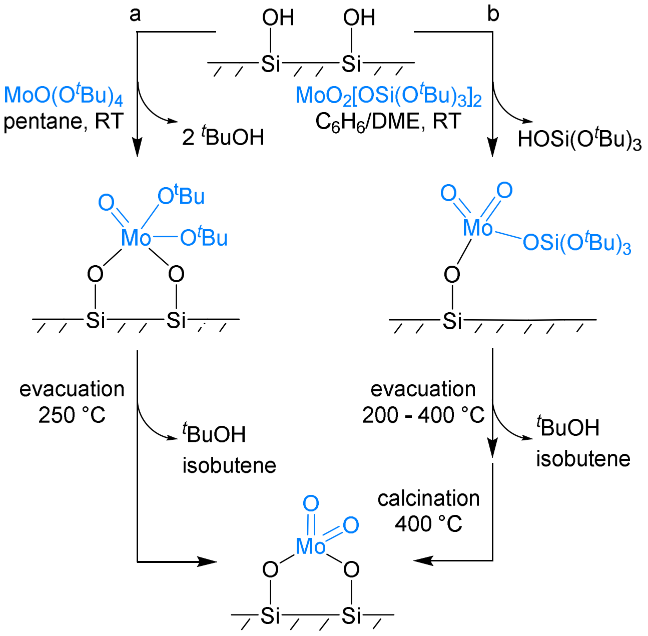

Both materials were characterized by XAS. The fitted Mo=O bond lengths (1.70 – 1.71 Å, Table S2.2) are consistent with values reported for molecular dioxomolybdates and DFT simulations,[88, 95, 132] as well as the value found in this work (1.68 Å). However, the Mo-O distance reported for the grafted molybdate derived from $Mo(=O)_2[OSi(O^tBu)_3]_2$ is slightly longer (1.92 Å) than the corresponding Mo-O paths in silica-supported materials made from $Mo(=O)(O^tBu)_4$ and MoO_2Cl_2 (1.87 and 1.88 Å, respectively). The appearance of the EXAFS for the monomolybdate sites obtained by the different grafting routes varies considerably in both *k*- and *R*-space. After calcination, the grafted molybdate made from MoO_2Cl_2 presents two well-resolved peaks in the FT magnitude with similar intensity in the range 1 – 2 Å (Figure 2.3b). A similar result was obtained for the molybdate made by grafting $Mo(=O)_2[OSi(O^tBu)_3]_2$ followed by calcination (Figure S2.6).[107] In contrast, the FT-EXAFS of the molybdate made by mild thermolysis of grafted $[Mo(=O)(O^tBu)_4]$ shows a single dominant peak (Figure S2.7).[108] The k^3-weighted $\chi(k)$ functions also vary (Figure S2.4-2.7). Based on a visual comparison of the data, the differences are not simply a result of variations in the *k*-space data range or quality.

The possibility of variable coordination of oxygen donor ligands was considered. In molecular and silica-supported $MoO_2Cl_2(THF)_2$, the THF ligands were modeled with a long Mo-O path at 2.24 Å.[8] In the model for $Mo(=O)_2(OSi)_2$ made by grafting $Mo(=O)(O^tBu)_4$, a very long Mo-O path at 2.39 Å was included representing a weakly coordinated siloxane, although the refined value for *N*(Mo-O) has a large uncertainty, (0.7 ± 0.5). For the silica-supported molybdate made by grafting MoO_2Cl_2, inclusion of a long Mo-O path in the curvefit returned a distance of 2.39 Å with an unrealistically large σ^2 value, 0.015 Å^2 (for *N* fixed at 1) or a low refined value of N, 0.4 ± 0.2. In a computational study of $Mo(=O)_2(OSi)_2$ sites at dozens of different locations on a model silica surface, only one $Mo(=O)_2(OSi)_2$ model showed a long Mo-O interaction.[95] It involved a high energy structure with a nearby silanol at 2.41 Å. All other long Mo-O distances in the models exceeded 3.35 Å. Therefore, we conclude that such paths are not significant contributors to the EXAFS of the supported molybdates.

To explore other possible origins for the differences in the spectra, the spectra of supported molybdates were simulated using reported curvefit distances for the two grafted oxoalkoxides (Table S2.2). The resulting $\chi(k)$ functions show extensive destructive interference between the Mo=O and Mo-O paths, Figure S2.8-2.9. Minor differences in these distances change the interference pattern and have a significant effect on the appearance of the EXAFS, Figure S2.10. A similar effect was seen for CrO_2Cl_2 grafted onto SiO_2 pretreated at 200 and 800 °C: the resulting $CrO_2(OSi)_2$ sites showed subtle differences in the Cr-O paths, resulting in changes in the appearance of the FT-EXAFS.[115] According to XANES analysis and DFT simulations, the changes likely arise from different distributions of chromasiloxane ring sizes (e.g., $CrSi_2O_3$ vs. $CrSi_3O_4$) on silicas pretreated at the different temperatures. In the preparation of grafted molybdates, different thermal treatments to remove residual ligands could influence the ring strain of the resulting $Mo(=O)_2(OSi)_2$ sites. The spectra of molybdates calcined at high temperatures are more similar, while the molybdate that was not calcined is distinctly different.

On amorphous silicas, molybdasiloxane rings of varying sizes can have a range of Mo-Si distances. A DFT simulation of $Mo(=O)_2(OSi)_2$ sites in conventional MoO_3/SiO_2 catalysts described Mo-Si distances differing by as much as 0.4 Å (from 3.27 to 3.52 Å), due to variations in the Mo-O-Si bond angles.[95] Another potential source of heterogeneity is unsymmetrical bonding within a single grafted molybdate site. For example, EXAFS analysis of grafted $Mo(=O)_2[OSi(O^tBu)_3]_2$ refined two Mo-Si distances at 3.39 and 3.52 Å, suggesting that the two Mo-O-Si linkages have very different angles. Destructive interference between such paths would reduce the intensity in the FT magnitude significantly, Figure S2.11.

This variability in the attachment of the metal site to the amorphous silica support (or, in the case of partially or fully crystalline supports, in the local environment including surface defects) can have major repercussions for the activation and subsequent reactivity of the grafted sites. It may be a principal cause for the low fraction of active sites in such materials, even when the first coordination sphere of the metal atom is relatively uniform. This phenomenon was reported for grafted chromates which spontaneously generate active sites for polymerization upon exposure to olefin,[134-135] and inspired the development of algorithms to relate the distortion of grafted structures to their activation barriers.[136-137]

2.4 Conclusions

Highly dispersed grafted dioxomonomolybdate sites, $Mo(=O)_2(OSi)_2$, were synthesized by a direct, solid-solid reaction between MoO_2Cl_2 and partially dehydroxylated SiO_2, followed by calcination at 600 °C to remove residual chloride ligands. Evidence from elemental analysis, IR spectroscopy, and X-ray absorption spectroscopy reveals that 6-coordinate MoO_2Cl_2 undergoes several structural changes as it is converted via $Mo(=O)Cl(OSi)_2$ to $Mo(=O)_2(OSi)_2$. The first coordination sphere of the grafted sites consists of two well-defined Mo=O and Mo–O bonds, similar to molecular analogs and consistent with simulations.[107-108] There is no evidence for siloxane coordination, or for molybdate oligomerization.

On the other hand, molybdate interactions with the amorphous silica surface are not uniform. Analysis of the Mo-Si paths in the EXAFS of molecular $MoO_2(OSiPh_3)_2$ shows that single-, double- and even triple-scattering paths combine to create a strong signal at ca. 3 Å. The single-scattering path is weak and relatively invariant to changes in the Mo-O-Si bond angle, while the contributions of the multiple-scattering paths are a strong function of this angle (164 ° for the molecular complex). In $Mo(=O)_2(OSi)_2$, the signal is very weak although the Mo-Si distance suggests a similar Mo-O-Si bond angle, 157 °. The low intensity is attributed to the distribution of molybdasiloxane ring sizes, and consequently Mo-O-Si bond angles; smaller rings with smaller angles result in little contribution to the FT magnitude. Consequently, only the fraction of grafted $Mo(=O)_2(OSi)_2$ sites with large Mo-O-Si angles contribute significantly to this signal. Variability in the Mo-Si distances also arises due to the range of angles, which suppresses the intensity further due to destructive interference.

Relatively uniform $Mo(=O)_2(OSi)_2$ sites are interesting to explore in terms of their reactivity. For example, $Mo(=O)_2(OSi)_2$ sites are often claimed to be the direct precursors of active sites in olefin metathesis.[36, 99] However, $Mo(=O)_2(OSi)_2$ sites prepared by grafting $Mo(=O)_2[OSi(O^tBu)_3]_2$ onto silica failed to activate in the presence of the cis-4-nonene at 70 °C (i.e., no metathesis activity ensued).[107] Our $Mo(=O)_2(OSi)_2$ sites made by the reaction of MoO_2Cl_2 with silica followed by calcination showed a similar inability to activate in the presence of the propylene even at 200 °C, despite the well-defined nuclearity and first coordination sphere. Despite the challenges in probing the consequences of site variability caused by differences in Mo-O-Si angles experimentally and computationally, such understanding will be needed to identify features of the Mo-support interaction essential to the activation of grafted sites.

2.5 Supporting Information

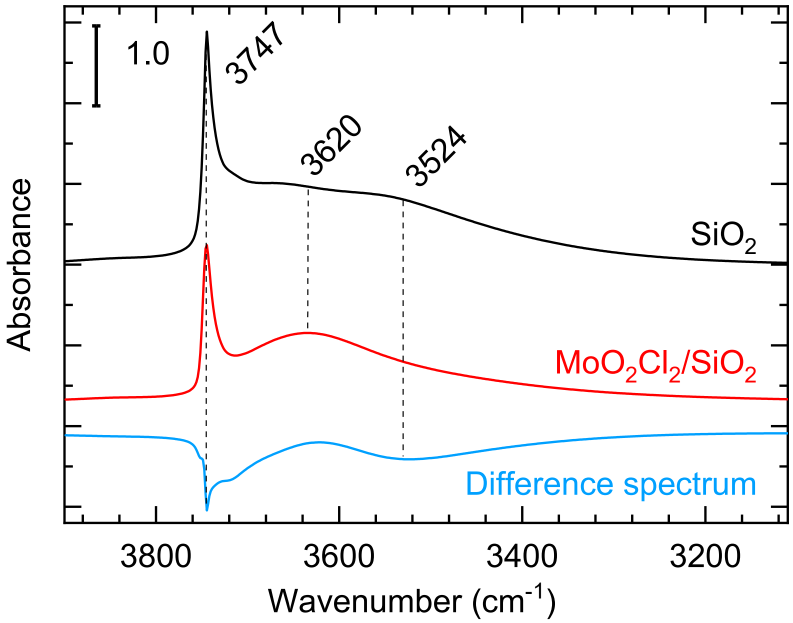

Figure S2.1 Difference (blue) between IR spectra of silica (Aerosil A380, pretreated overnight at 200 °C under dynamic vacuum), before (black) and after (red) grafting MoO_2Cl_2 in a solid-solid reaction at room temperature. Both spectra were baseline-corrected, then normalized to the absorbance of the silica overtone at 1865 cm^{-1}. The spectra are offset vertically for clarity.

Table S2.1 Mo pre-edge and K-edge positions [a] for standards and grafted molybdates

Compound or material	Pre-edge / eV	Edge / eV
Mo foil	N/A	20,000.0 [b]
MoO_2	N/A	20,011.0
$MoO_2(OSiPh_3)_2$	20,003.2	20,013.5
MoO_2Cl_2	20,004.2	20,011.6
Na_2MoO_4	20,003.4	20,016.7
MoO_3	20,006.4	20,015.0
MoO_2Cl_2/SiO_2	20,004.3	20,015.2
MoO_x/SiO_2	20,004.4	20,015.2

[a] The pre-edge position is defined as the position of the first peak in the Mo K-edge XANES (identified by the first zero-crossing in the first derivative of the XANES), while the edge position is defined as the first maximum after the pre-edge peak in the first derivative of the XANES. [b] By convention.[110]

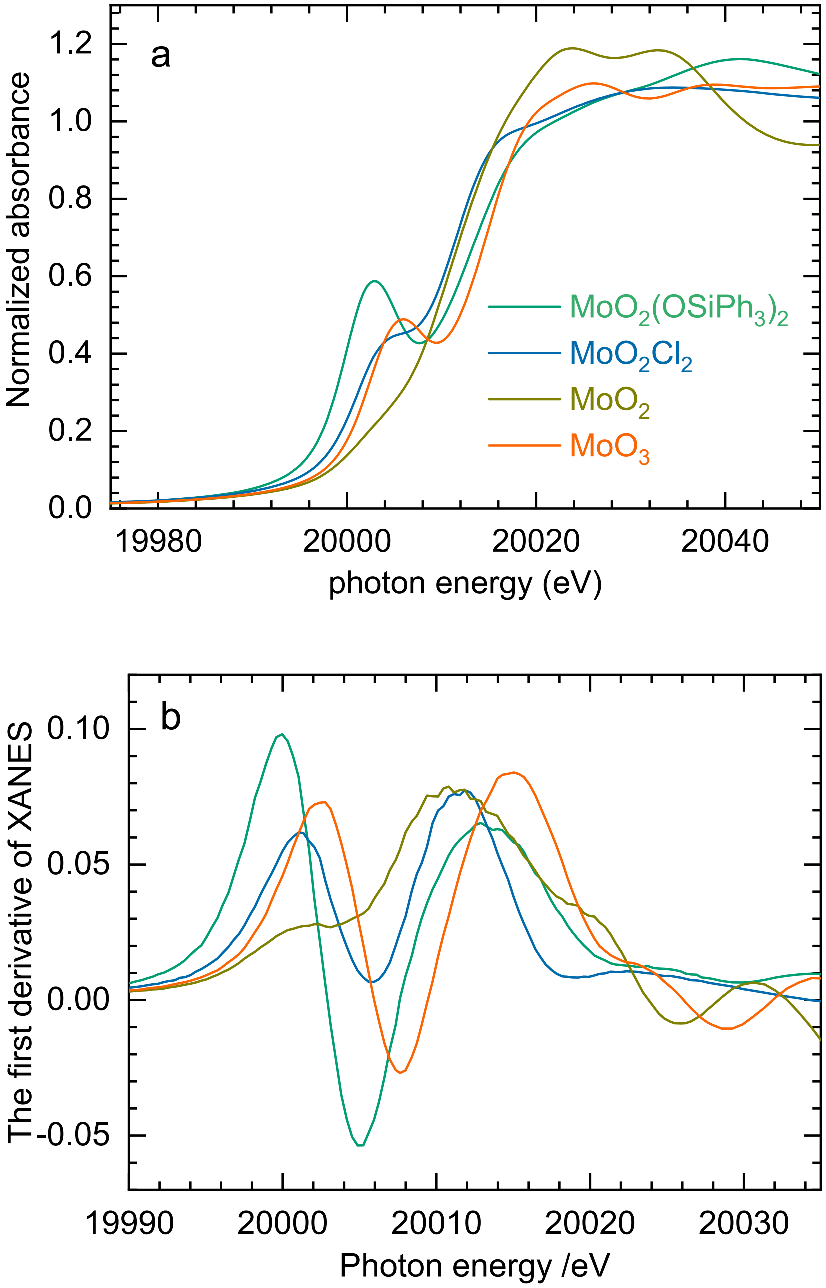

Figure S2.2 Comparison of Mo K-edge XAS for MoO_2Cl_2 (blue), with data for $MoO_2(OSiPh_3)_2$ (green), MoO_2 (olive) and MoO_3 (orange): (a) XANES, and (b) first derivative of the XANES.

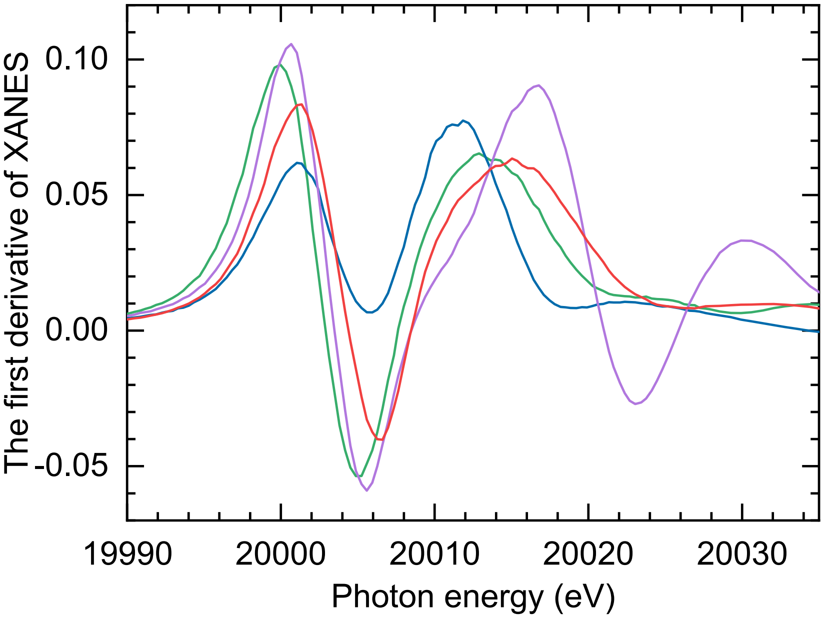

Figure S2.3 Comparison of the first derivatives of the XANES, for $MoO_2(OSiPh_3)_2$ (green), MoO_2Cl_2 (blue), Na_2MoO_4 (purple) and MoO_2Cl_2/SiO_2 (red).

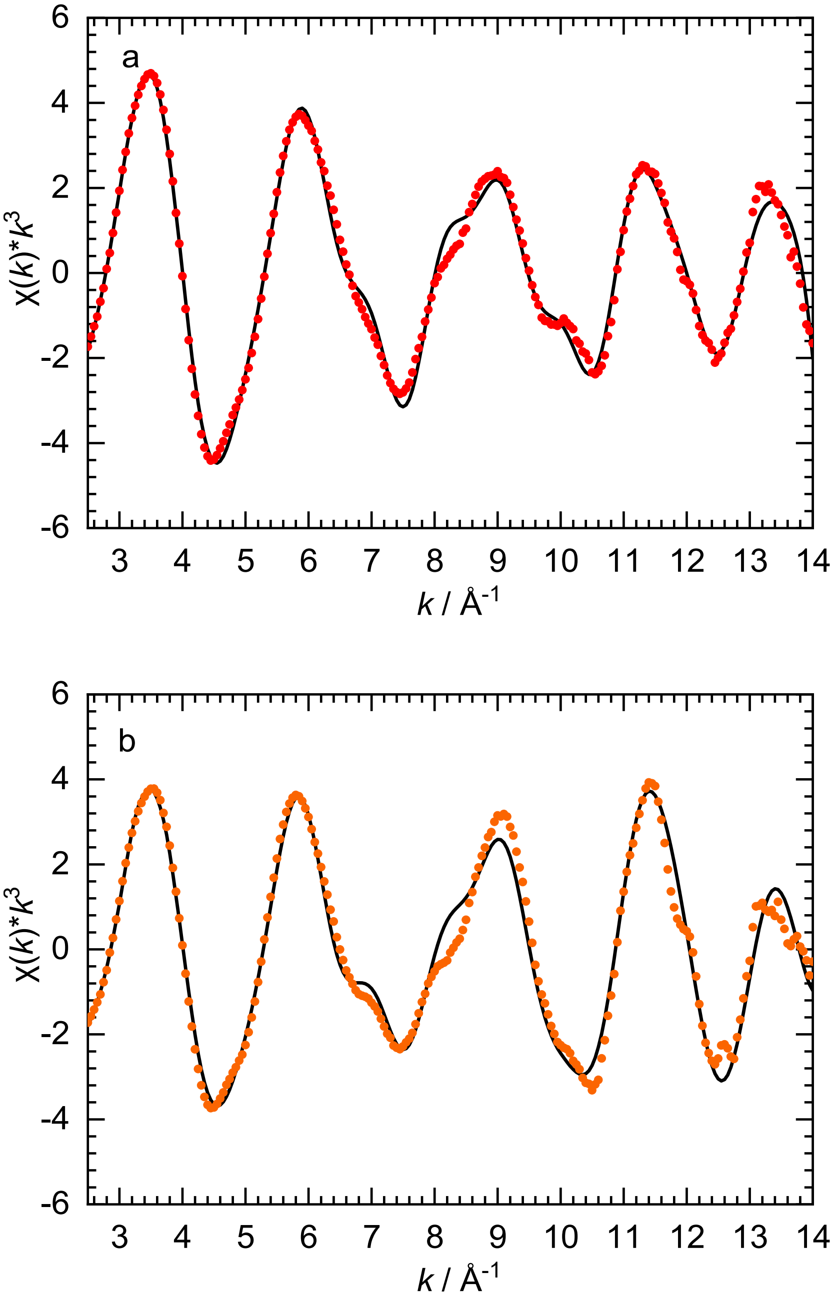

Figure S2.4 Curvefits (black lines) of the Mo K-edge EXAFS (points) in k^3-weighted *k*-space for MoO_2Cl_2/SiO_2: (a) before, and (b) after calcination.

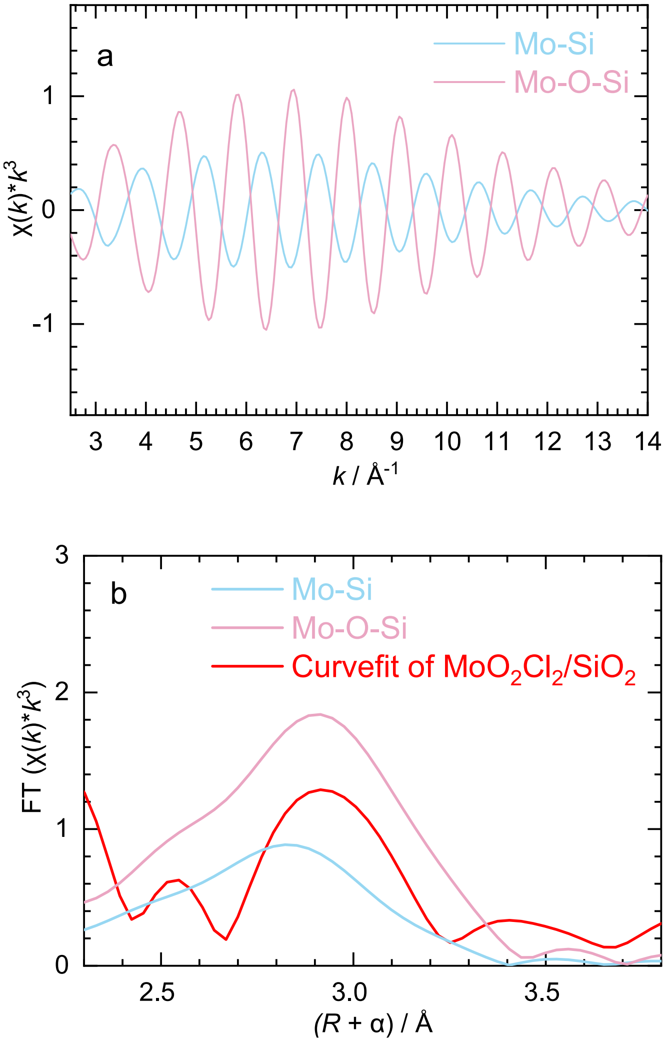

Figure S2.5 (a) k^3-weighted $\chi(k)$ functions, and (b) k^3-weighed FT magnitudes, for the Mo-Si single-scattering path (blue) and Mo-O-Si double-scattering path (pink), extracted from the EXAFS curvefit for MoO_2Cl_2/SiO_2 (red).

Table S2.2 EXAFS curvefit parameters for Mo(=O)$_2$(OSi)$_2$ made from different precursors

Precursor	Mo=O		Mo-O		Mo-Si	
	R / Å	σ^2 / Å^2	*R* / Å	σ^2 / Å^2	*R* / Å	σ^2 / Å^2
MoO$_2$Cl$_2$	1.68(1)	0.002(1)	1.88(2)	0.003(1)	3.48(4)	0.007(3)
MoO$_2$[SiO(O^{t}Bu)$_3$]$_2$ [a]	1.699(5)	0.0019(5)	1.921(6)	0.0032(11)	3.39(5), 3.52(5)	0.014(12)
MoO(O^{t}Bu)$_4$ [b]	1.705(10)	0.0021(3)	1.870(15)	0.0026(4)	3.27(5)	0.011(7)

[a] From ref. [107]. [b] From ref. [108].

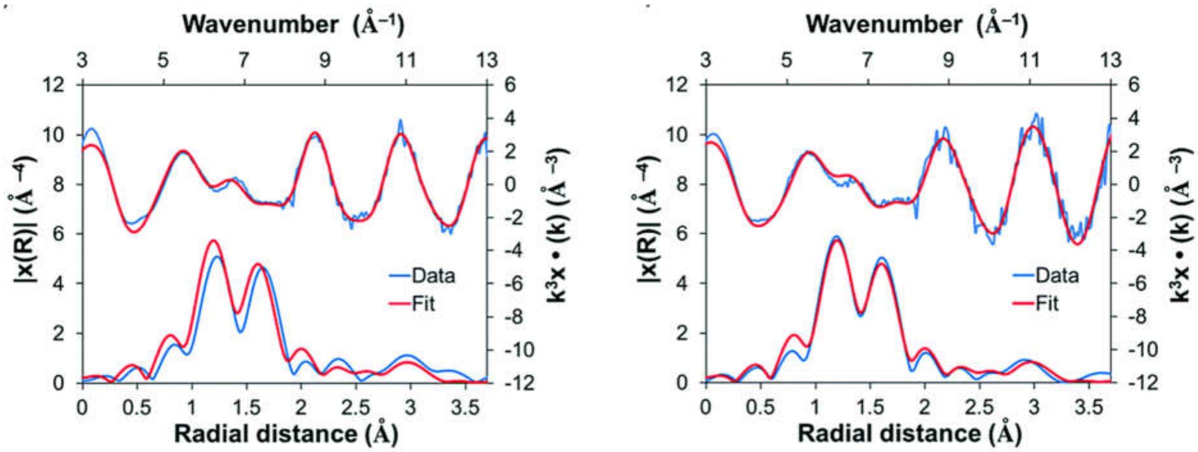

Figure S2.6 Mo K-edge EXAFS, in *k*-space (top) and *R*-space (bottom), and curvefits for Mo(O)$_2$[OSi(O^{t}Bu)$_3$]$_2$ (left) and (≡SiO)$_2$Mo(O)$_2$ made by grafting Mo(O)$_2$[OSi(O^{t}Bu)$_3$]$_2$ onto silica followed by calcination (right).[107] Reproduced from Ref. [107], with permission from the Royal Society of Chemistry.

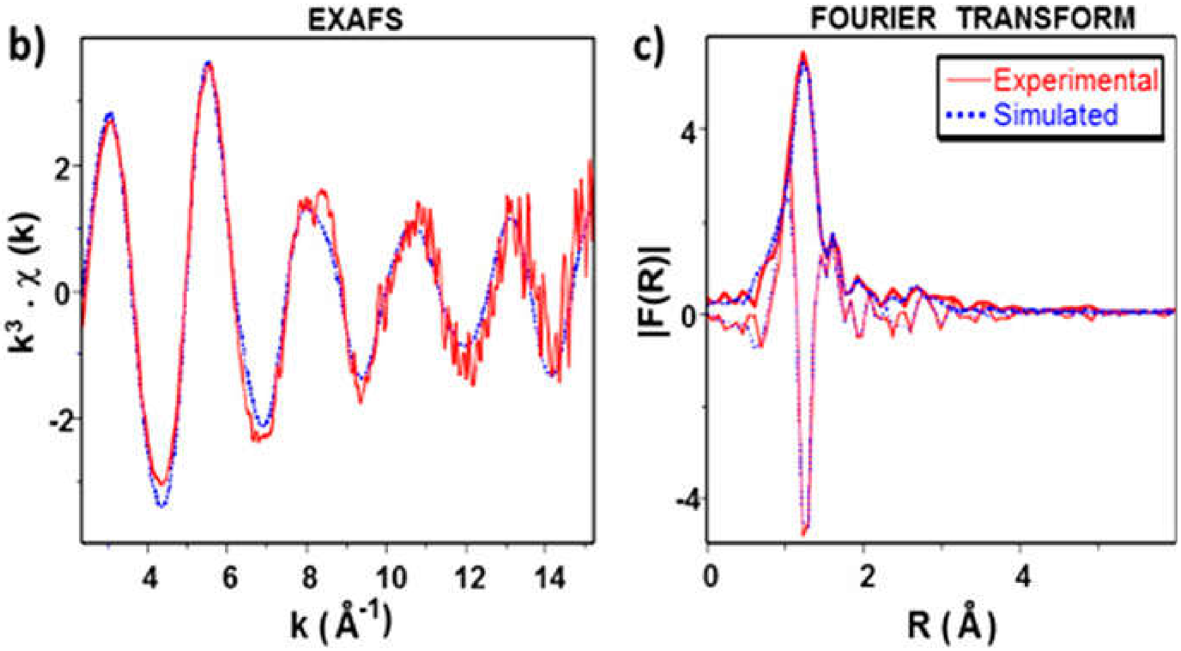

Figure S2.7 Mo K-edge EXAFS, in *k*-space (left) and *R*-space (right) for $(\equiv SiO)_2Mo(O)_2$ made by grafting $Mo(=O)(O^tBu)_4$ onto silica followed by mild heating.[108] Reprinted with permission from ref [108]. Copyright 2018 American Chemical Society.

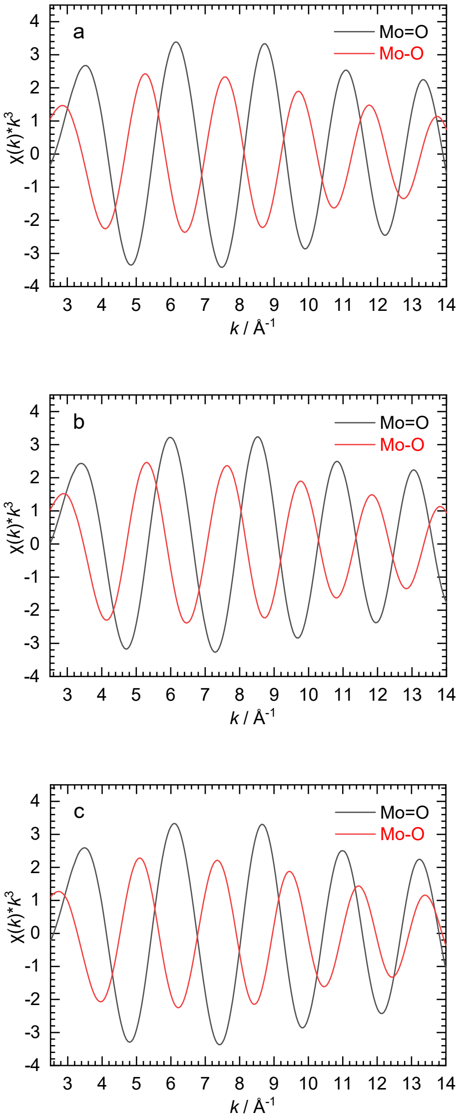

Figure S2.8 Individual simulated k^3-weighted $\chi(k)$ functions for two Mo=O (black) and two Mo-O (red) paths at (a) 1.68 and 1.87 Å (this work); (b) 1.71 and 1.86 Å (i.e., slightly longer Mo=O path, according to ref. 2); (c) 1.69 and 1.91 Å (i.e., slightly longer Mo-O path, according to ref 3), corresponding to curvefit distances reported for grafted molybdates made by different routes. The following parameters were fixed in the simulation: $S_0^2 = 1$, $\Delta E_0 = 0$ eV, σ^2(Mo=O) = 0.002 Å^2, σ^2(Mo-O) = 0.003 Å^2

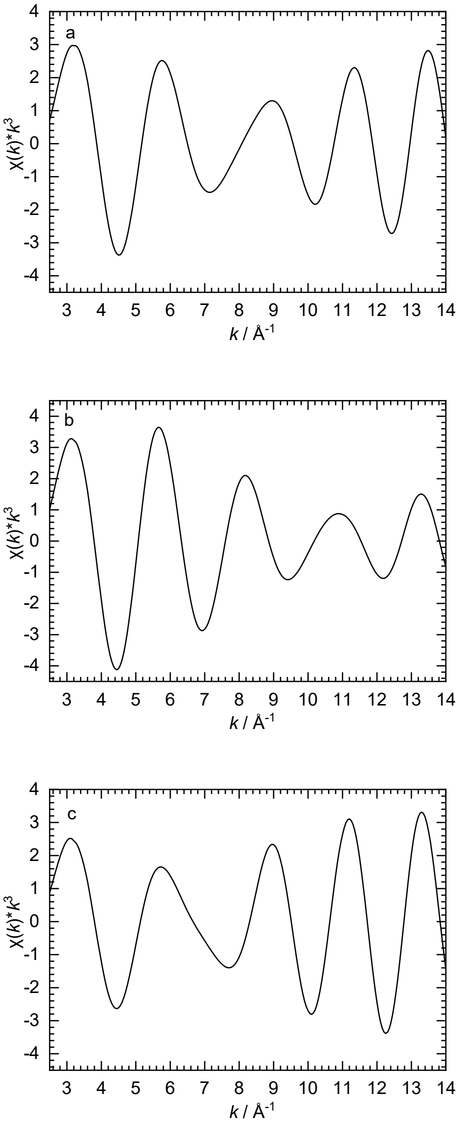

Figure S2.9 The sum of the simulated k^3-weighted $\chi(k)$ functions shown in Figure S8 for two Mo=O and two Mo-O paths at (a) 1.68 and 1.87 Å (this work); (b) 1.71 and 1.86 Å; (c) 1.69 and 1.91 Å, corresponding to curvefit distances reported for grafted molybdates made by different routes.

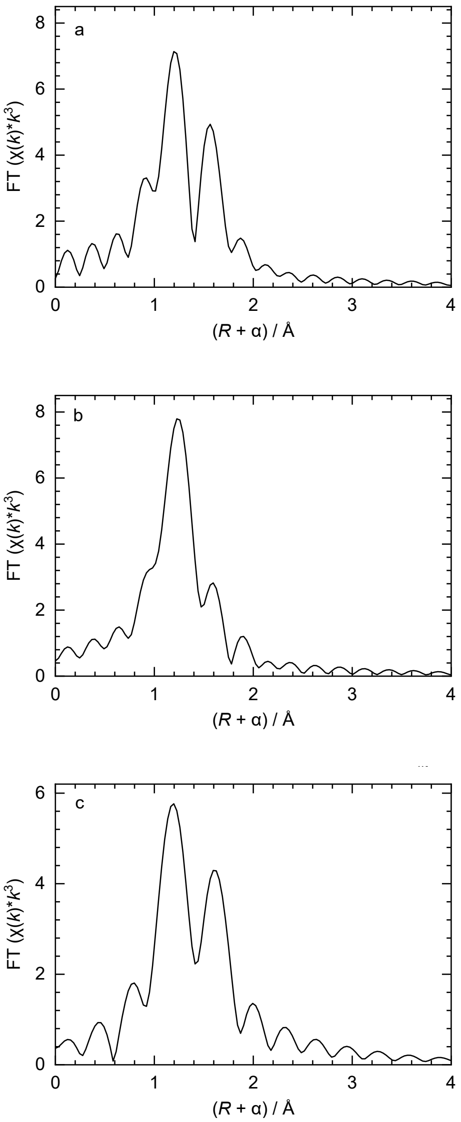

Figure S2.10 Fourier transforms of the simulated EXAFS shown in Figure S9, for two Mo=O and two Mo-O paths at (a) 1.68 and 1.87 Å (this work); (b) 1.71 and 1.86 Å (ref 2); (c) 1.69 and 1.91 Å (ref 3), corresponding to curvefit distances reported for grafted molybdates made by different routes.

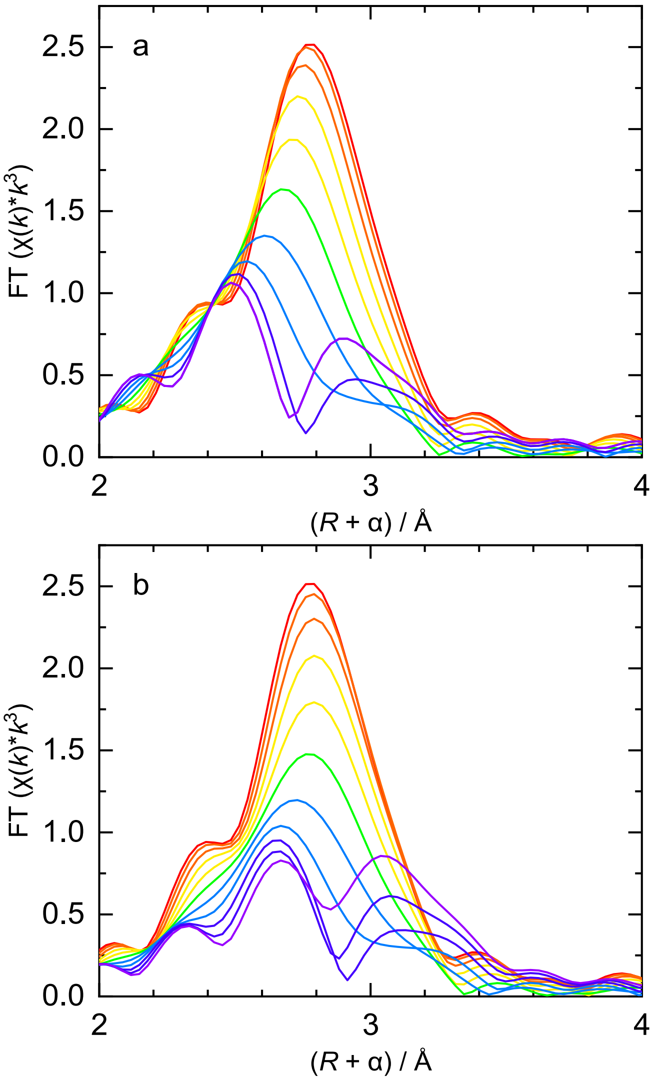

Figure S2.11 Simulation of the k^3-weighed EXAFS for two Mo-Si paths. One Mo-Si distance is fixed at 3.264 Å, while the second Mo-Si distance varies. The spectra show the effect of differences in path length (ΔR): (a) from 0 to -0.2 Å; and (b) from 0 to +0.2 Å, in intervals of 0.02 Å. Colors from red to purple reflect the increasing magnitude of ΔR. The following parameters were held fixed in the simulation: $S_0^2 = 0.98$, $\Delta E_0 = 0$ eV, $\sigma^2 = 0.003$ Å^2.

Chapter 3. Increasing the Fraction of Metathesis Active Sites in MoO_3/SiO_2

3.1 Introduction

Heterogeneous olefin metathesis catalysts are used in petrochemical processes such as the Phillips Triolefin Process,[138] the Shell Higher Olefins Process (SHOP),[139] and the production of neohexene.[28, 140] Most catalysts have simple compositions based on a dispersed transition metal oxide such as Mo, and require high-temperature calcination as part of the activation procedure. Alternative activation methods with reducing gases or alkylating co-catalysts can improve the activity, but all catalysts still suffer from the low fraction of active sites, typically < 2 %, according to active site counting and poisoning experiments.[36] A recently reported, highly effective activation method involves exposure to olefins at high temperatures (>500 °C), and the active site fraction can be as high as 10%.[32, 82] However, the co-existence of multiple types of metal sites makes it difficult to identify the active sites and to design more effective activation procedures.

An alternative strategy to improve activity is to create more uniform pre-active sites that should activate more efficiently. The most commonly proposed active site precursor for the MoO_3/SiO_2 olefin metathesis catalyst is the isolated dioxomonomolybdate site, $Mo(=O)_2(OSi)_2$.[36, 99] However, when $Mo(=O)_2(OSi)_2$ sites were prepared from $Mo(=O)_2[OSi(O^tBu)_3]_2$, most failed to catalyze *cis*-4-nonene metathesis at 70 °C.[107] The contradictory conclusions about $Mo(=O)_2(OSi)_2$ metathesis activity need to be resolved by only investigating this uniform site and examining its activity. Thus, we synthesized a silica material containing only this $Mo(=O)_2(OSi)_2$ site by grafting MoO_2Cl_2 onto silica, followed by calcination. Its subsequent activation for olefin metathesis was explored and compared to a conventional MoO_3/SiO_2 catalyst prepared by the incipient wetness method.

Investigating the activation of Mo(=O)$_2$(OSi)$_2$ sites can provide fundamental information about how active sites form and how to promote their formation more efficiently. The pseudo-Wittig mechanism is proposed as the pathway for activating Mo(=O)$_2$(OSi)$_2$.[84, 141-142] In the pseudo-Wittig mechanism, a Mo=O bond is proposed to react with a C=C bond by [2+2] cycloaddition to form a 4-membered metallaoxetane ring, Scheme 3.1. Cycloreversion results in a Mo-methylidene and aldehyde with no change in Mo oxidation state. Other mechanisms involve redox processes on the Mo sites. Interestingly, Mo(=O)$_2$(OSi)$_2$ sites derived from Mo(=O)(O*ᵗ*Bu)$_4$ catalyze metathetic oxidation of 2-butene to acetaldehyde at 300 – 450 °C.[108] The proposed catalytic mechanism is similar to the pseudo-Wittig mechanism. Therefore, unform Mo(=O)$_2$(OSi)$_2$ sites are a good candidate to investigate the pseudo-Wittig mechanism.

Scheme 3.1 Proposed pseudo-Wittig mechanism for activation of metal oxo sites[141-142]

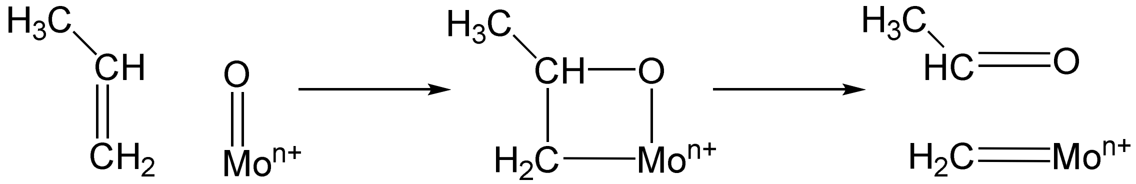

Here, we report high-temperature olefin treatment of Mo(=O)$_2$(OSi)$_2$ sites to increase the active site fraction for propene self-metathesis. This activation method turns out to work efficiently on only certain supported molybdenum-containing silicas. Although catalytic performance is enhanced, side-reactions co-occur, such as oligomerization and reduction. Preliminary evidence suggests that the pseudo-Wittig mechanism could generate active sites in MoO$_3$/SiO$_2$ catalysts. Meanwhile, the reduced or oligomerized Mo sites due to the side reactions may also be responsible for the metathesis activity, requiring further research.

3.2 Experimental Methods

General procedures. O_2 (UHP grade, Airgas), 10 vol% CO/N_2 (Airgas), propene (Praxair, 99.8 %), 2-butene (30/70 cis-/trans-mixture, Aldrich, > 99 %), ^{13}C-ethylene (99%, Sigma-Aldrich) and ethylene (Praxair, containing 2 % propane as internal standard) were purified by passage through a bed of activated 13X molecular sieves and BTS catalyst (Sigma-Aldrich), then stored in glass bulbs over 3 Å molecular sieves. Acetaldehyde (99.5%, extra pure, Acros Organics) and $(NH_4)_6Mo_7O_{24}\cdot 4H_2O$ (99.98%, Sigma-Aldrich) were used as received. Fumed SiO_2 (Aerosil 380, B.E.T. surface area 383 m^2/g) was obtained from Evonik Degussa.

Synthesis of supported molybdenum materials. The detailed synthesis of monodioxomolybdenum on silica, $Mo(=O)_2(OSi)_2$, is described in Chapter 2. In brief, MoO_2Cl_2 was grafted onto SiO_2 (pretreated under dynamic vacuum at 200 °C) at room temperature via a solvent-free solid-state reaction. The mixture was washed thoroughly with organic solvents. The grafted Mo material was dried under dynamic vacuum (0.1 mTorr) at room temperature overnight to ensure the complete removal of solvents. The dry material is denoted MoO_2Cl_2/SiO_2 (2.6 wt% Mo verified by ICP-AES)

A conventional supported molybdenum catalyst (MoO_3/SiO_2) was prepared by wet impregnation. SiO_2 was calcined at 500 °C overnight prior to use. The desired amount of $(NH_4)_6Mo_7O_{24}\cdot 4H_2O$ was dissolved in 20 mL deionized H_2O, then 500 mg SiO_2 was added. The mixture was stirred with a magnetic stirbar at room temperature overnight. The solvent was removed at 110 °C on a hot plate; then the catalyst was calcined at 600 °C for 12 h.

Spectroscopy. IR spectra were acquired using self-supporting pellets (ca. 20 mg, 5 mm diameter), made with a Quick Press (International Crystal Laboratories) inside an Ar-filled glovebox. Spectra were recorded in transmission mode over the range 4000 – 400 cm^{-1} using a Bruker Alpha FTIR spectrometer, accumulating 32 scans at a resolution of 2 cm^{-1}. The absorbance was normalized by the peak intensity of the silica overtone at 1856 cm^{-1}.

The molybdenum materials were packed and sealed into 4 mm zirconia rotors in an Ar-filled glovebox for NMR analysis. ^{13}C solid-state MAS NMR, frequency 125.74 MHz, was acquired on a Bruker AVANCE500 WB spectrometer (11.7 T), at a spinning frequency of 12 kHz, with a total number of scans of 16804.

XAS spectra were recorded at the Mo K-edge (20,000 eV) on beamline 4-1 at the Stanford Synchrotron Radiation Lightsource, which operates at 3.0 GeV with a current of 500 mA. Data were acquired in transmission mode, using N_2-filled ionization chambers as detectors. Spectra were acquired under a protective atmosphere of He in a cryostat at 10 K. For energy calibration, a Mo foil was placed after the second ionization chamber, following the incident beam direction. The energy of the first maximum in the first derivative of its XANES was defined to be 20,000 eV.[110]

XAS data were processed and analyzed using the Demeter software package.[111] A linear function was subtracted from the pre-edge region, then the edge jump was normalized using Athena software. The $\chi(k)$ data were isolated by subtracting a smooth, third-order polynomial approximating the absorption background of an isolated atom. The cut-off value for R_{bkg} was set to 1.0 to ensure removal of the artificial peak that can appear below 1.0 Å. The k^3-weighted $\chi(k)$ data were Fourier-transformed after applying a Hanning window function.

Activation, propene metathesis and carbene site counting. MoO_2Cl_2/SiO_2 (50 mg) was placed in a 145 mL quartz batch reactor. The reactor was filled with 100 Torr O_2, heated at 10 °C/min to 600 °C, and held at that temperature for 1 h. The reactor was evacuated for 10 min to remove residual chlorine. The flask was filled with 60 Torr ethylene or propene at the desired temperature and held at that temperature for 30 min, then evacuated for 10 min at the same temperature. The flask was then cooled to room temperature under dynamic vacuum. MoO_3/SiO_2 (50 mg) was heated in 100 Torr O_2 at 10 °C/min to 600 °C and held at that temperature for 1 h, before exposure to olefin.

The activity in propene self-metathesis was tested in a 145 mL batch reactor with 50 mg catalyst. The reactor was filled with 130 Torr propene (containing 1.99% propane as internal standard). Reaction products were analyzed by removal of timed aliquots and injection into a GC-FID (Shimadzu GC-2010) with separation on a capillary column (Supelco Alumina Sulfate plot, 30 m × 0.32 mm).

Carbene site counting was performed in a 145 mL batch reactor via the method adapted from the active site counting of supported metal oxide catalysts.[143] After calcination, MoO_2Cl_2/SiO_2 (50 mg) was exposed to 60 Torr ethylene for 30 min at 650 °C. The reactor was evacuated for 10 min at the same temperature, then cooled to room temperature under dynamic vacuum. Evacuation was continued for 6 h to ensure complete removal of volatile hydrocarbons. Finally, the catalyst was exposed to 130 Torr 2-butene (containing 1.99% butane as internal standard) for 3 h. The propene formed was analyzed by GC-FID. The analysis assumes that 2-butene reacts with the molybdenum methylidene to produce propene stoichiometrically.

Physical adsorption of acetaldehyde. 100 mg MoO_2Cl_2/SiO_2 was weighed and calcined at 500 °C for 1 h in a quartz flask, then cooled to the desired temperature. Acetaldehyde vapor (20 – 60 Torr) was added via a vacuum manifold. After 30 min reaction, the flask was evacuated for 10 min. The flask was transferred into an Ar-filled glovebox without exposure of the contents to air for analysis by IR.

3.3 Results and Discussion

Upon grafting MoO_2Cl_2 onto silica at room temperature, the IR spectrum shows a decrease in the intensity of the silanol stretch at 3747 cm^{-1}, indicating a reaction with surface hydroxyls. The XANES contains an intense pre-edge feature corresponding to a 4-coordinate Mo center. The EXAFS confirms that most chloride ligands are replaced by oxygen, and no Mo-Mo path is present. However, a mixture of two Mo sites, $Mo(=O)_2(OSi)_2$ and $Mo(=O)_2Cl(OSi)$ is present. Calcination at high temperatures (550 – 650 °C) removes the remaining chloride ligands. The EXAFS is consistent with uniform $Mo(=O)_2(OSi)_2$ sites. The details are described in the previous chapter.

Activation of $Mo(=O)_2(OSi)_2$ sites. Calcination[36] and reduction[141, 144] are reported to activate supported molybdenum catalysts. The $Mo(=O)_2(OSi)_2$ sites in calcined MoO_2Cl_2/SiO_2 (50 mg, 2.6 wt% Mo) were tested directly in metathesis of propene (130 Torr). No reaction was observed within 2 h at temperatures between 23 and 200 °C. Next, the $Mo(=O)_2(OSi)_2$ sites in calcined MoO_2Cl_2/SiO_2 (50 mg) were reduced at 600 °C with 30 Torr 10 vol% CO/N_2 in a batch reactor for 1 h. The color changed from white to grey, but there was still no metathesis activity towards propene (130 Torr) within 2 h at 23 – 200 °C. Treating calcined MoO_2Cl_2/SiO_2 (50 mg) with 30 Torr H_2 at 600 °C for 30 min also resulted in no metathesis activity under the same conditions. These differences call into question the hypothesis that $Mo(=O)_2(OSi)_2$ is the active site in conventionally-made supported molybdenum catalysts.

Recently, activation of supported molybdate catalysts was reported by heating in the presence of a flowing olefin (e.g., propene, ethene) at very high temperatures (> 500 °C).[82] This activation method was adapted for use in a batch reactor. After the activation and cooling down to room temperature (23 °C), 130 Torr propene was added, and the evolution of each olefin was monitored over time by GC-FID. The metathesis reaction proceeded rapidly to equilibrium within 2 h when the catalyst was pretreated in propene at ≥ 550 °C (Figure 3.1) or in ethylene at ≥ 600 °C (Figure 3.2). The kinetic profiles are pseudo-first-order. The rate constant k_{obs} was normalized by the total amount of Mo and the reactor volume to obtain the apparent second-order rate constant, Table 3.1. High-temperature propene activation exhibits a volcano trend in activity (550 > 650 >> 450 °C), consistent with results reported previously for a conventional catalyst (550 °C > 660 °C >> 450 °C).[82] Ethylene pretreatment was reported to be more effective at 600 vs. 550 °C.[82] Therefore, we tested ethylene pretreatments at 600 and 650 °C. Activation at 650 °C gave the higher initial turnover frequency (TOF). The value, 4.5 $mol_{C3}\ mol_{Mo}^{-1}\ min^{-1}$ at 23 °C, is 375× higher than the reported value for only calcined MoO_3/SiO_2 at 50 °C (initial TOF = 0.12 $mol_{C3}\ mol_{Mo}^{-1}\ min^{-1}$).[36]

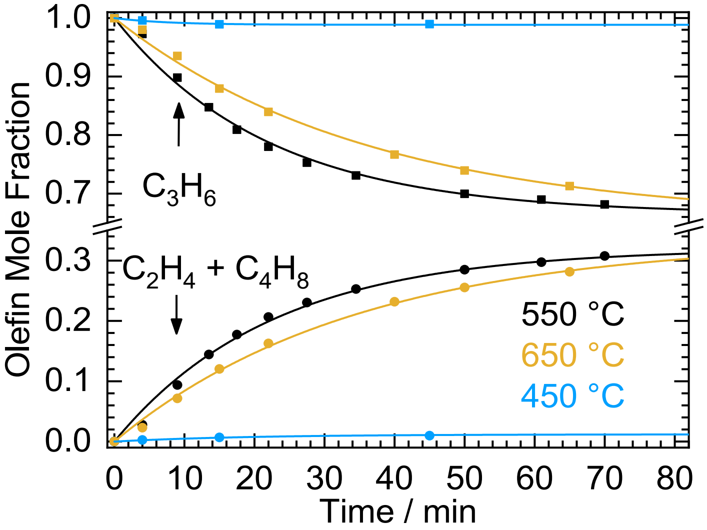

Figure 3.1 Kinetic profiles for propene self-metathesis and olefin product formation in a batch reactor. Mo(=O)$_2$(OSi)$_2$ was pre-activated by propene at 450 °C (blue), 550 °C (black) or 650 °C (yellow). Reaction conditions: 50 mg catalyst (2.6 wt% Mo), 23 °C, 0.145 L, 130 Torr propene.

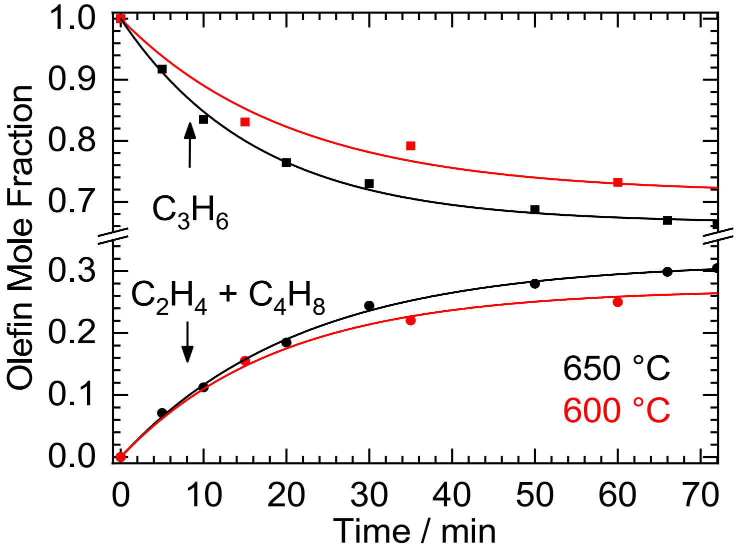

Figure 3.2 Kinetic profiles for propene self-metathesis and olefin product formation in a batch reactor. $Mo(=O)_2(OSi)_2$ sites were activated by ethylene at 600 °C (red) or 650 °C (black). Reaction conditions: 50 mg catalyst (2.6 wt% Mo), 23 °C, 0.145 L, 130 Torr propene.

Table 3.1 Comparison of propene metathesis activities after various olefin pretreatments

Activation gas	Activation temperature (°C)	k_{obs} (10^{-2} min^{-1})	k (L mol_{Mo}^{-1} min^{-1})	Initial TOF (mol_{C3} mol_{Mo}^{-1} min^{-1})
C_3H_6	450	0.51(0.05)	27(3)	0.38(0.04)
	550	4.6(0.3)	241(16)	3.4(0.2)
	650	2.9(0.1)	153(5)	2.2(0.1)
C_2H_4	600	5.2(0.3)	276(16)	3.9(0.2)
	650	6.1(0.2)	323(11)	4.5(0.1)

[a] Conditions: 0.145 L quartz batch reactor, 130 Torr propene, 23 °C, 50 mg catalyst (2.6 wt% Mo). k_{obs} was extracted from the first-order curve fits of the propene fraction. k is normalized by the total amount of Mo per reactor volume. The calculation is adapted from published work.[145]

The same propene activation treatment at 550 °C was tested on a conventional MoO_3/SiO_2 catalyst (2.6 wt% Mo) made via the incipient wetness method. Surprisingly, the catalyst deactivated very quickly, Figure 3.3. A similar result was reported by another group.[40] We note that both ineffective MoO_3/SiO_2 catalysts were made using a non-porous fumed silica, whereas the effective MoO_3/SiO_2 catalyst was made using porous precipitated silica.[82] Similarly, MoO_3/SiO_2 was reported to be activated by methane at 650 °C, using SBA-1 (mesoporous silica).[146] Although the similar ammonium molybdate precursor was used in each case, the different silicas may contain different molybdate sites. The porous silica support likely helps increase the fraction of $Mo(=O)_2(OSi)_2$ sites, while fumed silica cannot achieve such a high fraction with ammonia molybdate.[147] This comparison indicates that $Mo(=O)_2(OSi)_2$ sites exist only a small fraction in some conventional molybdena catalysts, and this activation method is effective for specific Mo sites.

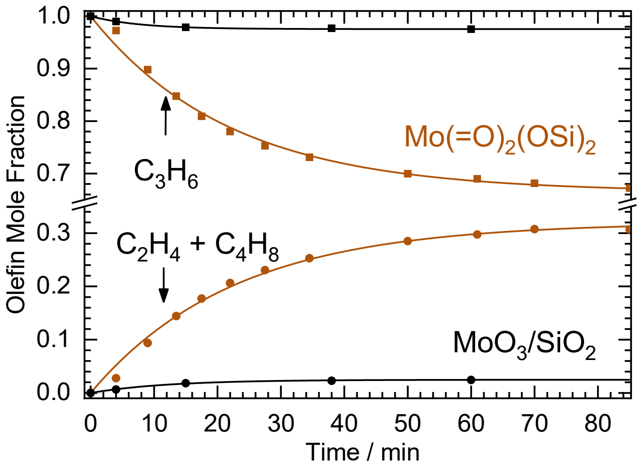

Figure 3.3 Kinetic profiles for propene self-metathesis and olefin product formation in a batch reactor, using conventional MoO_3/SiO_2 catalyst (black) and $Mo(=O)_2(OSi)_2$ (brown). Both

were pretreated with propene at 550 °C for 30 min. Reaction conditions: 50 mg catalyst (2.6 wt% Mo), 23 °C, 0.145 L,130 Torr propene.

Active Site Counting and Characterization. The changes in the Mo sites occurring during activation were investigated. The precatalyst activated by ethylene at 650 °C was chosen since it showed the highest metathesis activity. The method of active site counting was adapted from Chauvin and Commereuc.[143] Carbene sites are presumed to form upon exposure to ethylene at high temperature, Scheme 3.2. After ethylene activation at 650 °C, the flask was evacuated for 6 h at room temperature to remove physisorbed hydrocarbons. Excess 2-butene was added at the same temperature. After 2 h, the liberated propene was quantified by GC-FID. Assuming that each propene represents an active site, the fraction of Mo which exists as [$Mo=CH_2$] is ca. 36%, much higher than reported for calcination-activated MoO_3/SiO_2 (1 – 2 %, 50 °C)[36] or olefin-activated MoO_3/SiO_2 (0.7 – 10.9 %, 20°C).[82]

Scheme 3.2 Active site counting method.

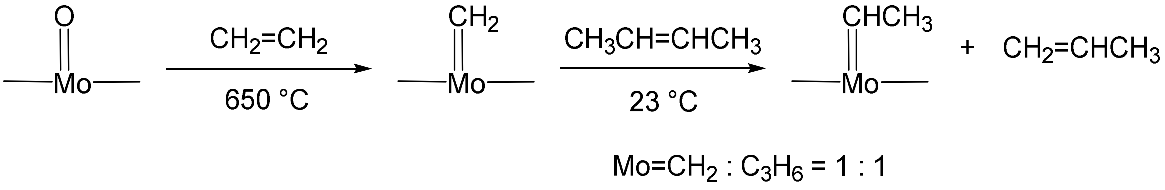

During olefin activation, the color of $Mo(=O)_2(OSi)_2$ changed from white to black. The black color is presumably due to the deposition of carbon residue. According to GC-FID high-temperature activation in propene results in the formation of C_1 – C_6 hydrocarbons including a mixture of alkanes, olefins and benzene. In the Mo K-edge XANES, the pre-edge peak characteristic of molybdate sites disappears and the edge position shifts lower by 2.2 eV, Figure 3.4, suggesting a change in the average Mo oxidation state. Compared to Mo(=O)$_2$(OSi)$_2$, the FT-EXAFS of the activated catalyst shows a very different shape and a much lower peak amplitude below 2 Å (representing scatterers in the first coordination sphere of Mo), Figure 3.4b. A new peak at ca. 2.6 Å appears after activation. Conducting the EXAFS curvefitting at 2 – 3 Å shows the peak could arise from a Mo-Mo path at (2.82 ± 0.01) Å, similar to the path in Mo metal, Figure S3.2 and Table S3.1. Therefore, it appears that Mo reduction and oligomerization occur even as a large fraction of molybdenum carbene sites are generated.

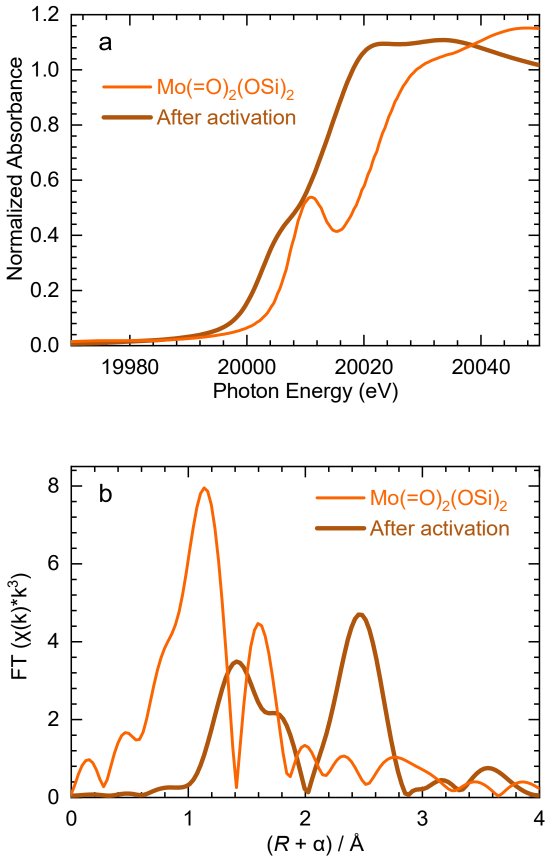

Figure 3.4 (a) Mo K-edge XANES, and (b) FT-EXAFS, for $Mo(=O)_2(OSi)_2$, before (orange) and after ethylene activation at 650 °C (brown).

The nature of the carbene species was investigated by ^{13}C CP/MAS solid-state NMR after activation of the $Mo(=O)_2(OSi)_2$ sites by ^{13}C-labeled ethylene at 650 °C. A strong, broad ^{13}C NMR peak at 120.12 ppm appears**,** Figure S3.1. Its chemical shift and stability upon exposure to air implies that it is primarily aromatic compounds.[148] By comparison to homogeneous Schrock-type Mo catalysts, the ^{13}C chemical shift for a Mo-methylidene should be higher than 250 ppm.[43, 149-151] No NMR signal for such a site was detected in the activated catalyst. To avoid NMR signals from aromatic residues, $Mo(=O)_2(OSi)_2$ was first activated with unlabeled ethylene, then exposed to ^{13}C-labeled ethylene at room temperature, Scheme 3.3. A sharp NMR signal at 19.84 ppm appears, along with a broad peak at 119 ppm, Figure 3.5. After 1 min exposure to air, the intensity of both NMR peaks decreased, showing that they correspond to carbon species that are air- and/or moisture-sensitive. Although there is still not carbene NMR signal, a previous DFT simulation predicted that Mo-methylidenes are less stable than molybdenacyclobutanes (MoC_3H_6);[152] therefore, the NMR signals could arise from a metallacyclobutane. The reported chemical shifts for α- and β-carbons in a Mo-cyclobutane compound were 100.19 and -0.80 ppm, respectively.[149] Similarly, a rhenacyclobutane was reported to have two peaks at ca. 120 and 20 ppm, respectively.[153] Therefore, the signals at 119 and 19.84 ppm may be assigned to the α- and β-carbons, respectively, in a molybdenacyclobutane.

Scheme 3.3 Formation of a ^{13}C-labelled molybdenacyclobutane at room temperature by reaction of ethylene-activated $Mo(=O)_2(OSi)_2$ with ^{13}C-labeled ethylene.

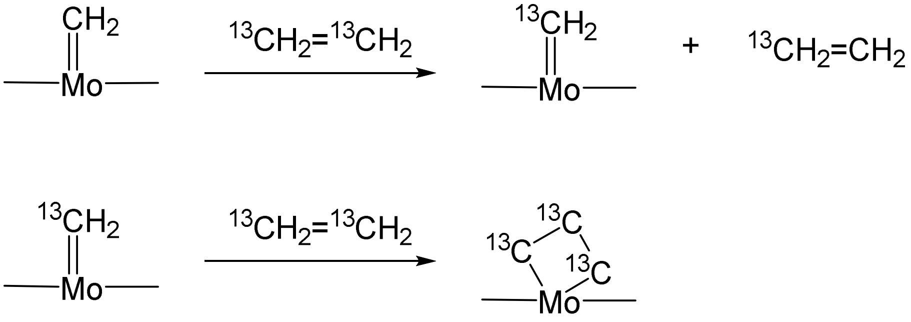

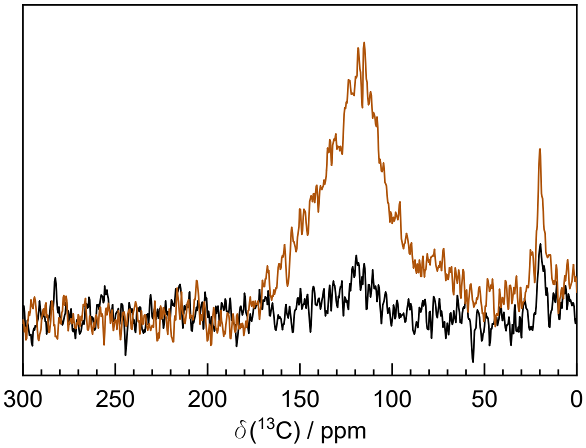

Figure 3.5 ^{13}C CP/MAS solid-state NMR of activated $Mo(=O)_2(OSi)_2$ exchanged with ^{13}C-labeled ethylene, before (brown) and after exposure to air (black).

A DFT study estimated the activation barrier for $Mo(=O)_2(OSi)_2$ to react with propene undergoing pseudo-Wittig mechanism, at 33.9 kcal/mol.[154] To obtain more evidence, the carbonyl product from the pseudo-Wittig pathway was sought. However, high temperature reactions with ethylene or propene (> 500 °C) lead to the decomposition of carbonyl compounds.[82] To lower the reaction temperature, 2-butene was used because $Mo(=O)_2(OSi)_2$ sites are reported to catalyze metathetical oxidation of 2-butene to acetaldehyde at temperatures as low as 300 °C.[108] A pseudo-Wittig mechanism was proposed for this metathetical oxidation, involving [2+2] cycloaddition of the olefin to the Mo=O bond. Since propene activation occurs at lower temperatures than ethylene activation, 2-butene is expected to react with $Mo(=O)_2(OSi)_2$ sites at even lower temperatures without acetaldehyde decomposition.

2-Butene was added at 400 °C to the flask containing $Mo(=O)_2(OSi)_2$ for 30 min, then IR measurement was conducted at room temperature. The IR spectrum of $Mo(=O)_2(OSi)_2$ sites after reaction with 2-butene contains a prominent peak at 1707 cm^{-1}, characteristic of C=O stretching (Figure 3.6). The adsorption of anhydrous acetaldehyde was performed at different temperatures for comparison. At room temperature, the C=O frequency, 1723 cm^{-1}, is similar to that of the pure compound, Figure 3.6.[155] However, if adding acetaldehyde at 400 °C, the C=O shifts to 1620 – 1680 cm^{-1} at room temperature, indicating several by-products form. The IR frequency varies over a wide range at 1730 – 1650 cm^{-1} depending on the condensation products.[156] The observed IR peaks of carbonyl species is consistent with a pseudo-Wittig reaction. Th $Mo(=O)_2(OSi)_2$ sites may undergo a pseudo-Wittig reaction with olefins at elevated temperatures. On the other hand, a different redox mechanism generating acetone was proposed for the activation of MoO_3/SiO_2 by propene at 50 °C.[36] Since the C=O band for acetone adsorbed on silica-alumina appears at 1690 – 1740 cm^{-1},[157] overlapping with acetaldehyde, we are unable to rule out the possibility of acetone.

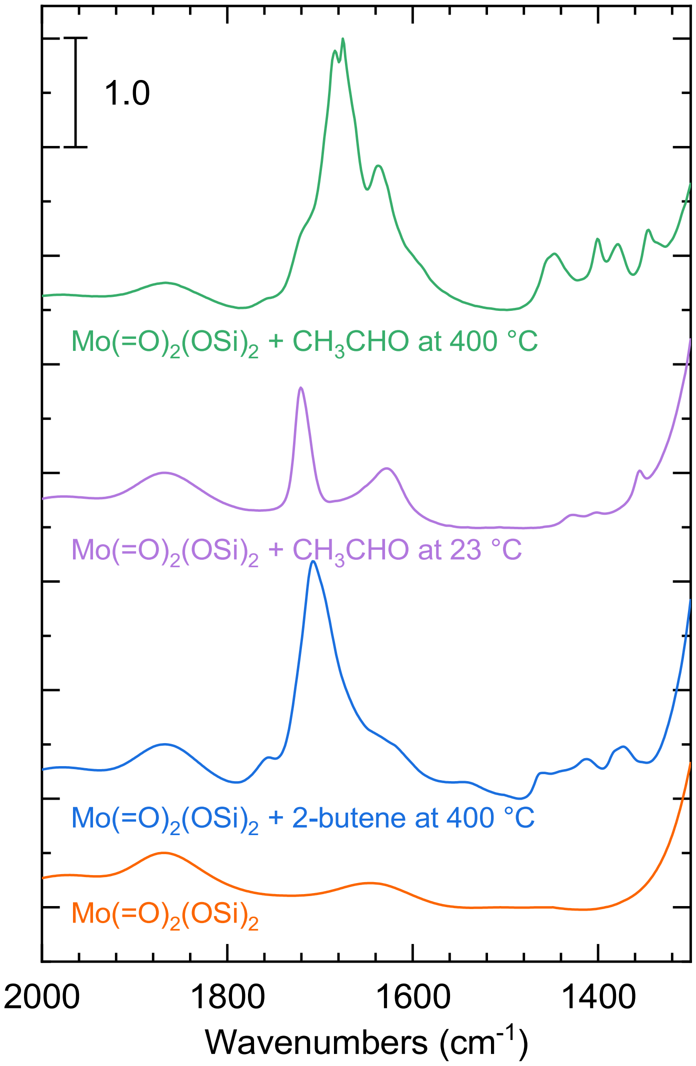

Figure 3.6 IR spectra of $Mo(=O)_2(OSi)_2$ sites treated with 2-butene and anhydrous acetaldehyde vapor at various temperatures.

3.4 Conclusions

Well-dispersed $Mo(=O)_2(OSi)_2$ sites were synthesized and their activation for olefin metathesis was explored. The molybdate sites are unable to promote olefin metathesis, even after calcination or reduction by CO or H_2. However, propene or ethylene treatment at high temperatures do activate the catalyst. At the same time, they induce aggregation and reduction of Mo(VI). The observation of carbonyl compounds suggests that activation may occur by a pseudo-Wittig mechanism.

3.5 Supporting Information

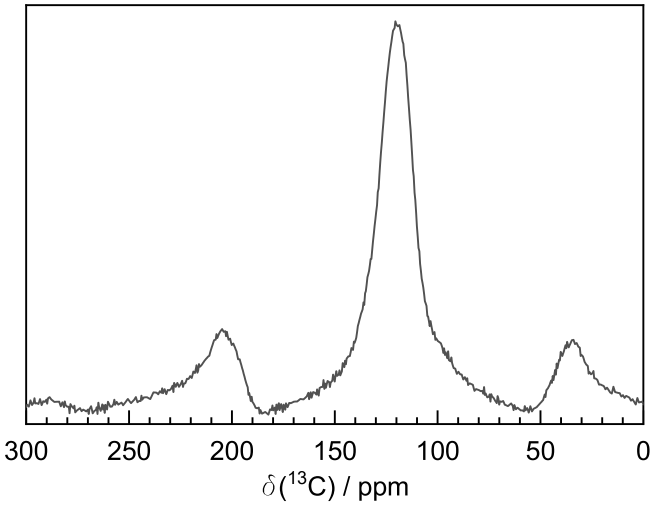

Figure S3.1 ^{13}C CP/MAS solid-state NMR of activated $Mo(=O)_2(OSi)_2$ by ^{13}C-labeled ethylene at 650 °C.

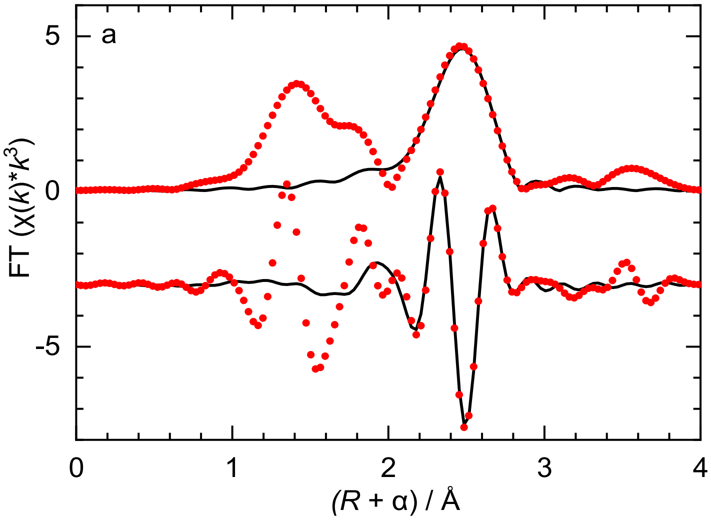

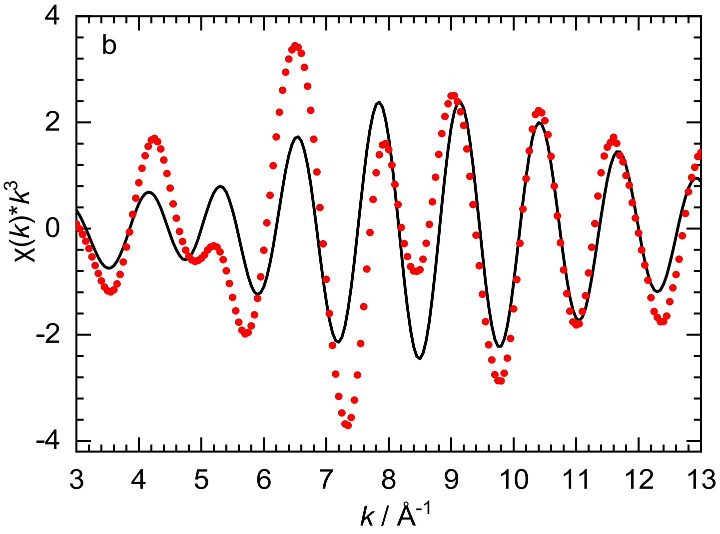

Figure S3.2 Curvefits of the Mo K-edge EXAFS in (a) *R*-space and (b) *k*-space for ethylene activated MoO_2Cl_2/SiO_2 at 650 °C, showing the fit (black lines) superposed on the FT magnitude and its imaginary component (points).

Table S3.1 Curvefit parameters [a] for the analysis of the Mo K-edge EXAFS of for ethylene activated MoO_2Cl_2/SiO_2 at 650 °C

Path	d / Å [b]	N	R / Å	$10^{-3}\ \sigma^2/Å^2$
Mo-Mo	2.743	2.6(3)	2.82(1)	8(1)

[a] S_0^2 was fixed at the value refined for Na_2MoO_4, 0.98. Data ranges: $2.4 \leq k \leq 14.0$ Å^{-1}, $2.0 \leq R \leq 3.0$ Å. ΔE_0 = -6(1) eV was refined as a global fit parameter. The total number of independent data points is 7.0. The total number of variable parameters in the fit is 4, with an *R*-factor of 0.011.[b] Reference distance for Mo-Mo is from the crystal structure of Mo metal.

Chapter 4. Investigation of Ga^iBu_3/Al_2O_3 structural evolution for propane dehydrogenation by *operando* X-ray absorption spectroscopy

4.1 Introduction

Propylene (C_3H_6) is the feedstock for various large-scale chemical products, including polypropylene, acrylonitrile, and propylene oxide.[158] In recent years, the shale gas revolution has resulted in a reduction in the amount of propylene supplied by crackers which, in conjunction with expanding production of polypropylene, has created an increasingly large, unmet "propylene gap" between supply and demand.[159-160] Newer technologies for manufacturing propylene include the Methanol-to-Olefins (MTO) process,[161] olefin metathesis,[140] and on-purpose propane dehydrogenation.[162-163] In particular, propane dehydrogenation has the benefit of providing propylene directly with high selectivity, along with H_2 as a valuable co-product. Two commercial on-purpose propylene processes, Catofin and Oleflex, are based on CrO_x/Al_2O_3 and $Pt\text{-}Sn/Al_2O_3$ catalysts, respectively.[45-47] The environmental hazards of Cr and the high cost of Pt, together with their complex modes of catalyst regeneration, motivate the search for alternative catalysts

One active area of research focuses on Ga dispersed on oxides. Gallium oxide dispersed on Al_2O_3 is reported to catalyze alkane dehydrogenation.[164-167] Different from well-dispersed Ga sites on H-ZSM5, Ga_2O_3/Al_2O_3 contains Ga atoms incorporated into Al_2O_3 support, along with Ga_2O_3 clusters.[168] Either pure Ga_2O_3 or Al_2O_3 can directly catalyze dehydrogenation reaction, but Ga_2O_3/Al_2O_3 achieves a higher reaction rate and a slower deactivation than pure compounds.[62, 169] Another advantage of alumina support is that the absence of strong Brønsted acid sites prevents the aromatization reaction seen in Ga/H-ZSM-5 catalysts. The dehydrogenation mechanism of Ga_2O_3/Al_2O_3 was proposed to be heterolytic C-H dissociation of alkane on a Ga-O bond, resulting in Ga-hydride and gallium alkoxide species.[166-167] Recently, a DFT study suggested the catalytical activity of Ga_2O_3 /Al_2O_3 may arise from the synergy between neighboring a 3-coordinate Al atom and a 4-coordinate Ga atom rather than the Ga site itself.[62]

The synthesis of Ga-based oxide catalysts for propane dehydrogenation is typically achieved by impregnating a high surface area support with an aqueous solution of Ga(III) ions, activated by calcination.[45] These materials can also be made by anhydrous deposition of an organogallium(III) complex onto the dry support without calcination.[50-53] Since propane dehydrogenation is highly endothermic, typically conducted at temperatures of 500 – 800 °C. Under these conditions, the desired reaction is often accompanied by undesired cracking and coking. The experimental availability of information regarding the active sites is limited by the severe conditions. Several *ex-situ* characterizations are deployed to identify present Ga oxide species on Al_2O_3, but most of the results are related to bulk Ga_2O_3 or the support.[164, 167, 170] In contrast, The identification of mononuclear Ga oxide species on Al_2O_3 is unclear, thwarting the efforts in the investigation of the dehydrogenation mechanism.

Grafting tri(isobutyl)gallium (Ga^iBu_3) onto partially dehydroxylated γ-alumina and amorphous silica was reported to result in different Ga species on the surfaces at room temperature.[53] Ga^iBu_3/Al_2O_3 has a mononuclear Ga structure, whereas Ga^iBu_3/SiO_2 is found to have dinuclear Ga sites. Then, the Ga catalysts were heated to 550 °C in flowing argon prior to propane dehydrogenation. Ga^iBu_3/Al_2O_3 reaches a maximum of 24% propane conversion, much higher than Ga^iBu_3/SiO_2 (8% conversion) under the same condition. Both Ga materials are carefully characterized by X-ray absorption spectroscopy at 10 K, as well as solid-state NMR at room temperature. However, the *ex-situ* characterizations are unable to provide direct Ga structural information under the reaction conditions. The alkyl ligands are expected to leave Ga under thermal treatment, but the pathway and the result are unknown.

To understand the evolution of Ga^iBu_3/Al_2O_3 under the thermal treatment and the catalytic process, we implemented the *operando* XAS technique to monitor the structural development of Ga species on Ga^iBu_3/Al_2O_3 from 23 to 550 °C. *Operando* XAS reveals replacing isobutyl ligands by an equivalent Ga-O bond, leading to a 3-coordinate mononuclear Ga site at 550 °C. Additionally, other minor Ga species may be formed. The EXAFS curvefitting suggests the Ga atom could be doped into Al_2O_3 support at 550 °C. This structural insight sheds light on the correlation between the mononuclear Ga site and the subsequent catalytic activity.

4.2 Experimental Methods

Materials. Ga^iBu_3/Al_2O_3 was synthesized according to a published method.[53] Helium gas (Research grade, Airgas) was used as received. Propane (99.99%, Praxair) was purified by an oxygen/moisture trap (Supelpure) before flowing into the reaction cell.

***Operando* X-ray Absorption Spectroscopy.** XAS spectra were recorded at the Ga K-edge (10,367 eV) on beamline 2-2, Si(220) phi = 90°, at Stanford Synchrotron Radiation Lightsource, which operates at 3.0 GeV with a current of 500 mA. For energy calibration, a W foil (L_{III}-edge, 10,207 eV) was placed after the second ion chamber following the incident beam direction. Data were acquired in transmission mode, using N_2-filled ionization chambers as detectors. Approximately 33 mg of Ga^iBu_3/Al_2O_3 (Ga 1.97 wt%)[53] was loaded into an *in-situ* XAS cell in an Ar-filled glove box and handled with careful air-free protection.[171] To handle the high temperature and minimize the incident beam absorption, the thin-wall quartz capillary (Hilgenberg GmbH, 100 mm in length, 3 mm O.D.) and quartz wool were used to accommodate samples. Each quick XAS scan takes about 92 seconds. 4 consecutive scans are merged at 550 °C in flowing propane to improve S/N. The pure He flow was set 30 mL/min under the thermal treatment and cooling down. 2 mL/min C_3H_8 and 8 mL/min He was set to test propane dehydrogenation reaction at 550 °C.

XAS data were processed and analyzed using the Demeter software package.[111] A linear function was subtracted from the pre-edge region, then the edge jump was normalized using the Athena program. The $\chi(k)$ data were isolated by subtracting a smooth, third-order polynomial approximating the absorption background of an isolated atom. The k^3-weighted $\chi(k)$ data were treated with Hanning window function then Fourier-transformed. The distances to the scattering atoms (R_i) and mean-squared displacements (σ_i^2) were obtained by nonlinear fitting with least-squares refinement of the EXAFS equation to the Fourier-transformed data in R-space, using the Artemis program. To simulate the EXAFS spectra of individual paths, the crystallographic information files were imported into Artemis. EXAFS spectra were generated using FEFF6.[111] Principle component analysis and linear combination fitting were conducted with Athena software.

Online Mass Spectroscopy. An online mass spectrometer (Hidden QGA) was connected after the *in-situ* XAS cell to monitor the gas products released during the reaction. m/z = 2, 4, 17, 28, 30, 32, 41, and 44 were scanned by a Faraday detector. m/z = 16, 39 and 43 were scanned by a SEM detector. The temperature data of Ga materials was measured and recorded simultaneously with MS data.

4.3 Results and Discussion

EXAFS analysis of as-prepared Ga^iBu_3/Al_2O_3. Previously, the reaction of Ga^iBu_3 with alumina was reported to remove one isobutyl ligand per Ga, and attachment of the complex to the support via a Ga-O-Al linkage. The EXAFS data, acquired at 10 K, were analyzed using a simple four-coordinate model, $(AlO)(Al_2O)Ga^iBu_2$, Scheme 4.1.[53] In the first coordination sphere, a shorter path ($N = 1$) is associated with the Ga-O bond at (1.89 ± 0.01) Å, in addition to a longer Ga-C1 path ($N = 2$) at (2.07 ± 0.02) Å.[53] Longer paths that may contribute FT magnitude intensity from 2-3 Å include weakly-bonded surface O, as well as non-bonded Ga – C2 and Ga-Al scattering.

Scheme 4.1 Proposed reaction of Ga^iBu_3 with partially dehydroxylated γ-Al_2O_3, resulting in mononuclear, four-coordinate grafted Ga sites.[53]

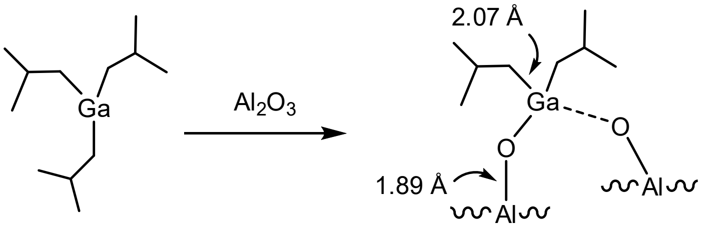

In this work, the EXAFS of as-prepared Ga^iBu_3/Al_2O_3 was acquired at room temperature. The data are consistent with the previously reported cryogenic data, Figure 4.1 and Figure S4.1, and the curvefit parameters are similar, Table 4.1. However, the Ga-C1 distance, (2.00 ± 0.01) Å, is slightly shorter in the fit of the room temperature data. It is still in the range of Ga-CH_2R distances, 1.97 – 2.06 Å, found in molecular organogallium complexes.[172-173] A long Ga-O path at ca. 2.5 Å, previously attributed to a weakly coordinated oxygen from the Al_2O_3, was again included in the curvefit. When the fit was performed without this path, the result is visually less satisfying and the R-factor increased from 1.7 to 3.5%, Figure S4.2 and Table S4.1.

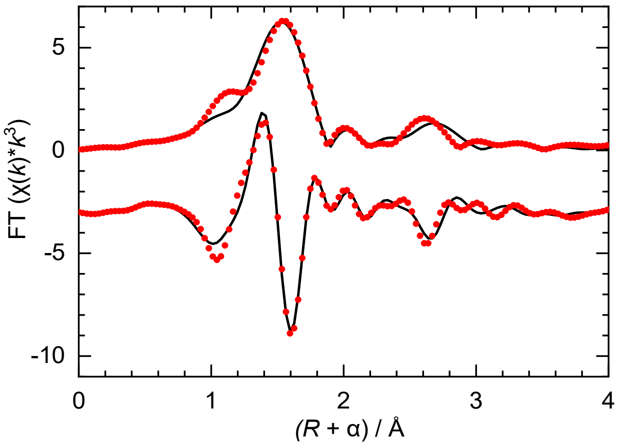

Figure 4.1 Ga K-edge EXAFS (point) for Ga^iBu_3/Al_2O_3 recorded at room temperature under He. The curvefit (line) includes a Ga-O path at ca. 2.5 Å.

Table 4.1 Curvefit Parameters[a] for Ga K-edge EXAFS of Ga^iBu_3/Al_2O_3, recorded at room temperature under He

Path	*d* [b]/ Å	*N* [c]	*R* / Å	σ^2 / Å^2
Ga – O1	1.863	1	1.86(2)	0.002(1)[d]
Ga – C1	2.066	2	2.00(1)	0.002(1)[d]
Ga – O2	2.585	1	2.49(3)	0.008(2)[e]
Ga – C2	2.976	2	2.96(3)	0.008(2)[e]
Ga – Al	3.325	1	3.24(4)	0.008(2)[e]

[a] S_0^2 was fixed at 1. ΔE_0 was refined as a global fit parameter, returning a value of (4 ± 1) eV. Data ranges: $3.0 \leq k \leq 13.0$ Å^{-1}, $1.0 \leq R \leq 3.2$ Å. The number of variable parameters is 8, out of a total of 13.8 independent data points. The R-factor for this fit is 1.7 %. [b] The Ga-O1 and Ga-O2 reference distances are from the crystal structure of Ga_2O_3 and $SrGa_2B_2O_7$, respectively.[174-175] The Ga-C and Ga-Al distances are from crystal structures of organogallium compounds.[176-177] [c] The coordination numbers were constrained to integer values, based on the model. [d] Constrained to the same value. [e] Constrained to the same value.

Evolution of the organogallium sites observed by *operando* XAS. The Ga K-edge XAS of Ga^iBu_3/Al_2O_3 was recorded as the sample was heated from room temperature to 550 °C at 10 °C/min in flowing He, Figure 4.2a. The initial edge position is 10,372.5 eV, with a maximum at 10,374.7 eV. For temperatures below 200 °C, the XANES shows only minor changes, Figure 4.3a. However, above 200 °C, the edge position shifts to higher energy, as the maximum at 10,374.7 eV is gradually replaced by a more intense peak at 10,376.8 eV, Figure 4.3b. As the temperature approaches 450 °C, the edge position stabilizes at 10,375.3 eV, Figure 4.3c. Since Ga is initially in its maximum oxidation state, this edge shift of nearly 3 eV must arise due to a change in ligand environment, such as replacing isobutyl ligands with O-donor ligands derived from the alumina surface.

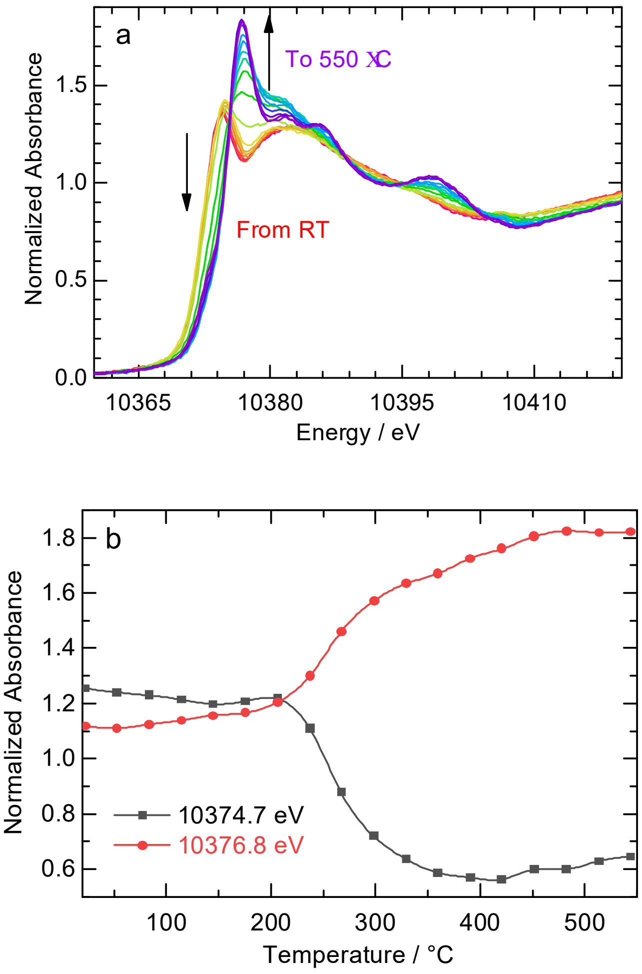

Figure 4.2 (a) Evolution of the Ga K-edge XANES for Ga^{i}Bu$_3$/Al$_2$O$_3$, recorded in flowing He while ramping the temperature from 23 °C (red) to 550 °C (purple) at 10 °C/min. Spectra in different temperature ranges are displayed in Figure 4.3. (b) Evolution of the Ga K-edge absorbance with temperature

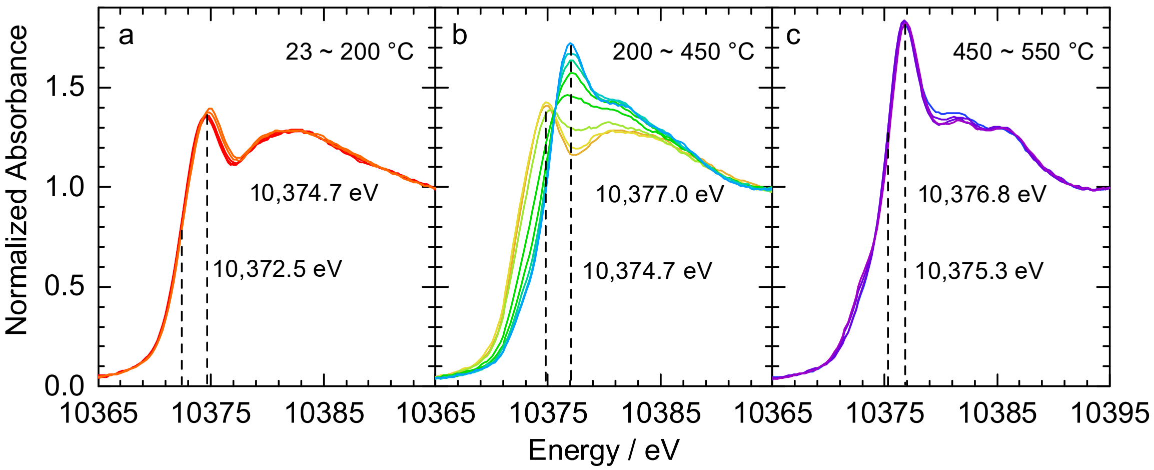

Figure 4.3 Evolution of the Ga K-edge XANES for Ga^iBu_3/Al_2O_3, recorded in flowing He while ramping the temperature from 23 to 550 °C at 10 °C/min: (a) 23 – 200 °C (red to orange); (b) 200 – 450 °C (from orange to blue); (c) 450 – 550 °C (blue to purple).

The volatile products released during heating were analyzed by online mass spectrometry. From 100 – 450 °C, the major hydrocarbons include the expected isobutane ($m/z = 43$) and isobutene ($m/z = 39$), as well as propane ($m/z = 29$) and propene ($m/z = 41$), Figure 4.4. All appear simultaneously in this temperature range. Isobutane presumably forms by protonolysis involving residual surface protons. Isobutene may form by β-H elimination, in a reaction resembling the thermal decomposition of GaR_3 (R = Et, ^{n}Pr, ^{n}Bu),[178-179] and the reaction of Et groups on the GaAs(100) surface.[180] The resulting hydride may also contribute to isobutane formation by reductive elimination, although the edge position is not consistent with this being a major pathway. Homolytic cleavage of the Ga-C bond is also known in organogallium decomposition mechanisms, particularly at higher temperatures. One study reported slightly lower barriers for homolysis relative to β-H elimination for larger alkyl groups on

GaAs(100).[180] However, these reactions also imply a reduction in oxidation state for Ga, which is inconsistent with the XANES.

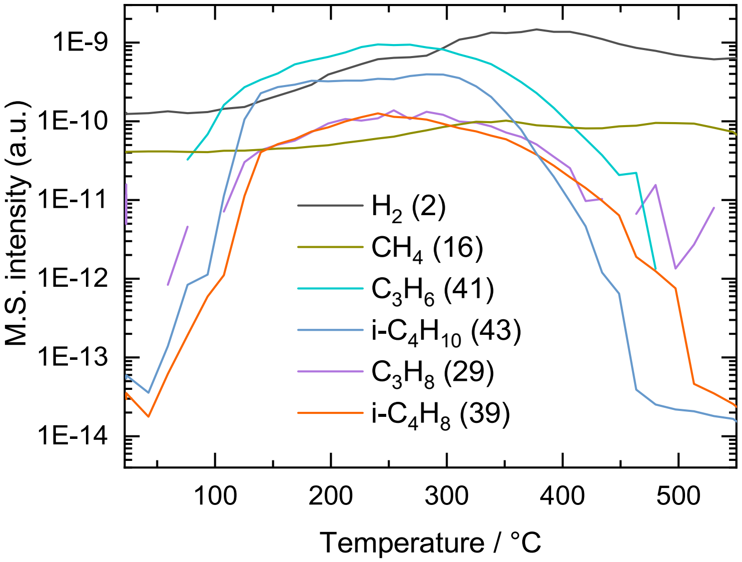

Figure 4.4 Evolution of gas products released from Ga^iBu_3/Al_2O_3 as a function of temperature recorded by mass spectroscopy in flowing He and while ramping the temperature from 23 °C to 550 °C at 10 °C/min.

Above 420 °C, few additional changes occur in the XANES, Figure 4.3c. However, a weak shoulder superimposed on the edge appears at 10,372.4 eV, seen more clearly in Figure S4.3 and Figure S4.4. Its emergence causes the intensity at 10,376.8 eV to rise slightly. In the gas phase, signals for H_2 ($m/z = 2$) and methane ($m/z = 16$) appear at higher temperatures, Figure 4.4. In principle, these products may arise via reductive elimination from [$Ga^{III}H_2$] and [Ga^{III}(H)(Me)] sites, respectively. However, such reactions would generate Ga(I) sites,[57] and since the edge position (10,375.3 eV) does not change significantly, it is unlikely that much Ga(III) is reduced.

The non-phase-corrected FT-EXAFS for Ga^{i}Bu$_3$/Al$_2$O$_3$ recorded at room temperature contains two prominent peaks, at ca. 1.5 and 2.6 Å, Figure 4.5. The peak intensity at ca. 1.5 Å initially decreases slightly as the temperature rises from 23 – 200 °C, then increases gradually and shifts to a slightly shorter distance (ca. 1.3 Å) as the temperature is raised to 450 °C, Figure S4.5. These changes are consistent with the replacement of isobutyl ligands by oxygen-donor ligands, since the value of d(Ga-O) = 1.89 Å is shorter than d(Ga-C$_\alpha$) = 2.00 Å. Above 100 °C, the peak at ca. 2.6 Å becomes broader, then new features appear between 2.5 and 3.5 Å. The wavelet-transform EXAFS reveals that the signal in the region 2.5 – 3.5 Å becomes stronger and more complex as the temperature is raised, Figure S4.6.

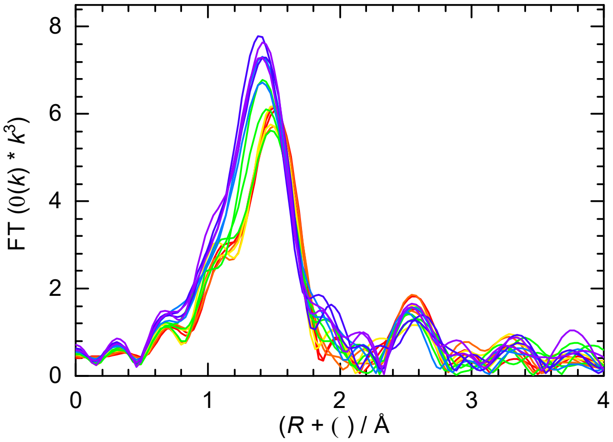

Figure 4.5 Evolution of the Ga K-edge EXAFS for Ga^{i}Bu$_3$/Al$_2$O$_3$, recorded in flowing He while ramping the temperature from 23 °C (red) to 550 °C (purple) at 10 °C/min.

Principal Component Analysis. The evolution of the XANES region for Ga^{i}Bu$_3$/Al$_2$O$_3$ from 23 to 550 °C was assessed via principal component analysis (PCA). All 18 XANES spectra from 23 to 550 °C, covering the region between 10,322 and 10,522 eV, were used to find the principal components. Just two components account for 0.9990 cumulative variance, Figure 4.6a. The first component (variance 0.9776) consists of a rising edge followed by oscillations, similar to a XANES spectrum. Its primary role is to reproduce the edge jump. The second component (variance 0.0214) is predominantly a simple oscillation at 10,368 – 10,381 eV. The contributions of the rest components are minimal.

The spectra were reconstructed by linear combination fitting (LCF) of the first two PCA components. Changes in the contributions of each component are shown as a function of temperature in Figure 4.6b. The contribution of the first component is unchanged over the whole temperature range. The contribution of the second component decreases slightly from 23 – 200 °C, becomes negative at higher temperatures, then starts to increase again above 400 °C. These changes create variations in absorbance at 10,374.7 and 10,376.8 eV in Figure 4.2b.

The XANES reconstructions suggest that the evolution of $Ga^{i}Bu_3/Al_2O_3$ from 23 to 550 °C can be represented primarily by a single, gradual process, i.e., the replacement of isobutyl ligands with oxygen-donor ligands derived from the alumina surface. It occurs mostly between 200 and 350 °C. The reconstructed XANES at 23 °C is a good match for the experimental spectrum, Figure S4.7. However, the reconstructed XANES at 550 °C lacks sufficient intensity at 10,378.6 eV and some of the post-edge oscillations. These discrepancies indicate contributions from minor sites not represented by the 2-component PCA. Being a bulk technique, XAS generally lacks sensitivity for minor sites.

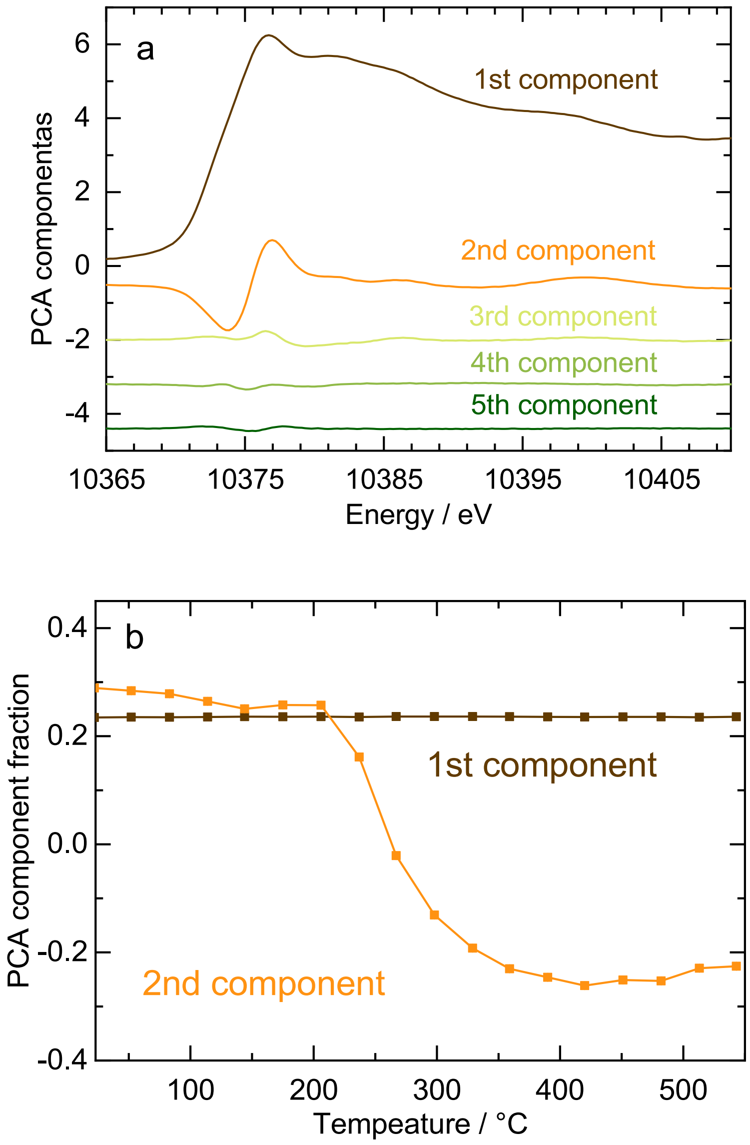

Figure 4.6 (a) The first five components extracted from principal component analysis of the XANES for Ga^{i}Bu$_3$/Al$_2$O$_3$, recorded as a function of temperature from 23 to 550 °C in He. (b) Contributions of the first and second components used to reconstruct the experimental XANES.

EXAFS analysis of $Ga^{i}Bu_3/Al_2O_3$ after thermal treatment. The structure of $Ga^{i}Bu_3/Al_2O_3$ was reassessed after heating to 550 °C in flowing He. During cooling to room temperature, the XANES of $Ga^{i}Bu_3/Al_2O_3$ almost remains unchanged, while the EXAFS amplitude in *k*-space increases with no other changes in appearance, Figure S4.8. Thus, the EXAFS after cooling reflects structural information about the Ga species present at 550 °C under He. Two prominent signals appear in the k^3-weighed FT-EXAFS after the thermal treatment, Figure 4.7. In particular, the signal at 2.5 – 3.5 Å is much stronger than the one in as-prepared $Ga^{i}Bu_3/Al_2O_3$, implying new features in the interaction between Ga and the Al_2O_3 support. To simplify the model, we consider that no Ga-C paths remain. The EXAFS curvefit of the region below 2 Å suggests that Ga is 3-coordinate with *R*(Ga-O) = 1.85 Å, Figure 4.8, Figure S4.9, and Table 4.2. Including a second, slightly longer Ga – O path did not improve the fit.

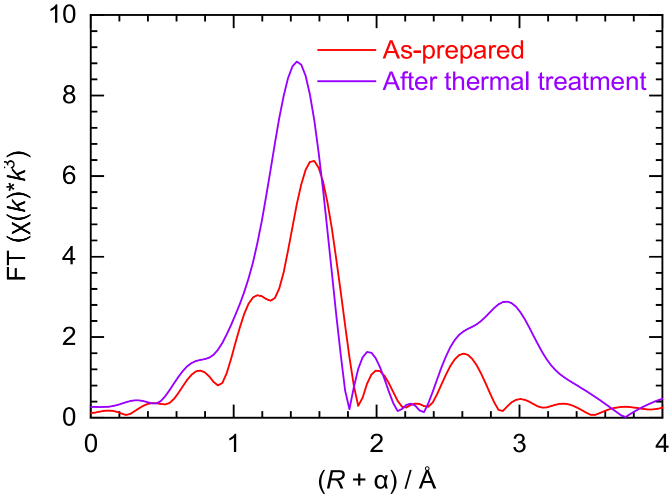

Figure 4.7 Comparison of Mo K-edge FT-EXAFS for $Ga^{i}Bu_3/Al_2O_3$, before (red) and after (purple) treatment at 550 °C in flowing He. Both spectra were recorded at 23 °C.

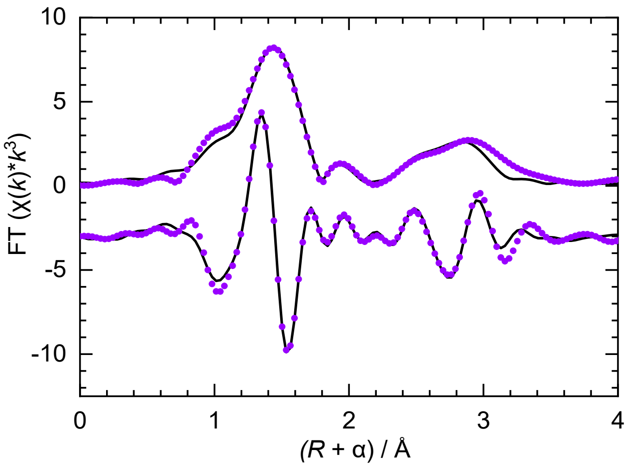

Figure 4.8 EXAFS (point) and curvefit (line) for Ga^iBu_3/Al_2O_3 after heating to 550 °C under He and cooling to room temperature.

Table 4.2 Curvefit parameters[a] for Ga K-edge EXAFS of Ga^iBu_3/Al_2O_3 after heating to 550 °C in He and cooling to room temperature.

Path	d [b]/ Å	N	R / Å	σ^2 / Å^2
Ga – O1	1.803	3.0(2) [c]	1.85(1)	0.004(1)
Ga – O2	2.772	1 [c]	2.97(4)	0.006(1) [d]
Ga – Al	3.511	3.0(2) [c]	3.30(2)	0.006(1) [d]

[a] S_0^2 was fixed at 1. Data ranges: $3.0 \leq k \leq 13.0$ Å^{-1}, $1.0 \leq R \leq 4.0$ Å. The number of independent data points is 18.9. ΔE_0 was refined as a global fit parameter, returning a value of (-1 ± 2) eV. The number of variable parameters is 8. The R-factor for this fit is 1.7 %. [b] The Ga-O and Ga-Al distances were extracted from a computational model for 3-coordinate Ga dispersed in Al_2O_3.[62] [c] N(Ga-O1) and N(Ga-Al) were constrained to the same value. N(Ga-O2)

was fixed at 1, based on the computational model.[62] [d] Constrained to the same value to reduce the number of variables in the fit.

The broad signals from 2.5 – 3.5 Å (Figure 4.7) suggest contributions from more than one path in this region. Candidates include Ga-O, Ga-Al, and Ga-Ga single-scattering, as well as multiple-scattering paths. Since surface heterogeneity complicates curvefitting in this region, we attempted to use the fewest paths possible to describe the average environment of the major Ga species. Including just one path (Ga-O, Ga-Al, or Ga-Ga) led to the conclusion that the broad feature at ca. 2.9 Å arises principally from a Ga-Al path ($N = 3.0$) at 3.30 Å, Table 4.2. A computational model for Ga doped into Al_2O_3 has a long (non-bonded) Ga-O path at 2.77 Å.[62] Including a similar Ga-O path in the curvefit (with N fixed at 1) resulted in a much longer distance, 2.97 Å. The Ga_2O_3 crystal structure has several Ga-Ga paths at ca. 2.9 Å.[174] An attempt to include such a path (with N fixed at 1) in the curvefit returned a distance of 2.95 Å and a large σ^2, 0.011 Å^2, Figure S4.10 and Table S4.2. Since the major contribution in this region arises from the Ga-Al path, EXAFS curvefitting cannot definitely identify other contributions. However, it seems unlikely that the initially mononuclear Ga site becomes dinuclear during thermal treatment in an inert atmosphere, particularly since the Ga loading is low (2 wt%).[53] Therefore, we conclude that thermal treatment of $Ga^{i}Bu_3/Al_2O_3$ in an inert atmosphere forms primarily mononuclear 3-coordinate Ga sites, Scheme 4.2.

Scheme 4.2 Proposed evolution of Ga^iBu_3/Al_2O_3 during heating to 550 °C in flowing He

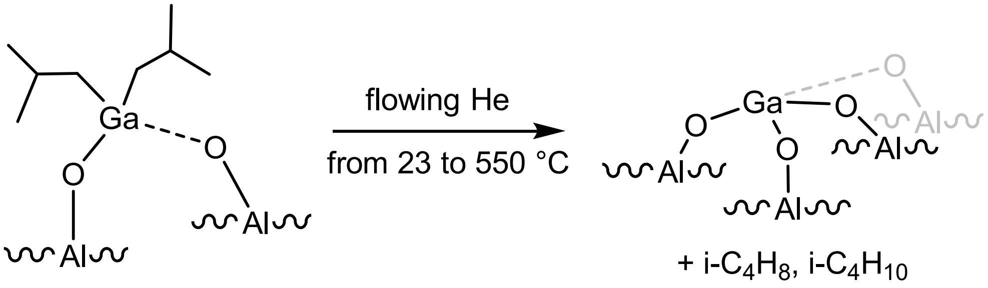

XAS of Ga^iBu_3/Al_2O_3 during propane dehydrogenation. The propane conversion by Ga^iBu_3/Al_2O_3 at 550 °C was reported to decrease gradually from 24 to 14% over 200 min.[53] Ga^iBu_3/Al_2O_3 heated to 550 °C under He was exposed to 20 vol% C_3H_8/He at the same temperature, and Ga K-edge XAS spectra were recorded while flowing propane for 200 min to monitor structural change in the Ga sites. Both XANES and EXAFS show small changes during this period, Figure 4.9 and Figure S4.11. Specifically, the intensity of the XANES shoulder at 10,371.0 eV decreases, while the intensity of the EXAFS peak at 1.4 Å in *R*-space increases slightly. The broad peaks at 2.5 – 3.5 Å remain essentially unchanged.

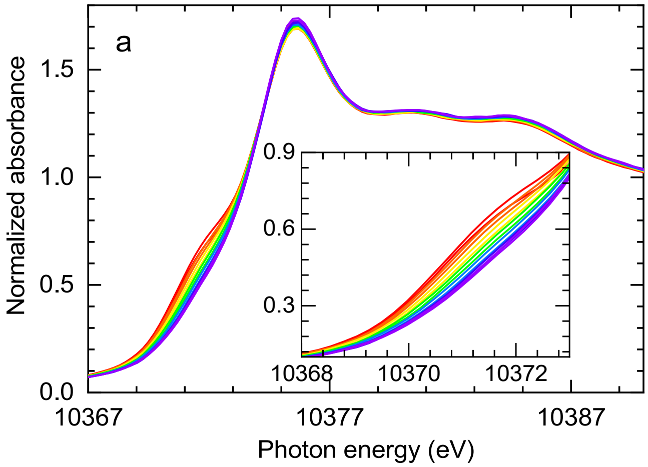

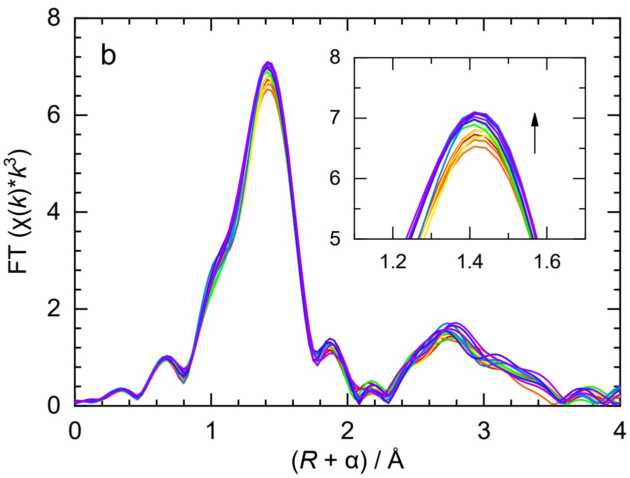

Figure 4.9 Evolution of the Ga K-edge XAS of Ga^{i}Bu$_3$/Al$_2$O$_3$, recorded in flowing 20 vol% C$_3$H$_8$/He at 550 °C for 200 min, in two regions: (a) XANES, and (b) EXAFS. The colors from red to purple show the time course (with inset showing the major spectrum changes).

These small changes may be linked to the minor Ga species generated by the thermal treatment above 450 °C (see above). Significantly, a XANES shoulder in a similar location (10374.2 eV) appeared in flowing He as the temperature was raised from 450 to 550 °C. The negative correlation between the XANES intensity at ca. 10,371 eV and the EXAFS peak intensity at ca. 1.4 Å (corresponding to Ga-O paths) has been reported for several Ga dehydrogenation catalysts upon H$_2$-treatment.[56, 63-64, 69-70, 181] However, the assignment of the low energy peak (ca. 10371 eV) in Ga K-edge XANES is controversial. Suggestions include Ga(I), Ga(III)-hydride or 3-coordinate Ga(III) sites.[1, 54, 70] The formation of Ga(III)-hydrides seems unlikely in our system since thermal treatment was performed in He rather than H$_2$ (although the isobutyl ligands may be a source of H). Three-coordinate Ga sites, with a XANES peak at ca. 10379 eV, are formed under He before introducing C$_3$H$_8$. It is possible that the shoulder at 10,371 eV arises from a small amount of Ga(I), possibly resulting from the reductive elimination of the isobutyl ligands.

The previously observed decline in catalytic activity suggests that the minority species such as Ga(I) may be responsible for much of the initial dehydrogenation activity, although they deactivate quickly. However, redox mechanisms for Ga(I) sites involve interconversion with Ga(III) sites. For example, oxidative addition of propane would form the ethyl hydride site $[Ga(H)(C_3H_7)]^+$.[50, 58] Alternatively, protonation of Ga(I) could give rise to a Ga(III) hydride.[54] The amplitude increase in the first coordination sphere is consistent with these two proposed activation mechanisms. Meanwhile, 3-coordinate Ga oxide species remain to catalyze propane dehydrogenation at a slower rate. Although the 3-coordinate Ga sites appear to be less active, they are more robust.[182] DFT simulations predicted that a 3-coordinate Ga oxide site can undergo concerted (simultaneous formation of alkene) or stepwise mechanisms (forming alkylGa sites) to catalyze propane dehydrogenation.[62, 182]

4.4 Conclusions

The structural evolution of Ga^iBu_3/Al_2O_3 from as-prepared to catalytic conditions was probed by *operando* X-ray absorption spectroscopy. Ga^iBu_3/Al_2O_3 undergoes step-wise ligand removal from 23 to 550 °C in flowing He. It is primarily transformed to 3-coordinate Ga(III). Replacement of the isobutyl ligands by O-donor ligands in the first coordination sphere alters the edge position and white line intensity in the XANES, without a change in oxidation state. Principal component analysis of the XANES during thermal treatment suggests that a minor fraction of Ga sites forms above 400 °C, presumably Ga(I). These minor sites are more effective catalysts for propane dehydrogenation but they deactivate rapidly. The remaining Ga(III) sites show a lower but more stable catalytic performance.

Supported organometallic catalysts allow to connect the structures of dispersed Ga sites to their catalytic activity. Previous studies of Ga/Al_2O_3 were complicated by the presence of Ga_2O_3 clusters, which also show measurable catalytic activity. *Operando* X-ray absorption spectroscopy enables the direct observation of even dilute metal sites under reaction conditions.

4.5 Supporting Information

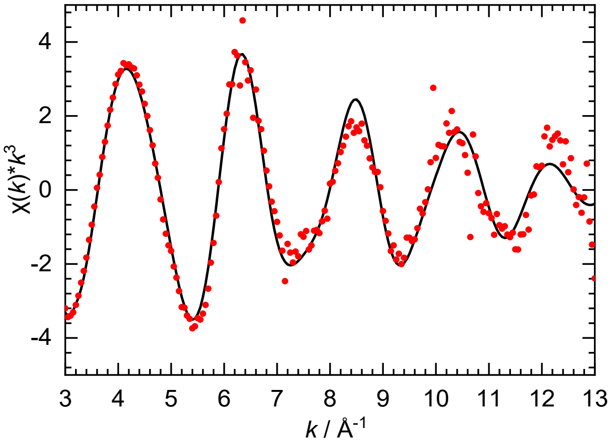

Figure S4.1 Curvefits (line) of the Mo K-edge EXAFS (points) in k^3-weighted k-space for Ga^iBu_3/Al_2O_3.

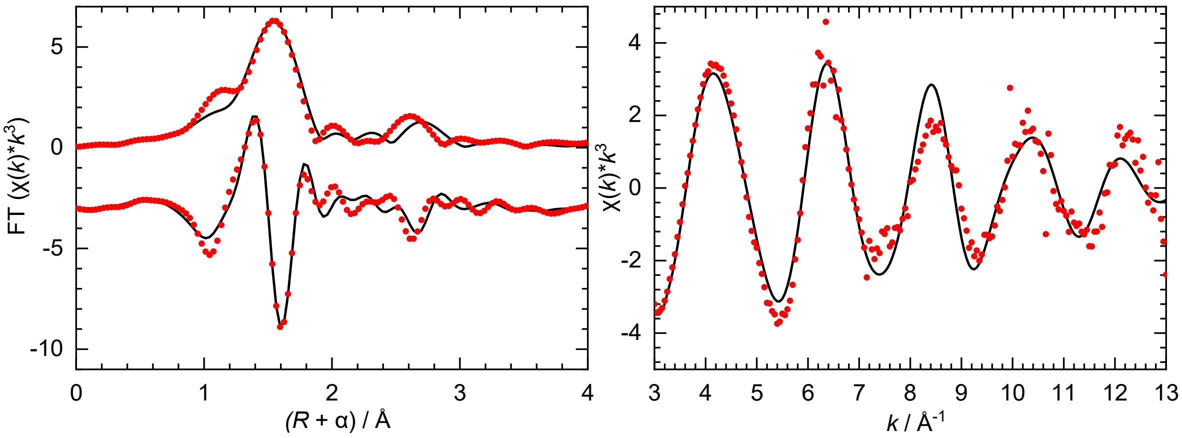

Figure S4.2 Ga K-edge EXAFS (point) for Ga^iBu_3/Al_2O_3 recorded at room temperature under He. The curvefit (line) DOES NOT include a Ga-O path at ca. 2.5 Å.

Table S4.1 Curvefit Parameters[a] for Ga K-edge EXAFS of Ga^iBu_3/Al_2O_3 without a Ga-O path at ca. 2.5 Å, recorded at room temperature under He

Path	d [b]/ Å	N [c]	R / Å	σ^2 / Å^2
Ga – O1	1.863	1	1.87(3)	0.002(2)[d]
Ga – C1	2.066	2	2.01(2)	0.002(2)[d]
Ga – C2	2.976	2	3.03(5)	0.010(5)[e]
Ga – Al	3.325	1	3.24(6)	0.010(5)[e]

[a] S_0^2 was fixed at 1. ΔE_0 was refined as a global fit parameter, returning a value of (6 ± 1) eV. Data ranges: $3.0 \leq k \leq 13.0$ Å^{-1}, $1.0 \leq R \leq 3.2$ Å. The number of variable parameters is 7, out of a total of 13.8 independent data points. The R-factor for this fit is 3.5 %. [b] The Ga-O1 and Ga-O2 reference distances are from the crystal structure of Ga_2O_3 and $SrGa_2B_2O_7$, respectively.[174-175] The Ga-C and Ga-Al distances are from crystal structures of organogallium

compouns.[176-177] [c] These coordination numbers were constrained to integer values, based on the model. [d] Constrained to the same value. [e] Constrained to the same value.

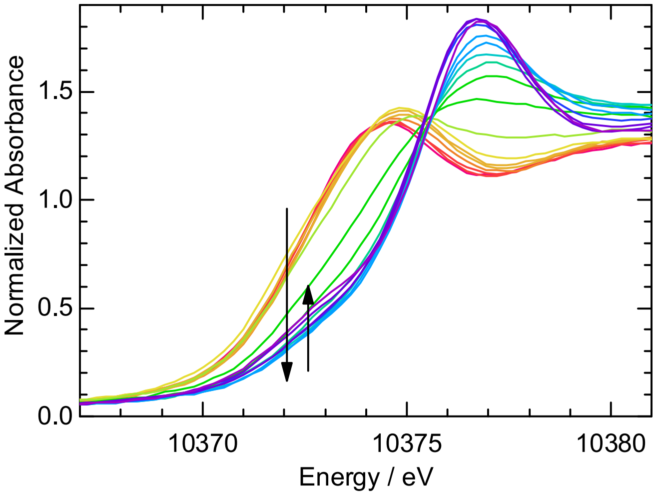

Figure S4.3 Closeup of the Ga K-edge XANES for Ga^iBu_3/Al_2O_3, recorded in flowing He while ramping the temperature from 23 °C (red) to 550 °C (purple) at 10 °C/min.

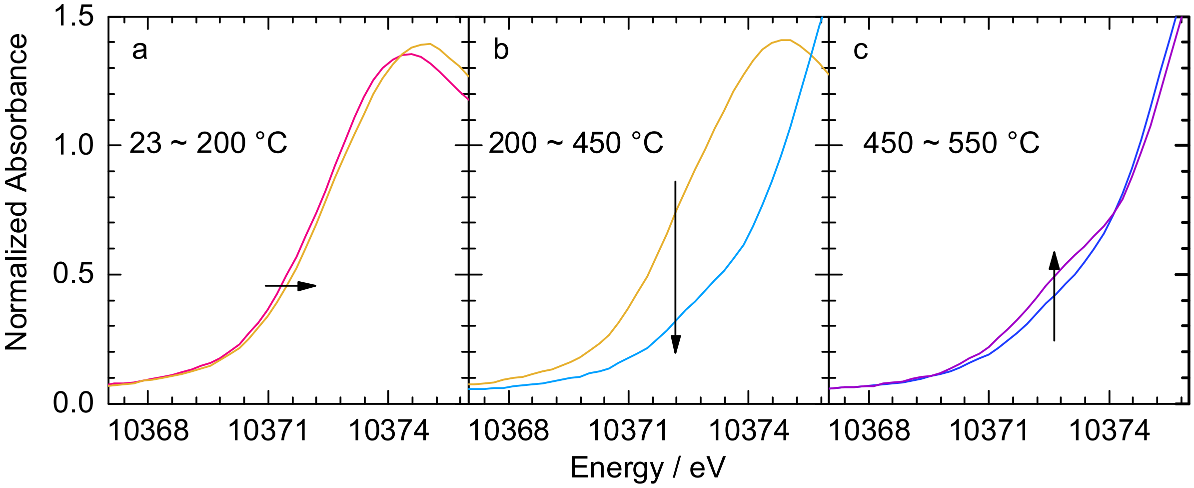

Figure S4.4 Closeup of the Ga K-edge XANES for Ga^{i}Bu$_3$/Al$_2$O$_3$, recorded in flowing He while ramping the temperature from 23 °C to 550 °C at 10 °C/min: (a) 23 – 200 °C (red to orange); (b) 200 – 450 °C (from orange to blue); (c) 450 – 550 °C (blue to purple).

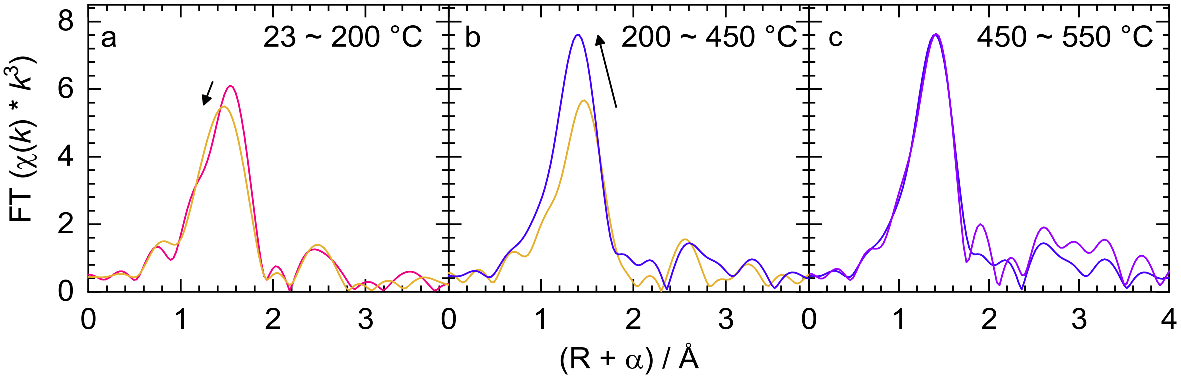

Figure S4.5 Evolution of the Ga K-edge EXAFS for GaiBu3/Al2O3, recorded in flowing He while ramping the temperature from 23 °C (red) to 550 °C (purple) at 10 °C/min. Left: 22 °C (red) and 83 °C (orange); Middle: 114 °C (orange) and 420 °C (blue); Right: 451 °C (blue) and 543 °C (purple).

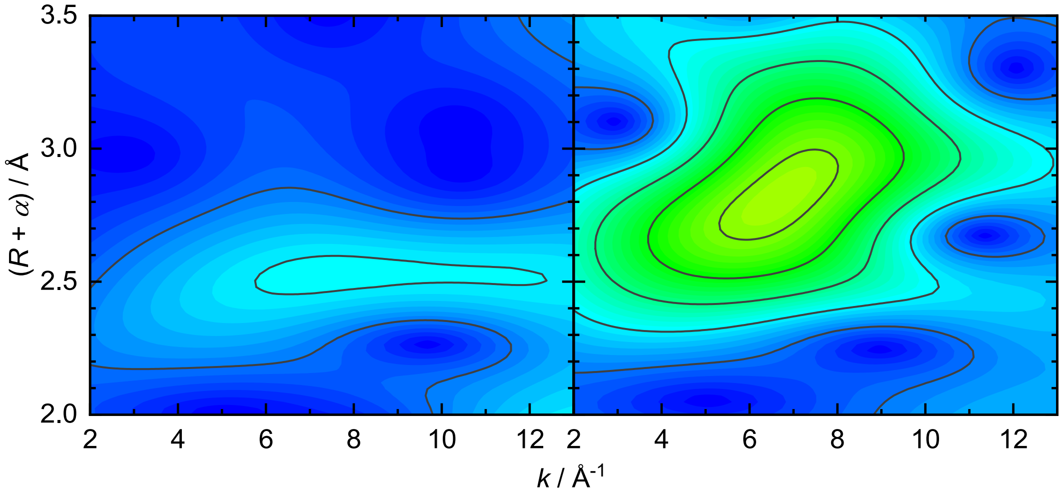

Figure S4.6 Wavelet-transform EXAFS of Ga^{i}Bu$_3$/Al$_2$O$_3$, at 23 °C (left) and 550 °C (right).

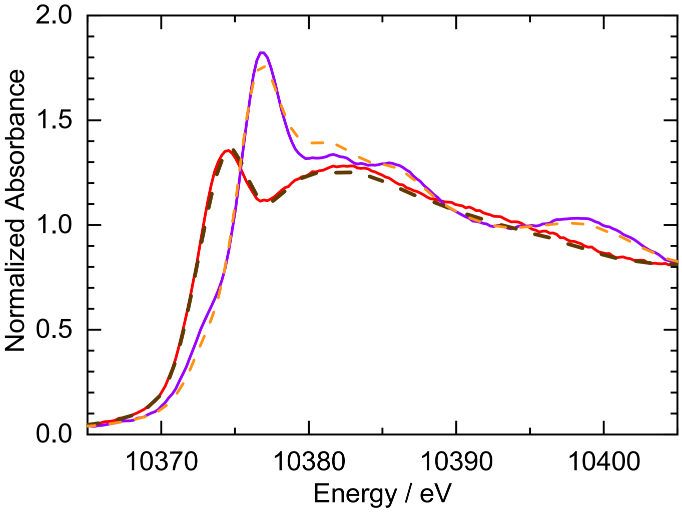

Figure S4.7 Ga K-edge XANES for Ga^{i}Bu$_3$/Al$_2$O$_3$ at 23 °C (red line) and 550 °C (purple line), in comparison with the reconstructed XANES from PCA components at 23 °C (brown dash line) and 550 °C (orange dash line).

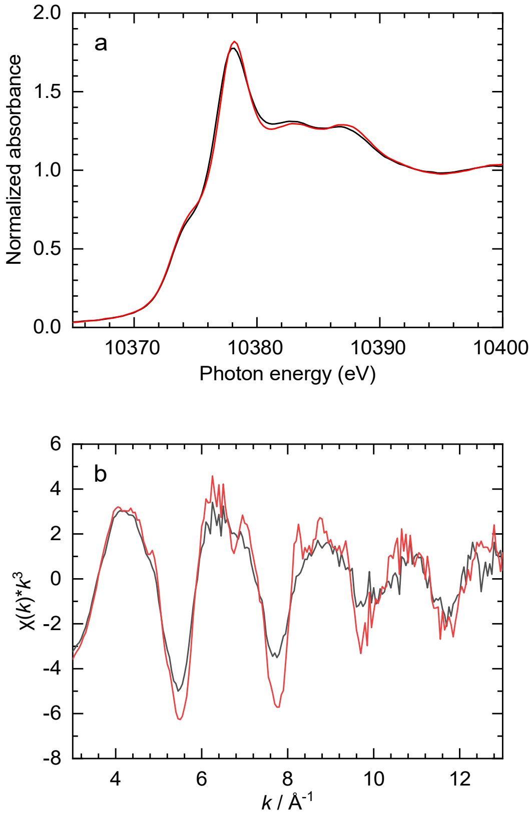
a
Normalized absorbance
2.0
1.5
1.0
0.5
0.0
10370
10380
10390
10400
Photon energy (eV)
b
$\chi(k)*k^3$
6
4
2
0
-2
-4
-6
-8
4
6
8
10
12
k / Å^{-1}

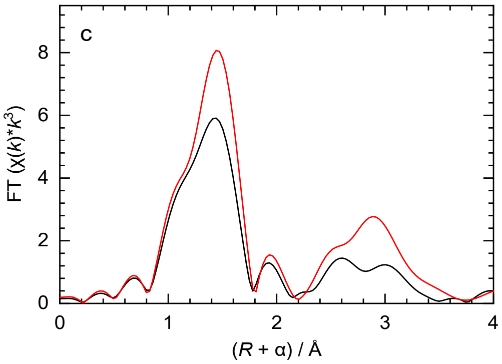

Figure S4.8 The comparison of Ga K-edge (a) XANES, (b) EXAFS in k^3-weighted k-space, and (c) k^3-weighted FT-EXAFS for Ga^{i}Bu$_3$/Al$_2$O$_3$ at 550 °C (black line) and cool down to 23 °C (red line).

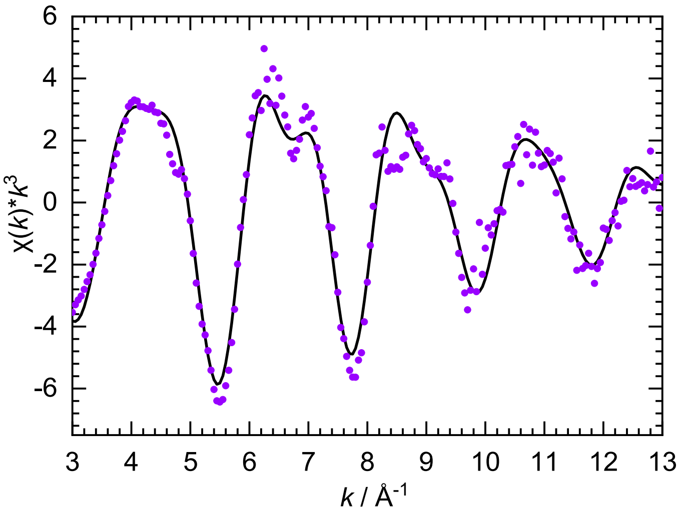

Figure S4.9 Curvefits (red) of the Ga K-edge EXAFS (points) in k^3-weighted k-space for Ga^{i}Bu$_3$/Al$_2$O$_3$ after heating to 550 °C under He and cooling to room temperature.

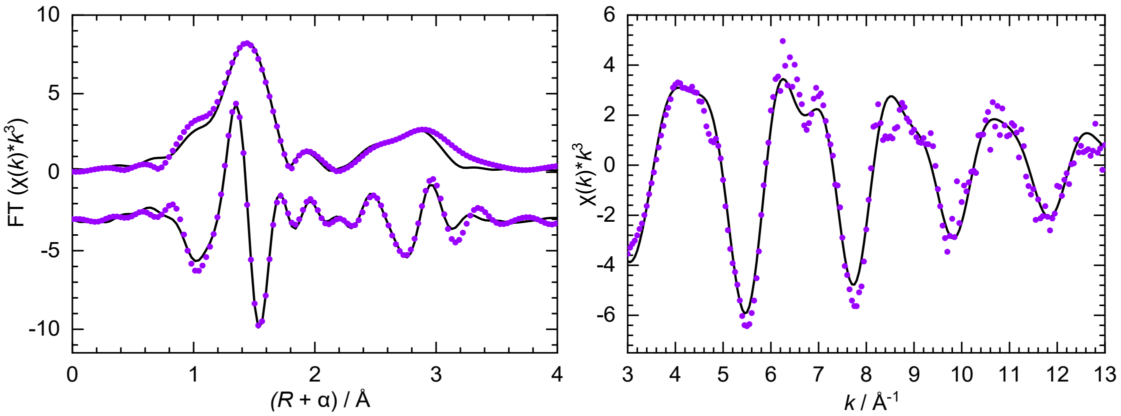

Figure S4.10 Curvefits (line) of the Ga K-edge EXAFS (points) in k^3-weighted *k*-space for Ga^{i}Bu$_3$/Al$_2$O$_3$ after heating to 550 °C under He and cooling to room temperature, with a dinuclear Ga model.

Table S4.2 Curvefit parameters[a] for Ga K-edge EXAFS of Ga^{i}Bu$_3$/Al$_2$O$_3$ after heating to 550 °C under He and cooling to room temperature, with a dinuclear Ga model.

Path	d^b/ Å	N	R / Å	σ^2 / Å^2
Ga – O1	1.803	3.0(3)	1.85(1)	0.004(1)
Ga – Ga1	3.037	1[c]	2.95(4)	0.011(4)
Ga – Al1	3.511	3[c]	3.31(2)	0.007(2)

[a] S_0^2 was fixed at 1. Data ranges: $3.0 \leq k \leq 13.0$ Å^{-1}, $1.0 \leq R \leq 4.0$ Å. The total independent data point is 18.9. ΔE_0 was refined as a global fit parameter, returning a value of (-1 ± 1) eV. The number of variable parameters is 8. The R-factor for this fit is 1.7 %. [b] The Ga-O and Ga-Al distances are extracted from a 3-coordinate doped mononuclear Ga on Al$_2$O$_3$ model.[62] The Ga-Ga distance is extracted from the crystal structure of Ga$_2$O$_3$.[174] [c] N was fixed based the dinuclear Ga structure.

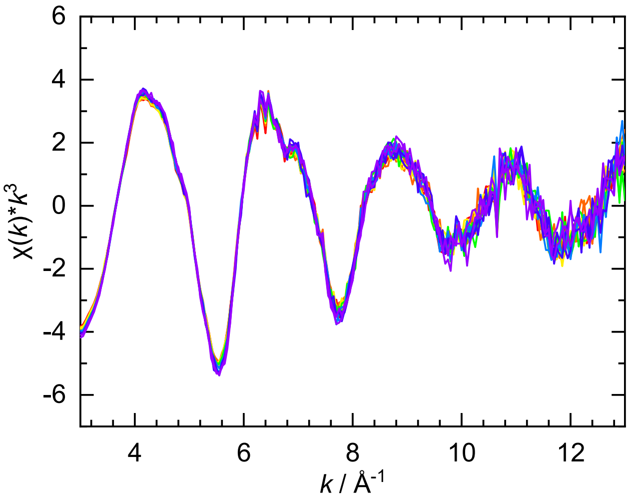

Figure S4.11 Evolution of the Ga K-edge EXAFS for GaiBu3/Al2O3 in k3-weighted k space, recorded in flowing 20 vol% C3H8/He at 550 °C for 3 h.

Chapter 5. Non-Innocent Carbon Support Enables a Redox-active Atomically-Dispersed Iron Catalyst for C–O Hydrogenolysis

5.1 Introduction

Heterogeneous catalysts with atomically-dispersed metal sites are emerging as a new frontier in catalytic transformations because of their maximal atom-utilization and unique selectivities.[183-185] When designing atomically-dispersed catalysts, both stability and activity need to be taken into consideration. Stability can be achieved when the metal center is firmly anchored onto the support, while the activity may be impacted by a lack of sufficient empty coordination sites to bind reactants.[186] This compromise between stability and activity can be overcome when a non-innocent support provides additional binding sites to assist in the chemisorption of intermediates in a catalytic cycle.[187] Therefore, atomic-level understanding of the metal-support interaction is critical to the design of new catalysts for complex transformations. However, the lack of long-range order for heterogeneous catalysts renders structural elucidation and mechanistic understanding rather challenging.[188]

The importance of metal-support interactions is well illustrated in the case of hydrotreating catalysts (for hydrogenation or hydrogenolysis).[189] Selective hydrogenation has been reported in the reduction of nitroarenes, carbonyls, and alkenes.[190-194] For example, a single-atom Pd catalyst on carbon nitride showed high activity and selectivity for the semi-hydrogenation of alkynes, in comparison to a catalyst with Pd nanoparticles.[191] These reactions do not require co-adsorption of unsaturated reactants and have been shown to follow the Eley-Rideal mechanism.[194] However, there are fewer examples of atomically-dispersed catalysts in hydrotreating of other functional groups even with precious metals, for instance, hydrogenolysis of ethers[195] and conversion of CO_2 to alcohols.[196-197] Possible explanations are the lack of vacant sites or flexible coordination structures to allow cleavage of both H-H and C-O bonds at the same metal center.[198]

Understanding metal-support interactions is particularly important for base metals (e.g., Fe, Co, Ni, and Cu) used as hydrotreating catalysts. Although base metals have weaker abilities to activate H_2[199] and higher oxophilicity[200] compared to precious metals, their high natural abundance and low cost[201] makes base metals desirable alternatives to precious metals in catalytic energy conversion and chemical transformations.[202] However, examples of hydrotreating with base metals are mostly limited to hydrogenation.[203-205] The use of non-innocent supports can enable base metals to achieve the cleavage and formation of multiple bonds in a catalytic cycle.[197]

Here, we report the synthesis and study of atomically-dispersed Fe on a non-innocent carbon support and demonstrate the role of the metal-support interaction for H_2 splitting and

C-O bond hydrogenolysis. The presence of atomically-dispersed, five-coordinate Fe sites is predominant in the as-synthesized catalyst, based on extensive characterization by X-ray absorption spectroscopy, X-ray photoelectron spectroscopy, and electron microscopy, as well as theoretical calculations. We further take advantage of the well-defined structure of the Fe-catalysts to establish the impact of the metal-support interaction on catalyst activation involving changes in the coordination number and oxidation state under reducing conditions. The contribution of the non-innocent support in catalysis is quantified by a series of probe reactions, including poisoning experiments, high temperature H_2-chemisorption, and H_2/D_2 exchange studies.

5.2 Results and Discussions

Catalyst synthesis and characterization. The atomically-dispersed Fe catalysts were prepared by a co-condensation approach. We adapt our recently-reported synthesis of nitrogen assembly carbocatalysts (NACs)[206] by *in situ* incorporation of Fe into the non-innocent NAC support, in which assemblies of closely-spaced graphitic N were identified as active sites for the activation of H-H, C-O, and C-H bonds.[206] Specifically, $Fe(acac)_3$ was dissolved in a mixture of ethylenediamine and carbon tetrachloride, which react at 90 °C to form C-N bonds while eliminating HCl. Ethylenediamine also serves as a ligand to coordinate and stabilize atomically-dispersed Fe species during this process. The condensation was conducted in the presence of ordered mesoporous silica (SBA-15) to ensure a high surface area and to maximize Fe accessibility. After carbonization at 600, 700, 800, or 900 °C, the silica template was removed by etching to afford mesoporous N-doped carbon embedded with atomically-dispersed Fe sites. These new Fe catalysts are named Fe-NAC-X (where X refers to the calcination temperature). High Fe loadings can be achieved, from 0.8, 0.9, 1.1 and 1.2 wt % for Fe-NAC-600, Fe-NAC-700, Fe-NAC-800 and Fe-NAC-900, respectively.

The Fe-NACs have a nanorod morphology with uniform particle sizes (~ 300 nm × 1 μm), according to transmission electron microscopy (TEM) (Figure 5.1a) and scanning electron microscopy (SEM) (Figure S5.1). High surface areas (530 - 770 m^2 g^{-1}) were determined by N_2 physisorption (Figure S5.2 and Table S5.1). Ordered mesopores are indicated by the diffraction peak at ca. $2\ \theta = 1°$ in the small-angle powder X-ray diffraction (SXRD, Figure S5.3). The mesopore sizes are centered at ~ 3.0 nm, according to N_2 physisorption (Figure S5.2and Table S5.1) and TEM (Figure 5.1b). In wide-angle X-ray powder diffraction (WXRD, Figure S5.4), no reflections attributable to iron-containing species (such as oxides or carbides) are present. Two broad peaks at 25 and 43° are assigned to the C(002) and C(004) reflections, respectively, of the N-doped carbon support. Furthermore, high-angle annular dark-field scanning transmission electron microscopy (HAADF-STEM) clearly demonstrates the presence of Fe atoms atomically-dispersed over the carbon nanorods in each of the four catalysts, Figure 5.1c and Figure S5.5. The absence of iron clusters or nanoparticles was confirmed by HAADF-STEM, except for Fe-NAC-900 (Figure S5.6). STEM-EDS mapping of Fe-NAC-800 indicates a homogeneous distribution of Fe and N over the whole carbon matrix, Figure 5.1d.

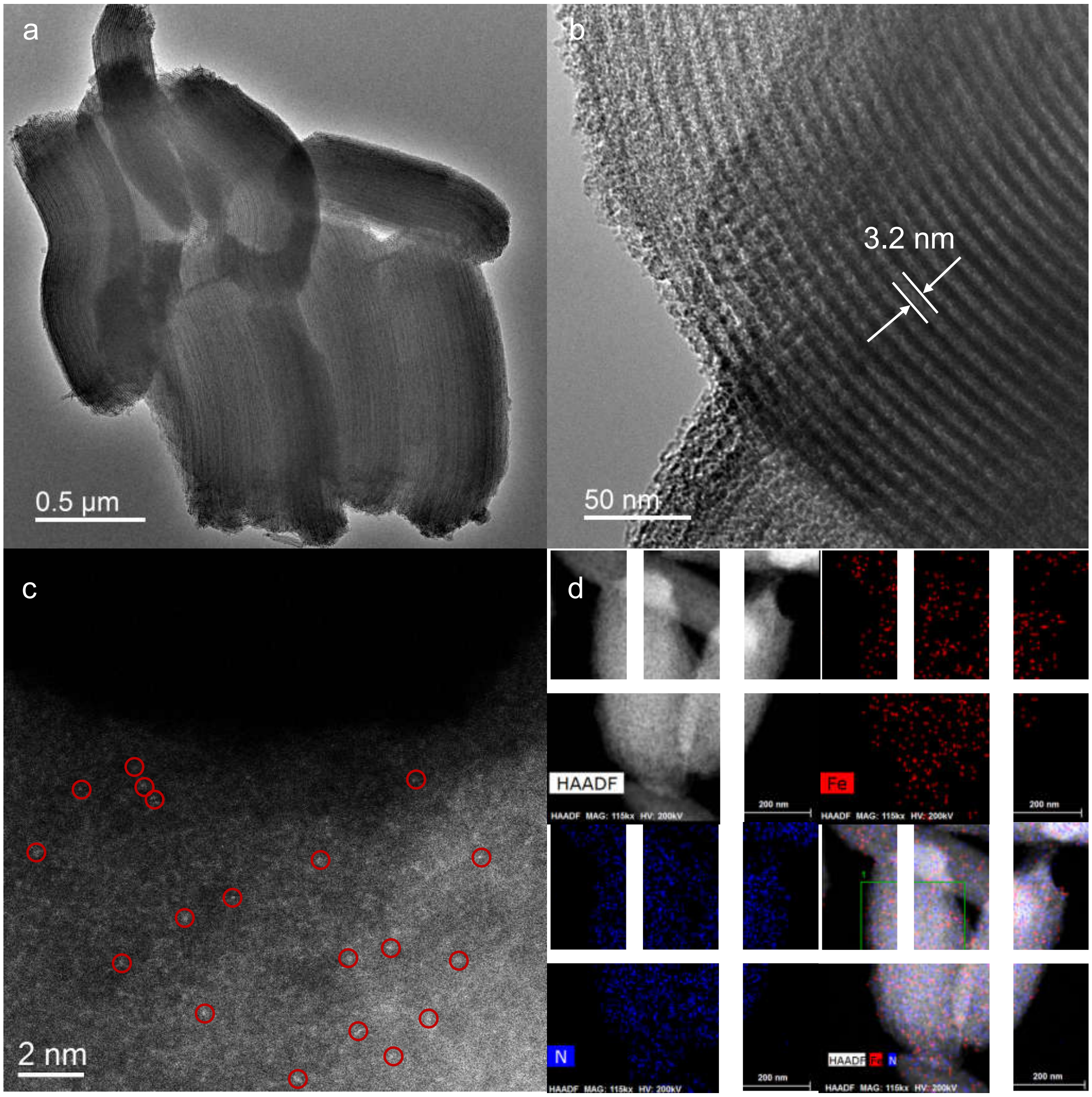

Figure 5.1 Electron microscopy images of Fe-NAC-800: (a, b) TEM, (c) aberration-corrected HAADF-STEM, (d) EDS mapping, showing Fe (red) and N (blue).

The electronic structure of Fe-NACs was further investigated. The X-Band EPR spectrum of Fe-NAC-800 (Figure 5.2a and Figure S5.7) reveals a signal at $g_{\mathrm{eff}} \sim 4.3$, characteristic of high-spin $\mathrm{Fe}^{\mathrm{III}}$ ($S = 5/2$) sites. In highly rhombic systems ($|E/D| \sim 1/3$),[207] such signals arise from a transition within the middle Kramers doublet $|\pm 3/2>$ and have isotropic character.

Simulation of this line afforded the zero-field splitting parameters $D = 0.79\ \mathrm{cm^{-1}}$ and $E = 0.26\ \mathrm{cm^{-1}}$ (E/D = 0.32). This ratio is commonly observed for iron-containing metalloenzymes.[207] Spin quantification[208] indicates that high-spin $\mathrm{Fe^{III}}$ sites comprise ~90% of the total iron present in Fe-NAC-800. X-ray photoelectron (XPS) survey spectra (Figure S5.9) only showed the existence of Fe signals, and other metals were below its detection limits. High resolution XPS in the Fe 2 $p_{3/2}$ region confirms that Fe is present as $\mathrm{Fe^{III}}$, Figure 5.2b and Figure S5.8.[209] Signals from N atoms bonded to the atomically-dispersed Fe sites are evident upon deconvolution of the N 1*s* region, Figure S5.10. Other N species present include pyridinic, pyrrolic, and graphitic N, as well as pyridine N-oxide (Table S5.2).[210] The total abundance of N in Fe-NAC-800 is 36.7 mol% (Table S5.2-5.3), and the content of N-Fe among all N is estimated to 8.1 mol%.

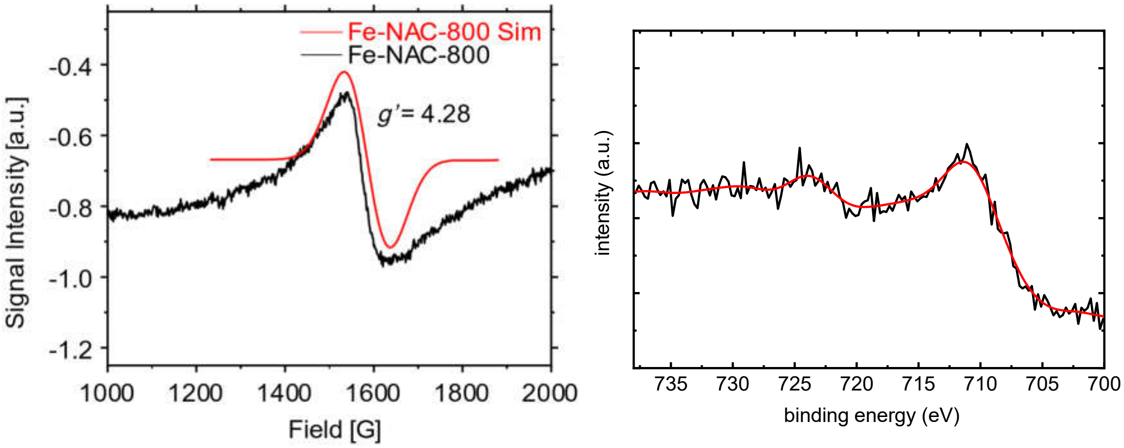

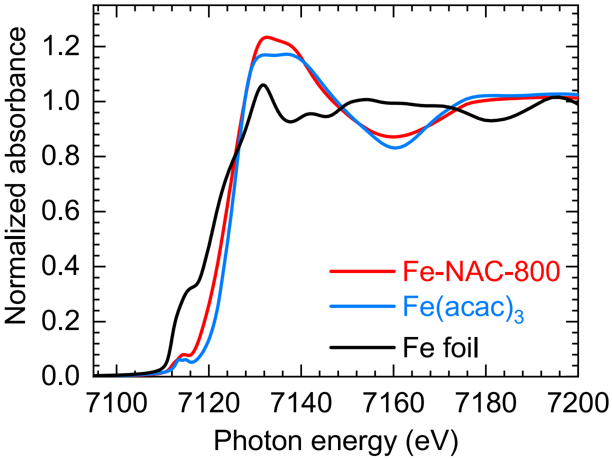

Figure 5.2 Spectroscopic analysis of Fe-NAC-800: (a) EPR spectrum and simulation, (b) high-resolution XPS spectrum, showing the Fe 2*p* region, (c) Fe K-edge XANES, showing comparisons to the spectra of Fe foil, and Fe(acac)$_3$.

Elucidation of Fe coordination. The Fe coordination environments in Fe-NACs were investigated by analysis of the extended X-ray absorption fine structure (EXAFS), and by density functional theory (DFT) calculations. The analysis of Fe-NAC-800 is representative. Variations in bonding structure for the other three Fe-NACs will be discussed below, in the context of their impact on catalysis.

The edge position of Fe-NAC-800, at 7,124.6 eV, is slightly lower than that of Fe(acac)$_3$ at 7,126.2 eV, Figure 5.2c. The FT-EXAFS magnitude shows a broad peak centered at 1.4 Å (not phase-corrected), with a shoulder at 1.8 Å (Figure 5.3a). These features arise from Fe-N and Fe-O single-scattering. There is also a broad, poorly resolved feature at 2 – 3 Å that may arise from non-bonded Fe-C and/or Fe-Fe single-scattering and/or multiple-scattering paths.[211] As a result, EXAFS curvefitting of this long-rang feature was not attempted. Instead, it was investigated qualitatively using the wavelet transform, which can help to distinguish between non-bonded scatterers based on atomic weight.[212] The WT-EXAFS of Fe-NAC-800 has two features (Figure 5.3b). The more intense feature has a maximum at 1.4 Å in non-phase-corrected *R*-space. It arises due to scattering by directly-coordinated light atoms (O, N), which give rise to a maximum in *k*-space at 4.9 Å^{-1}. The weaker feature has maxima in *R*-space and *k*-space at 2.3 Å and 4.4 Å^{-1}, respectively. The *k*-space value more closely resembles that for a simulated Fe-C path (4.8 Å^{-1}) than an Fe-Fe path (7.3 Å^{-1}), Figure S5.11-12. The location of the maximum in the WT-EXAFS of Fe-NAC-800 therefore suggests that the long-range feature results from Fe-C rather than Fe-Fe scattering. The EXAFS of Fe-NAC-800 is consistent with the HAADF-STEM observation of single-site Fe atoms.

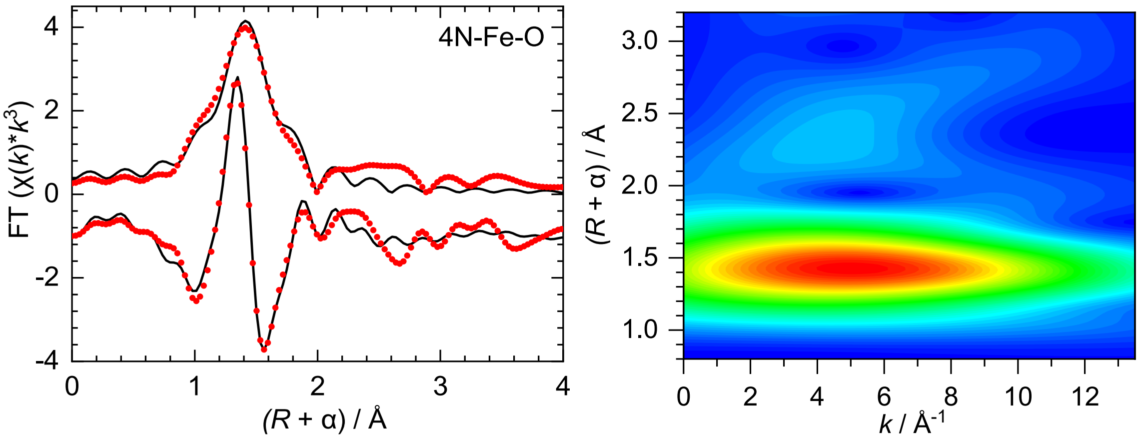

Figure 5.3 Fe K-edge EXAFS of Fe-NAC-800 in (a) non-phase-corrected *R*-space (FT-magnitude and its imaginary component, points), (b) wavelet transform. The curvefit (lines) represents refinement to the first-coordination sphere of a 4N-Fe-O model. Curvefit parameters are shown in Table S5.4.

The nature and number of Fe neighbors were investigated by EXAFS curvefitting. A model based on a reported tetra-coordinated Fe structure (4N-Fe)[213] was attempted first (Figure S5.13a). However, the fit with the 4N-Fe model does not match the experimental spectrum in *k*-space above 7 Å^{-1}, Figure S5.13b. Moreover, the k^3-weighed $\chi(k)$ function of Fe-NAC-800 shows a sudden decrease in amplitude at 8 Å^{-1}, implying a second path that is partially out-of-phase with the Fe-N path to provide destructive interference. Use of an 4N-Fe-O model gave the fit in Figure 5.3 and Table S5.4. The refined Fe-O distance, with coordination number *N* fixed at 1, is (1.87 ± 0.01) Å. This value is consistent with those reported for anionic O-donor ligands in 5-coordinate Fe(III) porphyrin derivatives (1.816 – 1.866 Å),[214-217] but shorter than distances for neutral O-donor ligands (2.090 – 2.314 Å).[218-221] The Fe-N distance, (2.03 ± 0.01) Å, falls within the range of distances reported for 5-coordinate Fe(III) phthalocyanine derivatives (2.012 – 2.066 Å).[214-217] Importantly, the Fe-O path is partially out of phase with the Fe-N path at $k > 8$ Å^{-1} (Figure S5.14), consistent with the destructive interference shown in Figure S5.13. A 6-coordinate model was also refined to the data. To balance the charge for Fe^{3+}, we consider that one O ligand is anionic while the other is neutral in this model. Since the neutral O ligand distance is similar to the Fe-N distance, they are indistinguishable in the EXAFS curvefit. Therefore the 6-coordinate model has *N*(Fe-N) = 5 to represent 4 Fe-N paths and 1 Fe-(neutral)O path, and *N*(Fe-O) = 1 for an anionic O ligand (5N-Fe-O). Although the fit reproduces the experimental data in *k*-space, the value of σ^2(Fe-N), (0.015 ± 0.003) Å^2, is suspiciously large, Figure S5.13 and Table S5.4. Therefore, the curvefit analysis suggests that a 6-coordinate Fe site is less likely represent to Fe-NAC-800.

To validate the structures proposed by EXAFS curvefitting, we performed spin-polarized DFT calculations of possible models. To create the active site, a carbon divacancy was first replaced by a Fe atom, followed by replacing the four carbon atoms coordinated with the Fe by four nitrogen atoms. The structure of $Fe^{II}N_4$ is shown in Figure 5.4a. The Fe-N bond length is about 1.88 and 1.89 Å. Next, an OH group or a water molecule was introduced to form a penta-coordinate Fe ($Fe^{III}N_4$-OH), with Fe-O bond lengths of 1.82 Å (Figure 5.4b) and 2.35 Å (Figure 5.4c), respectively. Note that coordination of OH causes the Fe-N bonds to be slightly elongated and the Fe to protrude locally with respect to the plane of the N atoms; the vertical height of Fe is about 0.26 Å above the average height (in the z-direction) of the four N atoms. Compared with ($Fe^{II}N_4$-OH_2), the $Fe^{III}N_4$-OH structure is the closest structure to the EXAFS curvefit for 5-coordinate Fe, with its Fe-O distance of 1.82 Å, although the calculated Fe-O and Fe-N bond lengths are slightly shorter than the curvefit values. We also considered the possible presence of a Fe=O moiety, by introducing a terminal oxygen on Fe. However, the Fe=O bond length in the optimized structure, 1.65 Å, is much too short compared to the curvefit value. We further compared with 6-coordinate species by introducing two water molecules, or two O atoms, resulting in $Fe^{II}N_4$-$(H_2O)_2$ and $Fe^{VI}N_4O_2$, respectively, in Figure 5.4e and Figure 5.4f. The Fe-O and Fe-N bond lengths are very similar to those in the corresponding 5-coordinate structures.

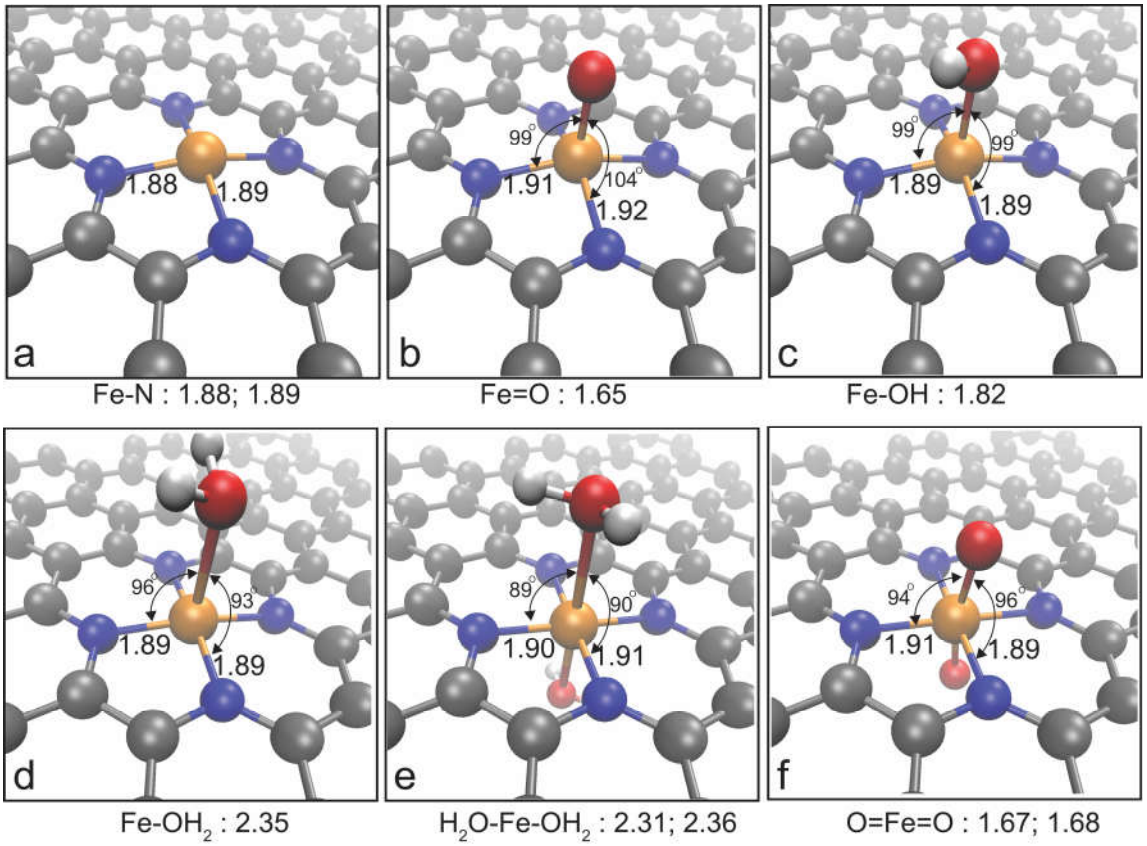

Figure 5.4 DFT-calculated structures for the Fe center, including (a) Fe-N_4, (b) coordinated with terminal O, (c) OH, and (d) water. Structures with (e) two coordinated waters (e) and (f) two terminal O, are included for comparison Fe, O, N, C, and H are colored orange, red, blue, gray, and white, respectively. The Fe-N bond length are indicated in the figure, as well as the N-Fe-O angles. Note that the Fe-O bond lengths in the water complexes can change slightly depending on the orientation of the water molecules.

Combining the information from the EXAFS and the DFT simulations, we conclude that the local environment of the Fe sites in Fe-NAC-800 is 5-coordinate, with four N donor ligands and one OH ligand. If we consider the carbon support to be an anionic ligand with a 2- change, by analogy to phthalocyanine, and the axial OH^- to be monoanionic ligand, then the local charge of the Fe^{III} complex is neutral. It should also be noted that $Fe^{III}N_4$-OH has been proposed as the active site for oxygen reduction in proton exchange membrane fuel cells.[222] The direct synthesis of such a structure could further advance the structural transformation of single-atom catalysts with base metals in electrocatalysis.

Catalytic cleavage of C-O bonds. We investigated the performance of Fe-NAC catalysts for the cleavage of the C-O bonds in 2-phenoxy-1-phenylethan-1-ol (PPE, ***1***), a model compound for β-O-4 linkage of lignin. In the presence of 20 bar H_2 and with 2-PrOH as solvent, the Fe-NACs, and Fe-NAC-800 in particular, show activity in hydrogenolysis at temperatures as low as 170 °C. The activities of the various Fe-NACs were compared at 230 °C. An initial rate of PPE conversion of 2.5 mM h^{-1} was observed for Fe-NAC-800. This value is higher than those for Fe-NAC-600, -700, and -900 of 0.2, 0.7, and 1.3 mM h^{-1}, respectively (Figure 5.5a). After 16 h, PPE is completely converted to phenol and ethylbenzene (Figure 5.5b). Three intermediates (Figure S5.15 and Table S5.5) were also identified for all Fe-NAC catalysts: styrene, 1-phenylethanol, and acetophenone. For each intermediate, the maximum yields in the presence of Fe-NAC-800 catalyst were 4 % (1 h), 6 % (4 h), and 6 % (8 h), respectively. A small amount of a minor product, phenethoxybenzene (PEB), was also detected (Figure S5.15 and Table S5.5) in all cases after hydrogenolysis of PPE C_α-OH.

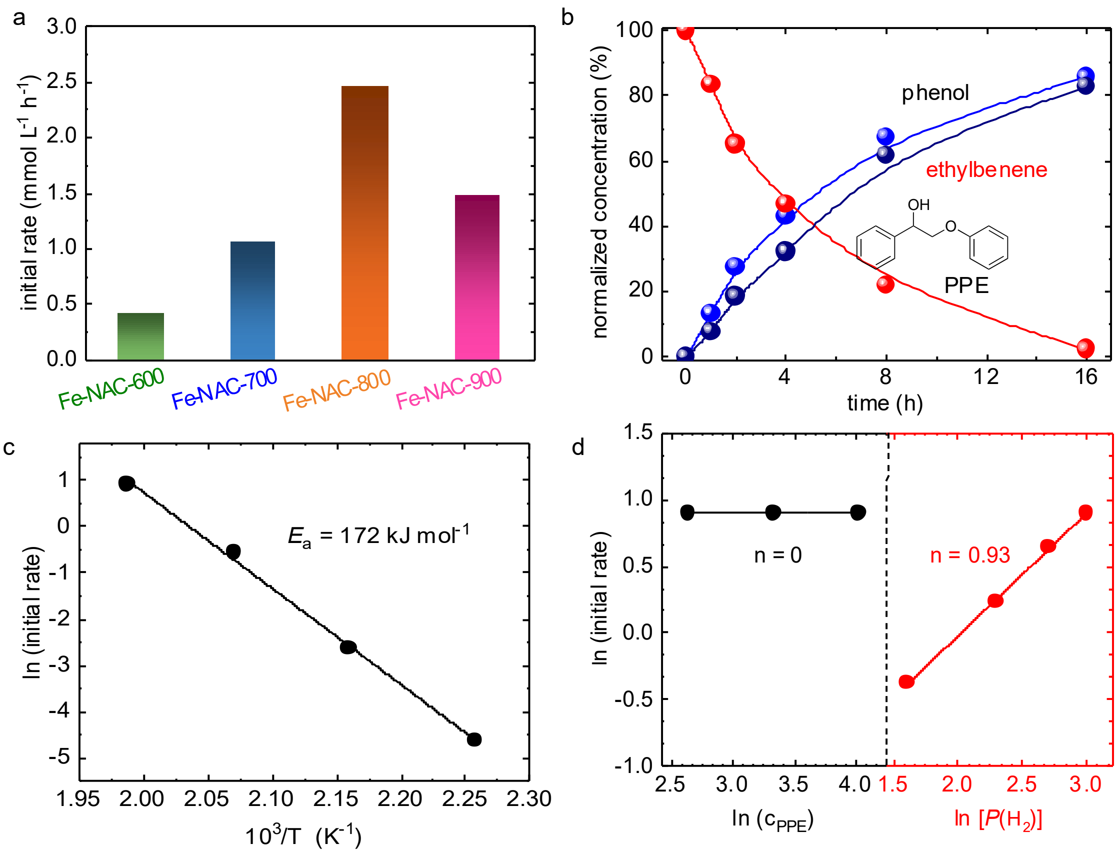

Figure 5.5 PPE conversion catalyzed by Fe-NAC materials at 230 °C: (a) initial rates, and (b) kinetic profiles for Fe-NAC-800, (c) reaction orders in H_2 and PPE for Fe-NAC-800, and (d) apparent activation energy for Fe-NAC-800. Reaction conditions: 14 mM PPE in 2-PrOH (1.50 mL), Fe-NAC (5.0 mg), 20 bar H_2.

Interestingly, no arene hydrogenation products were formed for any catalysts, showing the unique capability of Fe-NACs in the preservation of aromaticity. Hydrogenation of arenes, particularly for phenolics, is frequently encountered for conventional metal catalysts (such as Ni and Pd) under comparable reaction conditions.[223-224]

Kinetic studies carried out using the Fe-NAC-800 catalyst showing zeroth- and first-order behavior with respect to PPE and H_2, respectively, Figure 5.5d and Figure S5.16. The zeroth-order dependence on PPE suggests that the NAC support adsorbs the aromatic substrate strongly and thus increases the reaction rates. Therefore, the rate-determining step is suggested to be the dissociation of H_2 under the reaction conditions of this work. The activation energy was assessed by measuring initial rates in batch mode under 20 bar H_2 and Fe-NAC-800 at 170-230 °C. The apparent activation energy (E_a) for Fe-NAC-800 is 172 kJ mol^{-1}, Figure 5.5c.

To exclude contributions from leached Fe species in the liquid phase, control experiments were carried out using homogeneous catalysts, including $Fe(acac)_3$ and $FeCl_3$ with phenanthroline (2 equiv.), Table S5.5. As expected, no activity was observed. Therefore, we conclude that the observed catalytic activity originates from Fe-NAC and is not likely to be due to dissolved Fe species.

The robustness of the catalysts was explored by recycling the used material. The most active catalyst, Fe-NAC-800, was evaluated in 5 consecutive cycles at 230 °C (Figure 5.6). The reaction was stopped after 4 h in each cycle to ensure ca. 50 % (rather than full) conversion of PPE. The recycling experiments show that the Fe-NAC-800 is stable, with no apparent changes to either conversion (Figure 5.6a) or selectivity (Figure 5.6b). No apparent differences were observed between the recycled Fe-NAC-800 and the fresh catalyst in terms of textural parameters (such as N_2 physisorption and XRD powder pattern). (Table S5.1-5.2 and Table S5.6; Figure S5.2-5.4 and Figure S5.7-5.10). No leaching of Fe was observed (

entry	samples	XPS				CNH			ICP
		C(at%)	N(at%)	Fe(at%)	C:N (atomic)	C(wt%)	N(wt%)	C:N (atomic)	Fe (wt%)
1	Fe-NAC-600	80.44	12.43	0.18	6.5	66.72	17.59	4.4	0.84
2	Fe-NAC-700	79.03	12.94	0.20	6.1	64.63	15.56	4.9	0.94
3	Fe-NAC-800	83.38	11.08	0.21	7.5	70.40	12.58	6.5	1.1
4	Fe-NAC-	88.00	4.54	0.23	19.4	74.52	6.53	9.3	1.2

	900								
5	Fe-NAC-800 after 5 cycles	84.32	8.89	0.22	6.6	64.52	12.49	6.0	1.1

Table S5.3). Sintering to Fe-containing nanoparticles is also excluded, as indicated by TEM (Figure S5.1) and WXRD (Figure S5.4) studies. HAADF-STEM (Figure S5.17) characterization shows the atomically-dispersed Fe species are well-preserved. XAS analysis further confirms that the Fe sites remain atomically dispersed (*vide infra*). Therefore, we conclude that Fe-NAC-800 is stable at 230 °C.

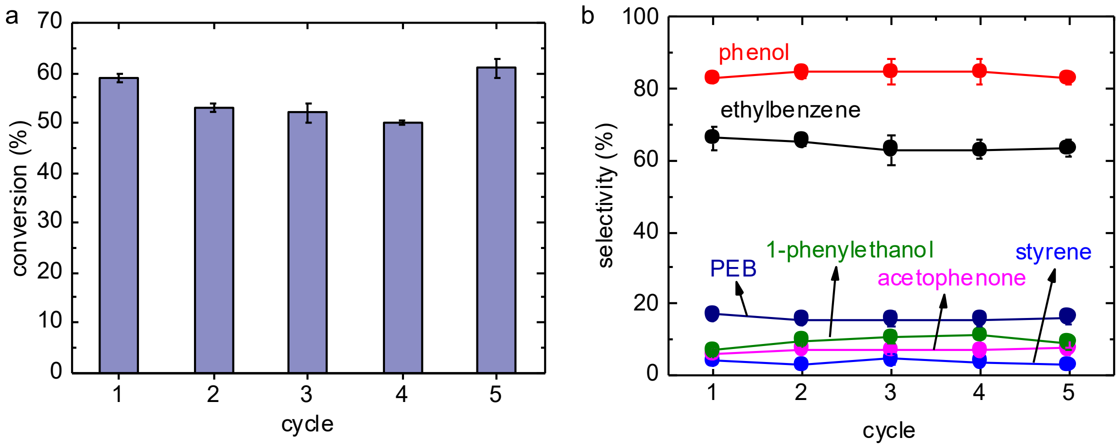

Figure 5.6 Recycling study of Fe-NAC-800: (a) Conversions of PPE, and (b) yields of major reaction species in each cycle. Reaction conditions: 14 mM PPE in 2-PrOH (1.50 mL), Fe-NAC-800 catalyst (5.0 mg), 20 bar H_2, 4 h, 230 °C.

Substrate Scope. The scope of hydrogenolysis catalyzed by Fe-NAC-800 was explored for the compounds in Figure 5.7. The catalyst reacts with benzyl phenyl ether and 1-phenylethanol, affording the corresponding hydrogenolysis products in high yields. In addition, 2-phenoxyacetophenone (PPK, **2**) is transformed completely to ethylbenzene and phenol, possibly after initial reduction to PPE. Direct conversion of PPK is another possibility since no PEB was observed. The PPE derivative **3**, with three methoxy groups, is transformed to the corresponding products at a faster rate than PPE itself. 2-Phenoxy-1-phenylpropane-1,3-diol (PPDE, **4**) bearing a C_γ-OH group is converted with full cleavage of the aromatic C_α-OH bond and the C_β-O ether linkage, forming propylbenzene, 1-phenyl-propene, and 3-phenylpropanol in addition to phenol. The methoxylated PPDE derivative (**5**) is converted even faster than PPDE, with complete cleavage of all three C-O linkages.

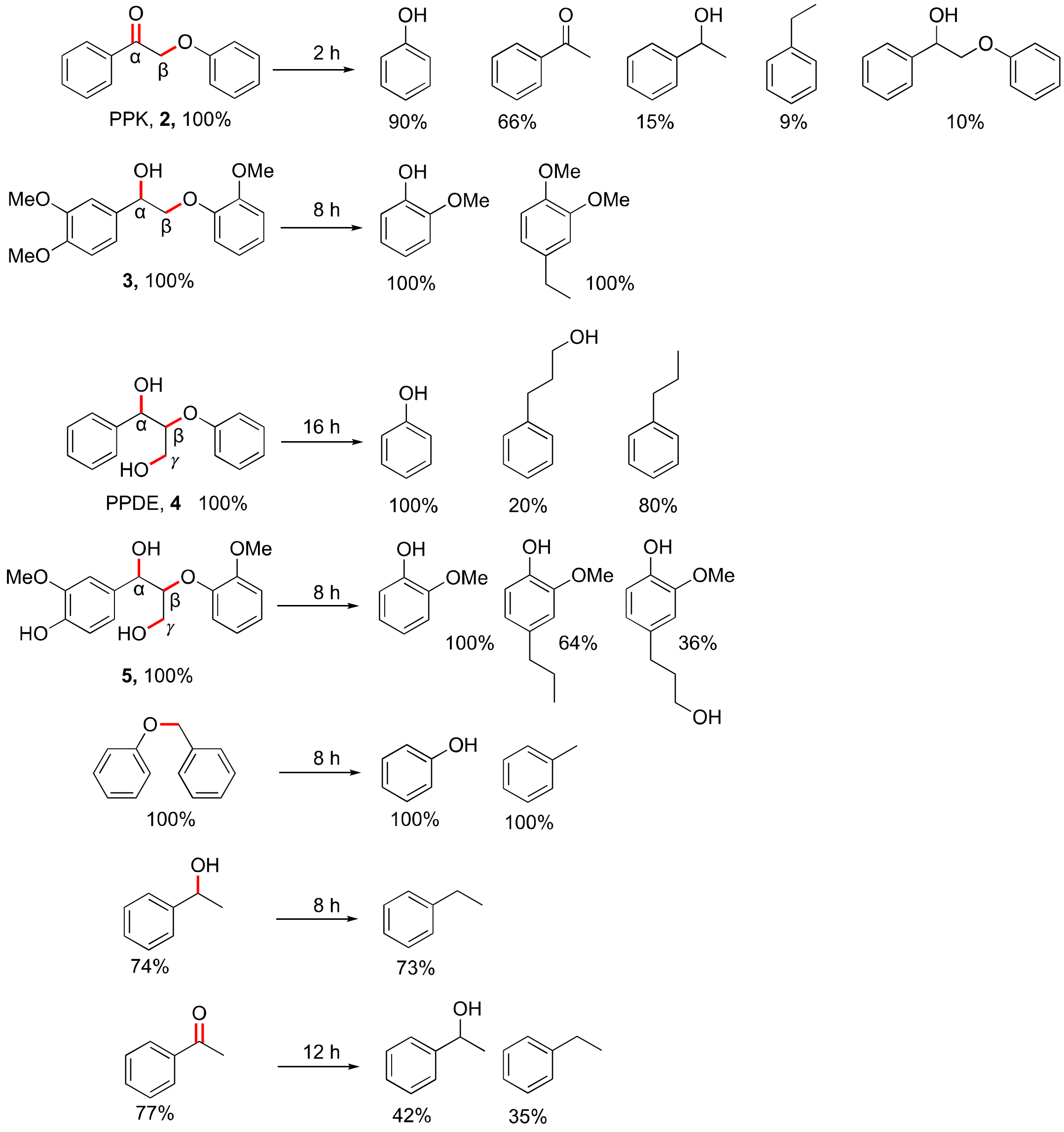

Figure 5.7 Hydrogenolysis of compounds catalyzed by Fe-NAC-800. Conversions and molar yields are shown below the reactants and corresponding products, respectively. Reaction conditions: 14 mM reactant in 2-PrOH (1.50 mL), Fe-NAC-800 (5.0 mg), 230 °C, 20 bar H_2.

Origin of hydrogenolysis activity. Hydrogenolysis reactions require the cleavage and formation of multiple bonds, and are rarely reported for single-site catalysts, particularly those with Fe active sites. Therefore, it is critical to understand the origin of the activity of Fe-NAC catalysts and differentiate the unique activity of the Fe$_{SA}$ sites from that of the non-innocent NAC support.

We first carried out poisoning experiments by adding different amounts of KSCN to Fe-NAC-800 prior to conducting PPE hydrogenolysis, Figure 5.8a. The strong binding of SCN$^-$ to Fe impedes its ability to split hydrogen.[209] Addition of 0.2 equiv. KSCN relative to the Fe content causes PPE conversion to decrease from 53% to 38%. The conversion decreases further to 32% and 20% in the presence of 0.5 and 1.0 equiv. KSCN, respectively. Introducing one extra equiv. KSCN resulted in little further impact on the activity. The poisoning study indicates that the atomically-dispersed Fe sites are fully accessible and catalytically active. The PPE conversion (20%) after full passivation of the Fe sites is almost identical to that of NAC-800 (19%) under the same reaction conditions, suggesting that the surface nitrogen assembly remains active and is resistant to KSCN poisoning.

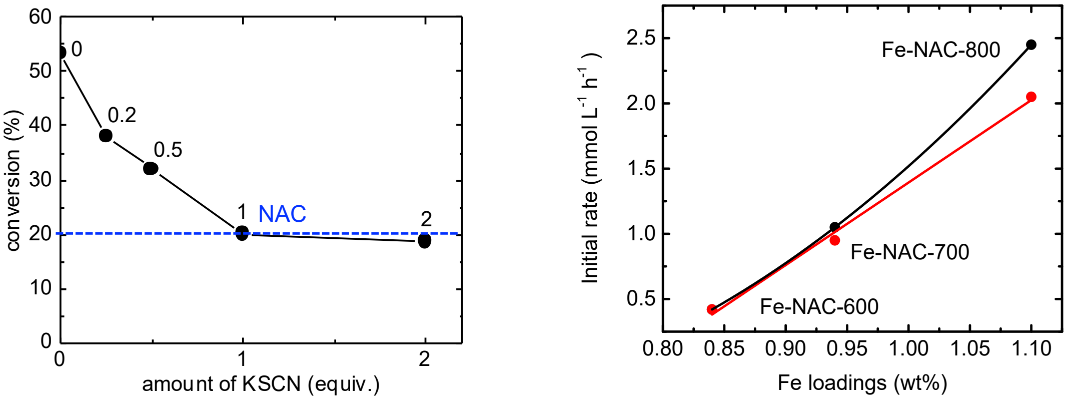

Figure 5.8 Control experiments to probe the reactivity of Fe sites in Fe-NAC-800: (a) KSCN poisoning of PPE conversion. Reaction conditions: 14 mM PPE in 2-PrOH (1.50 mL), Fe-NAC-800 catalyst (5.0 mg), 20 bar H$_2$, 4 h, 230 °C, and (b) estimation of reactivity for Fe sites (red) by subtraction of the support contribution from the observed initial rates (black). The

polynomial relation between initial rates and the graphitic N ratio (A_g), initial rate = $0.0644 * A_g^2 - 0.2083 * A_g + 0.182$), was adopted from a previous report.[206]

Further analysis of the kinetics shows that initial rates for PPE conversion correlate linearly with Fe loading (Figure 5.8b), except for Fe-NAC-900, which contains both Fe single-atoms and nanoparticles. As for Fe-NAC-900, the longer-range feature has a weaker intensity at maxima in *R*-space and *k*-space of 2.29 Å and 7.0 $Å^{-1}$, respectively, suggesting Fe-Fe paths. This is also consistent with the observation of Fe clusters by STEM (Figure S5.6). Thus only single-site Fe and not Fe-containing particles are catalytically active.

In particular, Fe-NAC-800 is almost 4 times more active than NAC-800, based on initial rates (2.45 *versus* 0.68 mM h^{-1}). Quantitative analysis of the XPS spectra (Figure S5.9) combined with deconvolution in the N 1*s* region (Table S5.6) shows that the molar content of graphitic N (4.1 mol%, Table S5.2) is more than one order of magnitude higher than that of Fe (0.22 mol% by XPS and ICP-AES) on the surface of Fe-NAC-800. The low Fe content and high reactivity of Fe-NAC-800, compared to Fe-NAC-900, imply that the Fe sites play a major role in the PPE conversion.

The contribution of Fe in catalysis can be estimated by subtracting the activity of the NAC support. The activity of the close-spaced graphitic N sites is correlated with the graphitic N content in a second-order polynomial relationship.[206] After subtraction of the NAC-contribution, the remaining activity attributable to the Fe sites in Fe-NAC-800, 700, and 600 are estimated as 2.05, 0.95, and 0.42 mM h^{-1}, respectively (Figure 5.8b). However, these dramatic differences in activities cannot be explained solely by the small variation in Fe loading (0.8 - 1.1 wt %). They must originate from the interaction between Fe and the NAC support.

To explore the origin of the support effect on Fe coordination, EXAFS curvefitting was conducted simultaneously for Fe-NAC-600, Fe-NAC-700, and Fe-NAC-800, while fixing the N values and constraining ΔE_0 to the same value for all spectra (Figure S5.19 and Table S5.7). All Fe sites are assumed to have a similar coordination environment (FeN_4-OH). The EXAFS analysis shows that the Fe-O path length remains essentially unchanged at 1.86 – 1.88 Å, whereas the Fe-N path lengths decrease from (2.08 ± 0.01) Å to (2.02 ± 0.01) Å as the calcination temperature increases from 600 to 800 °C. This change in bond length induced by the support is a unique feature of supported atomically dispersed catalysts, which cannot be difficult to be achieved with molecular catalysts. The degree of graphitization of the carbon support, influenced by the carbonization temperature, not only impacts the Fe site electronically but also directly influences the first coordination sphere of Fe site and beyond.

In addition, the Fe site may work in synergy with the nitrogen assembly sites by providing binding sites for chemisorbed intermediates. For instance, we showed previously that the nitrogen assembly selectively adsorbs styrene at the α-carbon, forming a C-N bond with the surface.[206] Notably, styrene is most likely the key intermediate leading to the formation of the product ethylbenzene (Figure S5.15). However, the absolute content of the various N species (e.g., pyridinic, graphitic, pyrrolic, or pyridine N-oxide) varies significantly after calcination at different temperatures (Table S5.2). Specifically, the graphitic N content peaks at 4.1 mol% for Fe-NAC-800, compared to 0.9, 2.8, and 2.3 mol% on Fe-NAC-600, Fe-NAC-700, and Fe-NAC-900, respectively (Table S5.2). The variation in graphitic N content can affect the distance with neighboring nitrogen assembly sites. Single-atom Fe sites are located far from the nitrogen assembly sites. Even if their surface concentration is high, they will likely be active for only H_2 splitting but not for C-O hydrogenolysis, resulting in the low observed activity of Fe-NAC-600.

Quantification of Hydrogen Activation. To better quantify the activity of Fe-NAC in hydrogen splitting, we carried out high-temperature pulsed H_2 chemisorption and reversible H_2/D_2 exchange. Both are critical physicochemical properties of Fe-NAC for future development of selective hydrogenolysis catalyst with earth abundant metals. The ability of Fe-NAC-800 to dissociate H_2 was directly measured using pulsed H_2 chemisorption (Figure 5.9 and Figure S5.20). At 60 °C, the H_2 uptake was around 2.0 μmol H_2 g_{cat}^{-1}. Upon raising the temperature to 240 °C, the H_2 uptake increased 11-fold, to 22 μmol H_2 g_{cat}^{-1}. The amount of chemisorbed H_2 decreased dramatically to 6 and 0 μmol H_2 g_{cat}^{-1} at 300 and 360 °C, respectively. Note that metal-free NAC-800 can also dissociate molecular hydrogen, with a capacity of 5.9 μmol H_2 g_{cat}^{-1} at 240 °C. This amount is about one-fourth of the capacity of Fe-NAC-800 (22 μmol H_2 g_{cat}^{-1}).

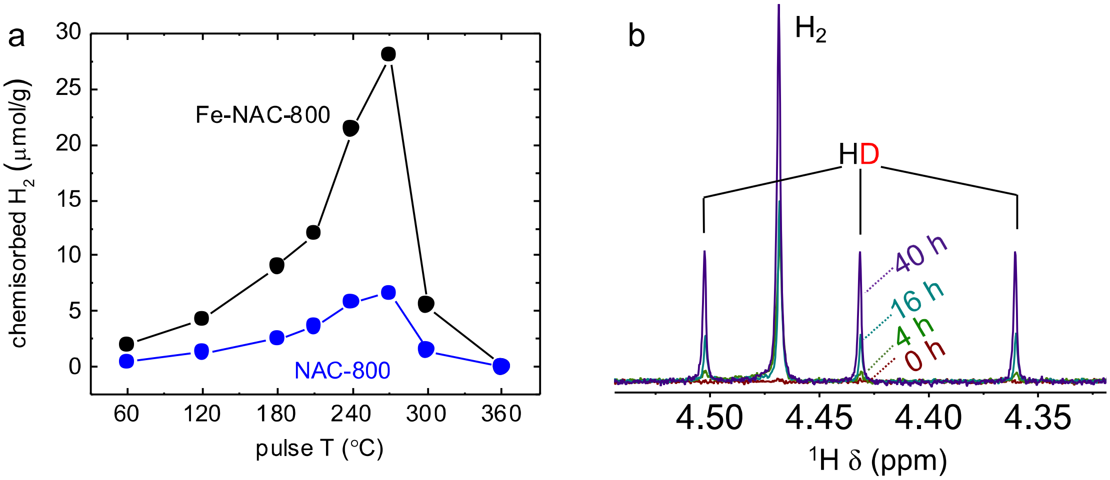

Figure 5.9 Determination of active sites for PPE conversion on Fe-NAC-800. (a) Pulsed H_2 chemisorption by Fe-NAC-800 (black) and NAC-800 (blue) at 60-360 °C. Some of the data for NAC-800 are published in ref [206]. (b) ^{1}H NMR spectra of benzene-d_6 with dissolved gas from the headspace after H_2/D_2 exchange catalyzed by Fe-NAC-800, showing the formation of gas HD. All spectra are normalized to the H_2 signal. Reaction conditions: NAC-800 (5.0 mg), n-decane (1.50 mL), 230 °C, total pressure 20 bar (D_2 and H_2, 1:1 v:v).

Reversible H_2 dissociation on Fe-NAC-800 was further demonstrated by performing H_2/D_2 exchange. The study was performed at 230 °C in n-decane rather than 2-PrOH (to avoid exchange with the solvent), starting with equimolar H_2 and D_2 (10 bar each). Formation of isotopically-mixed HD was detected by solution-state ^{1}H NMR, after the dissolution of the headspace gas in benzene-d_6 (Figure 5.9b).

Mechanistic investigation. To explore the impact of the metal-support interaction on the reaction mechanism, we first performed DFT calculations of the activation barrier for H_2 splitting on Fe centers in different coordination environments (Figure 5.10), considering the

H_2 activation is rate-limiting. With no O-donor axial ligand, dissociation of H_2 at the FeN_4 center needs to overcome an intrinsic activation barrier of 2.0 eV, forming a hydride bonded to Fe and a proton bonded to C adjacent to N. This reaction is endothermic by 1.0 eV. There could be an intermediate structure in which H_2 first adsorbs on the Fe center, at an energy cost of 0.1 eV (Figure S5.22). This hydrogen activation mechanism for Fe-NAC resembles those of [Fe]-hydrogenase[225] and molecular amine(imine)diphosphinoiron,[226] whose ligands are hypothesized to participate in H_2 activation.

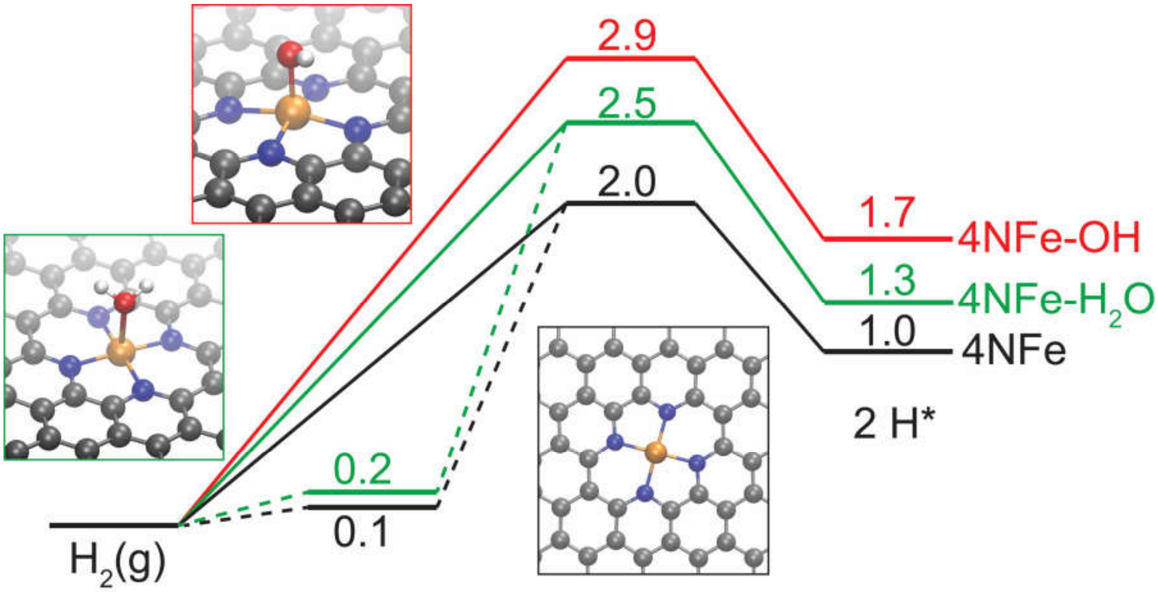

Figure 5.10 DFT-calculated reaction profile. The energy reference is H_2 in the gas phase. Three catalysts are compared, including pristine 4N-Fe (black), with a coordinated OH ligand (red), and with a coordinate water (green). The insets show the atomic structures of the three Fe sites. The energy unit is eV, and the bond length unit is Å.

In the presence of an axial OH ligand on the opposite side of the graphene sheet, the activation barrier for H_2 splitting increases to 2.5 eV, with an energy cost of 1.3 eV. With an axial water on the opposite site, H_2 activation needs to overcome an even higher barrier of 2.9 eV. This analysis of activation barriers suggests that the bare $Fe^{II}N_4$ site should be the most active site among the three structures. Note that an activation barrier of 2.0 eV is similar to the previously reported value for metal-free NAC,[206] and is slightly higher than the experimentally measured value ($E_{a,app}$ = 172 kJ mol^{-1}) in this study (Figure 5.5c).

To obtain more information about structural changes that the active sites undergo during reaction, Fe-NAC-800 was recovered after recycling 5 times and subjected to further XAS analysis. The edge position decreased by 1.4 eV (Figure S5.22) suggests that some of the Fe(III) sites had been reduced to Fe(II) because the oxidation states change from Fe(III) to Fe(II) usually causes ca. -2 eV shift. In the FT-EXAFS, the amplitude at 1.4 Å decreased (Figure S5.23), consistent with a change in the average Fe coordination environment. However, the broad peak at 2 – 3 Å changes little, implying that Fe sites are still located in the N-doped graphene plane (Figure S5.24). The EXAFS of fresh and recycled Fe-NAC-800 were curvefitted simultaneously to estimate the change in N(Fe-O). N(Fe-O) and ΔE_0 were refined, while N, R and σ^2 for the Fe-N path were constrained to the same values in the spectra of fresh and recycled Fe-NAC-800, Figure S5.24 and Table S5.8. The Fe-O and Fe-N distances, at (1.88 ± 0.01) Å and (2.03 ± 0.01) Å, respectively, are consistent with the curvefit results with fixed coordination numbers presented above for the fresh catalyst. In recycled Fe-NAC-800, the value of N(Fe-O) decreases slightly, from (1.0 ± 0.3) to (0.6 ± 0.3). This analysis supports the hypothesis that a portion of the Fe sites lacks an axial O-donor ligand. These are presumably the 4-coordinate Fe(II) sites.

Based on the structural comparison and the kinetic calculations, it is likely that bare $Fe^{II}N_4$ sites play a major role in activating H_2 molecules. It should be noted that the high barrier for hydrogen activation by $Fe^{III}N_4$-OH prohibits the reaction. Considering the non-innocent NAC support has a predicted barrier of 1.8-2.2 eV for H_2 activation,[206] the initial reduction of FeN_4-OH is likely triggered by hydrogen chemisorbed on the NAC support close to the Fe center. We calculated the activation barrier for the support-mediated reduction of a $Fe^{III}N_4$-OH to $Fe^{II}N_4$-H_2O to be 1.3 eV (Figure S5.25), which is smaller than the H_2 activation barriers. Desorption of water, with an energy cost of only 0.3 eV, leads to the formation of the bare $Fe^{II}N_4$ site. This moderate barrier thus suggests a feasible mechanism for the change in Fe coordination number under the reaction conditions.

The experimental results combined with DFT modeling suggest structural evolution in different stages of the reaction, as described in Scheme 5.1 Proposed structural evolution of Fe sites under reaction conditions.. Under the reaction conditions, H_2 is initially chemisorbed by sites on the NAC support, leading to the reduction of 5-coordinate $Fe^{III}N_4$-OH to 4-coordinate $Fe^{II}N_4$. The latter is the active site responsible for further H_2 splitting and C-O hydrogenolysis. The reduction of Fe is most likely rapid relative to the reaction timescale (hours); otherwise, the activity observed in the 5 catalyst recycles (4 h per cycle) would be different. After the reaction, $Fe^{II}N_4$ is partially oxidized upon re-exposure to air, resulting in a mixture of 5-coordinate Fe(III) and 4-coordinate Fe(II) sites in the recycled catalyst.

Scheme 5.1 Proposed structural evolution of Fe sites under reaction conditions.

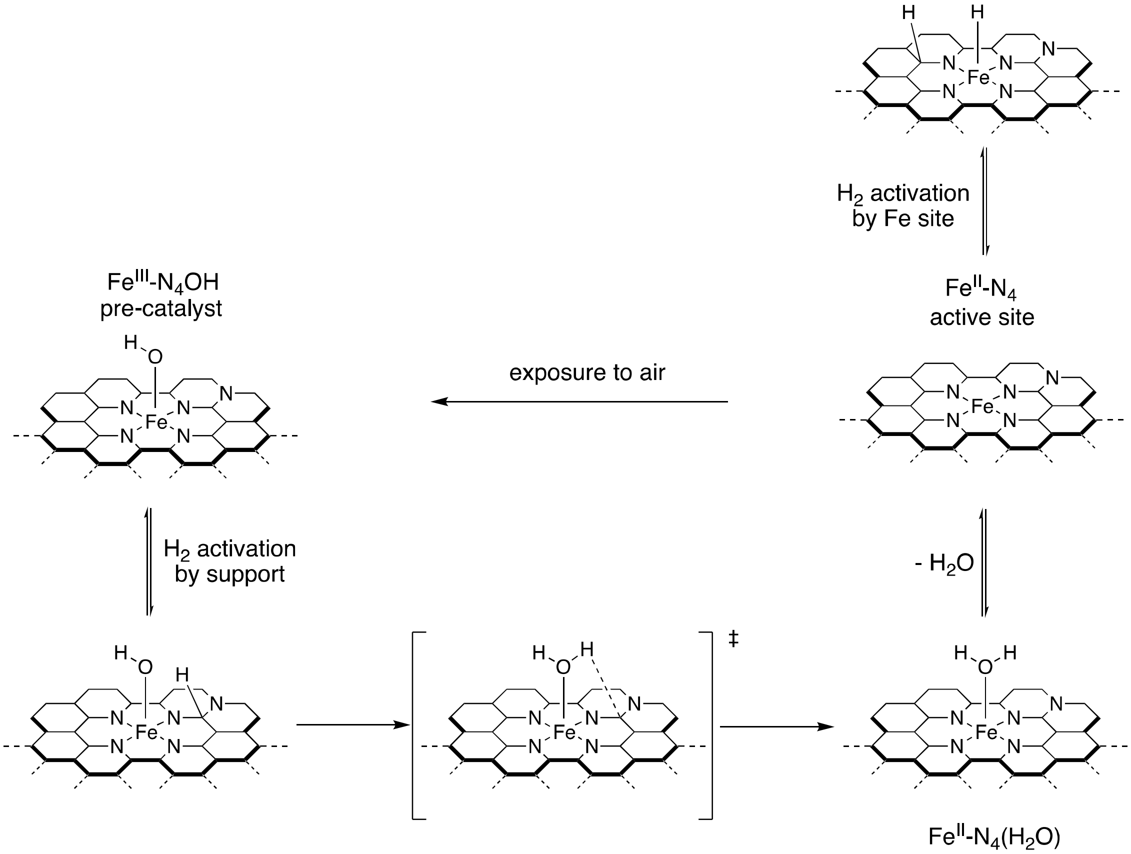

The activation of Fe sites generates water as a product, and the presence of water might retard the reaction by reversibly binding to Fe. We explored this hypothesis by examining the solvent effect (Table S5.9). Slightly higher PPE conversion was observed in n- decane (69%) compared to the reaction in 2-PrOH (53%), suggesting that 2-PrOH can bind weakly to the Fe center to inhibit the reaction. However, introducing 20 vol% water in 2-PrOH caused the PPE conversion to decrease significantly, to 4%. The result indicates that neither $Fe^{III}N_4$-H_2O nor $Fe^{III}N_4$-OH are as active as Fe(III)N_4 for the hydrogenolysis reaction. The inhibiting effect of water on the Fe-NAC-800 catalyst can also explain the deviation from apparent zeroth-order kinetics in PPE in the time-resolved study (Figure 5.5b and Figure 5.5d); more water is formed at higher conversions, the reaction slows down. This inhibition is reversible; otherwise, the catalyst would not be recyclable.

5.3 Conclusions

In this work, we report the synthesis of atomically dispersed Fe catalysts anchored on nitrogen assembly carbons (Fe-NACs) to achieve selective C-O bond hydrogenolysis, assisted by the metal-support interaction. Systematic studies using spectroscopic, microscopic, and theoretical methods reveal that the Fe(III) site in the as-synthesized catalyst is predominantly 5-coordinate, with four nitrogen donors and one hydroxyl ligand. Catalytic activities of Fe-NACs were explored in the hydrogenolysis of alkyl C-O linkages in various aromatic oxygenates, without arene hydrogenation. Stability against deactivation was observed even after five cycles for hydrogenolysis at 230 °C under 20 bar H_2. The reduction to 4-coordinate Fe(II) site generates the active sites for H_2 splitting under the reducing reaction conditions. DFT calculations reveal that the resulting site has a lower barrier for H_2 splitting; the transformation of the Fe sites is likely initiated by the non-innocent NAC support. Mechanistic studies distinguish between activity due to Fe sites and the support. The presence of Fe permits facile and reversible hydrogen chemisorption, which is the rate-determining step in the C-O hydrogenolysis reaction.

Overall, the observed activity originates from the cooperation of the metal center and the support in the relay of H_2 splitting and C-O bond cleavage. The critical roles of the support include, but are not limited to, stabilizing suitable local coordination structures, promoting the structural evolution of the metal site, and providing binding sites necessary to anchor reaction intermediates. Understanding the metal-support interaction allows the on-demand synthesis and switch of structures of atomically dispersed catalysts, in particular with base metals. The resulting catalysts can be broadly applied in many complex chemical transformations, such as hydrotreatment, electrochemical oxygen reduction reaction, and CO_2 reduction.

5.4 Supporting Information

Chemicals. Iron(III) acetylacetonate (≥99.5%, trace metal), ethylenediamine (≥99.5%), carbon tetrachloride (≥99.9%), P123 (Mn~5,800), TEOS (98%), 1-phenylethanol (99.5%), 2-phenylethanol (≥99%), ethylbenzene (≥99%), styrene (≥99%), benzyl phenyl ether (≥98%) decane (≥99%), guaiacol (≥98%), dodecane (≥99%) were purchased from Sigma-Aldrich. DMSO-d_6 (99.5%, 99.9 atom% D), benzene-d_6 (99.5%, 99.5 atom% D), $CDCl_3$-d (99.5%, 99.8 atom% D), methanol-d_4 (99.5%, 99 atom% D), 2-PrOH-d_8 (99.5%, 99.8 atom% D) were purchased from Cambridge Isotope Laboratories. HCl (TraceMetal grade), hydrofluoric acid (TraceMetal grade), acetophenone (99%), 2-PrOH (99.9%) were purchased from Fisher Chemical. Ethylenediamine (≥99%) was purchased from Acros Organics. Guaiacylglycerol-β-guaiacyl ether (≥97%) was purchased from TCI Chemical. PPE (99.89%) was purchased from BBLDpharm. H_2 (99.995%) and D_2 (99.99%) were purchased from MATHESON trigas. Pd/C (1 wt%) was purchased from Strem Chemicals. All chemicals were used as received.

Catalyst synthesis. Fe-NAC materials were synthesized based on a modified literature method [227]. $Fe(acac)_3$ (250 mg) was added into the solution of ethylenediamine (1.80 g) and carbon tetrachloride (4.00 g), followed by the addition of SBA-15 (0.80 g). (*Caution: this is an exothermic reaction with vigorous gas evolution*.) The condensation of the mixture was carried out at 90 °C for 6 h and dried for 12 h at 120 °C, affording a solid residue. The residue was carbonized (3 °C min^{-1}, 2 h) at a given temperature under following Ar flow (MATHESON trigas, 99.999%). The as-prepared sample was treated with a solution of 5 wt% HF in order to remove Si. The suspension was filtrated, washed with water for ≥10 times and dried under vacuum at 100 °C, named as NAC-*x* (*x*: calcination temperature). The NAC catalysts were stored in a desiccator under air before usage.

Materials characterization. Powder X-ray diffraction (XRD) was performed on a Bruker D8A25 diffractometer with Cu $K\alpha$ radiation (λ = 1.54184 Å) operating at 30 kV and 25 mA. N_2 physisorption was carried out at -196 °C using an auto-adsorption analyzer (Micromeritics, 3Flex). Before adsorption measurements, the samples were degassed at 250 °C overnight. The total pore volume was determined from the aggregation of N_2 vapor adsorbed at a relative pressure of 0.99. The specific surface area was calculated using the B.E.T. method, and the pore size were estimated using BJH method from the desorption branch of the isotherms. Transmission electron microscopy (TEM) images were acquired using a Tecnai G2 F20 electron microscope operated at 200 kV. Aberration Corrected Scanning Transmission Electron Microscope (STEM) images were recorded using the FEI Titan Themis with an aberration-ccorrected, mono-chromated, transmission electron microscope operated at 200 kV. Elementary analysis of all samples was carried out using a Perkin Elmer 2100 Series II CHN/S Analyzer. Scanning electron microscopy (SEM) images were acquired on a FEI Quanta 250 FE-SEM.

X-ray photoelectron spectra (XPS) were recorded on a PerkinElmer PHI ESCA system by Physical Electronics (PHI) with a detection limit of 1 at%. Monochromatic x-rays were generated by an Al Kα source (1486.6 eV). The binding energy values were calibrated using the C1s peak at 284.6 eV. For quantitative analysis with CASA software, the components were deconvoluted to Gaussian-Lorentzian lineshapes. The peak area was divided by a sensitivity factor obtained from the element-specific Scofield factor and the transmission function of the spectrometer. The uncertainties for deconvolution parameters were estimated using a Monte Carlo approach.

Pulsed H_2 chemisorption experiments were performed utilizing a micromeritics AutoChem II instrument under the flow of He at 20 mL min^{-1}. Fe-NAC-800 catalyst (100 mg) was mounted between quartz wool inside a quartz reactor assembled in a furnace. The temperature was measured at the sample position with a K-type thermocouple sealed in a quartz capillary. All samples were thermally pre-treated at 400 °C for 4 h to remove any possible surface contamination such as carbon species or water present in air. In the pulsed chemisorption experiment, H_2 consumption was monitored through a thermal conductivity detector that measures the signal difference of the desorbed gas versus a reference flow.

X-ray absorption spectra at the Fe K-edge (7,112 eV) were collected on beamline 4–3 at the Stanford Synchrotron Radiation Lightsource, which operates at 3.0 GeV with a current of 500 mA. The samples were mounted in motorized 4-slots sample holders and placed in a He-purging box at room temperature. $Fe(acac)_3$ was diluted to ca. 1 wt% Fe with BN Data were collected in fluorescence mode using a PIPS detector. For energy calibration, an iron foil was placed after the second ion chamber following the incident beam direction. The energy of the first maximum in the first derivative of the XANES was defined as 7,112 eV. The data were processed using Demeter software package, by subtraction of a linear pre-edge and normalization by the edge jump.[111] The $\chi(k)$ data were isolated by subtracting a smooth, third-order polynomial approximating the absorption background of an isolated atom. The data were k^3-weighted before Fourier-transform. The amplitude reduction factor (S_0^2), coordination numbers (N_i), distances to the scattering atoms (R_i), and mean-squared displacements (σ_i^2) were obtained by nonlinear fitting with least-squares refinement of the EXAFS equation to the Fourier-transformed data in *R*-space, using the Artemis program. To simulate the EXAFS spectra of individual paths, the crystallographic information files were imported into Artemis. EXAFS spectra were generated using FEFF6.

Continuous Cauchy wavelet transform (CCWT) EXAFS used MATLAB computation following a previously described procedure.[228] The spectra were generated using n = 200 (default) for Continuous Cauchy wavelet. For CCWT simulations, backscattering amplitude functions and phase shifts were calculated using FEFF6.

Catalytic hydrogenolysis and hydrogenation. The solution (1.50 mL) of the substrate of interest, containing 4.4 mmol L^{-1} dodecane as the internal standard, and Fe-NAC catalyst (5.0 mg) were added into a self-built Swagelok reactor (total volume: 5 mL). After purging the reactor with H_2 7 times, the reactor was pressurized with 20 bar H_2, and heated to desired temperature under stirring (300 rpm). After the reaction, the reactor was quickly quenched in room-temperature water. In addition to authentic samples, intermediates and products were also verified using GC-MS (Agilent 6890N/5975) with a 30 m capillary column (Agilent, HP-1) and He as the carrier gas. The concentrations of reaction species were quantified using GC-FID (Agilent 6890, FID detector) with a 30 m capillary column (Agilent, HP-1). External calibration was carried out with solutions prepared with authentic samples of related species (Figure S5.15) and also dodecane. Conversions and yields were further calculated based on the calibration curves established on the dependency of the chromatographic areas as a function of concentration.

The carbon balances were calculated for molecules containing C6 and C8 moieties. For example, in a typical PPE conversion catalyzed by Fe-NACs, the C6 carbon balance counts for phenol and PEB together with unconverted PPE; the C8 carbon balance includes styrene, acetophenone, 1-phenylethanol, ethylbenzene, and PEB together with unconverted PPE. The initial rates are determined, using data below 20% conversion. In the recycling study, the catalyst can be recovered by centrifugation and then washed three times with 40 mL 2-PrOH each, followed by drying at 100 °C overnight for the next cycle. The uncertainties were estimated based on results from multiple runs.

Exchange of H_2/D_2. Decane (1.50 mL) and Fe-NAC-800 catalyst (5.0 mg) were added into a self-built Swagelok reactor (total volume: 5 mL). After purging 7 times with H_2, the reactor was charged with a total of 20 bar H_2 and D_2 (1:1). The actual amount of H_2 and D_2 in the reactor were measured to be at 2.8 mg and 5.7 mg, respectively. The reactor was then heated to 230 °C under stirring (300 rpm). After different time intervals, the reactor was quickly quenched in room-temperature water. The gas (~2 bar) in the headspace of the reactor was bubbled into 0.5 mL benzene-d_6 inside a 5 mm solution NMR tube. ^{1}H NMR spectrum of the obtained benzene-d_6 with dissolved gas was acquired immediately using Bruker Avance III 600 spectrometer.

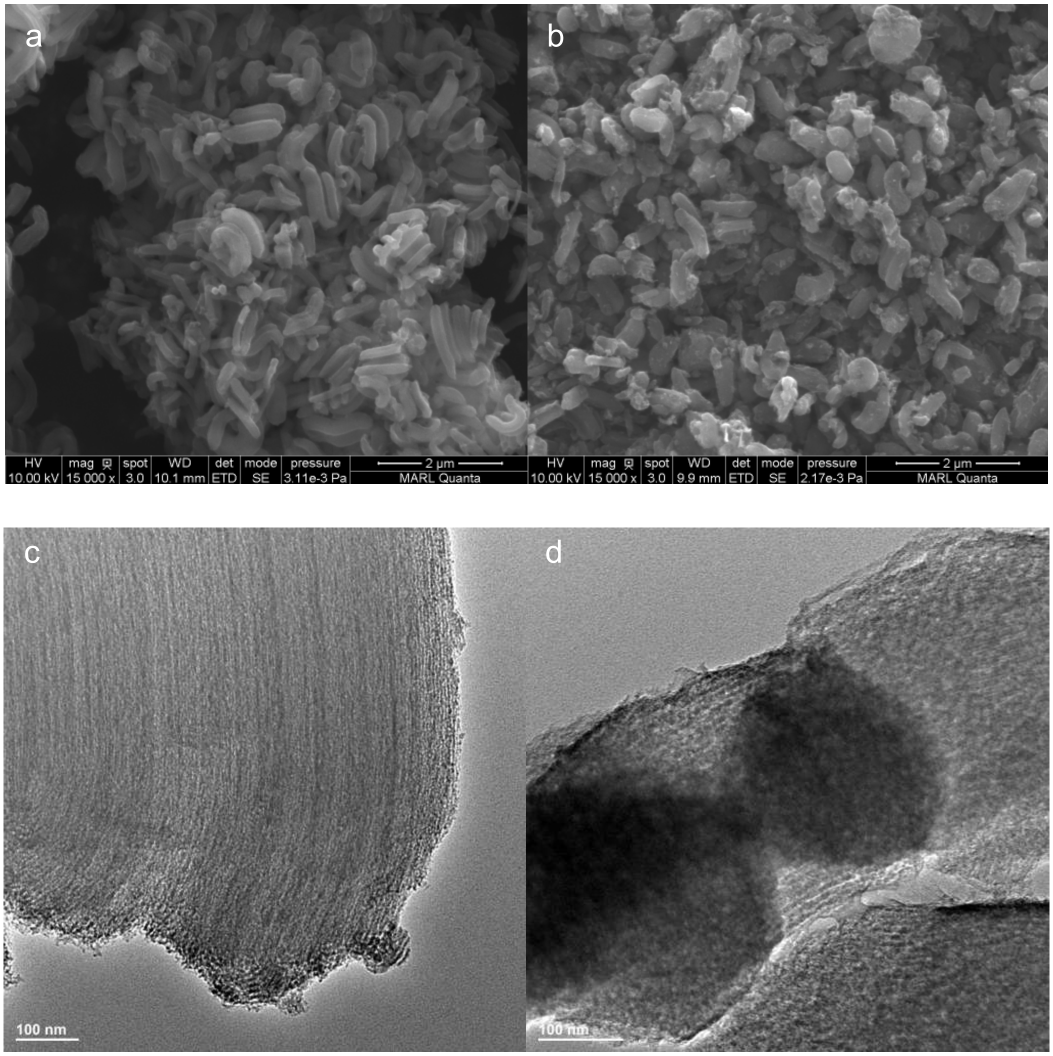

Figure S5.1 Microscopic characterizations. SEM images of (a) fresh and (b) Fe-NAC-800 after 5 reaction recycles. TEM images of (c) fresh and (d) Fe-NAC-800 after 5 reaction recycles.

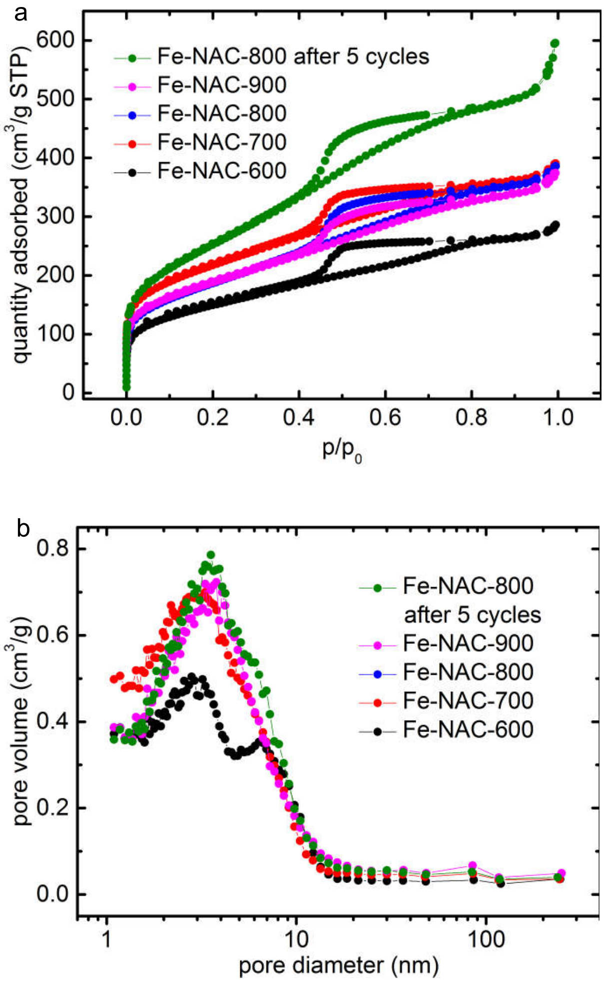

Figure S5.2 BET analysis of Fe-NACs. (a) N_2 sorption isotherms. (b) Pore size distributions.

Table S5.1 BET analysis of Fe-NACs.

entry	samples	S_{BET} (m^2/g)	V_{pore} (cm^3/g)	D_p (nm)
1	Fe-NAC-600	529	0.43	2.9
2	Fe-NAC-700	768	0.57	2.8
3	Fe-NAC-800	656	0.59	3.2
4	Fe-NAC-900	663	0.56	3.1
5	Fe-NAC-800 after 5 cycles	670	0.65	3.5

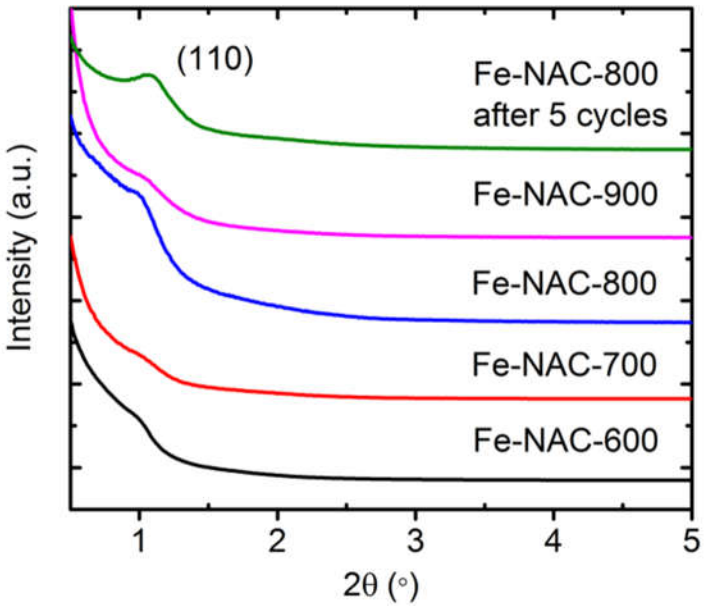

Figure S5.3 SXRD of Fe-NACs and Fe-NAC-800 after 5 reaction cycles

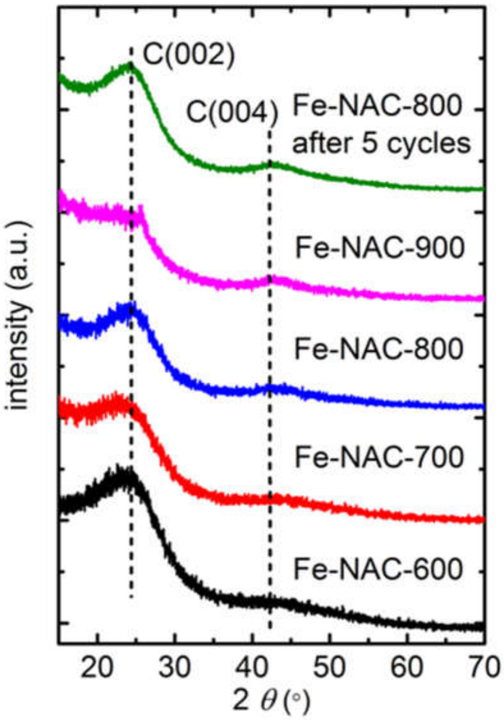

Figure S5.4 Powder XRD patterns of Fe-NACs catalysts, as well as the Fe-NAC-800 after 5 reaction cycles, which show the C (002) and C (004) planes in graphitized carbons.

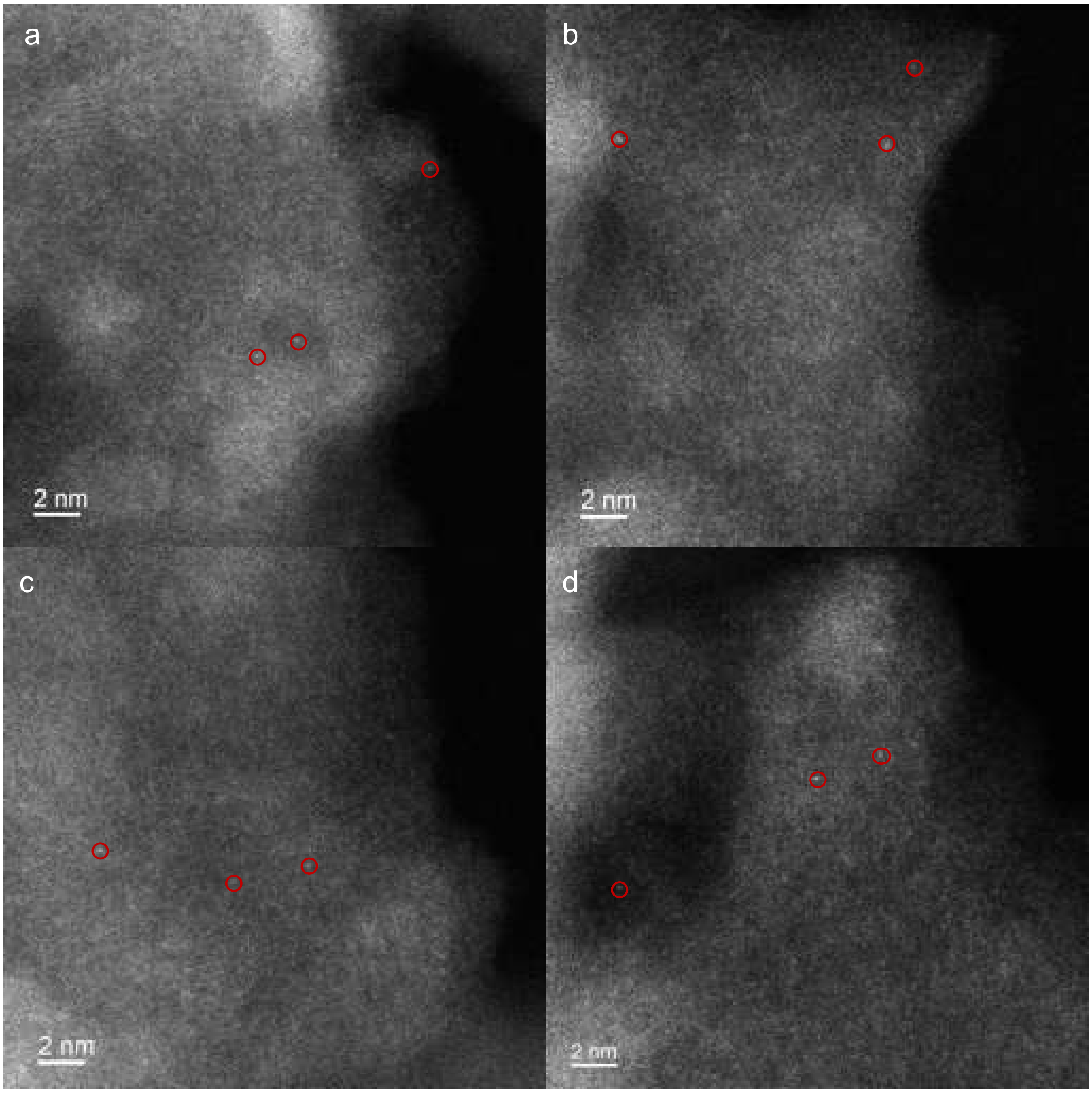

Figure S5.5 Aberration-corrected HAADF-STEM images (a) Fe-NAC-600, (b) Fe-NAC-700, (c) Fe-NAC-800, and (d) Fe-NAC-900. Aberration-corrected HAADF-STEM images showed the presence of single-atom Fe.

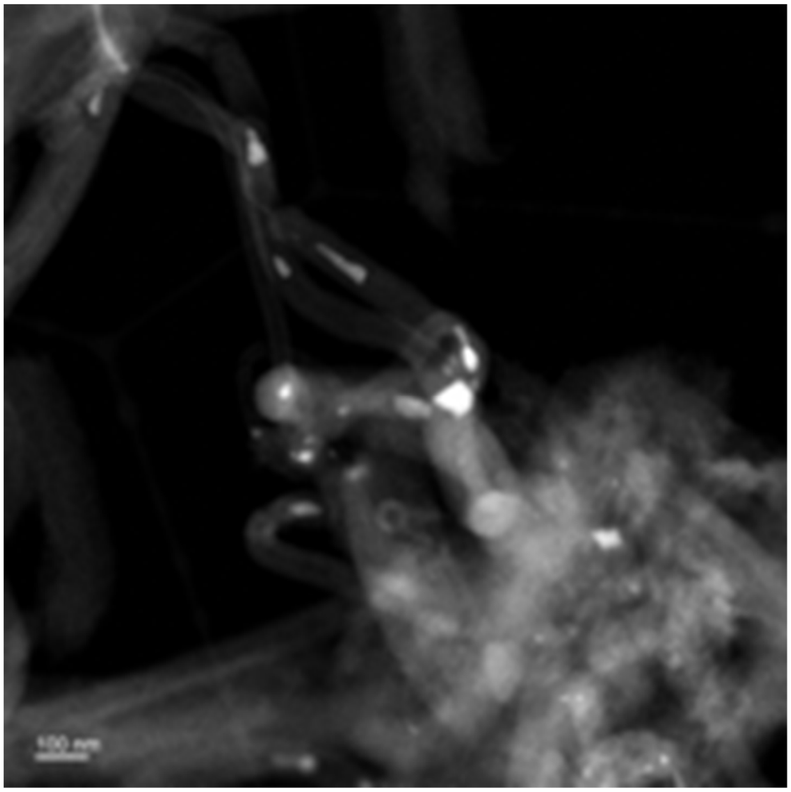

Figure S5.6 STEM image of Fe-NAC-900. STEM image showed the existence of nanoparticles of iron-related species.

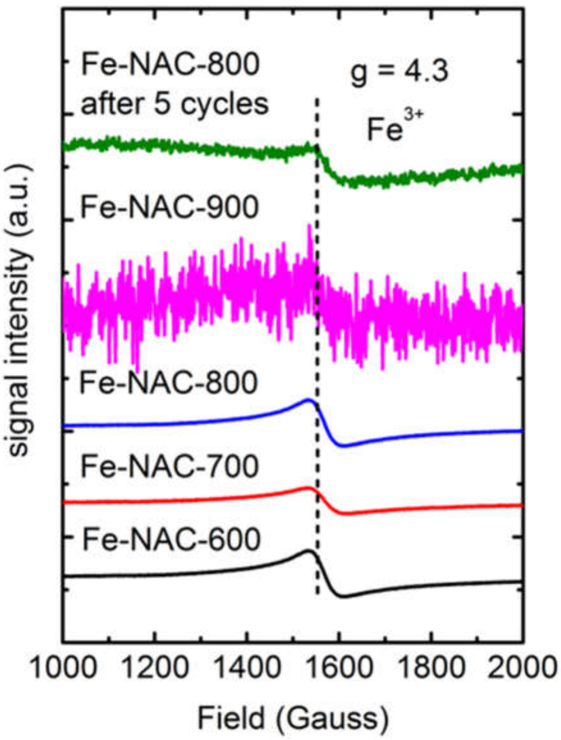

Figure S5.7 EPR spectrum of Fe-NACs catalysts and Fe-NAC-800 after 5 reaction recycles.

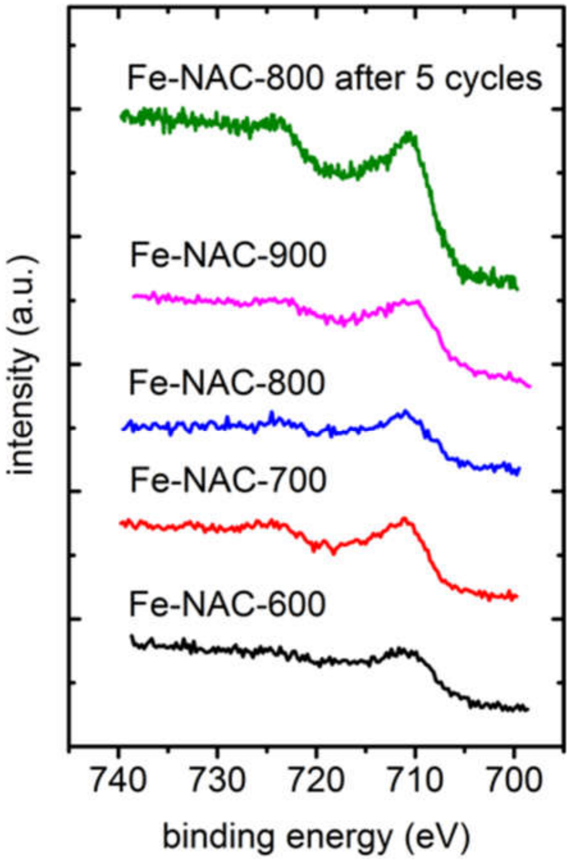

Figure S5.8 Fe 2p XPS of Fe-NACs and Fe-NAC-800 after 5 reaction cycles.

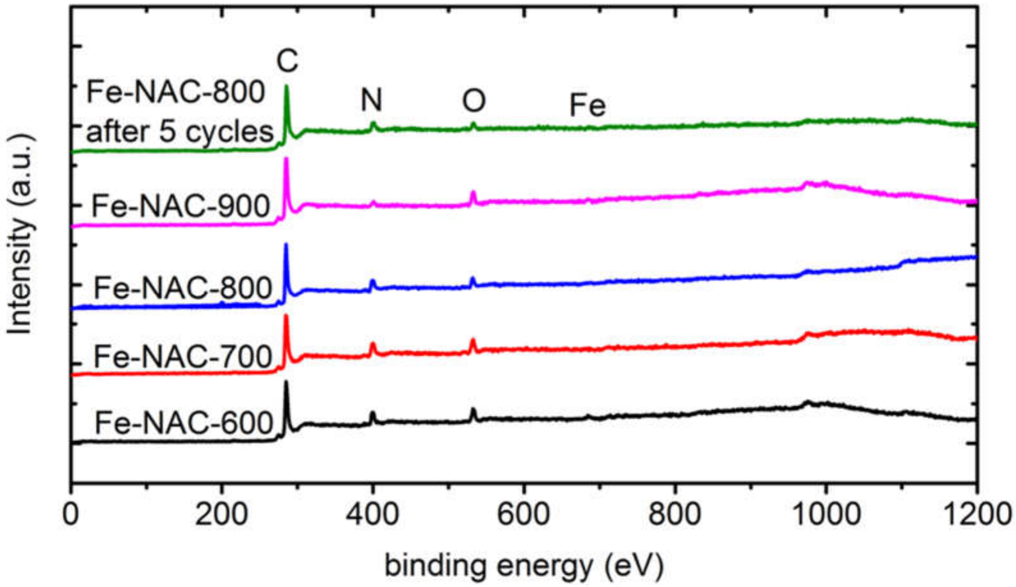

Figure S5.9 XPS wide-scan spectra of different Fe-NACs and Fe-NAC-800 after 5 cycles.

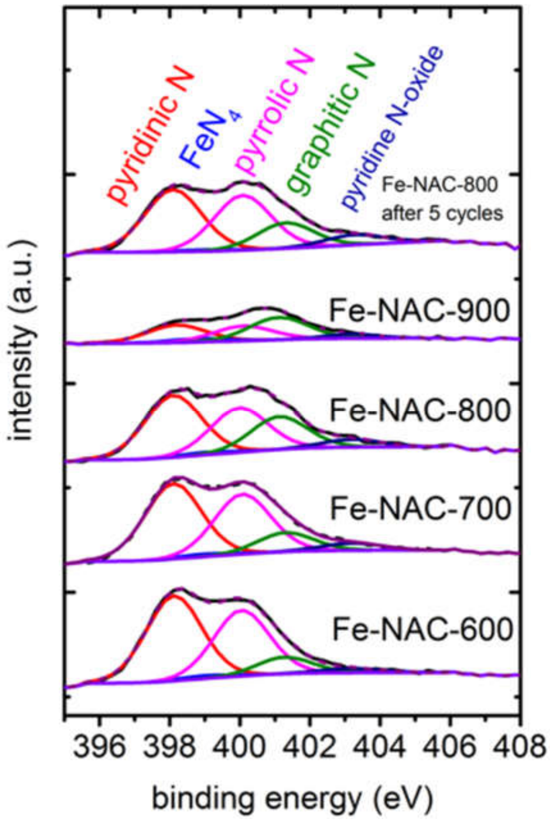

Figure S5.10 N1s XPS of Fe-NACs and Fe-NAC-800 after 5 reaction cycles.

Table S5.2 N1s fitting data of Fe-NACs.

entry	catalysts	N species (%)				
		pyridinic N	FeN_4	pyrrolic N	graphitic N	pyridine N-oxide
1	Fe-NAC-600	45.71	3.36	41.46	5.61	3.84
2	Fe-NAC-700	40.39	5.35	25.51	21.76	7.47
3	Fe-NAC-800	38.69	7.90	9.84	36.52	6.24
4	Fe-NAC-900	22.11	17.05	3.98	47.08	7.75
5	Fe-NAC-800 after 5 cycles	40.21	1.76	34.58	17.30	6.15

Table S5.3 XPS, Elemental analysis and ICP of Fe-NACs.

entry	samples	XPS				CNH			ICP
		C(at%)	N(at%)	Fe(at%)	C:N (atomic)	C(wt%)	N(wt%)	C:N (atomic)	Fe (wt%)
1	Fe-NAC-600	80.44	12.43	0.18	6.5	66.72	17.59	4.4	0.84
2	Fe-NAC-700	79.03	12.94	0.20	6.1	64.63	15.56	4.9	0.94
3	Fe-NAC-800	83.38	11.08	0.21	7.5	70.40	12.58	6.5	1.1
4	Fe-NAC-900	88.00	4.54	0.23	19.4	74.52	6.53	9.3	1.2
5	Fe-NAC-800 after 5 cycles	84.32	8.89	0.22	6.6	64.52	12.49	6.0	1.1

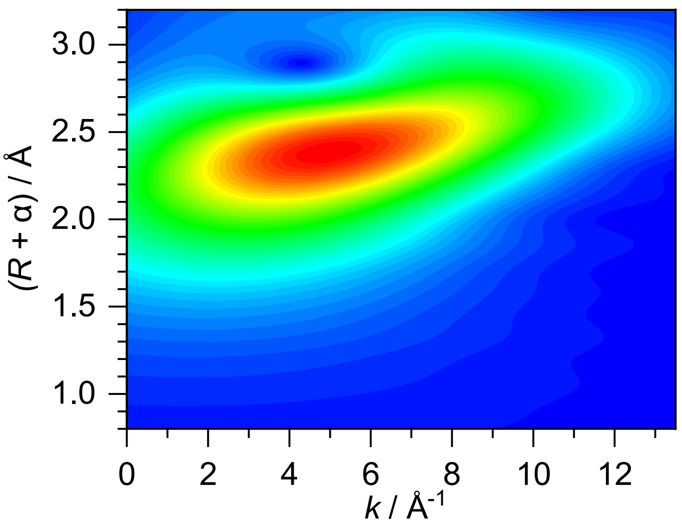

Figure S5.11 Wavelet-Transform EXAFS for Fe-C path. The following parameters were fixed in the FEFF Simulation: $S_0^2 = 0.8$, $\Delta E_0 = 0$ eV, $\sigma^2 = 0.010$ Å^2.

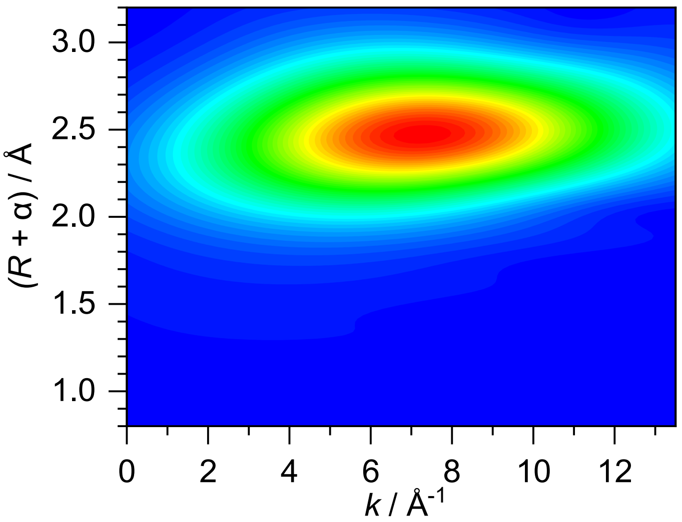

Figure S5.12 Wavelet-Transform EXAFS for Fe-Fe path. The following parameters were fixed in the FEFF simulation: $S_0^2 = 0.8$, $\Delta E_0 = 0$ eV, $\sigma^2 = 0.010$ Å^2.

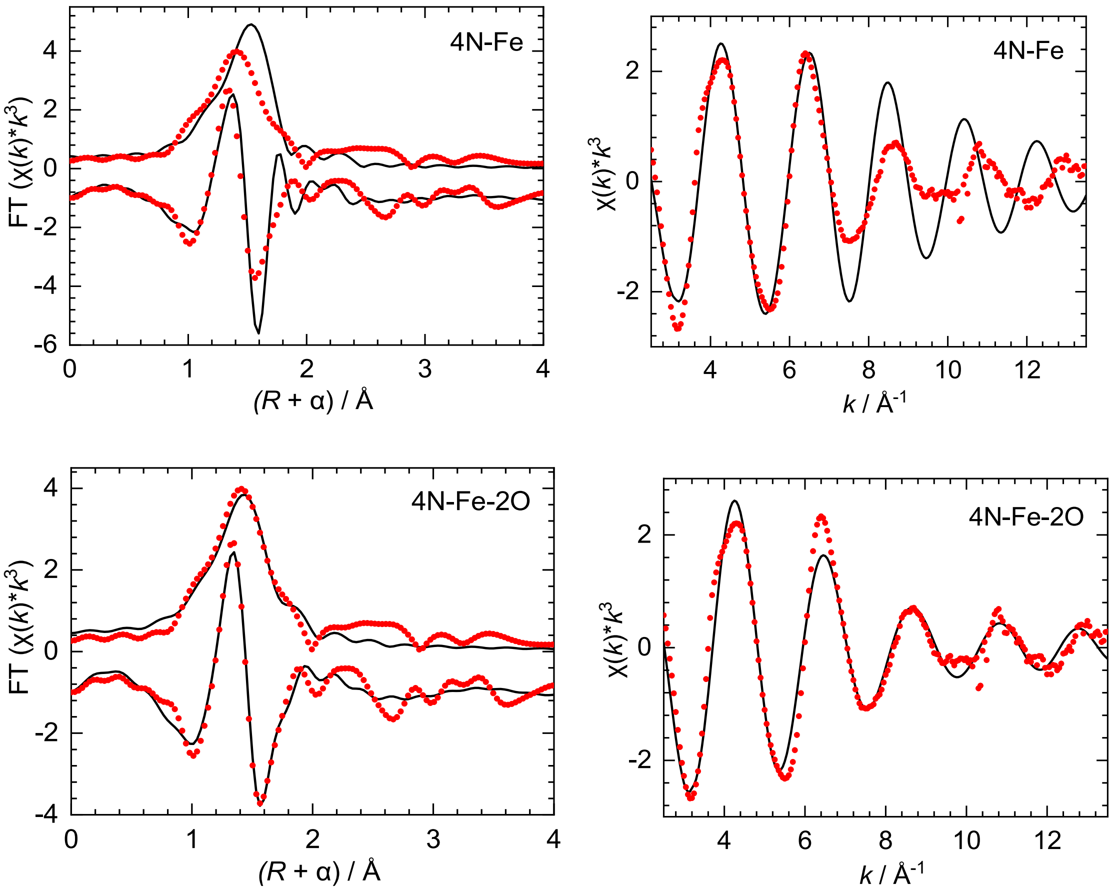

Figure S5.13 Curvefitting of the Fe K-edge EXAFS (left) and k^3-weighted k-space (right) for Fe-NAC-800 with 4N-Fe model (top) and 4N-Fe-2O (bottom), showing the fit (black lines) superposed on the FT magnitude and its imaginary component (points).

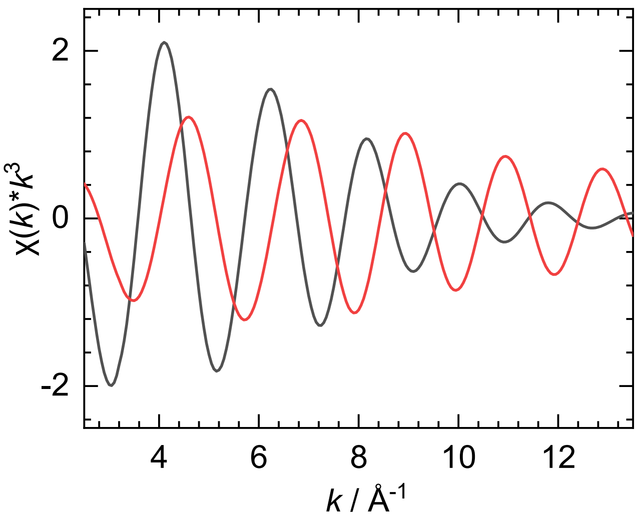

Figure S5.14 The k^3-weighted χ(k) functions for Fe-N (blue) and Fe-O path (red) in the EXAFS curvefitting of Fe-NAC-800 with 4N-Fe-O model.

Table S5.4 Curvefit Parameters[a] for Fe K-edge EXAFS of Fe-NAC-800.

Sample	Path	*N*	*R* /Å	σ^2/Å^2

4N-Fe[b]	Fe – N	4[c]	1.97(2)	0.007(1)
4N-Fe-O[d]	Fe – O	1[c]	1.87(1)	0.002(1)
	Fe – N	4[c]	2.03(1)	0.008(2)
5N-Fe-1O[e]	Fe – O	1[c]	1.88 (2)	0.004(2)
	Fe – N	5[c]	2.03(2)	0.015(3)

[a] $S_0^2 = 0.80$ was fixed at the value for Fe(acac)$_3$. Data range: $2.5 \leqslant k \leqslant 13.5$ Å^{-1}, $1.0 \leqslant R \leqslant 2.4$ Å. The total number of independent data points is 9.6. The reference distances for the Fe-O and Fe-N paths are taken from the crystal structure of halofantrine-ferriprotoporphyrin. [b] $\Delta E_0 = -2(2)$ eV was refined as a global fit parameter. The total number of variables is 3, with an R-factor of 10.0%. [c] The coordination number was fixed based on each model. [d] $\Delta E_0 = 0(2)$ eV was refined as a global fit parameter. The number of variables is 5 with an *R*-factor of 1.6%. [e] $\Delta E_0 = 0(2)$ eV was refined as a global fit parameter. The number of variables is 5, with an R-factor of 1.6%.

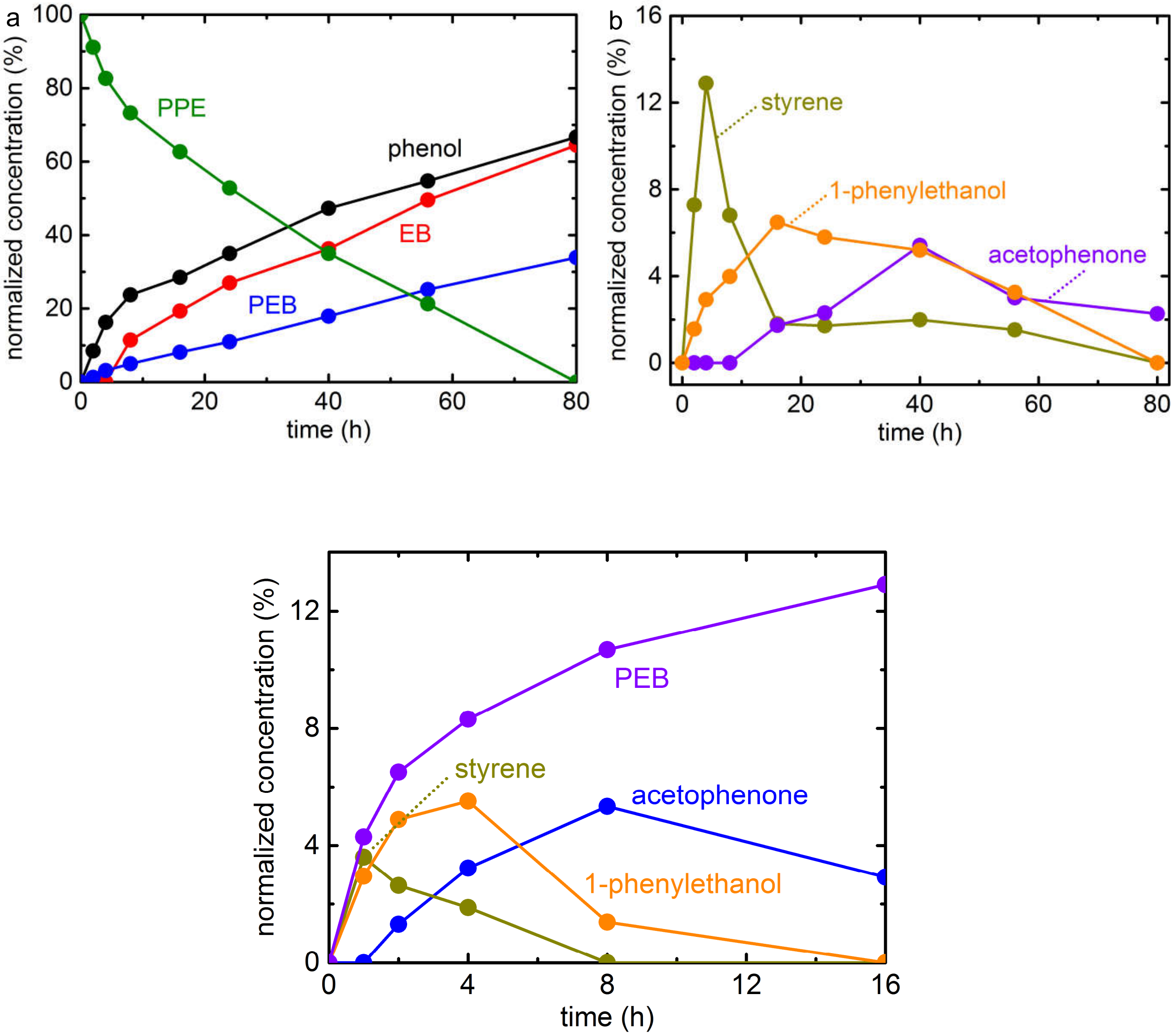

Figure S5.15 Time plots of concentrations of intermediate products during PPE conversion over Fe-NAC-800 catalyst. Reaction conditions: 14 mmol L^{-1} PPE in 2-PrOH (1.50 mL), Fe-NAC-800 (5.0 mg), 230 °C, 20 bar H_2.

Table S5.5 PPE conversion by various control catalysts and Fe-NACs.[a]

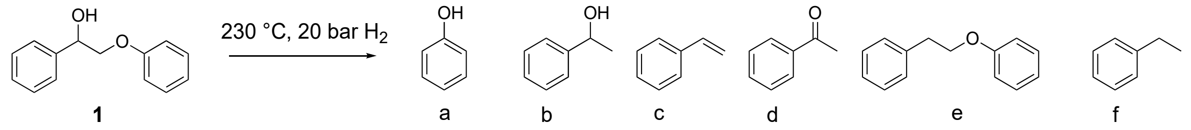

exp	catalysts	conversion (%)	yield (%)						carbon balance (%)	
			a	b	c	d	e	f	C6	C8
1	None	0	-	-	-	-	-	-	-	-
2	Fe(acac)$_3$[b]	0	-	-	-	-	-	-	-	-
4	FeCl$_3$[b] + phenanthroline[c]	0	-	-	-	-	-	-	-	-
6	NAC-800[d]	20	16	3	13	0	3	0	100	99
7	Fe-NAC-600[d]	6	5	1	3	0	2	0	101	99
8	Fe-NAC-700[d]	20	15	2	3	1	4	10	99	99
9	Fe-NAC-800[d]	53	44	4	2	4	9	34	100	99
10	Fe-NAC-900[d]	38	28	2	3	0	9	23	99	99

[a] Reaction conditions: catalyst, 14 mmol L^{-1} PPE in 2-PrOH (1.50 mL), H$_2$ (20 bar), 230 °C, 4 h. [b] 0.105 mmol; [c] 0.21 mmol; [d] 5.0 mg.

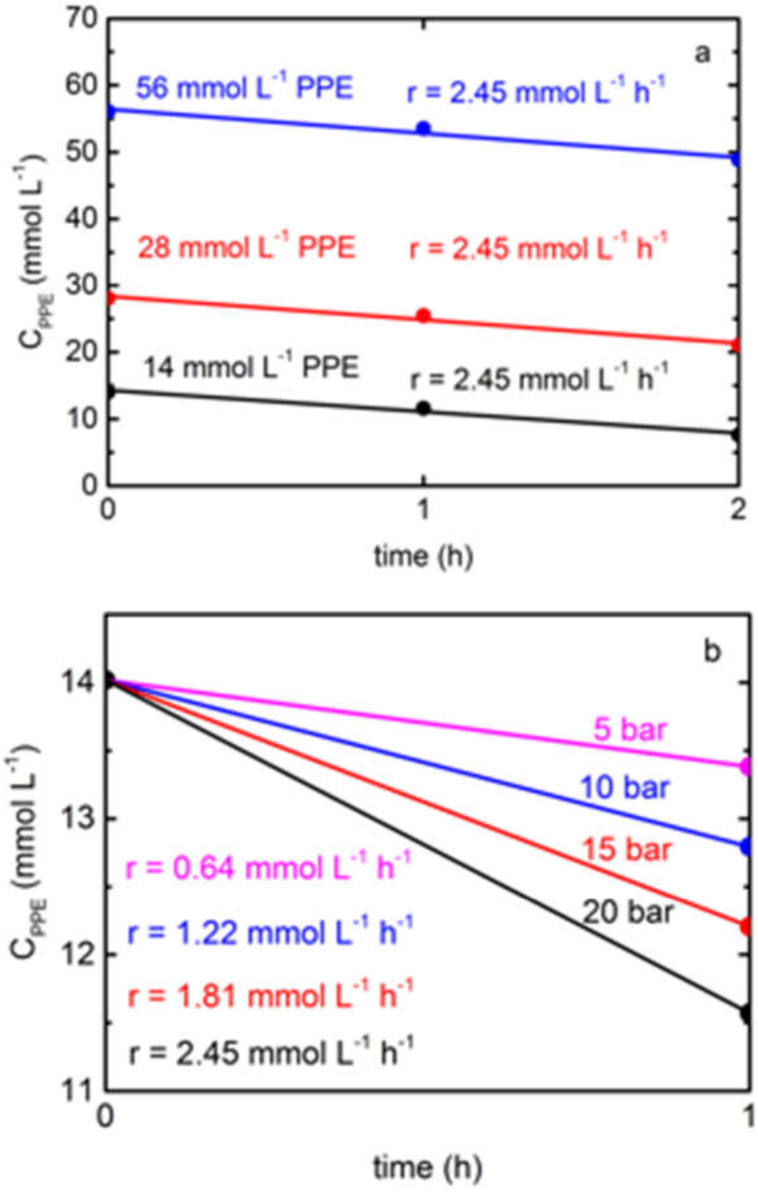

Figure S5.16 PPE concentrations at 230 °C versus time as functions of (a) PPE concentration (20 bar H_2) and (b) H_2 pressure (14 mmol L^{-1} PPE).

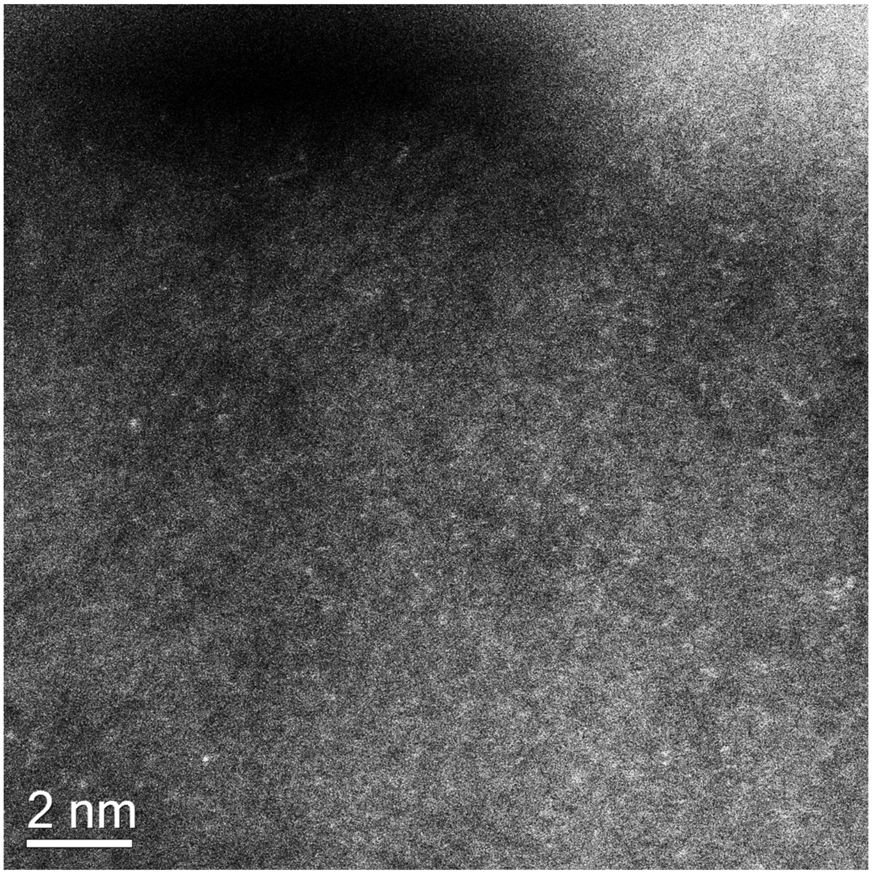

Figure S5.17 HAADF-STEM of Fe-NAC-800 after 5 reaction cycles.

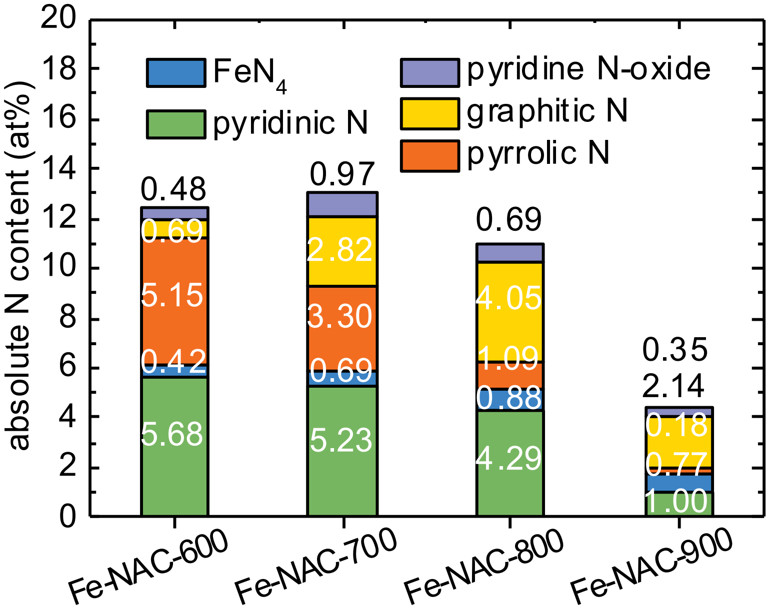

Figure S5.18 The absolute contents of pyridinic, FeN$_4$, pyrrolic, graphitic, and pyridine N-oxide nitrogen species in Fe-NACs by deconvolution of XPS spectra. Higher calcination temperature leads to the decrease of both pyridinic and pyrrolic N, while graphitic N increases with temperature first at 600-800 °C and then drop at 900 °C.

Table S5.6 N1*s* fitting parameters for NACs. The N1*s* peak of assigned N species are fitted with a narrow range for the binding energy according to theoretical calculation.

c	pyridinic N		FeN_4		pyrrolic N		graphitic N		pyridine N-oxide	
	position	FWHM	position	FWHM	position	FWHM	position	FWHM	position	FWHM
Fe-NAC-600	398.1	1.9	399	2.0	400.1	2.2	401.0	1.8	402.8	2.0
Fe-NAC-700	398.2	1.8	399.1	2.0	399.9	1.9	400.9	1.8	402.8	2.2
Fe-NAC-800	398.1	1.9	399.1	2.0	399.8	1.9	400.7	2.1	403.0	2.1
Fe-NAC-900	398.1	1.8	399.1	2.2	400.1	2.0	400.9	2.1	402.9	1.9

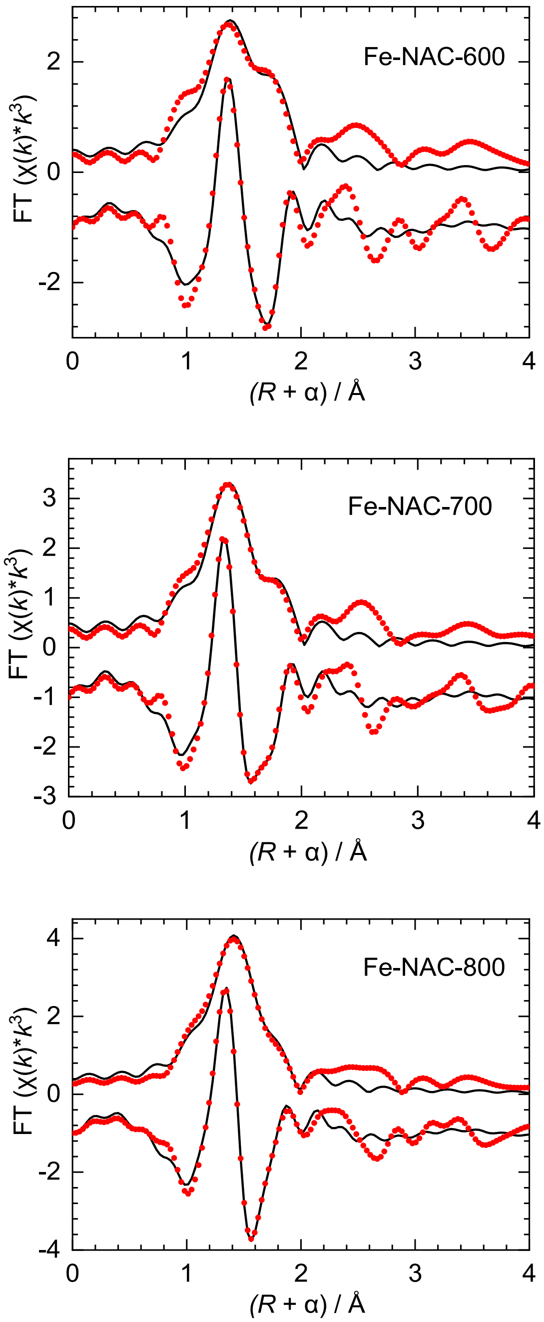

Figure S5.19 Curvefitting of the Fe K-edge EXAFS for Fe-NAC with 4N-Fe-O model, showing the fit (black lines) superposed on the FT magnitude and its imaginary component (points).

Table S5.7 Curvefit Parameters[a] for Fe K-edge EXAFS of Fe-NAC, using 4N-Fe-O model

Sample	Path	N^b	R /Å	σ^2/Å^2
Fe-NAC-600	Fe – O	1	1.88(1)	0.003(1)
	Fe – N	4	2.08(1)	0.008(2)
Fe-NAC-700	Fe – O	1	1.86(1)	0.002(1)
	Fe – N	4	2.05(1)	0.007(2)
Fe-NAC-800	Fe – O	1	1.86(1)	0.002(1)
	Fe – N	4	2.02(1)	0.008(1)

[a] $S_0^2 = 0.80$ was fixed at the value for Fe(acac)$_3$. $\Delta E_0 = 0(1)$ eV was refined as a global fit parameter. Data range: $2.5 \leqslant k \leqslant 13.5$ Å^{-1}, $1.0 \leqslant R \leqslant 2.0$ Å. The number of variables is 13, out of the total number of 20.5 independent data points. The R-factor for this fit is 0.4%. [b] The coordination numbers were fixed. The reference distances for the Fe-O and Fe-N paths are taken from the crystal structure of halofantrine-ferriprotoporphyrin.[229]

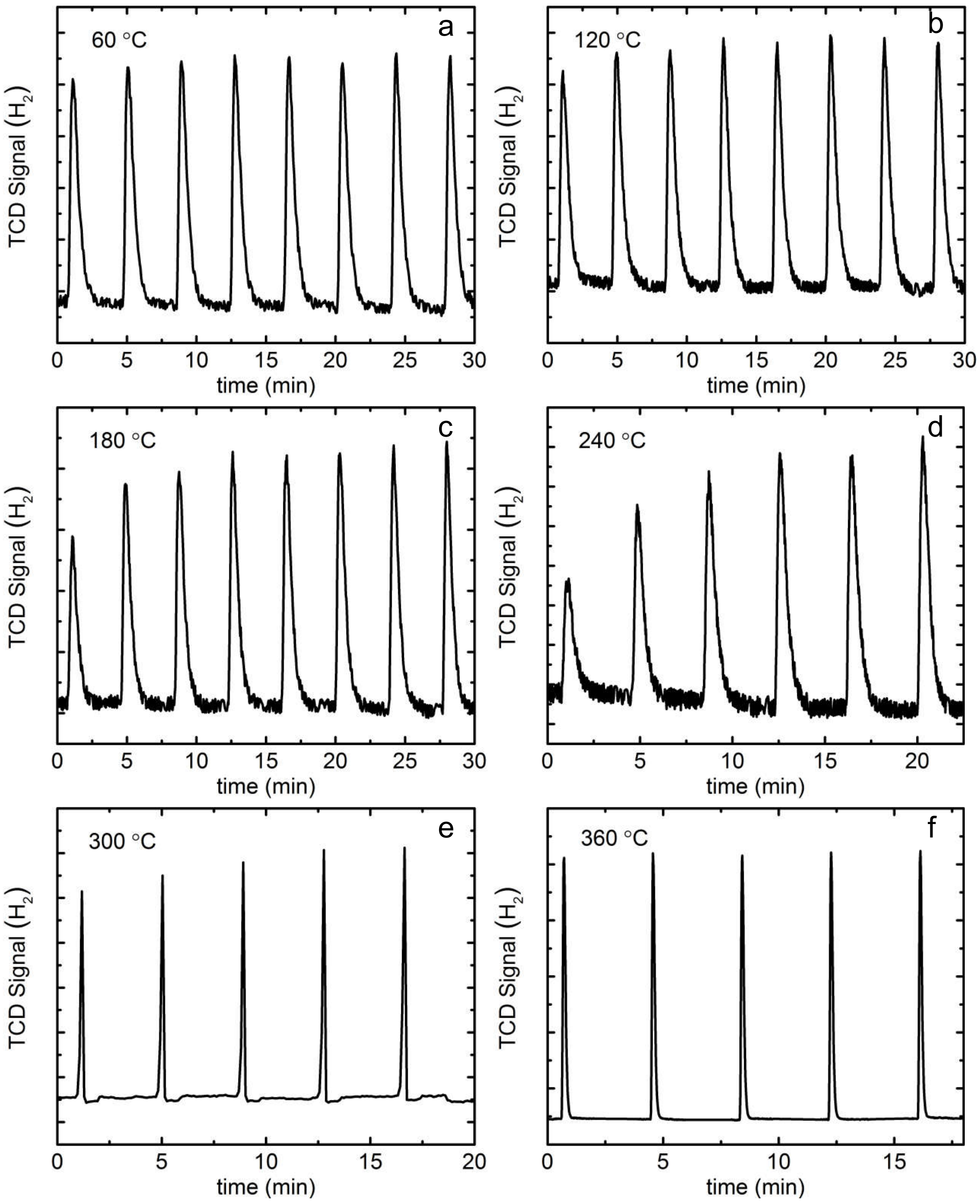

Figure S5.20 Hydrogen pulse chemisorption of Fe-NAC-800 at 60-360 °C.

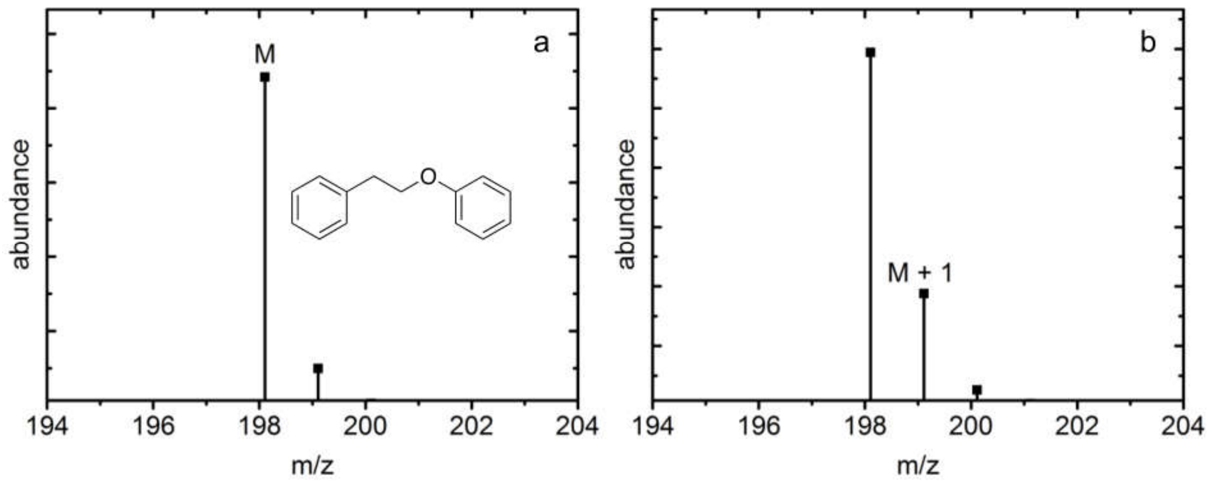

Figure S5.21 Mass spectra of PEB after PPE conversion over Fe-NAC-800 catalyst (a) in isopropanol and H_2 (20 bar), and (b) in decane and H_2 (10 bar) and D_2 (10 bar). Reaction conditions: Fe-NAC-800 (5.0 mg), 14 mmol L^{-1} PPE (1.50 mL), 230 °C, 4 h.

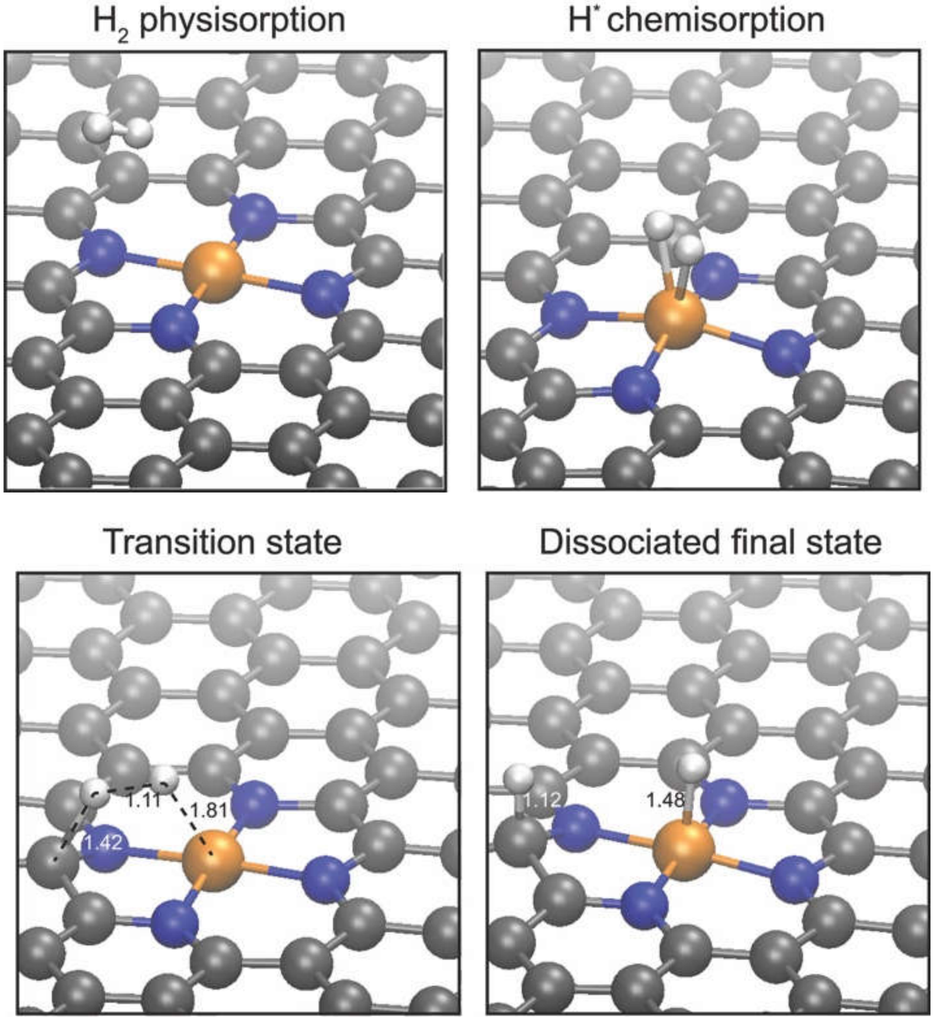

Figure S5.22 Structures for H_2 dissociation on the bare Fe-N_4 structures. The energy profile is shown in Figure 5.10 in the main text. The Fe-H, C-H and H-H bond lengths are labled in the transition state and the final dissociated state.

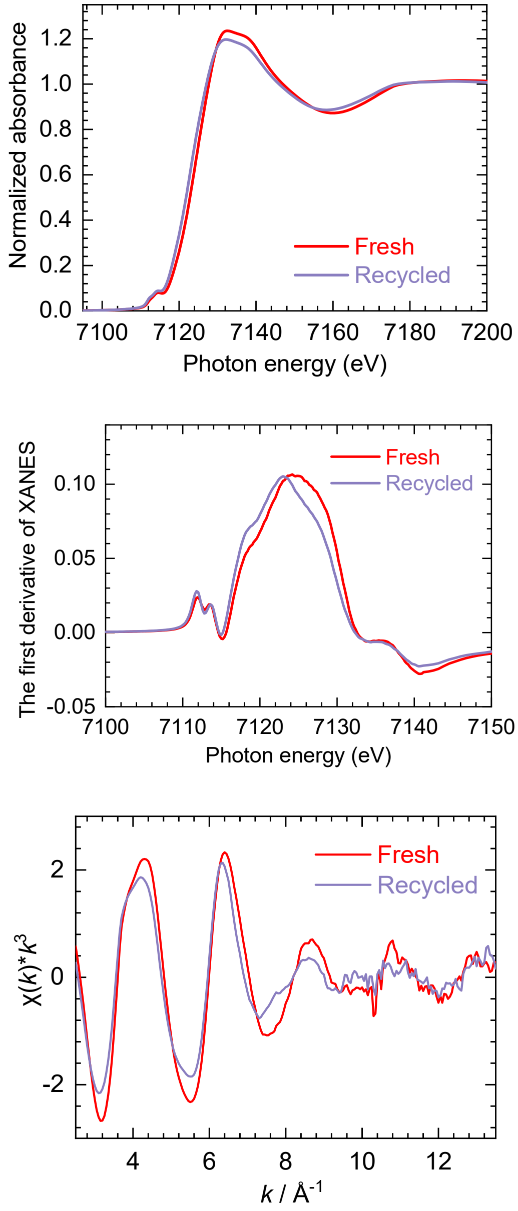

Figure S5.23 Comparison of Fe K-edge XAS: (top) XANES, (middle) the first derivative of XANES and (bottom) FT-EXAFS magnitude, for fresh Fe-NAC-800 (red) and recycled Fe-NAC-800 (purple).

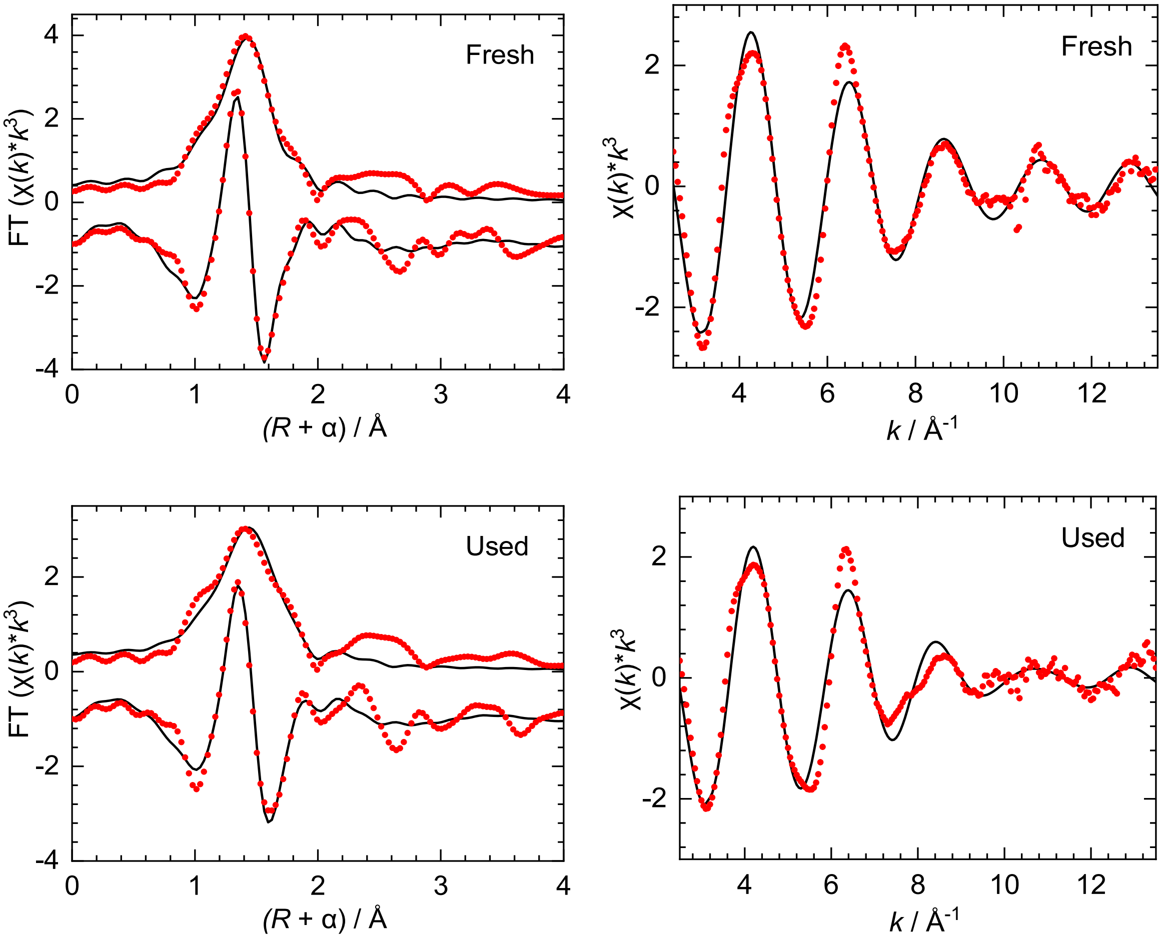

Figure S5.24 Curvefitting of the Fe K-edge EXAFS (left) and k^3-weighted k-space (right) for fresh (top) and recycled (bottom) Fe-NAC-800, showing the fit (black lines) superposed on the FT magnitude and its imaginary component (points).

Table S5.8 Curvefit Parameters[a] for Fe K-edge EXAFS of fresh and recycled Fe-NAC-800.

	Path	N	R /Å	σ^2/Å^2
Fresh[b]	Fe – O	1.0(3)	1.88(1)[d]	0.002(1)[f]
	Fe – N	4[c]	2.03(1)[e]	0.009(1)[g]
Recycled[h]	Fe – O	0.6(3)	1.88(1)[d]	0.002(1)
	Fe – N	4[c]	2.03(1)[e]	0.009(1)[g]

[a] $S_0^2 = 0.80$ was fixed at the value for Fe(acac)$_3$. Data range: $2.5 \leqslant k \leqslant 13.5$ Å^{-1}, $1.0 \leqslant R \leqslant 2.1$ Å. The R-factor for this fit is 0.7%. The total number of variables is 8, out of a total of 14.9 independent data point. [b] $\Delta E_0 = 1(1)$ eV was refined as a global fit parameter. [c] N(Fe-N) was fixed at 4. [d] Constrained to the same value. [e] Constrained to the same value. [f] Constrained to the same value. [g] Constrained to the same value. [h] $\Delta E_0 = -1(1)$ eV was refined as a global fit parameter.

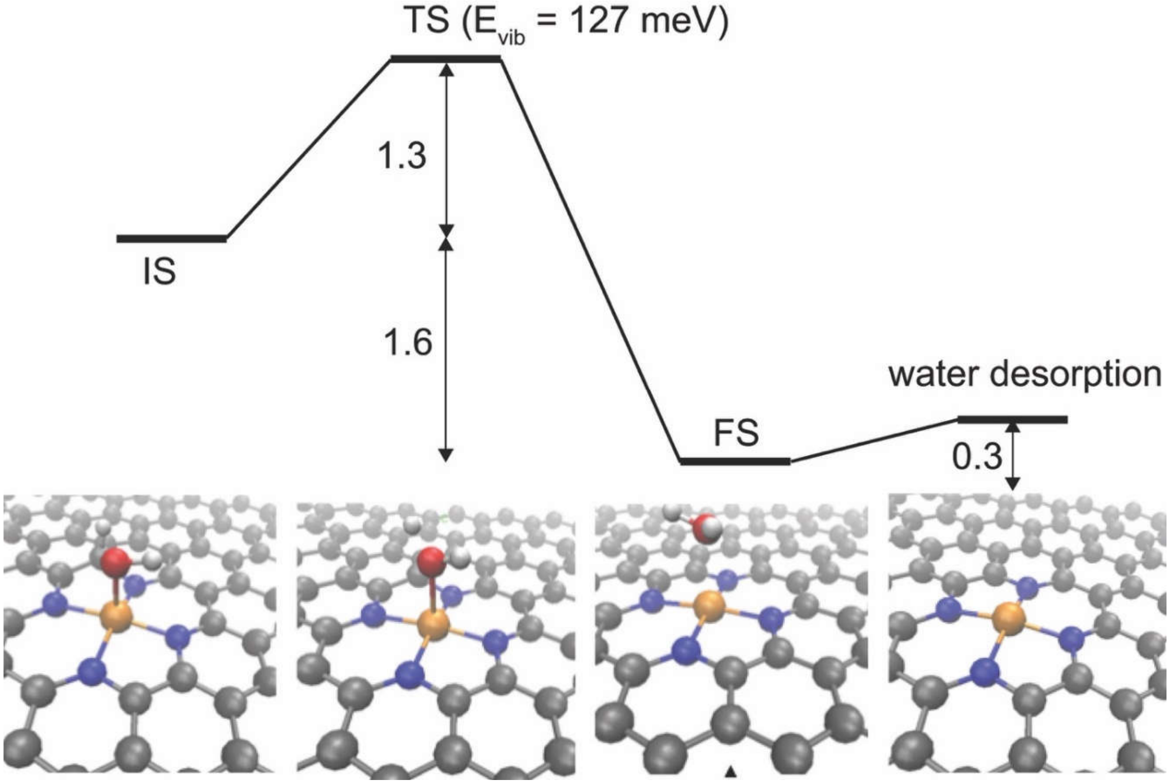

Figure S5.25 Conversion of Fe-OH to Fe-H_2O and then to a bare Fe-N_4 structure. A surface hydrogen binding with a carbon atom can react with the OH moiety to form water with a true barrier of 1.3 eV. This process gains energy of 1.6 eV. The formed water can desorb easily from the surface with an energy cost of 0.3 eV. This calculation thus suggests that the as-prepared Fe-OH may be reduced to a bare Fe-N_4 structure in the reduction environment.

Table S5.9 PPE conversion (4 hour) in different solvents.

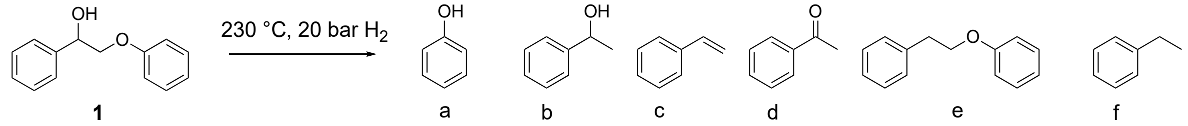

exp	catalysts	solvent	conversion (%)	yield (%)						carbon balance (%)	
				a	b	c	d	e	f	C6	C8
1	Fe-NAC-800	2-PrOH	53	44	4	2	4	9	34	100	99
2	Fe-NAC-800	2-PrOH: H_2O = 4:1	4.2	3.5	-	-	-	-	4.8	101	99
3	Fe-NAC-800	decane	69	56	7.7	8.7	11	12	28	99	98

5.5 Contributions

Zhicheng Luo, Renfeng Nie, Uddhav Kanbur, and Abhranil Biswas conducted the catalyst synthesis, kinetic measurement, and part of characterizations. Y T. Nguyen provided the simulation result.

Chapter 6. Conclusions and Future Directions

6.1 Conclusions

Highly dispersed grafted dioxomonomolybdate sites, $Mo(=O)_2(OSi)_2$, were synthesized by grafting MoO_2Cl_2 onto partially dehydroxylated SiO_2, followed by calcination at 600 °C. Analysis of the Mo-Si paths in the EXAFS of molecular compounds and $Mo(=O)_2(OSi)_2$ shows that the combination of single- and multiple-scattering paths contributes to the signal at ca. 3 Å. The intensity of multiple scattering strongly depends on Mo-O-Si bond angles. Besides the surface heterogeneity, the signal at ca. 3 Å in $Mo(=O)_2(OSi)_2$ is weak because of the destructive interference between Mo-Si and Mo-O-Si paths. The impact of the intrinsic heterogeneity of their attachments to the support on their reactivity must be considered.

The high-temperature olefin treatment effectively promotes $Mo(=O)_2(OSi)_2$, and mixtures of various Mo species are generated due to oligomerization and reduction. The common activation methods, including calcination and reducing gas treatments, cannot activate $Mo(=O)_2(OSi)_2$, which is different from conventional MoO_3/SiO_2 catalysts. The different olefin activation results in the literature arise from the porosity of silica supports. The MoO_3/SiO_2 made from porous SiO_2 can be activated by ethylene or propylene, whereas the olefin treatment does not work on the catalysts made from non-porous SiO_2. The carbonyl compound and Mo-methylidene from high-temperature olefin treatment strongly suggest that the Pseudo-Wittig mechanism can be the activation route.

Ga^iBu_3/Al_2O_3 undergoes step-wise ligand removal from 23 to 550 °C in flowing He, to become 3-coordinate Ga(III), $Ga(OAl)_3$. The XANES analysis indicates that minor Ga species formed during the thermal treatment. Based on the shoulder on the lower edge position, the minor species can be Ga(I) sites. The Ga(I) species are more effective for propane dehydrogenation but deactivate rapidly at 550 °C. The remaining Ga(III) sites show a lower but more stable catalytic performance.

The single-atom Fe(III) catalysts, Fe-NACs, are found to be five-coordinate with four nitrogen and one axial hydroxyl ligand. Fe-NACs materials catalyze the hydrogenolysis of alkyl C-O linkages in aromatic oxygenates without hydrogenation of the arenes. The catalyst is stable at 230 °C under 20 bar H_2 for five cycles. Under the reaction condition, the Fe(III) site is reduced to a more active, four-coordinate Fe(II) site by losing an axial ligand (-OH). The metal-support interaction is critical for reducing Fe(III) sites, catalyzing hydrogenation, and binding reactants.

6.2 Future Directions

Although $Mo(=O)_2(OSi)_2$ is successfully activated, the uniform sites become a mixture. The mixing Mo sites face the same difficulties in identifying the active sites as other conventional MoO_3/SiO_2 catalysts. If activation mechanisms are addressed in the future, the critical challenge is to keep the uniform sites after the activation. A mild activation method should replace the high-temperature ethylene/propene treatment, like using 2-butene instead. Hence, the side reactions can be avoided. Alternatively, other Mo oxide sites can be proposed as active sites in MoO_3/SiO_2. The strategy similar to grafting MoO_2Cl_2 will still be applicable for other Mo sites: look for suitable Mo precursors that allow the formation of a specific Mo site uniformly dispersed on the surface. Furthermore, the support porosity appears to be a critical factor to increase $Mo(=O)_2(OSi)_2$ fraction, where the experiments can help verify this hypothesis and optimize the activation condition. Besides SiO_2 support, olefin treatment may work efficiently on MoO_3/Al_2O_3 and other molybdate-supported catalysts.

The Ga K-edge XANES embeds much structural information, helping probe the Ga sites on the surface. The understanding of Ga XANES features is still incomplete, in particular the influence of Ga-hydride. Hydrogen atom does not contribute any signal in EXAFS but participates in the molecular orbital bonding. The XANES simulation for supported Ga-hydride species will guide the experimental spectra to identify "EXAFS invisible" Ga-hydride sites. To confirm the formation of Ga-hydride species, *operando* XAS may be incorporated with *operando* infrared spectroscopy to detect Ga-hydride IR bands at ca. 2000 cm^{-1} at the beamline.

References

1. Meitzner, G. D.; Iglesia, E.; Baumgartner, J. E.; Huang, E. S. The Chemical State of Gallium in Working Alkane Dehydrocyclodimerization Catalysts. *In situ* Gallium K-Edge X-Ray Absorption Spectroscopy. *J. Catal.* **1993,** *140*, 209-225.
2. Bordiga, S.; Groppo, E.; Agostini, G.; van Bokhoven, J. A.; Lamberti, C. Reactivity of Surface Species in Heterogeneous Catalysts Probed by In Situ X-ray Absorption Techniques. *Chem. Rev.* **2013,** *113*, 1736-1850.
3. Bare, S. R.; Ressler, T., Chapter 6 Characterization of Catalysts in Reactive Atmospheres by X-ray Absorption Spectroscopy. In *Advances in Catalysis*, Academic Press: 2009; Vol. 52, pp 339-465.
4. Rehr, J. J.; Ankudinov, A. L. Progress in the theory and interpretation of XANES. *Coord. Chem. Rev.* **2005,** *249*, 131-140.
5. Ganguly, S.; McCormick, L. J.; Conradie, J.; Gagnon, K. J.; Sarangi, R.; Ghosh, A. Electronic Structure of Manganese Corroles Revisited: X-ray Structures, Optical and X-ray Absorption Spectroscopies, and Electrochemistry as Probes of Ligand Noninnocence. *Inorg. Chem.* **2018,** *57*, 9656-9669.
6. Sarangi, R. X-ray absorption near-edge spectroscopy in bioinorganic chemistry: Application to M–O_2 systems. *Coord. Chem. Rev.* **2013,** *257*, 459-472.
7. Yamamoto, T. Assignment of pre-edge peaks in K-edge x-ray absorption spectra of 3d transition metal compounds: electric dipole or quadrupole? *X-Ray Spectrom.* **2008,** *37*, 572-584.
8. Nunes, C. D.; Valente, A. A.; Pillinger, M.; Rocha, J.; Gonçalves, I. S. Molecular Structure–Activity Relationships for the Oxidation of Organic Compounds Using

Mesoporous Silica Catalysts Derivatised with Bis(halogeno)dioxomolybdenum(VI) Complexes. *Chem. Eur. J.* **2003,** *9*, 4380-4390.

9. Fernández-García, M. XANES analysis of catalytic systems under reaction conditions. *Cat. Rev. Sci. Eng.* **2002,** *44*, 59-121.

10. Lengke, M. F.; Ravel, B.; Fleet, M. E.; Wanger, G.; Gordon, R. A.; Southam, G. Mechanisms of Gold Bioaccumulation by Filamentous Cyanobacteria from Gold(III)−Chloride Complex. *Environ. Sci. Technol.* **2006,** *40*, 6304-6309.

11. Shimizu, K.-i.; Takamatsu, M.; Nishi, K.; Yoshida, H.; Satsuma, A.; Tanaka, T.; Yoshida, S.; Hattori, T. Alumina-Supported Gallium Oxide Catalysts for NO Selective Reduction: Influence of the Local Structure of Surface Gallium Oxide Species on the Catalytic Activity. *J. Phys. Chem. B* **1999,** *103*, 1542-1549.

12. Rehr, J. J.; Kas, J. J.; Vila, F. D.; Prange, M. P.; Jorissen, K. Parameter-free calculations of X-ray spectra with FEFF9. *Phys. Chem. Chem. Phys.* **2010,** *12*, 5503-5513.

13. Hermann, K.; Pettersson, L. G. M.; Casida, M. E.; Daul, C.; Goursot, A.; Koester, A.; Proynov, E.; St-Amant, A.; Salahub, D. R.; Carravetta, V.; Duarte, H.; Godbout, N.; Guan, J.; Jamorski, C.; Leboeuf, M.; Malkin, V.; Malkina, O.; Nyberg, M.; Pedocchi, L.; Sim, F.; Triguero, L.; Vela, A. StoBe-deMon version 3.3. **2014**.

14. Neese, F. The ORCA program system. *WIREs Computational Molecular Science* **2012,** *2*, 73-78.

15. Henderson, G. S.; de Groot, F. M. F.; Moulton, B. J. A. X-ray Absorption Near-Edge Structure (XANES) Spectroscopy. *Reviews in Mineralogy and Geochemistry* **2014,** *78*, 75-138.

16. Liu, Y.; Marcella, N.; Timoshenko, J.; Halder, A.; Yang, B.; Kolipaka, L.; Pellin, M. J.; Seifert, S.; Vajda, S.; Liu, P.; Frenkel, A. I. Mapping XANES spectra on structural descriptors of copper oxide clusters using supervised machine learning. *J. Chem. Phys.* **2019,** *151*, 164201.

17. Timoshenko, J.; Frenkel, A. I. "Inverting" X-ray Absorption Spectra of Catalysts by Machine Learning in Search for Activity Descriptors. *ACS Catal.* **2019,** *9*, 10192-10211.

18. Guda, A. A.; Guda, S. A.; Lomachenko, K. A.; Soldatov, M. A.; Pankin, I. A.; Soldatov, A. V.; Braglia, L.; Bugaev, A. L.; Martini, A.; Signorile, M.; Groppo, E.; Piovano, A.; Borfecchia, E.; Lamberti, C. Quantitative structural determination of active sites from in situ and operando XANES spectra: From standard ab initio simulations to chemometric and machine learning approaches. *Catal. Today* **2019,** *336*, 3-21.

19. Chiarello, G. L.; Ferri, D. Modulated excitation extended X-ray absorption fine structure spectroscopy. *Phys. Chem. Chem. Phys.* **2015,** *17*, 10579-10591.

20. Timoshenko, J.; Roldan Cuenya, B. *In Situ/Operando* Electrocatalyst Characterization by X-ray Absorption Spectroscopy. *Chem. Rev.* **2021,** *121*, 882-961.

21. Frahm, R. New method for time dependent x‐ray absorption studies. *Rev. Sci. Instrum.* **1989,** *60*, 2515-2518.

22. Stötzel, J.; Lützenkirchen-Hecht, D.; Frahm, R. A new flexible monochromator setup for quick scanning x-ray absorption spectroscopy. *Rev. Sci. Instrum.* **2010,** *81*, 073109.

23. Müller, O.; Lützenkirchen-Hecht, D.; Frahm, R. Quick scanning monochromator for millisecond in situ and in operando X-ray absorption spectroscopy. *Rev. Sci. Instrum.* **2015,** *86*, 093905.

24. Nonaka, T.; Dohmae, K.; Araki, T.; Hayashi, Y.; Hirose, Y.; Uruga, T.; Yamazaki, H.; Mochizuki, T.; Tanida, H.; Goto, S. Quick-scanning x-ray absorption spectroscopy system with a servo-motor-driven channel-cut monochromator with a temporal resolution of 10 ms. *Rev. Sci. Instrum.* **2012,** *83*, 083112.

25. Nachtegaal, M.; Müller, O.; König, C.; Frahm, R., QEXAFS: Techniques and Scientific Applications for Time-Resolved XAS. In *X-Ray Absorption and X-Ray Emission Spectroscopy*, 2016; pp 155-183.

26. Schrock, R. R.; Hoveyda, A. H. Molybdenum and tungsten imido alkylidene complexes as efficient olefin-metathesis catalysts. *Angew. Chem. Int. Ed.* **2003,** *42*, 4592-4633.

27. Scholl, M.; Ding, S.; Lee, C. W.; Grubbs, R. H. Synthesis and activity of a new generation of ruthenium-based olefin metathesis catalysts coordinated with 1,3-dimesityl-4,5-dihydroimidazol-2-ylidene ligands. *Org. Lett.* **1999,** *1*, 953-956.

28. Singh, O. M. Metathesis catalysts: Historical perspective, recent developments and practical applications. *J. Sci. Ind. Res.* **2006,** *65*, 957-965.

29. Oikawa, T.; Ookoshi, T.; Tanaka, T.; Yamamoto, T.; Onaka, M. A new heterogeneous olefin metathesis catalyst composed of rhenium oxide and mesoporous alumina. *Microporous Mesoporous Mater.* **2004,** *74*, 93-103.

30. Debecker, D. P.; Stoyanova, M.; Rodemerck, U.; Gaigneaux, E. M. Preparation of MoO_3/SiO_2-Al_2O_3 metathesis catalysts via wet impregnation with different Mo precursors. *J. Mol. Catal. A: Chem.* **2011,** *340*, 65-76.

31. Spamer, A.; Dube, T. I.; Moodley, D. J.; van Schalkwyk, C.; Botha, J. M. The reduction of isomerisation activity on a WO_3/SiO_2 metathesis catalyst. *Appl. Catal., A* **2003,** *255*, 153-167.

32. Bykov, V. I.; Belyaev, B. A.; Butenko, T. A.; Finkelshtein, E. S. Kinetics of α-olefin metathesis over the heterogeneous catalytic system ($MoOCl_4/SiO_2$)-$SnMe_4$. *Kinet. Catal.* **2012,** *53*, 353-356.

33. Louis, C.; Che, M.; Anpo, M. Characterization and Modeling of the Mo Species in Grafted Mo/SiO_2 Catalysts after Redox Thermal Treatments. *J. Catal.* **1993,** *141*, 453-464.

34. Mol, J. C. Olefin metathesis over supported rhenium oxide catalysts. *Catal. Today* **1999,** *51*, 289-299.

35. Handzlik, J.; Ogonowski, J. Dynamic Chemical Counting of Active Centers of Molybdena–Alumina Metathesis Catalysts. *Catal. Lett.* **2003,** *88*, 119-122.

36. Amakawa, K.; Wrabetz, S.; Kröhnert, J.; Tzolova-Müller, G.; Schlögl, R.; Trunschke, A. In Situ Generation of Active Sites in Olefin Metathesis. *J. Am. Chem. Soc.* **2012,** *134*, 11462-11473.

37. Radhakrishnan, R.; Reed, C.; Oyama, S. T.; Seman, M.; Kondo, J. N.; Domen, K.; Ohminami, Y.; Asakura, K. Variability in the structure of supported MoO_3 catalysts: Studies using Raman and X-ray absorption spectroscopy with ab initio calculations. *J. Phys. Chem. B* **2001,** *105*, 8519-8530.

38. Amakawa, K.; Sun, L.; Guo, C.; Hävecker, M.; Kube, P.; Wachs, I. E.; Lwin, S.; Frenkel, A. I.; Patlolla, A.; Hermann, K. J. How strain affects the reactivity of surface metal oxide catalysts. *Angew. Chem. Int. Ed.* **2013,** *52*, 13553-13557.

39. Gallo, A.; Fong, A.; Szeto, K. C.; Rieb, J.; Delevoye, L.; Gauvin, R. g. M.; Taoufik, M.; Peters, B.; Scott, S. L. Ligand exchange-mediated activation and stabilization of a Re-based olefin metathesis catalyst by chlorinated alumina. *J. Am. Chem. Soc.* **2016,** *138*, 12935-12947.

40. Merle, N.; Le Quéméner, F.; Bouhoute, Y.; Szeto, K. C.; De Mallmann, A.; Barman, S.; Samantaray, M. K.; Delevoye, L.; Gauvin, R. M.; Taoufik, M.; Basset, J.-M. Well-Defined Molybdenum Oxo Alkyl Complex Supported on Silica by Surface Organometallic Chemistry: A Highly Active Olefin Metathesis Precatalyst. *J. Am. Chem. Soc.* **2017,** *139*, 2144-2147.

41. Andreini, A.; Xiaoding, X.; Mol, J. C. Activity of $Re_2O_7/SiO_2 \cdot Al_2O_3$ catalysts for propene metathesis and the influence of alkyltin promotors. *Appl. Catal.* **1986,** *27*, 31-40.

42. Wang, Y.; Chen, Q.; Yang, W.; Xie, Z.; Xu, W.; Huang, D. Effect of support nature on WO_3/SiO_2 structure and butene-1 metathesis. *Appl. Catal., A* **2003,** *250*, 25-37.

43. Schrock, R. R. Recent Advances in High Oxidation State Mo and W Imido Alkylidene Chemistry. *Chem. Rev.* **2009,** *109*, 3211-3226.

44. Stangland, E. E. Shale Gas Implications for C_2-C_3 Olefin Production: Incumbent and Future Technology. *Annu. Rev. Chem. Biomol. Eng.* **2018,** *9*, 341-364.

45. Sattler, J. J. H. B.; Ruiz-Martinez, J.; Santillan-Jimenez, E.; Weckhuysen, B. M. Catalytic Dehydrogenation of Light Alkanes on Metals and Metal Oxides. *Chem. Rev.* **2014,** *114*, 10613-10653.

46. Maddah, H. A. A Comparative Study between Propane Dehydrogenation (PDH) Technologies and Plants in Saudi Arabia. *Am. Sci. Res. J. Eng. Technol. Sci.* **2018,** *45*, 49-63.

47. Gosling, C. D.; Hamm, D. A. Process for the production of benzene from light hydrocarbons. US-5258563-A, 1993.

48. Mowry, J.; Anderson, R.; Johnson, J. Process makes aromatics from LPG. *Oil Gas J.* **1985,** *83*, 128-131.

49. Bhan, A.; Nicholas Delgass, W. Propane Aromatization over HZSM-5 and Ga/HZSM-5 Catalysts. *Cat. Rev. Sci. Eng.* **2008,** *50*, 19-151.

50. Rane, N.; Overweg, A. R.; Kazansky, V. B.; van Santen, R. A.; Hensen, E. J. M. Characterization and reactivity of Ga^+ and GaO^+ cations in zeolite ZSM-5. *J. Catal.* **2006,** *239*, 478-485.

51. Szeto, K. C.; Gallo, A.; Hernández-Morejudo, S.; Olsbye, U.; De Mallmann, A.; Lefebvre, F.; Gauvin, R. M.; Delevoye, L.; Scott, S. L.; Taoufik, M. Selective Grafting of $Ga(i\text{-}Bu)_3$ on the Silanols of Mesoporous H-ZSM-5 by Surface Organometallic Chemistry. *J. Phys. Chem. C* **2015,** *119*, 26611-26619.

52. Searles, K.; Siddiqi, G.; Safonova, O. V.; Copéret, C. Silica-supported isolated gallium sites as highly active, selective and stable propane dehydrogenation catalysts. *Chem. Sci.* **2017,** *8*, 2661-2666.

53. Szeto, K. C.; Jones, Z. R.; Merle, N.; Rios, C.; Gallo, A.; Le Quemener, F.; Delevoye, L.; Gauvin, R. M.; Scott, S. L.; Taoufik, M. A Strong Support Effect in Selective Propane Dehydrogenation Catalyzed by $Ga(i\text{-}Bu)_3$ Grafted onto γ-Alumina and Silica. *ACS Catal.* **2018,** *8*, 7566-7577.

54. Schreiber, M. W.; Plaisance, C. P.; Baumgärtl, M.; Reuter, K.; Jentys, A.; Bermejo-Deval, R.; Lercher, J. A. Lewis–Brønsted Acid Pairs in Ga/H-ZSM-5 To Catalyze Dehydrogenation of Light Alkanes. *J. Am. Chem. Soc.* **2018,** *140*, 4849-4859.

55. Phadke, N. M.; Mansoor, E.; Bondil, M.; Head-Gordon, M.; Bell, A. T. Mechanism and Kinetics of Propane Dehydrogenation and Cracking over Ga/H-MFI Prepared via Vapor-Phase Exchange of H-MFI with $GaCl_3$. *J. Am. Chem. Soc.* **2019,** *141*, 1614-1627.

56. Mansoor, E.; Head-Gordon, M.; Bell, A. T. Computational Modeling of the Nature and Role of Ga Species for Light Alkane Dehydrogenation Catalyzed by Ga/H-MFI. *ACS Catal.* **2018,** *8*, 6146-6162.

57. Hensen, E. J. M.; Pidko, E. A.; Rane, N.; van Santen, R. A., Modification of Brønsted acidity of zeolites by Ga^+, GaO^+ and AlO^+: comparison for alkane activation. In *Stud. Surf. Sci. Catal.*, Xu, R.; Gao, Z.; Chen, J.; Yan, W., Eds. Elsevier: 2007; Vol. 170, pp 1182-1189.

58. Pidko, E. A.; Kazansky, V. B.; Hensen, E. J. M.; van Santen, R. A. A comprehensive density functional theory study of ethane dehydrogenation over reduced extra-framework gallium species in ZSM-5 zeolite. *J. Catal.* **2006,** *240*, 73-84.

59. Joshi, Y. V.; Thomson, K. T. The roles of gallium hydride and Brønsted acidity in light alkane dehydrogenation mechanisms using Ga-exchanged HZSM-5 catalysts: A DFT pathway analysis. *Catal. Today* **2005,** *105*, 106-121.

60. Buckles, G.; Hutchings, G. J.; Williams, C. D. Aromatization of propane over Ga/H-ZSM-5: An explanation of the synergy observed between Ga^{3+} and H^+. *Catal. Lett.* **1991,** *11*, 89-93.

61. Pereira, M. S.; Chaer Nascimento, M. A. Theoretical Study on the Dehydrogenation Reaction of Alkanes Catalyzed by Zeolites Containing Nonframework Gallium Species. *J. Phys. Chem. B* **2006,** *110*, 3231-3238.

62. Batchu, S. P.; Wang, H.-L.; Chen, W.; Zheng, W.; Caratzoulas, S.; Lobo, R. F.; Vlachos, D. G. Ethane Dehydrogenation on Single and Dual Centers of Ga-modified γ-Al_2O_3. *ACS Catal.* **2021**, 1380-1391.

63. Phadke, N. M.; Van der Mynsbrugge, J.; Mansoor, E.; Getsoian, A. B.; Head-Gordon, M.; Bell, A. T. Characterization of Isolated Ga^{3+} Cations in Ga/H-MFI Prepared by Vapor-Phase Exchange of H-MFI Zeolite with $GaCl_3$. *ACS Catal.* **2018,** *8*, 6106-6126.

64. Hensen, E. J. M.; García-Sánchez, M.; Rane, N.; Magusin, P. C. M. M.; Liu, P.-H.; Chao, K.-J.; van Santen, R. A. *In situ* Ga K edge XANES study of the activation of Ga/ZSM-5 prepared by chemical vapor deposition of trimethylgallium. *Catal. Lett.* **2005,** *101*, 79-85.

65. Zhidomirov, G. M.; Shubin, A. A.; Milov, M. A.; Kazansky, V. B.; van Santen, R. A.; Hensen, E. J. M. Cluster Model DFT Study of CO Adsorption to Gallium Ions in Ga/HZSM-5. *J. Phys. Chem. C* **2008,** *112*, 3321-3326.

66. Kuz'min, I. V.; Zhidomirov, G. M.; Solkan, V. N.; Kazanskii, V. B. Quantum chemical calculation of the catalytic reaction of ethane dehydrogenation on gallium oxide-hydroxide binuclear clusters in oxidized GaO/ZSM-5 zeolite. *Kinet. Catal.* **2009,** *50*, 752.

67. Yuan, Y.; Brady, C.; Annamalai, L.; Lobo, R. F.; Xu, B. Ga speciation in Ga/H-ZSM-5 by in-situ transmission FTIR spectroscopy. *J. Catal.* **2021,** *393*, 60-69.

68. Collins, S. E.; Baltanás, M. A.; Bonivardi, A. L. Hydrogen Chemisorption on Gallium Oxide Polymorphs. *Langmuir* **2005,** *21*, 962-970.

69. Cybulskis, V. J.; Pradhan, S. U.; Lovón-Quintana, J. J.; Hock, A. S.; Hu, B.; Zhang, G.; Delgass, W. N.; Ribeiro, F. H.; Miller, J. T. The Nature of the Isolated Gallium Active Center for Propane Dehydrogenation on Ga/SiO_2. *Catal. Lett.* **2017,** *147*, 1252-1262.

70. Getsoian, A. B.; Das, U.; Camacho-Bunquin, J.; Zhang, G.; Gallagher, J. R.; Hu, B.; Cheah, S.; Schaidle, J. A.; Ruddy, D. A.; Hensley, J. E.; Krause, T. R.; Curtiss, L. A.; Miller, J. T.; Hock, A. S. Organometallic model complexes elucidate the active gallium species in alkane dehydrogenation catalysts based on ligand effects in Ga K-edge XANES. *Catal. Sci. Technol.* **2016,** *6*, 6339-6353.

71. Nishi, K.; Shimizu, K.-i.; Takamatsu, M.; Yoshida, H.; Satsuma, A.; Tanaka, T.; Yoshida, S.; Hattori, T. Deconvolution Analysis of Ga K-Edge XANES for Quantification of Gallium Coordinations in Oxide Environments. *J. Phys. Chem. B* **1998,** *102*, 10190-10195.

72. Sun, K.; Ginosar, D. M.; He, T.; Zhang, Y.; Fan, M.; Chen, R. Progress in Nonoxidative Dehydroaromatization of Methane in the Last 6 Years. *Ind. Eng. Chem. Res.* **2018,** *57*, 1768-1789.

73. Ma, S.; Guo, X.; Zhao, L.; Scott, S.; Bao, X. Recent progress in methane dehydroaromatization: From laboratory curiosities to promising technology. *Journal of Energy Chemistry* **2013,** *22*, 1-20.

74. de Lucas, A.; Valverde, J. L.; Rodriguez, L.; Sanchez, P.; Garcia, M. T. Partial oxidation of methane to formaldehyde over Mo/HZSM-5 catalysts. *Appl. Catal., A* **2000,** *203*, 81-90.

75. Yang, T.-J.; Lunsford, J. H. Partial oxidation of methanol to formaldehyde over molybdenum oxide on silica. *J. Catal.* **1987,** *103*, 55-64.

76. Marcinkowska, K.; Kaliaguine, S.; Roberge, P. C. Photocatalytic oxidation of propane by oxygen on supported $MoSiO_2$ catalysts. *J. Catal.* **1984,** *90*, 49-58.

77. Banares, M. A.; Fierro, J. L. G.; Moffat, J. B. The Partial Oxidation of Methane on MoO_3/SiO_2 Catalysts: Influence of the Molybdenum Content and Type of Oxidant. *J. Catal.* **1993,** *142*, 406-417.

78. Xu, C.; Zhang, C.; Li, H.; Zhao, X.; Song, L.; Li, X. An Overview of Selective Oxidation of Alcohols: Catalysts, Oxidants and Reaction Mechanisms. *Catalysis Surveys from Asia* **2016,** *20*, 13-22.

79. Guo, Z.; Liu, B.; Zhang, Q.; Deng, W.; Wang, Y.; Yang, Y. Recent advances in heterogeneous selective oxidation catalysis for sustainable chemistry. *Chem. Soc. Rev.* **2014,** *43*, 3480-3524.

80. Grasselli, R. K. Advances and future trends in selective oxidation and ammoxidation catalysis. *Catal. Today* **1999,** *49*, 141-153.

81. Védrine, J. C. Heterogeneous Partial (amm)Oxidation and Oxidative Dehydrogenation Catalysis on Mixed Metal Oxides. *Catalysts* **2016,** *6*, 22.

82. Ding, K.; Gulec, A.; Johnson, A. M.; Drake, T. L.; Wu, W.; Lin, Y.; Weitz, E.; Marks, L. D.; Stair, P. C. Highly Efficient Activation, Regeneration, and Active Site Identification of Oxide-Based Olefin Metathesis Catalysts. *ACS Catal.* **2016,** *6*, 5740-5746.

83. Shen, Y.; Jiang, P.; Wai, P. T.; Gu, Q.; Zhang, W. Recent Progress in Application of Molybdenum-Based Catalysts for Epoxidation of Alkenes. *Catalysts* **2019,** *9*, 31.

84. Lwin, S.; Wachs, I. E. Olefin Metathesis by Supported Metal Oxide Catalysts. *ACS Catal.* **2014,** *4*, 2505-2520.

85. Mestl, G.; Srinivasan, T. K. K. Raman Spectroscopy of Monolayer-Type Catalysts: Supported Molybdenum Oxides. *Cat. Rev. Sci. Eng.* **1998,** *40*, 451-570.

86. Jarupatrakorn, J.; Coles, M. P.; Tilley, T. D. Synthesis and Characterization of $MO[OSi(O^tBu)_3]_4$ and $MO_2[OSi(O^tBu)_3]_2$ (M = Mo, W): Models for Isolated Oxo-Molybdenum and -Tungsten Sites on Silica and Precursors to Molybdena− and Tungsta−Silica Materials. *Chem. Mater.* **2005,** *17*, 1818-1828.

87. Chisholm, M. H.; Folting, K.; Huffman, J. C.; Kirkpatrick, C. C. Reactions of metal-metal multiple bonds. 10. Reactions of $Mo_2(OR)_6$ ($M \equiv M$) and $[Mo(OR)_4]_x$ compounds with molecular oxygen. Preparation and characterization of oxo alkoxides of molybdenum: $MoO_2(OR)_2$, $MoO_2(OR)_2(bpy)$, $MoO(OR)_4$, $Mo_3O(OR)_{10}$, $Mo_4O_8(OR)_4(py)_4$, and $Mo_6O_{10}(OR)_{12}$. *Inorg. Chem.* **1984,** *23*, 1021-1037.

88. Huang, M.; DeKock, C. W. Triphenylsiloxy complexes. A novel compound containing a molybdenum(VI)-phosphorus bond: dioxo(triphenylphosphine)bis(triphenylsiloxo)molybdenum. *Inorg. Chem.* **1993,** *32*, 2287-2291.

89. Hille, R.; Hall, J.; Basu, P. The Mononuclear Molybdenum Enzymes. *Chem. Rev.* **2014,** *114*, 3963-4038.

90. Kamenar, B.; Penavić, M.; Korpar-Čolig, B.; Marković, B. Preparation and crystal structure of two oxo-molybdenum complexes with dimethoxyethane. *Inorg. Chim. Acta* **1982,** *65*, 245-247.

91. Schustereit, T.; Schleid, T.; Hartenbach, I. The Non - Centrosymmetric Crystal Structure of Molybdenum(VI) Oxide Bromide MoO_2Br_2. *Z. Anorg. Allg. Chem.* **2011,** *637*, 1159-1161.

92. de Boer, M.; van Dillen, A. J.; Koningsberger, D. C.; Geus, J. W.; Vuurman, M. A.; Wachs, I. E. Remarkable spreading behavior of molybdena on silica catalysts. An *in situ* EXAFS-Raman study. *Catal. Lett.* **1991,** *11*, 227-239.

93. Chempath, S.; Zhang, Y.; Bell, A. T. DFT Studies of the Structure and Vibrational Spectra of Isolated Molybdena Species Supported on Silica. *J. Phys. Chem. C* **2007,** *111*, 1291-1298.

94. Handzlik, J.; Ogonowski, J. Structure of Isolated Molybdenum(VI) and Molybdenum(IV) Oxide Species on Silica: Periodic and Cluster DFT Studies. *J. Phys. Chem. C* **2012,** *116*, 5571-5584.

95. Kurleto, K.; Tielens, F.; Handzlik, J. Isolated Molybdenum(VI) and Tungsten(VI) Oxide Species on Partly Dehydroxylated Silica: A Computational Perspective. *J. Phys. Chem. C* **2020,** *124*, 3002-3013.

96. Tian, H.; Roberts, C. A.; Wachs, I. E. Molecular Structural Determination of Molybdena in Different Environments: Aqueous Solutions, Bulk Mixed Oxides, and Supported MoO_3 Catalysts. *J. Phys. Chem. C* **2010,** *114*, 14110-14120.

97. Thielemann, J. P.; Ressler, T.; Walter, A.; Tzolova-Müller, G.; Hess, C. Structure of molybdenum oxide supported on silica SBA-15 studied by Raman, UV–Vis and X-ray absorption spectroscopy. *Appl. Catal., A* **2011,** *399*, 28-34.

98. Guesmi, H.; Gryboś, R.; Handzlik, J.; Tielens, F. Characterization of molybdenum monomeric oxide species supported on hydroxylated silica: a DFT study. *Phys. Chem. Chem. Phys.* **2014,** *16*, 18253-18260.

99. Amakawa, K.; Kröhnert, J.; Wrabetz, S.; Frank, B.; Hemmann, F.; Jäger, C.; Schlögl, R.; Trunschke, A. Active Sites in Olefin Metathesis over Supported Molybdena Catalysts. *ChemCatChem* **2015,** *7*, 4059-4065.

100. Kühn, F. E.; Groarke, M.; Bencze, É.; Herdtweck, E.; Prazeres, A.; Santos, A. M.; Calhorda, M. J.; Romão, C. C.; Gonçalves, I. S.; Lopes, A. D.; Pillinger, M. Octahedral Bipyridine and Bipyrimidine Dioxomolybdenum(VI) Complexes: Characterization, Application in Catalytic Epoxidation, and Density Functional Mechanistic Study. *Chem. Eur. J.* **2002,** *8*, 2370-2383.

101. Hursthouse, M. B.; Levason, W.; Ratnani, R.; Reid, G. Synthesis and spectroscopic properties of Mo(VI) complexes with phosphine oxide ligands and the crystal structures of $[MoO_2X_2(OPMe_3)_2]$ (X=Cl or Br) and $[MoO_2Br_2\{o\text{-}C_6H_4(P(O)Ph_2)_2\}]\cdot 2CH_2Cl_2$. *Polyhedron* **2004,** *23*, 1915-1921.

102. Al-Ajlouni, A. M.; Günyar, A.; Zhou, M.-D.; Baxter, P. N. W.; Kühn, F. E. Adduct Formation of Dichloridodioxidomolybdenum(VI) and Methyltrioxidorhenium(VII) with a Series of Bidentate Nitrogen Donor Ligands. *Eur. J. Inorg. Chem.* **2009,** *2009*, 1019-1026.

103. Banares, M. A.; Hu, H. C.; Wachs, I. E. Molybdena on Silica Catalysts: Role of Preparation Methods on the Structure-Selectivity Properties for the Oxidation of Methanol. *J. Catal.* **1994,** *150*, 407-420.

104. Debecker, D. P.; Stoyanova, M.; Rodemerck, U.; Léonard, A.; Su, B.-L.; Gaigneaux, E. M. Genesis of active and inactive species during the preparation of $MoO_3/SiO_2–Al_2O_3$ metathesis catalysts via wet impregnation. *Catal. Today* **2011,** *169*, 60-68.

105. Goldsmith, B. R.; Peters, B.; Johnson, J. K.; Gates, B. C.; Scott, S. L. Beyond Ordered Materials: Understanding Catalytic Sites on Amorphous Solids. *ACS Catal.* **2017,** *7*, 7543-7557.

106. Mouat, A. R.; Lohr, T. L.; Wegener, E. C.; Miller, J. T.; Delferro, M.; Stair, P. C.; Marks, T. J. Reactivity of a Carbon-Supported Single-Site Molybdenum Dioxo Catalyst for Biodiesel Synthesis. *ACS Catal.* **2016,** *6*, 6762-6769.

107. Yamamoto, K.; Chan, K. W.; Mougel, V.; Nagae, H.; Tsurugi, H.; Safonova, O. V.; Mashima, K.; Copéret, C. Silica-supported isolated molybdenum di-oxo species: formation and activation with organosilicon agent for olefin metathesis. *Chem. Commun.* **2018,** *54*, 3989-3992.

108. Le Quéméner, F.; Barman, S.; Merle, N.; Aljuhani, M. A.; Samantaray, M. K.; Saih, Y.; Szeto, K. C.; De Mallmann, A.; Minenkov, Y.; Huang, K.-W.; Cavallo, L.; Taoufik, M.; Basset, J.-M. Metathetic Oxidation of 2-Butenes to Acetaldehyde by Molecular Oxygen Using the Single-Site Olefin Metathesis Catalyst $(\equiv SiO)_2Mo(=O)_2$. *ACS Catal.* **2018,** *8*, 7549-7555.

109. Bouhoute, Y.; Garron, A.; Grekov, D.; Merle, N.; Szeto, K. C.; De Mallmann, A.; Del Rosal, I.; Maron, L.; Girard, G.; Gauvin, R. M.; Delevoye, L.; Taoufik, M. Well-Defined Supported Mononuclear Tungsten Oxo Species as Olefin Metathesis Pre-Catalysts. *ACS Catal.* **2014,** *4*, 4232-4241.

110. Thompson, A. C.; Vaughan, D., *X-ray data booklet*. Lawrence Berkeley National Laboratory, University of California Berkeley, CA: 2001; Vol. 8.

111. Ravel, B.; Newville, M. *ATHENA, ARTEMIS, HEPHAESTUS*: data analysis for X-ray absorption spectroscopy using *IFEFFIT*. *J. Synchrotron Radiat.* **2005,** *12*, 537-541.

112. Demmelmaier, C. A.; White, R. E.; van Bokhoven, J. A.; Scott, S. L. Nature of $\equiv SiOCrO_2Cl$ and $(\equiv SiO)_2CrO_2$ Sites Prepared by Grafting CrO_2Cl_2 onto Silica. *Chem. Eur. J.* **2008,** *112*, 6439-6449.

113. Carmichael, W. M.; Edwards, D. A.; Fowles, G. W. A.; Marshall, P. R. Molybdenum (VI) dioxidedihalide complexes. *Inorg. Chim. Acta* **1967,** *1*, 93-96.

114. Ferreira, P.; Gonçalves, I. S.; Kühn, F. E.; Lopes, A. D.; Martins, M. A.; Pillinger, M.; Pina, A.; Rocha, J.; Romão, C. C.; Santos, A. M. Mesoporous silicas modified with dioxomolybdenum (VI) complexes: Synthesis and catalysis. *Eur. J. Inorg. Chem.* **2000,** *2000*, 2263-2270.

115. Demmelmaier, C. A.; White, R. E.; van Bokhoven, J. A.; Scott, S. L. Evidence for a chromasiloxane ring size effect in Phillips (Cr/SiO_2) polymerization catalysts. *J. Catal.* **2009,** *262*, 44-56.

116. Hess, H.; Hartung, H. Die Kristallstruktur von Wolframoxidchlorid $WOCl_4$ und Wolframoxidbromid $WOBr_4$. *Z. Anorg. Allg. Chem.* **1966,** *344*, 157-166.

117. Luna, A. E. C.; Ponzi, M. I.; Rivarola, J. B. Vapor pressure of tungsten chloride oxide ($WOCl_4$). *J. Chem. Eng. Data* **1983,** *28*, 349-350.

118. Taha, Z. A. Silica-supported vanadium complexes: Structure, characterization and reactivity, especially towards olefins. University of Ottawa (Canada), 2004.

119. Morrow, B.; McFarlan, A. Infrared and gravimetric study of an aerosil and a precipitated silica using chemical and hydrogen/deuterium exchange probes. *Langmuir* **1991,** *7*, 1695-1701.

120. Taha, Z. A.; Deguns, E. W.; Chattopadhyay, S.; Scott, S. L. Formation of Digallium Sites in the Reaction of Trimethylgallium with Silica. *Organometallics* **2006,** *25*, 1891-1899.

121. McCool, B.; Tripp, C. P. Inaccessible Hydroxyl Groups on Silica Are Accessible in Supercritical CO_2. *J. Phys. Chem. B* **2005,** *109*, 8914-8919.

122. Borg, S.; Liu, W.; Etschmann, B.; Tian, Y.; Brugger, J. An XAS study of molybdenum speciation in hydrothermal chloride solutions from 25–385 °C and 600 bar. *Geochim. Cosmochim. Acta* **2012,** *92*, 292-307.

123. Davenport, A. J.; Dent, A. J.; Monir, M.; Hammons, J. A.; Ghahari, S. M.; Quinn, P. D.; Rayment, T. XANES Study of the Chemistry of Molybdenum in Artificial Corrosion Pits in 316L Stainless Steel. *J. Electrochem. Soc.* **2011,** *158*, C111-C117.

124. Atovmyan, L. O.; Aliev, Z. G.; Tarakanov, B. M. The crystal structure of MoO_2Cl_2 and WO_2I_2. *J. Struct. Chem.* **1969,** *9*, 985-986.

125. Abrahams, I.; Nowinski, J. L.; Bruce, P. G.; Gibson, V. C. The Disordered Structure of WO_2Cl_2: A Powder Diffraction Study. *J. Solid State Chem.* **1993,** *102*, 140-145.

126. Dimakis, N.; Bunker, G. Ab initio single- and multiple-scattering EXAFS Debye-Waller factors: Raman and infrared data. *Phys. Rev. B* **1998,** *58*, 2467-2475.

127. Rehr, J. J.; Albers, R. C. Theoretical approaches to x-ray absorption fine structure. *Rev. Mod. Phys.* **2000,** *72*, 621-654.

128. Taylor, M. J.; Jirong, W.; Rickard, C. E. F. Preparation and Crystal-Structure of $MoO_2Cl_2(H_2O)_2 \cdot H_2O \cdot Et_4NCl$ in Relation to the Nature of the Molybdenum(VI) Species in Hydrochloric-Acid Solutions. *Polyhedron* **1993,** *12*, 1433-1435.

129. Ichikuni, N.; Nakao, Y.; Ishizuki, K.; Hara, T.; Shimazu, S. Effect of Local Structure of Mo Oxide on Selective Photo-Oxidation of Propane to Acetone. *Catal. Lett.* **2013,** *143*, 154-158.

130. Ohler, N.; Bell, A. T. Study of the Elementary Processes Involved in the Selective Oxidation of Methane over MoO_x/SiO_2. *J. Phys. Chem. B* **2006,** *110*, 2700-2709.

131. Takenaka, S.; Tanaka, T.; Funabiki, T.; Yoshida, S. Structures of Molybdenum Species in Silica-Supported Molybdenum Oxide and Alkali-Ion-Modified Silica-Supported Molybdenum Oxide. *J. Phys. Chem. B* **1998,** *102*, 2960-2969.

132. Handzlik, J. Application of the ONIOM (QM/QM) method in the study of molybdena–silica system active in olefin metathesis. *Int. J. Quantum Chem.* **2007,** *107*, 2111-2119.

133. Fleischman, S. D.; Scott, S. L. Evidence for the pairwise disposition of grafting sites on highly dehydroxylated silicas via their reactions with $Ga(CH_3)_3$. *J. Am. Chem. Soc.* **2011,** *133*, 4847-55.

134. Fong, A.; Yuan, Y.; Ivry, S. L.; Scott, S. L.; Peters, B. Computational Kinetic Discrimination of Ethylene Polymerization Mechanisms for the Phillips (Cr/SiO_2) Catalyst. *ACS Catal.* **2015,** *5*, 3360-3374.

135. Fong, A.; Peters, B.; Scott, S. L. One-Electron-Redox Activation of the Reduced Phillips Polymerization Catalyst, via Alkylchromium(IV) Homolysis: A Computational Assessment. *ACS Catal.* **2016,** *6*, 6073-6085.

136. Goldsmith, B. R.; Sanderson, E. D.; Bean, D.; Peters, B. Isolated catalyst sites on amorphous supports: A systematic algorithm for understanding heterogeneities in structure and reactivity. *J. Chem. Phys.* **2013,** *138*, 204105.

137. Peters, B.; Scott, S. L. Single atom catalysts on amorphous supports: A quenched disorder perspective. *J. Chem. Phys.* **2015,** *142*, 104708.

138. Heckelsberg, L. F.; Banks, R. L.; Bailey, G. C. A Tungsten Oxide on Silica Catalyst for Phillips Triolefin Process. *Ind. Eng. Chem. Prod. Res. Dev.* **1968,** *7*, 29-31.

139. Lutz, E. F. Shell Higher Olefins Process. *J. Chem. Educ.* **1986,** *63*, 202-203.

140. Mol, J. C. Industrial applications of olefin metathesis. *J. Mol. Catal. A: Chem.* **2004,** *213*, 39-45.

141. Grünert, W.; Stakheev, A. Y.; Feldhaus, R.; Anders, K.; Shpiro, E. S.; Minachev, K. M. Reduction and metathesis activity of MoO_3/Al_2O_3 catalysts II. The activation of MoO_3/Al_2O_3 catalysts. *J. Catal.* **1992,** *135*, 287-299.

142. Rappe, A. K.; Goddard, W. A. Olefin Metathesis. A mechanistic Study of High-Valent Group 6 Catalysts. *J. Am. Chem. Soc.* **1982,** *104*, 448-456.

143. Chauvin, Y.; Commereuc, D. Chemical counting and characterization of the active sites in the rhenium oxide/alumina metathesis catalyst. *J. Chem. Soc., Chem. Commun.* **1992**, 462-464.

144. Shelimov, B.; Elev, L.; Kazansky, V. Use of photoreduction for activation of silica-molybdena catalysts for propylene metathesis: Comparison with thermal reduction. *J. Catal.* **1986,** *98*, 70-81.

145. Zhang, F.; Szeto, K. C.; Taoufik, M.; Delevoye, L.; Gauvin, R. M.; Scott, S. L. Enhanced Metathesis Activity and Stability of Methyltrioxorhenium on a Mostly

Amorphous Alumina: Role of the Local Grafting Environment. *J. Am. Chem. Soc.* **2018,** *140*, 13854-13868.

146. Michorczyk, P.; Węgrzyniak, A.; Węgrzynowicz, A.; Handzlik, J. Simple and Efficient Way of Molybdenum Oxide-Based Catalyst Activation for Olefins Metathesis by Methane Pretreatment. *ACS Catal.* **2019**, 11461-11467.

147. Lin, C.; Tao, K.; Yu, H.; Hua, D.; Zhou, S. Enhanced catalytic performance of molybdenum-doped mesoporous SBA-15 for metathesis of 1-butene and ethene to propene. *Catal. Sci. Technol.* **2014,** *4*, 4010-4019.

148. Mazur, A. S.; Vovk, M. A.; Tolstoy, P. M. Solid-state ^{13}C NMR of carbon nanostructures (milled graphite, graphene, carbon nanotubes, nanodiamonds, fullerenes) in 2000–2019: a mini-review. *Fullerenes, Nanotubes and Carbon Nanostructures* **2020,** *28*, 202-213.

149. Schrock, R. R.; Jiang, A. J.; Marinescu, S. C.; Simpson, J. H.; Müller, P. Fundamental Studies of Molybdenum and Tungsten Methylidene and Metallacyclobutane Complexes. *Organometallics* **2010,** *29*, 5241-5251.

150. Schrock, R. R.; Parshall, G. W. σ-Alkyl and-Aryl Complexes of the Group 4-7 Transition Metals. *Chem. Rev.* **1976,** *76*, 243-268.

151. Fox, H. H.; Lee, J. K.; Park, L. Y.; Schrock, R. R. Synthesis of five-and six-coordinate alkylidene complexes of the type $Mo(CHR)(NAr)[OCMe(CF_3)_2]_2S_x$ and their use as living ROMP initiators or Wittig reagents. *Organometallics* **1993,** *12*, 759-768.

152. Handzlik, J.; Ogonowski, J. DFT study of ethene metathesis proceeding on monomeric Mo^{VI} centres of MoO_3/Al_2O_3 catalyst: The role of the molybdacyclobutane intermediate. *J. Mol. Catal. A: Chem.* **2002,** *184*, 371-377.

153. Gordon, C. P.; Yamamoto, K.; Liao, W.-C.; Allouche, F.; Andersen, R. A.; Copéret, C.; Raynaud, C.; Eisenstein, O. Metathesis Activity Encoded in the Metallacyclobutane Carbon-13 NMR Chemical Shift Tensors. *ACS Cent. Sci.* **2017,** *3*, 759-768.

154. Guan, J.; Yang, G.; Zhou, D.; Zhang, W.; Liu, X.; Han, X.; Bao, X. The formation mechanism of Mo-methylidene species over Mo/HBeta catalysts for heterogeneous olefin metathesis: A density functional theory study. *J. Mol. Catal. A: Chem.* **2009,** *300*, 41-47.

155. Evans, J. C.; Bernstein, H. J. THE VIBRATIONAL SPECTRA OF ACETALDEHYDE AND ACETALDEHYDE-d_1. *Can. J. Chem.* **1956,** *34*, 1083-1092.

156. Singh, M.; Zhou, N.; Paul, D. K.; Klabunde, K. J. IR spectral evidence of aldol condensation: Acetaldehyde adsorption over TiO_2 surface. *J. Catal.* **2008,** *260*, 371-379.

157. Zaki, M. I.; Hasan, M. A.; Al-Sagheer, F. A.; Pasupulety, L. Surface Chemistry of Acetone on Metal Oxides: IR Observation of Acetone Adsorption and Consequent Surface Reactions on Silica−Alumina versus Silica and Alumina. *Langmuir* **2000,** *16*, 430-436.

158. Lavrenov, A. V.; Saifulina, L. F.; Buluchevskii, E. A.; Bogdanets, E. N. Propylene production technology: Today and tomorrow. *Catalysis in Industry* **2015,** *7*, 175-187.

159. Blay, V.; Epelde, E.; Miravalles, R.; Perea, L. A. Converting olefins to propene: Ethene to propene and olefin cracking. *Cat. Rev. Sci. Eng.* **2018,** *60*, 278-335.

160. Amghizar, I.; Vandewalle, L. A.; Van Geem, K. M.; Marin, G. B. New Trends in Olefin Production. *Engineering* **2017,** *3*, 171-178.

161. Olsbye, U.; Svelle, S.; Bjørgen, M.; Beato, P.; Janssens, T. V.; Joensen, F.; Bordiga, S.; Lillerud, K. P. Conversion of methanol to hydrocarbons: how zeolite cavity and pore size controls product selectivity. *Angew. Chem. Int. Ed.* **2012,** *51*, 5810-5831.

162. Chen, D.; Holmen, A.; Sui, Z.; Zhou, X. Carbon mediated catalysis: A review on oxidative dehydrogenation. *Chin. J. Catal.* **2014,** *35*, 824-841.

163. Nawaz, Z. Light alkane dehydrogenation to light olefin technologies: a comprehensive review. *Rev. Chem. Eng.* **2015,** *31*, 413-436.

164. Chen, M.; Xu, J.; Su, F.-Z.; Liu, Y.-M.; Cao, Y.; He, H.-Y.; Fan, K.-N. Dehydrogenation of propane over spinel-type gallia–alumina solid solution catalysts. *J. Catal.* **2008,** *256*, 293-300.

165. Matveyeva, A. N.; Zaitseva, N. A.; Mäki-Arvela, P.; Aho, A.; Bachina, A. K.; Fedorov, S. P.; Murzin, D. Y.; Pakhomov, N. A. Fluidized-Bed Isobutane Dehydrogenation over Alumina-Supported Ga_2O_3 and Ga_2O_3–Cr_2O_3 Catalysts. *Ind. Eng. Chem. Res.* **2018,** *57*, 927-938.

166. Xiao, H.; Zhang, J.; Wang, P.; Wang, X.; Pang, F.; Zhang, Z.; Tan, Y. Dehydrogenation of propane over a hydrothermal-synthesized Ga_2O_3–Al_2O_3 catalyst in the presence of carbon dioxide. *Catal. Sci. Technol.* **2016,** *6*, 5183-5195.

167. Xu, B.; Zheng, B.; Hua, W.; Yue, Y.; Gao, Z. Support effect in dehydrogenation of propane in the presence of CO_2 over supported gallium oxide catalysts. *J. Catal.* **2006,** *239*, 470-477.

168. Afonasenko, T. N.; Leont’eva, N. N.; Talzi, V. P.; Smirnova, N. S.; Savel’eva, G. G.; Shilova, A. V.; Tsyrul’nikov, P. G. Synthesis and properties of γ-Ga_2O_3–Al_2O_3 solid solutions. *Russ. J. Phys. Chem.* **2017,** *91*, 1939-1945.

169. Wang, P.; Xu, Z.; Wang, T.; Yue, Y.; Bao, X.; Zhu, H. Unmodified bulk alumina as an efficient catalyst for propane dehydrogenation. *Catal. Sci. Technol.* **2020,** *10*, 3537-3541.

170. Castro-Fernández, P.; Mance, D.; Liu, C.; Moroz, I. B.; Abdala, P. M.; Pidko, E. A.; Copéret, C.; Fedorov, A.; Müller, C. R. Propane Dehydrogenation on Ga_2O_3-Based Catalysts: Contrasting Performance with Coordination Environment and Acidity of Surface Sites. *ACS Catal.* **2021**, 907-924.

171. Hoffman, A. S.; Singh, J. A.; Bent, S. F.; Bare, S. R. In situ observation of phase changes of a silica-supported cobalt catalyst for the Fischer-Tropsch process by the development of a synchrotron-compatible in situ/operando powder X-ray diffraction cell. *J. Synchrotron Radiat.* **2018,** *25*, 1673-1682.

172. Beachley, O. T.; Noble, M. J.; Churchill, M. R.; Lake, C. H. The Dihydronaphthalene Elimination Reaction as a Route to Gallium−Nitrogen Compounds. Crystal and Molecular Structure of $[(PhMe_2CCH_2)_2GaNHPh]_2$. *Organometallics* **1998,** *17*, 3311-3315.

173. Banks, M. A.; Beachley, O. T.; Maloney, J. D.; Rogers, R. D. The chemistry of diphenylphosphine adducts of tris(neopentyl) and tris(trimethylsilyl-methyl)gallium and -indium including the crystal and molecular structure of $(Me_3CCH_2)_3Ga\cdot P(H)Ph_2$. *Polyhedron* **1990,** *9*, 335-342.

174. Ahman, J.; Svensson, G.; Albertsson, J. A Reinvestigation of *β*-Gallium Oxide. *Acta Cryst. C* **1996,** *52*, 1336-1338.

175. Park, H.; Barbier, J. Crystal Structures of New Gallo-Borates $MGa_2B_2O_7$, M=Sr, Ba. *J. Solid State Chem.* **2000,** *154*, 598-602.

176. Robinson, G. H.; Pennington, W. T.; Lee, B.; Self, M. F.; Hrncir, D. C. Isolation of unusual conformations of the [14]aneN_4 aza crown ether: syntheses and molecular structures of $[M(CH_3)_3]_2$[14]aneN_4 (M = aluminum, gallium) and the group 13 heterobimetallic complex $[Al(CH_3)]_2$[14]ane$N_4$$[Ga(CH_3)_3]_2$. *Inorg. Chem.* **1991,** *30*, 809-812.

177. Mason, M. R.; Song, B.; Han, Y.; Hu, X. Reaction of carbon monoxide with tri-tert-butylgallium: The first example of CO insertion into a gallium–carbon bond. *Inorg. Chim. Acta* **2008,** *361*, 3332-3337.

178. Aleksandrov, Y. A.; Druzhkov, O. N.; Baryshnikov, Y. Y.; Postnikova, T. K.; Makin, G. I.; Kozyrkin, B. I. *Russ. J. Gen. Chem* **1980,** *50*, 2129.

179. Aleksandrov, Y. A.; Makin, G. I.; Druzhkov, O. N.; Baryshnikov, Y. Y.; Postnikova, T. K.; Kozyrkin, B. I. Thermal decomposition of triatkyl compounds of gallium. *Russ. J. Gen. Chem* **1981,** *51*, 61.

180. Wong, K. C.; McBurnett, B. G.; Culp, R. D.; Cowley, A. H.; Ekerdt, J. G. Homolysis versus β-hydride elimination in the decomposition of trialkylgallium on GaAs(100). *Surf. Sci.* **1998,** *416*, 480-487.

181. LiBretto, N. J.; Xu, Y.; Quigley, A.; Edwards, E.; Nargund, R.; Vega-Vila, J. C.; Caulkins, R.; Saxena, A.; Gounder, R.; Greeley, J.; Zhang, G.; Miller, J. T. Olefin oligomerization by main group Ga^{3+} and Zn^{2+} single site catalysts on SiO_2. *Nat. Commun.* **2021,** *12*, 2322.

182. Abdelgaid, M.; Dean, J.; Mpourmpakis, G. Improving alkane dehydrogenation activity on γ-Al_2O_3 through Ga doping. *Catal. Sci. Technol.* **2020,** *10*, 7194-7202.

183. Liu, L.; Corma, A. Metal Catalysts for Heterogeneous Catalysis: From Single Atoms to Nanoclusters and Nanoparticles. *Chem Rev* **2018,** *118*, 4981-5079.

184. Gawande, M. B.; Fornasiero, P.; Zboril, R. Carbon-Based Single-Atom Catalysts for Advanced Applications. *ACS Catal.* **2020,** *10*, 2231-2259.

185. Ding, S. P.; Hulsey, M. J.; Perez-Ramirez, J.; Yang, N. Transforming Energy with Single-Atom Catalysts. *Joule* **2019,** *3*, 2897-2929.

186. Qin, R.; Liu, K.; Wu, Q.; Zheng, N. Surface Coordination Chemistry of Atomically Dispersed Metal Catalysts. *Chem. Rev.* **2020,** *120*, 11810-11899.

187. Gerber, I. C.; Serp, P. A Theory/Experience Description of Support Effects in Carbon-Supported Catalysts. *Chem Rev* **2020,** *120*, 1250-1349.

188. Qin, R.; Liu, K.; Wu, Q.; Zheng, N. Surface Coordination Chemistry of Atomically Dispersed Metal Catalysts. *Chem. Rev.* **2020,** *120*, 11810-11899.

189. Zhang, L.; Zhou, M.; Wang, A.; Zhang, T. Selective Hydrogenation over Supported Metal Catalysts: From Nanoparticles to Single Atoms. *Chem Rev* **2020,** *120*, 683-733.

190. Wang, J.; Zhao, X.; Lei, N.; Li, L.; Zhang, L.; Xu, S.; Miao, S.; Pan, X.; Wang, A.; Zhang, T. Hydrogenolysis of Glycerol to 1,3-propanediol under Low Hydrogen Pressure over WOx -Supported Single/Pseudo-Single Atom Pt Catalyst. *ChemSusChem* **2016,** *9*, 784-90.

191. Vile, G.; Albani, D.; Nachtegaal, M.; Chen, Z.; Dontsova, D.; Antonietti, M.; Lopez, N.; Perez-Ramirez, J. A stable single-site palladium catalyst for hydrogenations. *Angew Chem Int Ed* **2015,** *54*, 11265-9.

192. Zhang, B.; Asakura, H.; Zhang, J.; Zhang, J.; De, S.; Yan, N. Stabilizing a Platinum1 Single-Atom Catalyst on Supported Phosphomolybdic Acid without Compromising Hydrogenation Activity. *Angew. Chem. Int. Ed. Engl.* **2016,** *55*, 8319-23.

193. Lin, L.; Yao, S.; Gao, R.; Liang, X.; Yu, Q.; Deng, Y.; Liu, J.; Peng, M.; Jiang, Z.; Li, S.; Li, Y. W.; Wen, X. D.; Zhou, W.; Ma, D. A highly CO-tolerant atomically dispersed Pt catalyst for chemoselective hydrogenation. *Nat Nanotechnol* **2019,** *14*, 354-361.

194. Liu, P.; Zhao, Y.; Qin, R.; Mo, S.; Chen, G.; Gu, L.; Chevrier, D. M.; Zhang, P.; Guo, Q.; Zang, D.; Wu, B.; Fu, G.; Zheng, N. Photochemical route for synthesizing atomically dispersed palladium catalysts. *Science* **2016,** *352*, 797-801.

195. Wang, S.; Zhang, K.; Li, H.; Xiao, L.-P.; Song, G. Selective hydrogenolysis of catechyl lignin into propenylcatechol over an atomically dispersed ruthenium catalyst. *Nat. Commun.* **2021,** *12*, 416.

196. Ye, X.; Yang, C.; Pan, X.; Ma, J.; Zhang, Y.; Ren, Y.; Liu, X.; Li, L.; Huang, Y. Highly Selective Hydrogenation of CO2 to Ethanol via Designed Bifunctional Ir1–In2O3 Single-Atom Catalyst. *J. Am. Chem. Soc.* **2020,** *142*, 19001-19005.

197. Liu, G.; Robertson, A. W.; Li, M. M.-J.; Kuo, W. C.; Darby, M. T.; Muhieddine, M. H.; Lin, Y.-C.; Suenaga, K.; Stamatakis, M.; Warner, J. H. MoS 2 monolayer catalyst doped with isolated Co atoms for the hydrodeoxygenation reaction. *Nature chemistry* **2017,** *9*, 810.

198. Liu, L.; Corma, A. Isolated metal atoms and clusters for alkane activation: translating knowledge from enzymatic and homogeneous to heterogeneous systems. *Chem* **2021**.

199. Nordlander, P.; Holloway, S.; Nørskov, J. K. Hydrogen adsorption on metal surfaces. *Surf. Sci.* **1984,** *136*, 59-81.

200. Dunham, N. P.; Arnold, F. H. Nature's Machinery, Repurposed: Expanding the Repertoire of Iron-Dependent Oxygenases. *ACS Catal* **2020,** *10*, 12239-12255.

201. Li, J.; Zhang, J.; Wang, S.; Xu, G.; Wang, H.; Vlachos, D. G. Chemoselective Hydrodeoxygenation of Carboxylic Acids to Hydrocarbons over Nitrogen-Doped Carbon–Alumina Hybrid Supported Iron Catalysts. *ACS Catal.* **2019,** *9*, 1564-1577.

202. Bullock, R. M.; Chen, J. G.; Gagliardi, L.; Chirik, P. J.; Farha, O. K.; Hendon, C. H.; Jones, C. W.; Keith, J. A.; Klosin, J.; Minteer, S. D.; Morris, R. H.; Radosevich, A. T.; Rauchfuss, T. B.; Strotman, N. A.; Vojvodic, A.; Ward, T. R.; Yang, J. Y.; Surendranath, Y. Using nature's blueprint to expand catalysis with Earth-abundant metals. *Science* **2020,** *369*, eabc3183.

203. Tejeda-Serrano, M.; Mon, M.; Ross, B.; Gonell, F.; Ferrando-Soria, J.; Corma, A.; Leyva-Perez, A.; Armentano, D.; Pardo, E. Isolated Fe(III)-O Sites Catalyze the Hydrogenation of Acetylene in Ethylene Flows under Front-End Industrial Conditions. *J Am Chem Soc* **2018,** *140*, 8827-8832.

204. Langeslay, R. R.; Sohn, H.; Hu, B.; Mohar, J. S.; Ferrandon, M.; Liu, C.; Kim, H.; Jeremy Kropf, A.; Yang, C.; Niklas, J.; Poluektov, O. G.; Ercan Alp, E.; Ignacio-de Leon, P.; Sattelberger, A. P.; Hock, A. S.; Delferro, M. Nuclearity effects in supported, single-site Fe(ii) hydrogenation pre-catalysts. *Dalton Trans.* **2018,** *47*, 10842-10846.

205. Liu, W.; Chen, Y.; Qi, H.; Zhang, L.; Yan, W.; Liu, X.; Yang, X.; Miao, S.; Wang, W.; Liu, C.; Wang, A.; Li, J.; Zhang, T. A Durable Nickel Single-Atom Catalyst for Hydrogenation Reactions and Cellulose Valorization under Harsh Conditions. *Angew. Chem. Int. Ed.* **2018,** *57*, 7071-7075.

206. Luo, Z.; Nie, R.; Nguyen, V. T.; Biswas, A.; Behera, R. K.; Wu, X.; Kobayashi, T.; Sadow, A.; Wang, B.; Huang, W.; Qi, L. Transition metal-like carbocatalyst. *Nat Commun* **2020,** *11*, 4091.

207. Aasa, R. Powder Line Shapes in the Electron Paramagnetic Resonance Spectra of High‐Spin Ferric Complexes. *J. Chem. Phys.* **1970,** *52*, 3919-3930.

208. Bou-Abdallah, F.; Chasteen, N. D. Spin concentration measurements of high-spin (g′ = 4.3) rhombic iron(III) ions in biological samples: theory and application. *JBIC Journal of Biological Inorganic Chemistry* **2008,** *13*, 15-24.

209. Liu, W.; Zhang, L.; Liu, X.; Liu, X.; Yang, X.; Miao, S.; Wang, W.; Wang, A.; Zhang, T. Discriminating Catalytically Active FeNx Species of Atomically Dispersed Fe-N-C Catalyst for Selective Oxidation of the C-H Bond. *J Am Chem Soc* **2017,** *139*, 10790-10798.

210. Jiang, R.; Li, L.; Sheng, T.; Hu, G.; Chen, Y.; Wang, L. Edge-Site Engineering of Atomically Dispersed Fe-N4 by Selective C-N Bond Cleavage for Enhanced Oxygen Reduction Reaction Activities. *J Am Chem Soc* **2018,** *140*, 11594-11598.

211. Rossi, G.; d'Acapito, F.; Amidani, L.; Boscherini, F.; Pedio, M. Local environment of metal ions in phthalocyanines: K-edge X-ray absorption spectra. *Phys. Chem. Chem. Phys.* **2016,** *18*, 23686-23694.

212. Funke, H.; Chukalina, M.; Scheinost, A. C. A new FEFF-based wavelet for EXAFS data analysis. *J Synchrotron Radiat* **2007,** *14*, 426-32.

213. Gu, J.; Hsu, C.-S.; Bai, L.; Chen, H. M.; Hu, X. Atomically dispersed Fe³⁺ sites catalyze efficient CO₂ electroreduction to CO. *Science* **2019,** *364*, 1091.

214. de Villiers, K. A.; Marques, H. M.; Egan, T. J. The crystal structure of halofantrine-ferriprotoporphyrin IX and the mechanism of action of arylmethanol antimalarials. *J. Inorg. Biochem.* **2008,** *102*, 1660-7.

215. de Villiers, K. A.; Gildenhuys, J.; le Roex, T. Iron(III) protoporphyrin IX complexes of the antimalarial Cinchona alkaloids quinine and quinidine. *ACS Chem Biol* **2012,** *7*, 666-71.

216. Ma, B.; Jiang, J. X.; Hu, C. J. Synthesis and Characterization of a Novel Phenol-tailed Porphyrin Ligand and Its Iron(III) Complex. *Z. Anorg. Allg. Chem.* **2013,** *639*, 676-680.

217. Kanamori, D.; Yamada, Y.; Onoda, A.; Okamura, T.-a.; Adachi, S.; Yamamoto, H.; Ueyama, N. Structures and properties of octaethylporphinato(phenolate)iron(III) complexes with NH···O hydrogen bonds: modulation of Fe–O bond character by the hydrogen bond. *Inorg. Chim. Acta* **2005,** *358*, 331-338.

218. Barkigia, K. M.; Palacio, M.; Sun, Y.; Nogues, M.; Renner, M. W.; Varret, F.; Battioni, P.; Mansuy, D.; Fajer, J. Air-stable, electron-deficient Fe(II) catalytic porphyrins. Characterization and molecular structures of rare high spin Fe(II) hexacoordinated porphyrins. *Inorg Chem* **2002,** *41*, 5647-9.

219. Wang, J.; Schopfer, M. P.; Puiu, S. C.; Sarjeant, A. A.; Karlin, K. D. Reductive coupling of nitrogen monoxide (*NO) facilitated by heme/copper complexes. *Inorg Chem* **2010,** *49*, 1404-19.

220. Kastner, M. E.; Scheidt, W. R.; Mashiko, T.; Reed, C. A. Molecular structure of diaquo-.alpha.,.beta.,.gamma.,.delta.-tetraphenylporphinatoiron(III) perchlorate and perchlorato-.alpha.,.beta.,.gamma.,.delta.-tetraphenylporphinatoiron(III). Two new structural types for iron(III) porphyrins. *J. Am. Chem. Soc.* **2002,** *100*, 666-667.

221. Thompson, D. W.; Kretzer, R. M.; Lebeau, E. L.; Scaltrito, D. V.; Ghiladi, R. A.; Lam, K. C.; Rheingold, A. L.; Karlin, K. D.; Meyer, G. J. Synthesis, characterization, and laser flash photolysis reactivity of a carbonmonoxy heme complex. *Inorg Chem* **2003,** *42*, 5211-8.

222. Li, X.; Cao, C.-S.; Hung, S.-F.; Lu, Y.-R.; Cai, W.; Rykov, A. I.; Miao, S.; Xi, S.; Yang, H.; Hu, Z.; Wang, J.; Zhao, J.; Alp, E. E.; Xu, W.; Chan, T.-S.; Chen, H.; Xiong, Q.; Xiao, H.; Huang, Y.; Li, J.; Zhang, T.; Liu, B. Identification of the Electronic and Structural Dynamics of Catalytic Centers in Single-Fe-Atom Material. *Chem* **2020,** *6*, 3440-3454.

223. Zhang, J.; Teo, J.; Chen, X.; Asakura, H.; Tanaka, T.; Teramura, K.; Yan, N. A Series of NiM (M = Ru, Rh, and Pd) Bimetallic Catalysts for Effective Lignin Hydrogenolysis in Water. *ACS Catal.* **2014,** *4*, 1574-1583.

224. Gao, F.; Webb, J. D.; Sorek, H.; Wemmer, D. E.; Hartwig, J. F. Fragmentation of Lignin Samples with Commercial Pd/C under Ambient Pressure of Hydrogen. *ACS Catal.* **2016,** *6*, 7385-7392.

225. Huang, G.; Wagner, T.; Wodrich, M. D.; Ataka, K.; Bill, E.; Ermler, U.; Hu, X.; Shima, S. The atomic-resolution crystal structure of activated [Fe]-hydrogenase. *Nature Catalysis* **2019,** *2*, 537-543.

226. Zuo, W.; Lough, A. J.; Li, Y. F.; Morris, R. H. Amine(imine)diphosphine Iron Catalysts for Asymmetric Transfer Hydrogenation of Ketones and Imines. *Science* **2013,** *342*, 1080-1083.

227. Vinu, A. Two-Dimensional Hexagonally-Ordered Mesoporous Carbon Nitrides with Tunable Pore Diameter, Surface Area and Nitrogen Content. *Adv. Funct. Mater.* **2008,** *18*, 816-827.

228. Muñoz, M.; Argoul, P.; Farges, F. o. Continuous Cauchy wavelet transform analyses of EXAFS spectra: A qualitative approach. *Am. Mineral.* **2003,** *88*, 694-700.

229. de Villiers, K. A.; Marques, H. M.; Egan, T. J. The crystal structure of halofantrine–ferriprotoporphyrin IX and the mechanism of action of arylmethanol antimalarials. *J. Inorg. Biochem.* **2008,** *102*, 1660-1667.